

FINAL REPORT

Development of Demonstrably Predictive Models for Emissions
from Alternative Fuels Based Aircraft Engines

SERDP Project WP-2151

MAY 2017

Venkat Raman
University of Michigan

Noel Clemens
University of Texas at Austin

Michael Frenklach
University of California, Berkeley

Heinz Pitsch
RWTH University

Distribution Statement A
This document has been cleared for public release



Page Intentionally Left Blank

This report was prepared under contract to the Department of Defense Strategic Environmental Research and Development Program (SERDP). The publication of this report does not indicate endorsement by the Department of Defense, nor should the contents be construed as reflecting the official policy or position of the Department of Defense. Reference herein to any specific commercial product, process, or service by trade name, trademark, manufacturer, or otherwise, does not necessarily constitute or imply its endorsement, recommendation, or favoring by the Department of Defense.

Page Intentionally Left Blank

REPORT DOCUMENTATION PAGE

*Form Approved
OMB No. 0704-0188*

Public reporting burden for this collection of information is estimated to average 1 hour per response, including the time for reviewing instructions, searching existing data sources, gathering and maintaining the data needed, and completing and reviewing this collection of information. Send comments regarding this burden estimate or any other aspect of this collection of information, including suggestions for reducing this burden to Department of Defense, Washington Headquarters Services, Directorate for Information Operations and Reports (0704-0188), 1215 Jefferson Davis Highway, Suite 1204, Arlington, VA 22202-4302. Respondents should be aware that notwithstanding any other provision of law, no person shall be subject to any penalty for failing to comply with a collection of information if it does not display a currently valid OMB control number. **PLEASE DO NOT RETURN YOUR FORM TO THE ABOVE ADDRESS.**

1. REPORT DATE (DD-MM-YYYY) 04-28-2017	2. REPORT TYPE Project Final Report	3. DATES COVERED (From - To) 05/2011-03/2017		
4. TITLE AND SUBTITLE Development of Demonstrably Predictive Models for Emissions from Alternative Fuels Based Aircraft Engines			5a. CONTRACT NUMBER W912HQ-11-C-0035	5b. GRANT NUMBER WP-2151
			5c. PROGRAM ELEMENT NUMBER	
6. AUTHOR(S) Venkat Raman, Michael Frenklach, Noel Clemens and Heinz Pitsch			5d. PROJECT NUMBER	
			5e. TASK NUMBER	
			5f. WORK UNIT NUMBER	
7. PERFORMING ORGANIZATION NAME(S) AND ADDRESS(ES) AND ADDRESS(ES) The University of Texas at Austin, Austin, TX 78712			8. PERFORMING ORGANIZATION REPORT NUMBER	
9. SPONSORING / MONITORING AGENCY NAME(S) AND ADDRESS(ES) Strategic Environmental Research and Development Program			10. SPONSOR/MONITOR'S ACRONYM(S)	
			11. SPONSOR/MONITOR'S REPORT NUMBER(S)	
12. DISTRIBUTION / AVAILABILITY STATEMENT				
13. SUPPLEMENTARY NOTES				
14. ABSTRACT Renewable bio-derived alternative fuels provide viable options for reducing net greenhouse gas emissions, while increasing energy security by relying on locally-sourced feedstock. Unlike conventional aircraft fuels, which maintain tight bounds on fuel specs, such as physical and chemical properties, alternative fuels might have widely varying composition and properties. This variability introduces uncertainty in their utility, both for fuel certification purposes and their ultimate use as transportation fuel. Hence, the practical use of alternative fuels is predicated on the availability of reliable tools that can estimate performance given some basic information about the physical and chemical composition. In this program, this issue of predictability of fuel performance is addressed. The overarching objective is to develop physics-based models that are fuel-composition sensitive, such that aircraft combustors can be directly simulated to estimate emissions performance.				
15. SUBJECT TERMS Alternative fuels, soot oxidation, laser diagnostics, large eddy simulations				
16. SECURITY CLASSIFICATION OF:		17. LIMITATION OF ABSTRACT UU	18. NUMBER OF PAGES 164	19a. NAME OF RESPONSIBLE PERSON
a. REPORT U	b. ABSTRACT U	c. THIS PAGE U		19b. TELEPHONE NUMBER (include area code)

Page Intentionally Left Blank

Abstract

Objectives: Renewable bio-derived alternative fuels are seen as a viable option to reduce net greenhouse gas emissions, and also provide energy security by relying on locally-sourced feedstock. Unlike conventional aircraft fuels, which maintain tight bounds on fuel specs, such as physical and chemical properties, alternative fuels might have widely varying composition and properties. This variability introduces uncertainty in their utility, both for fuel certification purposes and their ultimate use as transportation fuel. Hence, the practical use of alternative fuels is predicated on the availability of reliable tools that can estimate performance given some basic information about the physical and chemical composition. In particular, the prediction of fuel emissions is important. In this program, this issue of predictability of fuel performance is addressed. The overarching objective is to develop physics-based models that are fuel-composition sensitive, such that aircraft combustors can be directly simulated to estimate emissions performance.

Technical Approach: A fully validated physics-based model for simulating emissions from aircraft combustors is sought. For this purpose, an atomistic to full-scale modeling program was commissioned. In particular, chemistry models that describe both fuel oxidation and particulate emissions from gas turbines were developed. Due to the sensitivity of emissions formation to turbulent mixing, the unsteady and three-dimensional large eddy simulation (LES) approach was used for modeling the full-scale combustors. A critical bottleneck in assessing models is the lack of high-fidelity validation data for turbulence-combustion interaction in alternative fuels based flames. For this purpose, novel laser-diagnostics approaches were used to simultaneously measure soot-velocity-temperature fields that vastly enhanced validation capabilities.

Results: The main outcomes of this program are: a) a surrogate-fuel based description of alternative fuels, which allows the development of fuel oxidation mechanisms for any given fuel composition, b) a molecular-dynamics driven oxidation mechanism for soot particulates, which allows fuel-sensitive prediction of particulate emissions, c) a comprehensive large eddy simulation (LES) model for soot-turbulence interaction, developed and implemented in an open source solver and applicable to full-scale gas turbine combustor simulations, and d) an extensive database of high-fidelity laser-diagnostics based planar imaging of alternative-fuels burning turbulent flames, with simultaneous measurement of key validation quantities.

Benefits: This project has significantly advanced the fundamental understanding of emissions formation in aircraft combustors. The main products from this program are a) a comprehensive and openly distributed simulation software for emissions from aircraft combustors, b) an extensive database of high quality validation data, c) fundamental models for soot formation, fuel chemistry, and turbulence-chemistry interactions. Each of these have broader applied beyond aircraft engines, in power generation, chemical processing, and atmospheric transport of particulates.

Contents

A. Summary of Project	1
A-1 Objectives	1
A-2 Approach	1
A-3 Project Team	2
A-4 Main Scientific Outcomes and Key Results	3
A-5 Research Products and Student Training	5
B. Experimental Studies for Alternative Fuels	7
B-1 Jet-Flames-in-Crossflow	8
B-1.1 Experimental Setup	8
B-1.2 Flame Luminosity Measurements	11
B-1.3 Time Averaged velocity, root mean square velocity	12
B-1.4 Conditional Averaging for LES Validation	13
B-2 Simultaneous Mixture Fraction, Soot Volume Fraction and Velocity	16
B-2.1 Motivation	16
B-2.2 Experimental Approach	17
B-2.3 Methodology for Inferring Mixture Fraction and Temperature	21
B-2.4 Kr PLIF Results	22
B-2.5 Summary	28
B-3 Soot Measurements in Surrogate-Fuel Jet Flames	29
B-3.1 Flow Facility	29
B-3.2 Fuel vaporization system	30
B-3.3 Experimental Conditions	31
B-3.4 Soot Volume Fraction	34
B-3.5 Simultaneous LII and PIV	39
C. Fundamental Models for Emissions	44
C-1 Introduction	44
C-2 Methodology	45

C-3	Detailed Kinetic Monte Carlo Simulations of Graphene-Edge Oxidation by Molecular Oxygen	54
C-4	Reactivity of Graphene Edges with Embedded Five-Member Rings	59
C-5	KMC Simulations of High-Temperature Oxidation of Soot Particles in an H ₂ /O ₂ Mixture	72
	C-5.0.1 Effect of Atomic Hydrogen Production	84
C-6	Summary	87
D.	DNS-based analysis of emissions modeling	89
D-1	Introduction	89
D-2	Modeling background	91
D-3	Reduced-order DNS Simulation	92
	D-3.1 Flow specifications	92
	D-3.2 Results	93
D-4	Subfilter Modeling of Soot	95
	D-4.1 Double-delta PDF model	98
	D-4.2 A priori evaluation results	98
E.	Large Eddy Simulation of Soot Formation in Model Aircraft Combustors	102
E-1	DLR atmospheric pressure swirl combustor	105
	E-1.1 Simulation Configuration and Numerical Details	105
	E-1.2 Non-reacting Flow Case	107
	E-1.3 Reacting Flow Cases	108
	E-1.3.1 Gas Phase Results	108
	E-1.3.2 Soot Volume Fraction Results	110
E-2	DLR High Pressure Combustor Configuration	112
	E-2.1 Model and Simulation details	113
	E-2.2 Results and Discussion	115
	E-2.2.1 Gas-Phase Results	115
	E-2.2.2 Statistics and Dynamics of Soot	118
E-3	Conclusions	125
F.	Simulation Tools	127

F-1 Low Dissipation LES Solver in OpenFOAM	127	F-2
Adjoint approach for flames	129	
F-2.1 Background	129	
F-2.2 Computational Methodology	131	
F-2.3 Results	131	
F-2.3.1 Laminar flame simulation results	131	
F-2.3.2 Laminar flame sensitivity results	132	
F-2.4 Conclusions	134	
G. Conclusions and Implications for Future Research		135
H. References		137

List of Figures

1	(Left) Instantaneous images of soot-volume fraction fields of a Jet A/H ₂ flame, U _{st} = 1.5 m/s. (Right) Instantaneous images of soot-volume fraction fields of an m-xylene/H ₂ flame.	3
2	Representative structures seen in the oxidation-only simulations. The displayed snapshot are from a KMC simulation at 2000 K and x _{O2} = 0.001: (a) at the end of the growth period and just before the onset of oxidation, (b) after 1.8 ms of the oxidation. The H atoms saturating the edge carbon atoms are not shown for clarity.	4
3	Contour plot of volume fraction, with red areas corresponding to volume fractions greater than 0.5 parts per million. Isolines are shown for mixture fraction values of Z = 0:6 and Z = 0:8.	5
4	Instantaneous soot volume fraction snapshots separated by 2.5 ms, and overlaid with isocontour of equivalence ratio, = 1:5. White arrows follow a soot pocket generated on the lower center part.	6
5	Schematic diagram of the jet-in-crossflow experiment	9
6	Schematic diagram of the optical setup for combining the lasers.	10
7	Flame luminosity images for partially premixed methane jet flame in cross-flow, (a) Re = 1750, (b) Re = 2000, (c) Re = 3000, (d) Re = 4000, (e) Re = 6000, (f) Re = 8300	11
8	Mean velocity fields for the methane jet in crossflow at a Reynolds number of 2400: (a) u, (b) v, (c) w	12
9	RMS velocity fields for a methane jet in crossflow at a Reynolds number of 2400: (a) uRMS, (b) vRMS, (c) wRMS	13
10	Instantaneous velocities conditioned on the LES-window-averaged values for a 2 mm 2 mm LES window. (a) u velocity, (b) v velocity, and (c) w velocity	15
11	Squared velocity fluctuations conditioned on the LES-window-averaged values for a 2 mm 2 mm LES window. (a) u-velocity, (b) v – velocity, (c) w-velocity.	16
12	Velocity gradients conditioned on the LES-window-averaged values for a 2 mm 2 mm LES window. (a) du/dx conditioned on du=dx ; (b) dv/dx conditioned on dv=dx.	17
13	Energy level diagram for the two photon excitation of krypton.	18
14	Simplified schematics of laser and optical setup for the simultaneous PLIF/PIV/LII measurements.	19

15	A photograph of the non-premixed ethylene-N ₂ -Kr-jet flame. The approximate location of the 10d downstream of the jet exit is marked by the red box.	20
16	A flowchart for mapping Kr PLIF signal to mixture fraction.	23
17	Temperature (left axis), Kr PLIF signal normalized to the reference signal, and mole fraction of Kr times 25 (right axis) against mixture fraction using OPPDIF simulation and collisional quenching rates for 50%C ₂ H ₄ /46%N ₂ /4%Kr (by volume) non-premixed flames depending on various strain rates. Solid line: K _{local} = 300 s ⁻¹ ; dashed line: K _{local} = 800 s ⁻¹ ; and dashed-dotted line: K _{local} = 1000 s ⁻¹	24
18	Instantaneous simultaneous f _v (gray-scale-contour line) and U _{stoic} (white line) derived from the PIV field. The (a) Z from the Kr PLIF, and (b) T from the Kr PLIF are superimposed on the axial velocity field. f _{v,max} = 5.4 ppb ..	25
19	(a) Profiles of instantaneous Z by Kr PLIF (Z _{st} = 0.128) and axial velocity by PIV (U _{stoic} = 2.2 m/s) (b) and (c) Profiles of instantaneous temperature by Kr PLIF and soot volume fraction by LII. Measurements are made at 10d above the jet exit. Black dashed lines mark Z _{st} = 0.128 and red dotted lines mark Z = 0.3	26
20	Profiles of mean temperature and mixture fraction by Kr PLIF, and nor-malized f _v by LII over 1280 instantaneous images at 10d above the jet exit. Comparisons of temperature profiles mapped from mixture fraction (red line) by the Kr PLIF signal and thermocouple measurements with 51 m wire diameter (symbols) along the radial direction at the location of 10d above the jet exit.	27
21	PDF of axial velocity U conditioned on Z _{stoic} (0.127 < Z < 0.129).	28
22	Joint PDFs of mixture fraction (left panel) and soot volume fraction, and temperature (right panel) and soot volume fraction at x/d = 10.	29
23	Experimental setup of a simple jet burner nozzle and co-flow system	30
24	Fuel vaporization system.	31
25	Photographs of Jet A/N ₂ flame with X _{fuel} = 0.2, U ₀ = 3 m/s, and d = 2 cm (left); n-dodecane/N ₂ flame with X _{fuel} = 0.2, U ₀ = 3 m/s, and d = 2 cm (middle); and n-dodecane/N ₂ /H ₂ (0.15/0.07/0.77 by volume) flame with U ₀ = 10 m/s and d = 1 cm (right).	34
26	Photographs of n-dodecane, m-xylene, Jet-A, and JP-8 surrogate	36
27	Instantaneous LII images of the turbulent JetA, JP-8 surrogate, m-xylene, n-dodecane jet flames. Each distribution is composed of stacked slices at different heights. Reynolds number, Re = 8000. Incident laser beam is coming from the RHS.	37

28	Mean (a,b) and RMS (c,d) soot volume fraction measured by LII imaging in a Re = 8000 turbulent non-premixed Jet A and JP-8 surrogate flames. The mean and RMS statistics are computed from 700 instantaneous images taken at each height. Max 36 ppb for JP-8 surrogate and 28 ppb for Jet A.	38
29	Mean profiles of soot volume fraction for Jet-A and JP-8 surrogate at x/d = 7 (top) and 12 (bottom).	39
30	Probability Density Functions of soot volume fraction at x/d = 7 in a Re= 8000 turbulent non-premixed surrogate fuel (left) and Jet-A (right) flames conditioned on $0.95 < jr/dj < 1.05$. The statistics are computed from 500 in-stantaneous images.	40
31	Probability density Function of soot volume fraction at x/d = 12 in a Re = 8000 turbulent non-premixed Jet-A flames conditioned on $0.95 < jr/dj < 1.05$. A scatter plot is shown on the right panel. The statistics are computed from 500 instantaneous images.	41
33	Instantaneous images of soot volume fraction fields of a Jet A/H ₂ flame, U _{st} = 1.5 m/s.	41
32	Mean soot volume fraction measured by LII imaging in a Re = 8000 turbulent non-premixed m-xylene and n-dodecane flames. The mean statistics are computed from 700 instantaneous images taken at each height.	42
34	Instantaneous images of soot volume fraction fields of an m-xylene/H ₂ flame.	42
35	Instantaneous images of soot volume fraction fields of an n-dodecane/H ₂ flame.	43
36	Radial profiles of mean soot volume fraction and axial velocity for (a) Jet A/H ₂ /N ₂ flames and (b) m-xylene/H ₂ /N ₂ flames at x/d = 5.5.	43
37	Diagram of two major pathways: Thermal decomposition of oxyradicals (green) and regeneration of an aromatic radical site (red).	56
38	Substrate size (left) and five-member ring fraction (right) for the oxidation-and-growth simulations at temperatures (a) 1500 K, (b) 2000 K, and (c) 2500 K.	57
39	Reaction-event counts for O ₂ attack on a radical site (blue), thermal decomposition of an oxyradical (green), and regeneration of an aromatic radical (red) for the oxidation-and-growth simulations.	58
40	Substrate size (left) and five-member ring fraction (right) for the oxidation-only simulations at temperatures (a) 1500 K, (b) 2000 K, and (c) 2500 K.	59
41	Reaction-event counts for O ₂ attack on a radical site (blue), thermal decomposition of an oxyradical (green), and regeneration of an aromatic radical site (red) for the oxidation-only simulations.	60

42	Representative structures seen in the oxidation-only simulations. The displayed snapshot are from a KMC simulation at 2000 K and $x_{O_2} = 0.001$: (a) at the end of the growth period and just before the onset of oxidation, (b) after 1.8 ms of the oxidation. The H atoms saturating the edge carbon atoms are not shown for clarity.	61
43	Graphene structures obtained in a KMC simulation at 2000 K and $x_{O_2} = 0.001$ (a) toward the end of the growth period, just before the onset of oxidation, and (b) after 1.6 ms of oxidation. The H atoms saturating the edge carbon atoms are not shown for clarity.	62
44	Cedge-H/Cbasal site ratio versus time.	63
45	Cedge-H/Cbasal site ratio computed at the same conditions as those of upper left corner of Figure 3 with the addition of 1 ms annealing period between growth and oxidation.	64
46	Snapshots of substrates grown at (a) 1500 K and (b) 2000 K at 5 ms. The H atoms saturating the edge carbon atoms are not shown for clarity.	65
47	Event counts for thermal desorption reactions versus time for substrates oxidized at three sets of conditions.	67
48	Number of five-member rings versus time for substrates grown at 1500 (left) or 2000 K (right), and oxidized at 1500 K with $x_{O_2} = 0.1$	68
49	Site distribution at 5 ms (start of annealing), 6 ms (start of oxidation), and 6.2 ms (after 0.2 ms of oxidation) for substrates grown and oxidized under different conditions.	70
50	Diagram of sites used in Figure 12.	71
51	Diagram of the coupling between gas phase and surface chemistry.	74
52	[CO] and [CO ₂] versus time for test cases where the final ring can either fall apart to produce CO and H or not.	75
53	Initial substrates for KMC simulations. The H atoms saturating the edge carbon atoms are not shown for clarity.	76
54	CO and CO ₂ concentration versus time for KMC simulations with different initial substrate sizes.	77
55	Event counts for oxidation and thermal desorption reactions for KMC simulations with different initial substrate sizes.	78
56	Share of carbon atoms removed from the substrate by oxidation and thermal desorption reactions for KMC simulations with different initial substrate size.	79
57	CO and CO ₂ concentration versus time for KMC simulations with different initial substrate shapes.	80

58	Share of carbon atoms removed from the substrate by oxidation and thermal desorption reactions for KMC simulations with different initial sub-strate shape.	80
59	CO and CO ₂ concentration versus time for KMC simulations with different extents of oxidation allowed. Circumcoronene was the initial substrate.	82
60	Event counts for oxidation and thermal desorption reactions for KMC simulations with different extents of oxidation allowed.	83
61	Share of carbon atoms removed by oxidation and thermal desorption reactions for KMC simulations with different extents of oxidation allowed.	83
62	CO and CO ₂ concentration versus time for KMC simulations with different levels of atomic hydrogen production. Circumcoronene was the initial substrate and the extent of oxidation allowed was 100 %.	85
63	[H] versus time for KMC simulations with different rates of atomic hydrogen production. Circumcoronene was the initial substrate and the extent of oxidation allowed was 100 %	85
64	Event counts for oxidation and thermal desorption reactions for KMC simulations with different rates of atomic hydrogen production.	86
65	Share of carbon atoms removed by oxidation and thermal desorption reactions for KMC simulations with different rates of atomic hydrogen production.	87
66	Comparison of mean statistics, conditioned on mixture fraction Z, of the finite-rate chemistry DNS (red) and reduced-order DNS using the FPV model (blue). The left column shows results for temperature T (in Kelvin) at (a) 5 ms (b) 10 ms (c) 15 ms (d) 20 ms. The right column shows results for the mass fraction of OH, Y _{OH} , at (e) 5 ms (f) 10 ms (g) 15 ms (h) 20 ms. .	94
67	Comparison of mean statistics, conditioned on mixture fraction Z, of the finite-rate chemistry DNS (red) and reduced-order DNS directly using the FPV model (green) and using the PAH transport equation model (black). The left column shows results for PAH mass fraction Y _{PAH} (equivalent to naphthalene mass fraction in the finite-rate chemistry DNS) at (a) 5 ms (b) 10 ms (c) 15 ms (d) 20 ms. The right column shows results for chemical reaction rate (solid lines) and dimerization rate (dashed lines), both in units of kg=m ³ =s at (e) 5 ms (f) 10 ms (g) 15 ms (h) 20 ms.	96
68	Contour plots of PAH mass fraction from the reduced-order DNS simulation at 15 ms. (Left) direct evaluation of Y _{PAH} from the FPV model (Right) Y _{PAH} obtained using the PAH transport equation model. The black lines indicate isolines of Z = 0:2 and Z = 0:6.	97
69	Comparison of soot intermittency using the double-delta model to the ex-act value at (a) 7 ms (b) 14 ms. Markers are colored by the value of mixture fraction. The solid line indicates a 1:1 relationship.	99

70	Error in soot intermittency prediction using the double-delta () subfilter pdf for the soot moments plotted against the mixture fraction value Z. The same points are shown in both plots, but different variables are used to color the points: (a) ! (b) M_{10}^g . Results are shown at 7 ms.	100
71	Same as Figure 70, but for results at 14 ms.	101
72	Contour plot of volume fraction, with red areas corresponding to volume fractions greater than 0.5 parts per million. Isolines are shown for mixture fraction values of Z = 0:6 and Z = 0:8.	102
73	Error in soot intermittency prediction using the single-delta () subfilter pdf for the soot moments plotted against the mixture fraction value Z. The same points are shown in both plots, but different variables are used to color the points: (a) ! (from the double-delta model) (b) M_{10}^g . Results are shown at 7 ms.	103
74	Same as Figure 73, but for results at 14 ms.	103
75	(Left) Full three-dimensional grid with secondary inlets marked, (right) The center plane mesh with Pope's critierion. M = 0:2 along the solid lines.	106
76	Flamelet solutions showing (left) progress variable source term and (right) key soot chemistry source terms.	107
77	Mean axial (Uy) and tangential (Ux) velocity contours from LES. The axial velocity is zero along the solid lines.	107
78	Mean axial and tangential velocitues from LES (solid lines) compared to experimental data (circles) at different axial locations.	108
79	Mean axial velocities for the case with and without secondary injection, compared to the experimental PIV data [1]. The axial velocity is zero along the solid lines.	109
80	Mean mixture fraction and temperature fields.	109
81	Mean and RMS temperature profiles along the centerline and two off-center axial lines for the case with secondary air injection. Solid lines and filled cirlces are mean temperature profiles, while dashes and empty circles are RMS values, respectively.	109
82	Instantaneous soot volume fraction snapshots at the center plane every 8 ms for the case without secondary injection.	110
83	Instantaneous soot volume fraction snapshots at the center plane every 8 ms for the case with secondary injection.	111
84	Soot volume fraction statistics for the case without secondary air injection compared to the experiment.	111

85	Soot volume fraction statistics for the case with secondary air injection compared to the experiment.	112
86	Burner geometry, nozzle details, and cross sections at the height of oxidation air injection and the middle of the chamber.	113
87	(Left) Dimer production rate and progress variable source from flamelet library; (right) same quantities along lines (A) and (B) normalized by corresponding peak value at 1 bar pressure.	115
88	3D view and a plane view of the lower half of the computational mesh.	116
89	Center plane view of the two resolutions (coarse on the left, dense on the right) with the Pope's criterion. M=0.2 along the solid lines.	116
90	(Top) Time-averaged and (bottom) instantaneous snapshots of the axial velocity for the two pressure cases and two mesh resolutions for the 3 bar case.	117
91	Axial and tangential velocity profiles at selected axial locations obtained from the 3 bar case compared to the corresponding experiment data, for coarse and dense mesh resolution cases.	119
92	Time-averaged mixture fraction fields for the two pressure cases and two mesh resolutions for 3 bar case.	120
93	(Top) Axial and (bottom) off-center temperature profiles compared to the experimental data obtained at 3 bar conditions. Only dense mesh results are shown for the off-center profiles.	120
94	Instantaneous OH mass fractions from dense grid LES compared to the experiment signal.	121
95	Time-averaged OH mass fractions from dense grid LES compared to the experiment signal.	121
96	Mean soot volume fraction compared to the experiment for the 3 bar case. .	122
97	Mean soot volume fraction compared to the experiment for the 5 bar case. .	122
98	Radial soot volume fraction profiles of dense mesh LES results compared to the experiment.	123
99	Four soot evolution sources of the 5 bar case.	123
100	Soot evolution sources of the 5 bar case plotted along the jet (following line A marked at Fig. 99) and the centerline (line B). Moments are normalized by maximum values obtained in the simulation.	124
101	Instantaneous soot volume fraction snapshots separated by 2.5 ms, and overlaid with isocontour of equivalence ratio, = 1:5. White arrows follow a soot pocket generated on the lower center part.	125

102 Instantaneous snapshots of mixture fraction near the fuel inlet overlaid with soot number density isocontours: (a) 3 bar result on the coarse mesh, (b) 3 bar dense mesh case at different times showcasing the jet-flapping process.	126
103 RMS of soot volume fraction for the two pressure cases.	127
104 Velocity magnitude contours after 1 second of simulation time, for orthogonal and skewed meshes.	128
105 Temporal kinetic energy decay between different numerical approaches for orthogonal and skewed meshes, for two different timestep sizes. Ham and Iaccarino (solid lines,[2]) correspond to both orthogonal and skewed mesh cases.	129
106 Simulation domain	132
107 Temperature (K)	132
108 NOx fields	133
109 Adjoint variable fields for H ₂ , O ₂ , and N ₂	134
110 Adjoint variable fields for OH, O, and N	135

List of Tables

1	The temperature dependence of quenching rates	22
2	Fuel Properties	32
3	Chemicals used	32
4	Common characteristics of jet fuels	33
5	Composition of fuel and operating conditions	35
6	Soot index of refraction	37
7	Proposed vs Accomplished Tasks	44
8	KMC Reactions	47
9	Oxidation rates (C-atom/ms) computed with and without regeneration pathway included	59
10	Initial oxidation rates (C-atom/ms) for substrates with different curvature. . .	66
11	H ₂ /O ₂ combustion mechanism employed in coupled KMC/PFR simulation	73
12	Event counts for oxidation and thermal desorption reactions for KMC simulations with different initial substrate sizes	78
13	Share of carbon atoms removed from the substrate by oxidation and thermal desorption reactions for KMC simulations with different initial substrate size	79
14	Share of carbon atoms removed from the substrate by oxidation and thermal desorption reactions for KMC simulations with different initial substrate shape	81
15	Event counts for oxidation and thermal desorption reactions for KMC simulations with different extents of oxidation allowed	82
16	Share of carbon atoms removed by oxidation and thermal desorption reactions for KMC simulations with different extents of oxidation allowed . . .	84
17	Event counts for oxidation and thermal desorption reactions for KMC simulations with different rates of atomic hydrogen production	87
18	Share of carbon atoms removed by oxidation and thermal desorption reactions for KMC simulations with different rates of atomic hydrogen production.	88
19	Flow parameters used for the simulations. global indicates the global equivalence ratio for these inflow conditions.	113
20	Inlet flow properties	132

A. Summary of Project

In this section, a complete summary of the project, including objectives, personnel, approach, key outcomes and products are provided.

A-1 Objectives

Renewable bio-derived alternative fuels are seen as a viable option to reduce net greenhouse gas emissions, and also provide energy security by relying on locally-sourced feedstock. Unlike conventional aircraft fuels, which maintain tight bounds on fuel specs, such as physical and chemical properties, alternative fuels might have widely varying composition and properties. This variability introduces uncertainty in their utility, both for fuel certification purposes and their ultimate use as transportation fuel. Hence, the practical use of alternative fuels is predicated on the availability of reliable tools that can estimate performance given some basic information about the physical and chemical composition. In particular, the prediction of fuel emissions is important.

In this program, this issue of predictability of fuel performance is addressed. The overarching objective is to develop physics-based models that are fuel-composition sensitive, such that aircraft combustors can be directly simulated to estimate emissions performance.

A-2 Approach

Since the modeling of full scale aircraft combustors is a complex multi-scale multi-physics process, developing a robust model for alternative fuels requires progress on multiple fronts. In particular, robustness in models have to be verified/validated for each sub-process that is part of the overall combustor physics. The overall approach is summarized as follows:

The fuel properties are taken into account using a surrogate model framework. Here, a mixture of well-studied surrogate components are used to match the physical and chemical properties of a given alternative fuel. As long as the models can capture the surrogate component behavior for the range of compositions used, they are deemed accurate to predict the performance of alternative fuels.

To describe a gas turbine combustor, the turbulent combustion process as well as the evolution of soot or other emissions in this background flow needs to be modeled. Such a task requires detailed models from the small scales (chemical reactions, soot evolution) to the largest scales (energy containing turbulence features). The modeling group has experts in each of these areas such that the tools developed here can be bridged to simulate full scale combustors. In particular, we have developed models for soot and NO_x formation, turbulence-chemistry interaction, and full-scale combustor simulations.

At each scale, the models have to be validated. The research program consists of a ded-

icated experimental group that develops diagnostic tools as well as data for validating turbulent combustion models. At the same time, this data has been used to answer fundamental issues regarding turbulence-soot interaction, as well as to develop methods for comparing simulation and experimental data. When in-house experiments are not available, we have used reliable external data for validation.

As will be discussed below, one of the intended products of this project is the public dissemination of models, tools, and data generated through this program. For this purpose, we have adopted an open source framework, whereby our models are directly incorporated into community-wide toolbase. Hence, the development of models were directly tied to this end product, necessitating resources for the advancement of some of the baseline tools available to the community.

A-3 Project Team

The project team consists of the following members

Venkat Raman (PI, University of Michigan): Responsible for the coordination fo the project, reporting to SERDP, as well as external collaborations. For the research program, Raman and his group conduct full scale combustor simulations, and develop tools and models for large eddy simulation of reacting flows with soot formation.

Noel Clemens (co-I, The University of Texas at Austin): Responsible for the experimen-tal part of the program. Clemens and his research group develop laser diagnostic tools for measuring emissions in turbulent flames burning alternative fuels. In addition, he uses other diagnostic approaches to simultaneously measure multiple flow-related quantities (such as velocity, temperature etc.) that provide insight into the physics of soot formation.

Michael Frenklach (co-I, University of California, Berkeley): Responsible for the modeling of soot processes, focusing specifically on the oxidation process that is sensitive to the gas-phase composition. Frenklach and his group develop chemical kinetics mod-els for emissions processes, and have used ab initio techniques to extract rates using a combination of computational chemistry and molecular dynamics.

Heinz Pitsch (co-I, Stanford University & RWTH Aachen University): Responsible for surrogate model development and for understanding the interaction of NO_x and soot emissions inside aircraft combustors. Pitsch and his team develop gas phase kinetics models, numerical approaches for simulating soot population balance equation, and direct numerical simulation of soot processes in turbulent reacting environment.

Each research group consisted of at least one graduate student pursuing a PhD program in their respective institutions. In addition, some research groups employed postdoctoral research associates to accelerate progress in key areas.

A-4 Main Scientific Outcomes and Key Results

A comprehensive discussion of the research outcomes are provided in subsequent sections. Here, the main outcomes along with a sample of the results are summarized.

A comprehensive database of turbulent jet flame measurements for different fuels, that includes detailed measurements of soot volume fraction, mixture fraction, and velocity profiles. Many of these measurements include joint statistics, which is the first of its kind in the study of turbulent sooting flames. As part of this work, a novel Krpyton-planar laser induced fluourescense method was developed, which is now widely used for measuring mixture fraction in turbulent flames.

Figure 1 shows sample images for jet-A and m-xylene fuels. It is seen that soot volume fraction increases substantially as the aromatic content increases in the fuel. The data constains simultaneous velocity and soot volume fraction measurements, providing ac-cess to the impact of turbulence on the evolution of soot structures. Long-time averages were used to obtain statistical information as well.

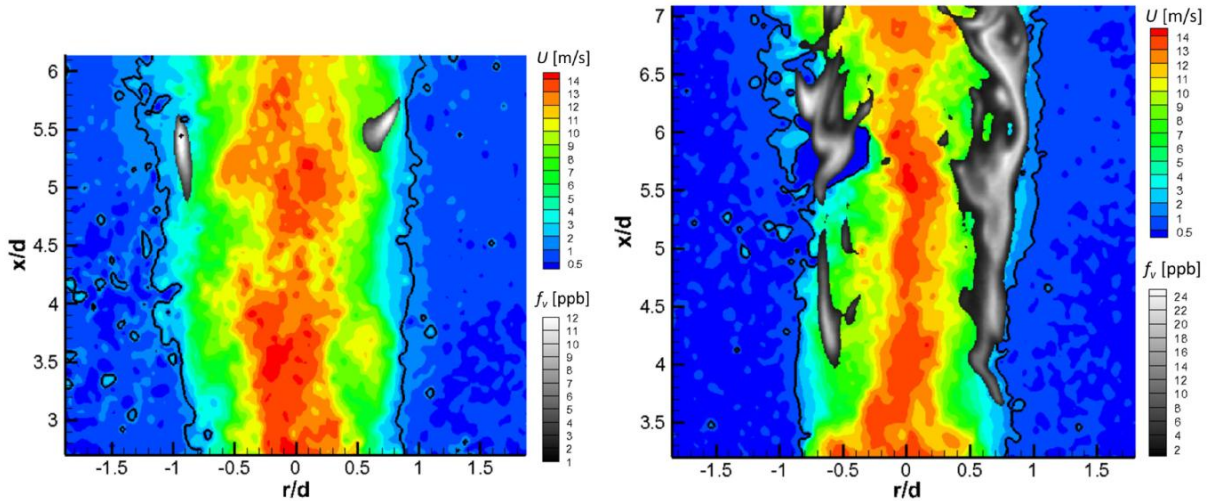


Figure 1: (Left) Instantaneous images of soot-volume fraction fields of a Jet A/H₂ flame, $U_{st} = 1.5$ m/s. (Right) Instantaneous images of soot-volume fraction fields of an m-xylene/H₂ flame.

A new kinetics model for soot oxidation, especially for use in oxygenated fuels, has been developed. This method used very detailed morphological information about soot particles to identify the key physical processes by which oxygen atoms and OH radi-cals attack soot surface, thereby initiating the oxidation process. The resulting kinetics mechanism is included in this report, and published in archival literature. Figure 2 shows sample intermediate soot structures obtained using the ab initio derived kinetic Monte Carlo approach. Such detailed simulations were used to build the reaction rates for the oxidation process.

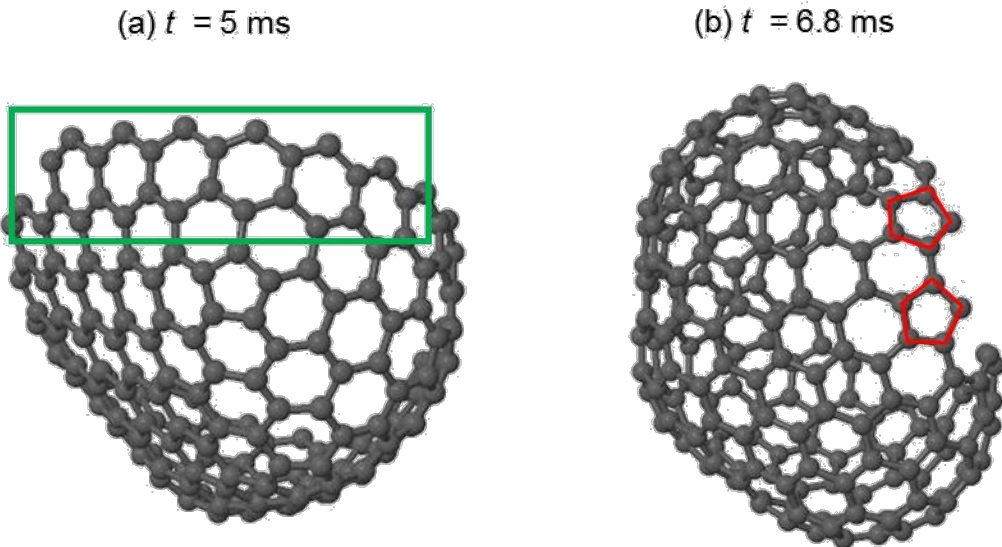


Figure 2: Representative structures seen in the oxidation-only simulations. The displayed snapshot are from a KMC simulation at 2000 K and $x_{O_2} = 0.001$: (a) at the end of the growth period and just before the onset of oxidation, (b) after 1.8 ms of the oxidation. The H atoms saturating the edge carbon atoms are not shown for clarity.

A model for turbulence-soot interactions has been developed based on a database of direct numerical simulations of turbulent sooting flames. In particular, the effect of small-scale soot spatial structure on its evolution has been modeled. Termed soot inter-mittency, this quantity describes the probability that soot is present in any finite volume of the fluid domain. In combination with other tools developed in this program, this model for soot evolution represents the most detailed description of particulate processes. The models are published in archival journals. Figure 3 shows an instantaneous snapshot from the DNS data indicating regions of large soot volume fraction. Further direct validation using experimental data have also been carried out.

Large eddy simulation approach for simulating aircraft combustors burning alternative fuels, and the development of reliable models for such solvers. The LES models include the description of gas phase chemistry using a combintion of probability density function and flamelet/progress variable approach, which has been tested in turbulent jet flames and complex combustors. LES models also require simultaneous advances in numerical algorithms due to the inextricable coupling between computational and modeling components. For this purpose, energy-conserving numerical discretization on collocated numerical grids have been developed. These tools have been used to simulate both simple turbulent jet flames (for validation purposes), and complex aircraft combustor models. Figure 4 shows soot volume fraction contours for a model aircraft combustor, simulated using this low-Mach number LES solver.

Based on these tools, a reliable simulation platform for a variety of fuels has been built. The models have been validated using available experimental data. Further, the entire

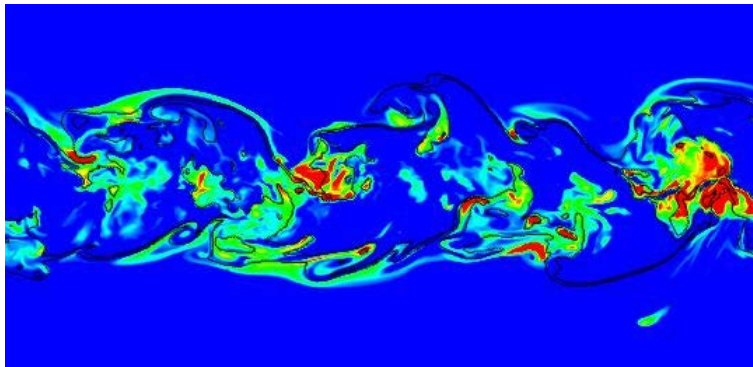


Figure 3: Contour plot of volume fraction, with red areas corresponding to volume fractions greater than 0.5 parts per million. Isolines are shown for mixture fraction values of $Z = 0:6$ and $Z = 0:8$.

tool set is highly modular, allowing any advances in models, experimental data, or numerical approaches to be directly incorporated.

A-5 Research Products and Student Training

The main tangible outcomes of this project can be summarized as follows:

Scientific outcomes: As detailed in Sec. A-4, the outcomes are four-fold: 1) Detailed experiments of alterantive fuels combustion in turbulent flames, 2) Kinetics models for soot oxidation for a range of fuels, 3) LES based models for soot evolution, and 4) LES tools for simulating alternative fuels combustion.

1. D. Yu. Zubarev, X. You, J. McClean, W. A. Lester, Jr., and M. Frenklach, "Patterns of local aromaticity in graphene oxyradicals," *J. Mater. Chem.* **21**, 3404-3409 (2011).
2. X. You, D. Yu. Zubarev, W. A. Lester, Jr., and M. Frenklach, "Thermal decomposition of pentacene oxyradicals," *J. Phys. Chem. A* **115**, 14184-14190 (2011).
3. D. Yu. Zubarev, X. You, M. Frenklach, and W. A. Lester, Jr., "Delocalization effects in pristine and oxidized graphene substrates," in *Advances in the Theory of Quantum Systems in Chemistry and Physics* (P. E. Hoggan, E. J. Brandas, J. Maruani, P. Piecuch, and G. Delgado-Barrio, Eds.), *Progress in Theoretical Chemistry and Physics*, Vol. 22, Springer, Dordrecht, 2012, Chapter 29, pp. 553-569.
4. D. E. Edwards, X. You, D. Yu. Zubarev, W. A. Lester, Jr., and M. Frenklach, "Thermal decomposition of graphene armchair oxyradicals," *Proc. Combust. Inst.* **34**, 1759-1766 (2013).
5. D. E. Edwards, D. Yu. Zubarev, W. A. Lester, Jr., and M. Frenklach, "Pathways to soot oxidation: Reaction of OH with phenanthrene radicals," *J. Phys. Chem. A* **118**, 8606-8613 (2014).
6. V. V. Kislov, R. I. Singh, D. E. Edwards, A. M. Mebel, M. Frenklach, "Rate coefficients and product branching ratios for the oxidation of phenyl and naphthyl radicals: A

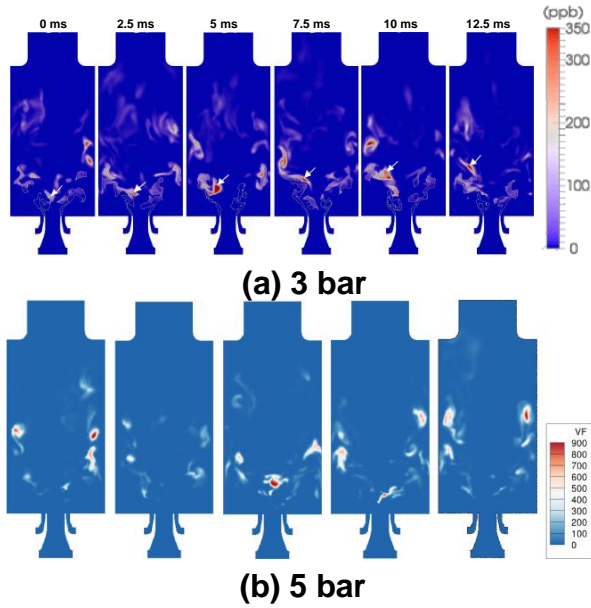


Figure 4: Instantaneous soot volume fraction snapshots separated by 2.5 ms, and overlaid with isocontour of equivalence ratio, = 1:5. White arrows follow a soot pocket generated on the lower center part.

- theoretical RRKM-ME study,” Proc. Combust. Inst. **35**, 1861–1869 (2015).
7. R. Whitesides and M. Frenklach, Z “Effect of reaction kinetics on graphene-edge morphology and composition.”. Phys. Chem. **229**, 597-614 (2015).
 8. R. I. Singh, A. M. Mebel, and M. Frenklach, “Oxidation of graphene-edge six- and five-member rings by molecular oxygen,” J. Phys. Chem. A **119**, 7528–7547 (2015).
 9. R. Singh and M. Frenklach, “A mechanistic study of the influence of graphene curvature on the rate of high-temperature oxidation by molecular oxygen,” Carbon **101**, 203-212 (2016).
 10. P. Donde and V. Raman and M. E. Mueller and H. Pitsch, “LES/PDF based modeling of sootturbulence interactions in turbulent flames”, Proc. Comb. Inst. **34** 1183–1192 (2013).
 11. M. E. Mueller and V. Raman, “Effects of turbulent combustion modeling errors on soot evolution in a turbulent nonpremixed jet flame”, Comb. Flame **161** 1842–1848 (2014)
 12. K. Braman, T. A. Oliver, and V. Raman, ‘Adjoint-based sensitivity analysis of flames”, Comb. Theory Modell. **19**, 29–56 (2015).
 13. H. Koo, M. Hassanaly, V. Raman, M. E. Mueller and K. P. Geigle “Large-eddy simulation of soot formation in a model gas turbine combustor”, J. Engg. Gas Turb. Power **139** 031503 (2016)
 14. V. Raman and R. O. Fox, “Fine particle formation in turbulent flames”, Ann. Rev. of Fluid Mech. **48** 159–190 (2016)

15. L. Cai, H. Pitsch, S. Y. Mohamed, V. Raman, J. Bugler, H. Curran and S. Mani Sarathy, "Optimized reaction mechanism rate rules for ignition of normal alkanes", **Comb. Flame** 173 468–482 (2016).

Databases and Computational Software: The research program generated two different databases: 1) A database of experimental measurements for turbulent jet flames and a variety of fuel compositions, 2) a database of DNS studies aimed at understanding soot-turbulence interactions. Finally, a combustor simulation toolkit has been developed using OpenFOAM open source solver, leading to the first freely disseminated LES tool for aircraft combustors. This solver has been shared with nearly a dozen institutions around the world, and is used by at least industrial research groups. This solver distribution can be obtained by directly contacting the PI (Raman). We plan to curate these solvers for the foreseeable future on large scale data storage systems at both University of Michigan (UM) and the Texas Advanced Computing Center (TACC).

Student training: As part of this program, a number of PhD and post-doctoral students participated in the development of experimental and computational tools. In particular, Ravi Singh (UC Berkeley), Alex Chong (UM), James Sung (UT Austin), Pratik Donde (UT Austin), Ok Joo (UT Austin), Heeseok Koo (UM), Alireza Najafiyazdi (McGill University), and Colleen Kaul (Stanford University) were supported fully or partially through this program.

External collaborations: In order to provide a more robust validation exercise, the PI and the computational groups coordinated with multiple experimental groups around the world, including Profs. Graham Nathan and Bassam Dally at University of Adelaide (Australia), Dr. Wolfgang Mier and Dr. Klaus Peter Geigle at DLR (Germany), and Dr. Christopher Shaddix (Sandia National Laboratory). These collaborations partially contributed to the establishment of an International Sooting Flames Workshop (ISF), which has spanned the duration of the project. This workshop has led to interesting insights on model performance, as well the commissioning of experiments tailored for model validation.

In summary, we are pleased to report a step change in the understanding, modeling, and simulation of aircraft combustor emissions, and incorporation of fuel sensitivity in these models.

In the following sections, detailed reports on the findings in the individual programs will be provided. Finally, a section on auxiliary tools generated during this project is provided.

B. Experimental Studies for Alternative Fuels

The focus of the experimental program was to provide validation data to aid in the improvement of the LES-based combustion models, and so the experiments were specifically designed with validation in mind. Specifically, the flow geometry, operating conditions, and the type of measurements made, were carefully selected to provide data that were

most likely to reveal model inadequacies. It was further necessary to make measurements of quantities to which the models showed significant sensitivity. These considerations both shaped the initial experiments and guided mid-course corrections to the validation plan. With this background in mind, we focused on three main types of experiments.

1. **Jet-flames-in-crossflow.** This flow configuration provides a high degree turbulence-flame interaction and thus provides a challenging test case for the turbulence models. Extensive measurements of the velocity field using particle image velocimetry (PIV) were made over a range of conditions. In the proposed work, we were going to pursue extensive measurements of NO_x emissions, however, later work showed that the combustion models did not exhibit sufficient sensitivity to NO_x emissions to justify these measurements. For this reason, a greater focus was placed on making measurements of soot in simple jet flames.
2. **Mixture Fraction, Velocity and Soot Volume Fraction in Ethylene Jet Flames.** These experiments focused on obtaining validation data in sooting flames that previously were not available. In particular, there were previously no measurements of mixture fraction, temperature and soot volume fraction in sooting flames; however, such data are important quantities in soot modeling. In these experiments we proposed to employ a newly-developed diagnostic, planar laser-induced fluorescence (PLIF) of kryp-ton, to enable mixture fraction measurements to be made in sooting flames. Kr PLIF was combined with laser-induced incandescence (LII) and PIV to obtain simultaneous measurements of mixture fraction, soot volume fraction and velocity in ethylene jet flames. The data that was obtained provide a unique data set that are suitable for validation purposes.
3. **Soot Measurements in Surrogate-Fuel Jet Flames.** About midway through the project, it became clear that it was critical to develop a more detailed database of soot characteristics in turbulent flames burning jet fuel and jet-fuel surrogates. Therefore, a series of experiments were conducted where LII and PIV measurements were made in jet flames with the following fuels: Jet A, m-xylene, n-dodecane, and jet-fuel surrogate (combination of m-xylene + n-dodecane). The data on surrogate fuels, represents a unique data set that are of suitable quality for validation purposes.

B-1 Jet-Flames-in-Crossflow

B-1.1 Experimental Setup

Jet flames in crossflow were studied using the primary diagnostic of stereo-PIV. The jet-in-crossflow facility is shown schematically in Fig. 5, and uses a centrifugal fan to drive the cross-flow of air with a velocity ranging from 1 to 2 m/s. The test section has a cross-section of 0.5m x 0.5m. The jet issues from the floor of the test section. The tunnel is directly connected to an exhaust system to remove the combustion products, and to aid in emissions measurements. Stereoscopic PIV images were taken for two cases using a methane jet. Case 1: $Re_D=2400$, $u_1=0.87$ m/s, and momentum ratio $r = 6.4$; Case 2: $Re_D=6000$, $u_1=0.87$ m/s, and momentum ratio $r=14.5$. Apart from carrying stereoscopic

PIV studies in turbulent combustion, images of flames at various Reynolds number ranging from 1750 to 8300 were taken to visualize attached and detached flame configurations and identifying the most interesting configurations suitable for detailed investigations.

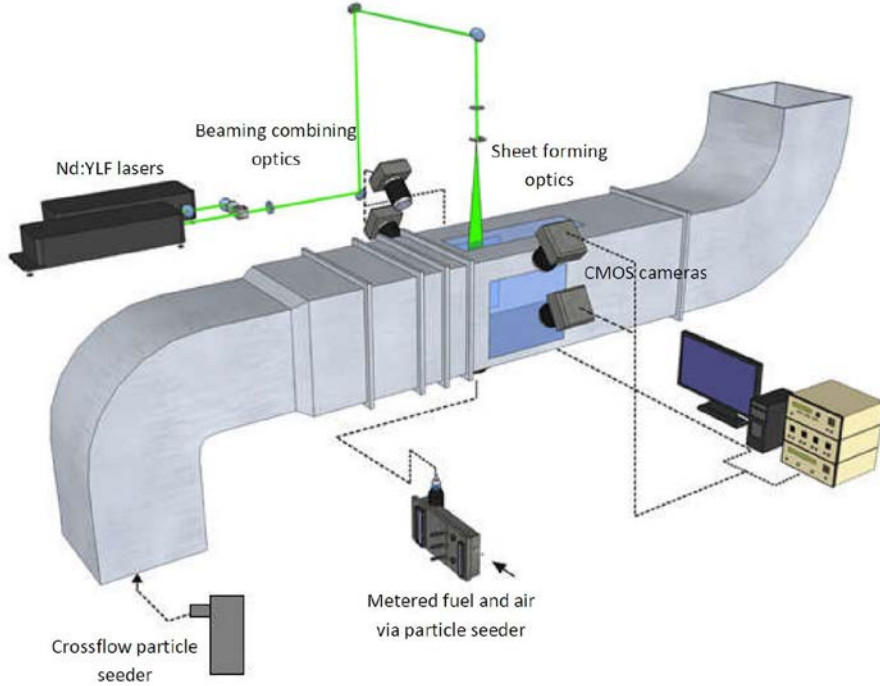


Figure 5: Schematic diagram of the jet-in-crossflow experiment

The stereo PIV system setup, also shown in Fig. 5, employs a pair of high-power, high-repetition rate diode pumped, frequency-doubled Nd:YLF lasers (Coherent Evolution-90) operating at 527 nm to provide the double-pulse illumination of the flow. The Nd:YLF lasers were operated at 3 kHz and 10 mJ per pulse. The two laser beams were combined using standard beam combining techniques. Fig. 6 shows a schematic diagram of the optical arrangement used to combine the output beams from the pair of Nd:YLF lasers. The polarization of one of the two beams (laser pulse 1) was rotated by 90 degrees using a half-wave plate to obtain a vertically polarized beam. The two beams were then combined using a polarizing beam splitter cube (BS) used in reverse. A polarizing beam splitter cube split the incoming laser beam into two orthogonally polarized components. The P-polarized component was transmitted through the cube whereas the S-polarized component was reflected by 90 degrees. By using the polarizing beam splitter cube in reverse two laser beams with orthogonal polarization could be combined into one single beam. The combined beam was therefore cross polarized. It was then necessary to rotate the polarization angle of both components in order to achieve similar light scattering signals (in Mie scattering, that PIV relies on, the scattering properties are strongly influenced by the polarization of the illuminating light). Therefore, a second half-wave plate was installed after the beam splitter polarizing cube. A system of laser mirrors was used to redirect the combined 527 nm double-pulse laser beam to the appropriate location in the flow. A combination of cylindrical and spherical lenses was used to form a thin laser

sheet that covered the field of view of interest.

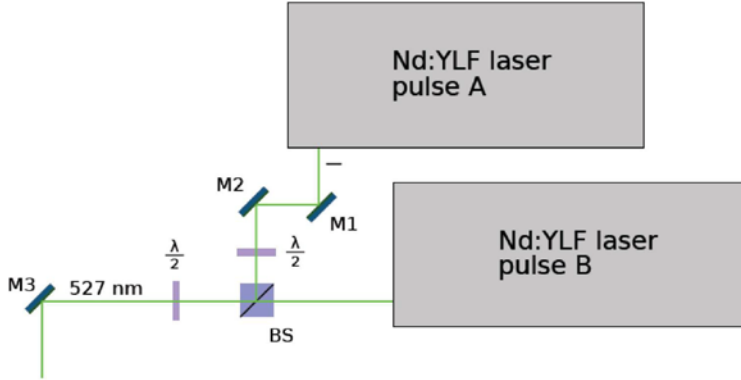


Figure 6: Schematic diagram of the optical setup for combining the lasers.

The particle-field imaging was carried out using high-framing rate CMOS digital cameras (Photron APX) operated in stereoscopic configuration. A forward-backward scattering configuration was employed. The cameras were fitted with Schiempfug adapters and Nikon 105 mm, F/4.0 macro lenses. Achieving the Schiempfug condition enables one to focus across the entire field of view, even though the cameras are tilted with respect to the imaging plane. The cameras were operated in double frame, single exposure frame straddling mode with framing rate twice the triggering frequency of the laser pair. The effective acquisition rate was hence determined by the laser repetition rate.

For the Reynolds number of 2400 case, the cameras were operated at framing rate of 6 kHz and resolution of 512 512 pixels. One camera was operated in forward scatter and the other in backward scatter. The field of view was 40 mm 50 mm giving 12 pixels/mm. For the Reynolds number of 6000 case the framing rate was 2 kHz (with lasers operating at 1 kHz). The field of view is 90 mm 90 mm giving 12 pixels/mm.

The velocity fields were computed using commercial PIV software (LaVision Davis 7.2) with an adaptive, multigrid cross-correlation approach. In this approach, the raw par-ticle images were processed in a multi-pass/ multistep interrogation from 32x32 pixel windows to 12x12 pixel windows with 50% overlap. Prior to processing, the raw images were preprocessed by employing background subtraction on the collected particle images to reduce the background. A standard cross-correlation with no zero padding was em-ployed for extraction of the vector field. A second order cross-correlation was employed for the initial passes and high accuracy Whittaker reconstruction was employed for the fi-nal pass for computing the result. Typically, close to 97% of the vectors were valid and the invalid vectors were removed and replaced using a median filter, 3x3 Gaussian smooth-ing in the vector post processing. Calibration images for stereoscopic reconstruction were generated by translating a calibration grid target placed in the plane of the laser sheet.

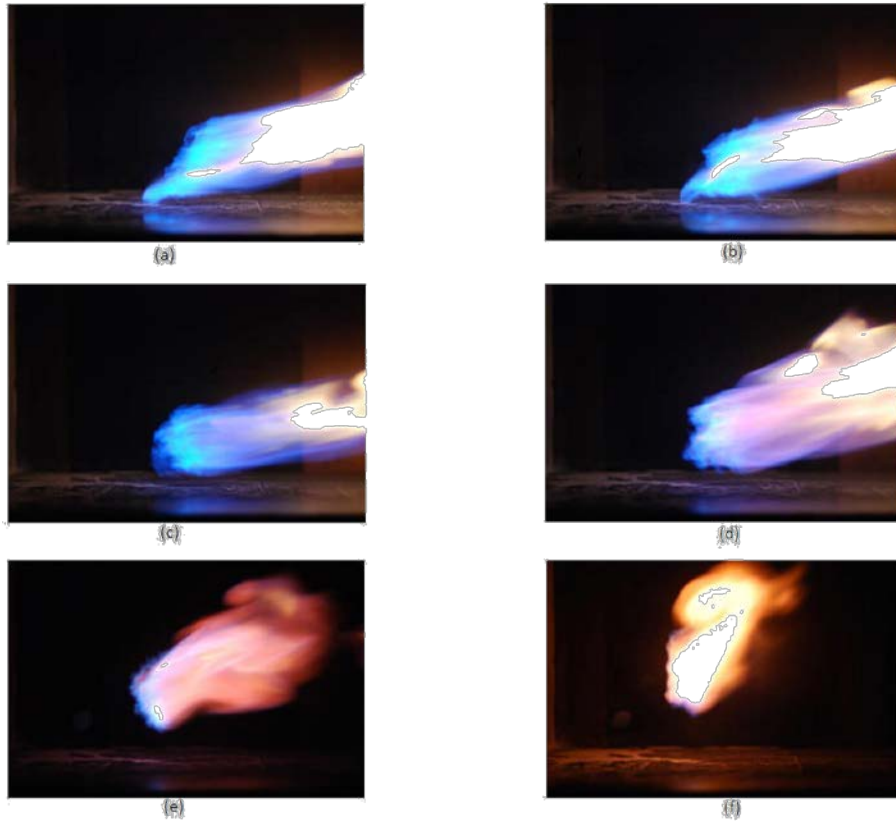


Figure 7: Flame luminosity images for partially premixed methane jet flame in crossflow, (a) $Re = 1750$, (b) $Re = 2000$, (c) $Re = 3000$, (d) $Re = 4000$, (e) $Re = 6000$, (f) $Re = 8300$

B-1.2 Flame Luminosity Measurements

The flames were imaged using a digital SLR camera (Nikon D 80) to investigate the effects of varying Reynolds number on the flame structure. A series of images at increasing Reynolds number are shown in Fig. 7. The crossflow is from left to right at a velocity of 0.87 m/s. It is evident that the flames are attached to the leeward side of the nozzle up to a Reynolds number of 2000, but beyond this extinction is seen on the windward side first and then the flames completely detach for Reynolds numbers above 4000. The lower Reynolds number cases show that the initial region of the flame is blue, and then becomes yellow/white farther downstream. The yellow/white region designates soot formation. The initial blue region is likely extended owing to partial-premixing that occurs due to the lifted section on the windward side of the jet. Note that as the Reynolds number increases, from Fig. 7 (a) to (f), the momentum flux ratio also increases, since the increased Reynolds number is achieved by increasing the jet velocity. Therefore, the reason the highest Reynolds number case is primarily yellow is because its momentum flux ratio is high enough that it penetrates nearly vertically into the cross-flow and so its structure is closer to that of a simple jet flame than a jet-flame-in-crossflow. Essentially, under high momentum-flux conditions, the enhanced mixing of the jet-in-crossflow configuration is not sufficient to consume the added fuel, and so it burns primarily as a non-premixed

flame.

B-1.3 Time Averaged velocity, root mean square velocity

The mean velocity fields, obtained from the stereo-PIV measurements, for all the three velocity components, are shown in Fig. 8. The highest velocities are for the transverse component (v) corresponding to the jet exit velocity and the streamwise component (u) corresponding to the crossflow velocity. At the symmetry plane the cross-stream component (w) averages to a near zero value.

The root-mean-square (RMS) velocities for the three components are shown in Fig. 9. Unlike the mean velocities, the fluctuating velocities are found to occur mainly in the high shear regions associated with the boundaries of the jet. The fluctuations in u , v and w tend to be of similar magnitude on the windward portion of the flame, which is dominated by the shear layer. This result is expected since the shear layer is a highly turbulent region and the windward side of the flame is extinguished, and so it is least affected by the presence of the flame. However, on the leeward side of the flame the u and w components are of similar magnitude, but the v component is smaller. We believe the reason for this is that the leeward side the flow is significantly laminarized and thus the transverse velocity fluctuations are suppressed.

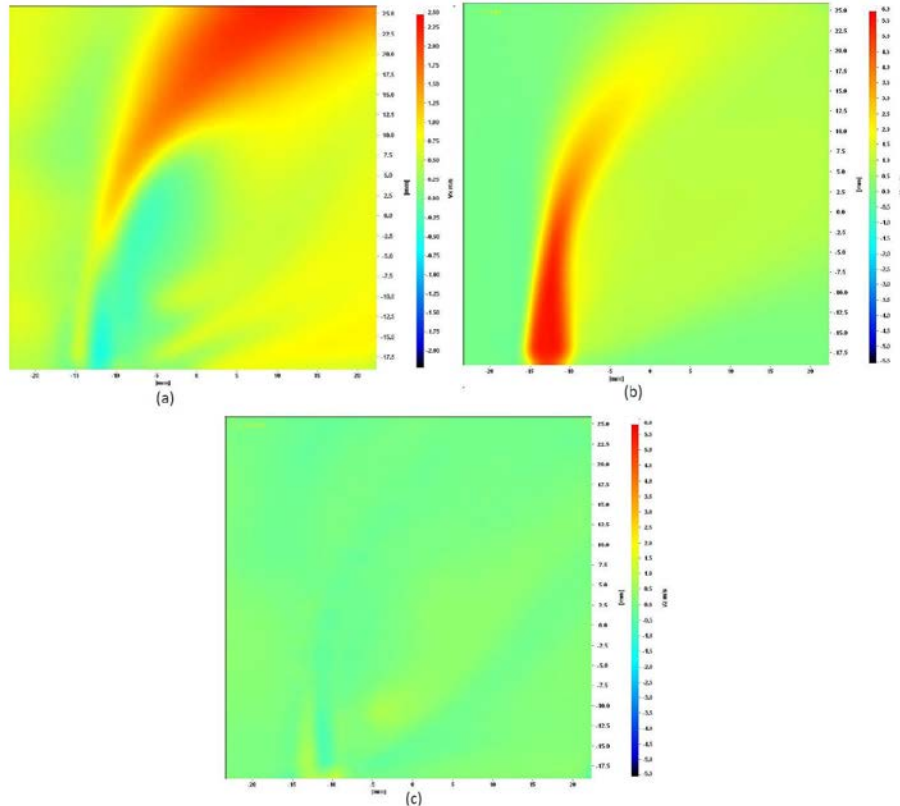


Figure 8: Mean velocity fields for the methane jet in crossflow at a Reynolds number of 2400: (a) u , (b) v , (c) w

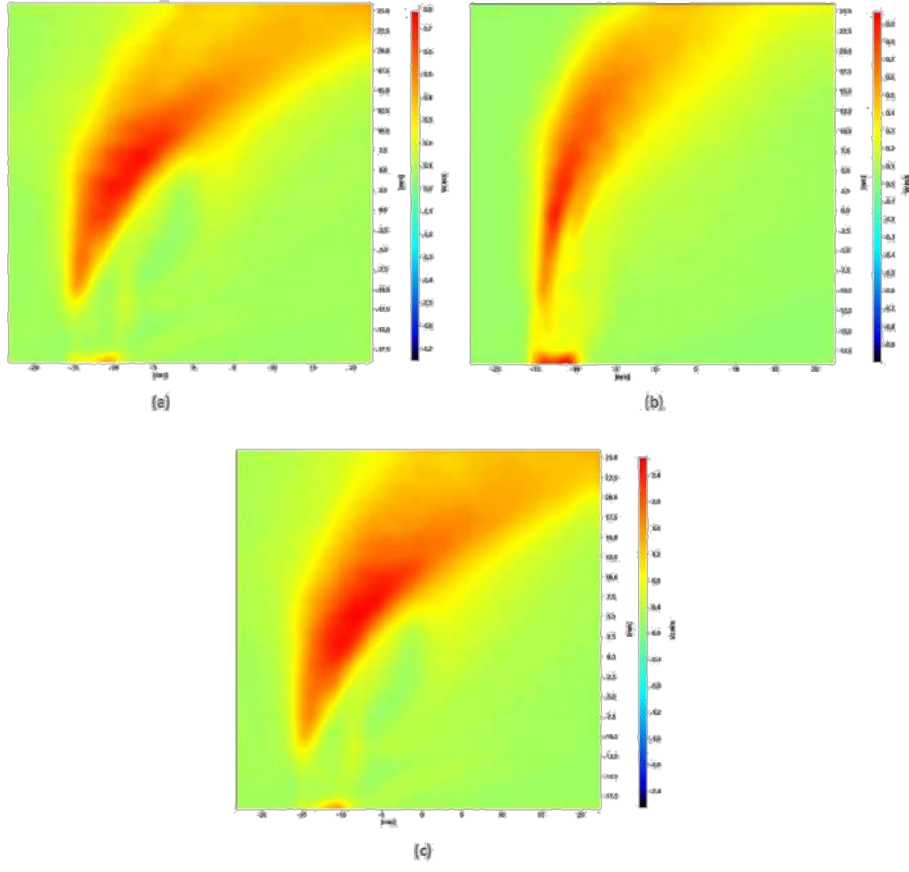


Figure 9: RMS velocity fields for a methane jet in crossflow at a Reynolds number of 2400:
 (a) u_{RMS} , (b) v_{RMS} , (c) w_{RMS}

B-1.4 Conditional Averaging for LES Validation

One of the main purposes of these experiments is to test a new way to compare experimental data with LES to provide an improved validation process. In particular, the proper comparison of LES with experimental data requires that the experiments provide conditional-filtered statistics of the measured quantity, its fluctuations and gradients. These statistical quantities are similar in form to those modeled with LES. For example, we have computed the following statistics using the methane jet-flame-in-crossflow PIV data: (i) instantaneous velocity conditioned on the instantaneous mean velocity computed over an LES filter window, (ii) velocity fluctuation squared conditioned on the LES-filtered fluctuation squared, and (iii) gradients conditioned on the LES-filtered gradient. This analysis shows that the subfilter models are adequate for the velocity itself, but is not accurate for the fluctuations and gradients. This analysis is helpful for guiding the development of new subfilter turbulence models and could be extended to other types of measurements such as temperature and mixture fraction.

Having detailed turbulent fluctuation data in the JICF configuration enables us to process the data in a way that sheds light on the modeling assumptions that underlie the LES technique. LES relies on modeling of the turbulent fluctuations at the subgrid scale, and it is

possible to use PIV data to test the accuracy of these modeling assumptions. For example, consider a 2 mm 2 mm region of the flow that is equivalent to an LES subfilter window. We can create a scatter plot that compares the instantaneous velocity at the center of that window with the “LES averaged” equivalent value at that same instant in time, which is the locally-averaged instantaneous value of the velocity for that window. We will refer to this as the instantaneous velocity conditioned on the LES-averaged velocity.

In other words, a 2 mm 2 mm LES window encompasses a total of 5 5 vectors (25 total vectors). The spatial averaging is calculated for a vector field per the relation,

$$u(t) = \frac{1}{n} \sum_{j=1}^n u_j;$$

where, j is the number of PIV vectors in the LES-window, and t indicates it is an instantaneous value. This equation is for one of the velocity components, but it is repeated for the two others as well (v , w).

Figure10 shows a plot of the instantaneous velocity conditioned on the LES-averaged velocity for a given point in the flow and for about 800 velocity fields. It is evident that the spatially-averaged values closely follow the instantaneous values, for all three components of velocity. Also, as expected the data spread increases with size of the LES window, as is evident from the plots for 4 mm 4 mm LES window comprising about 100 vectors (not shown). Larger windows are expected to give worse results owing to velocity gradients that are more likely to be present in the larger windows. These results indicate that the LES subgrid model provides an excellent surrogate for the true local instantaneous velocity.

A more rigorous test of the subfilter models is to look at the mean squared velocity fluctuation, where the mean is an ensemble average for a large number of values obtained at different times. So here we compute two different types of averaged values. The first is an ensemble-average of the square of the fluctuating velocity values for all the three components at the center of the LES window. This ensemble-average value is viewed as the “true” mean squared value and is computed as,

$$u_{\text{RMS}}^2(t) = \langle u^2 \rangle - \bar{u}^2;$$

where the brackets designate an ensemble average over multiple points in time, but for only the central point in the LES window. We then compare this to the LES equivalent value that is computed as follows,

$$\bar{u}_{\text{RMS}}^2 = \bar{u}^2 - \bar{u}^2;$$

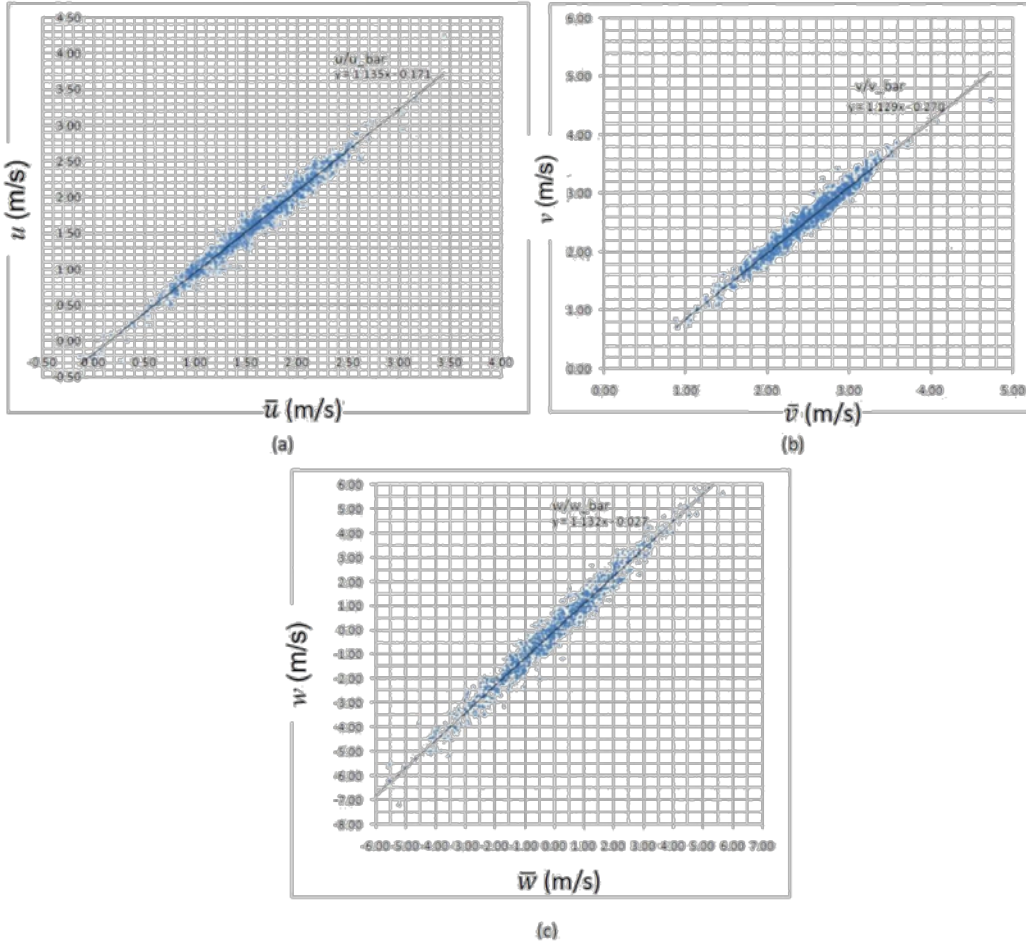


Figure 10: Instantaneous velocities conditioned on the LES-window-averaged values for a 2 mm 2 mm LES window. (a) u velocity, (b) v velocity, and (c) w velocity

where the bar represents a spatial average over the LES window.

The conditional statistics for the squared velocity fluctuations are shown in Fig. 11 for a 2 mm 2 mm LES window. In contrast to the velocity itself, the squared fluctuations exhibit a substantial amount of spread. The spread indicates that the models do not accurately represent the fluctuations that occur at the subgrid scale, and thus provide indication that modeling improvements should be made.

A similar study was carried out for the velocity gradients for all the three vector components using a central differencing scheme for calculation. Typical plots for the velocity gradients with spatially averaged gradient values for statistically independent data set are shown in Fig. 12. These conditional data show that the gradients are relatively well represented by the subgrid models. We believe that these new analysis techniques provide new information about the validity of LES models that have not been previously explored.

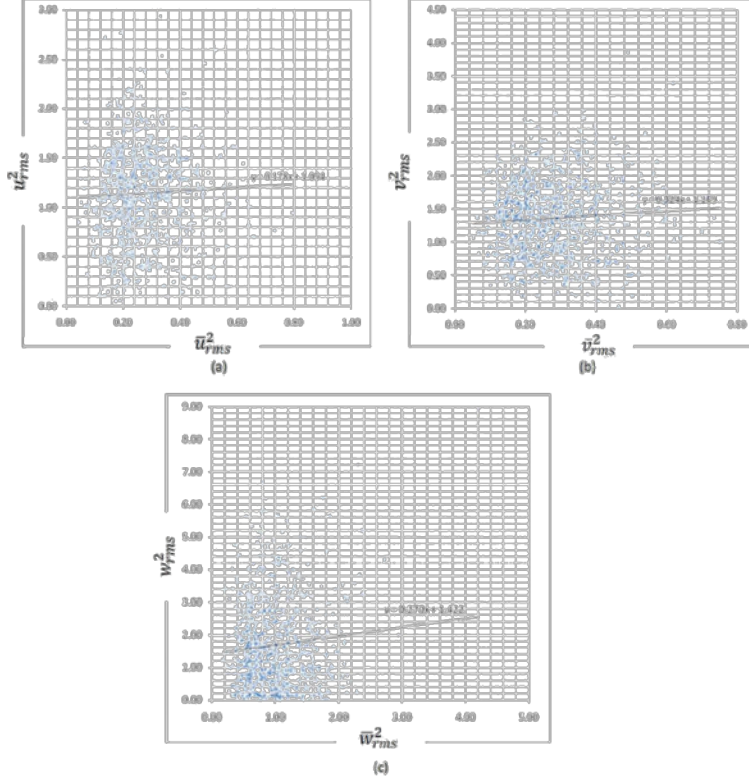


Figure 11: Squared velocity fluctuations conditioned on the LES-window-averaged values for a 2 mm 2 mm LES window. (a) u-velocity, (b) v – velocity, (c) w-velocity.

B-2 Simultaneous Mixture Fraction, Soot Volume Fraction and Velocity

B-2.1 Motivation

Validation of sooting flame simulations is limited by the type of data that are available in sooting flames. The greatest need is for data that include quantities such as mixture fraction (Z) and temperature together with the soot volume fraction. Although Raman scattering is the most effective tool for obtaining multi-species information in turbulent flames, it suffers from substantial interference from PAH fluorescence in sooting flames, and so it has not been effectively used to produce the types of mixture fraction statistics that are available for non-sooting flames. During this project we investigated the application of a new technique to get the type of data needed for validation, but which was previously not possible with existing techniques. This technique is based on the two-photon laser-induced fluorescence of krypton gas seeded into the fuel stream. During the course of this project we demonstrated that krypton PLIF was an effective new diagnostic that could provide the type of data that are needed for sooting flame validation. In particular, using Kr PLIF together with other techniques, it is possible to extract mixture fraction and temperature (and their gradients), simultaneous with other quantities such as soot volume fraction and velocity. To achieve this, co-flowing ethylene jet flames were studied where the fuel was seeded with 4% krypton to enable Kr PLIF, and the jet and co-

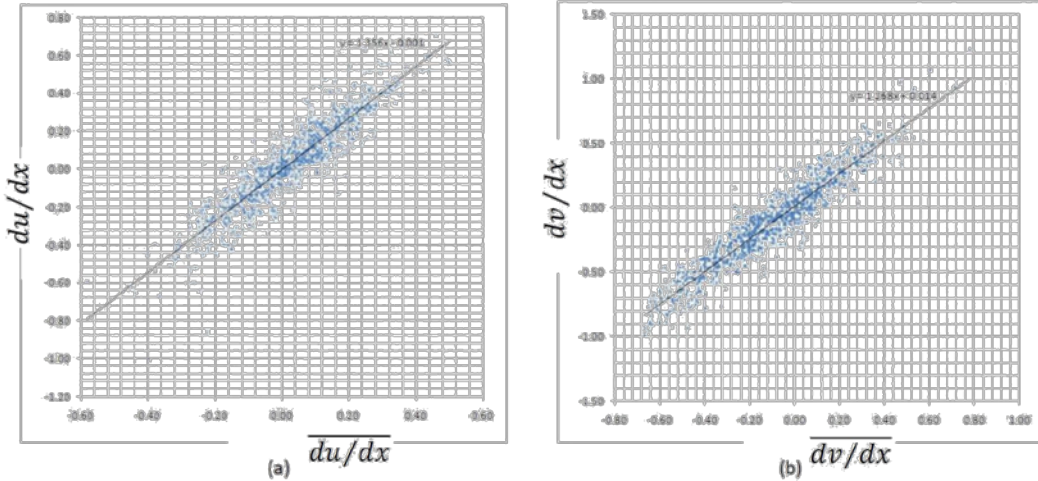


Figure 12: Velocity gradients conditioned on the LES-window-averaged values for a 2 mm 2 mm LES window. (a) du/dx conditioned on $\overline{du/dx}$; (b) dv/dx conditioned on $\overline{dv/dx}$.

flow were seeded with particles to enable PIV measurements to be made. Laser-induced incandescence was used simultaneously to obtain measurements of the soot volume fraction.

Two-photon Kr PLIF is a relatively new technique that has proven useful for making Z measurements in Sandia target flames (Hsu et al. 2011) [3]. Kr is a noble gas and is chemically inert in the presence of combustion, and thus its concentration can be related to Z provided a suitable state relationship is available to account for density and fluorescence quenching effects. The work conducted in this project demonstrated measurements of Z and soot-volume fraction (f_v) fields, and kinematics in the near-field soot-inception region of a jet flame using simultaneous diagnostics including two-photon Kr PLIF, stereo-scopic particle image velocimetry (sPIV) and LII. The flame of interest is a turbulent, non-premixed C₂H₄/N₂/Kr jet flame at a jet Reynolds number of 8300. From these measurements simultaneous planar fields of mixture fraction, temperature, three-component velocity and soot volume fraction are measured in the soot inception region to provide new information on the formation and transport of soot in a turbulent flame.

B-2.2 Experimental Approach

Experiments were performed in a turbulent non-premixed jet flame that was surrounded by a co-flow of air. The co-flow was generated using a nozzle with a contraction area ratio of 2.8:1, and which had a $36 \times 36 \text{ cm}^2$ exit area and a length of 76.2 cm. The co-flow velocity U_{co} was 0.7 m/s. The length of the jet delivery tube was 130 cm and the jet nozzle diameter, d was 1 cm. The bulk jet velocity was about 12.5 m/s. The Reynolds number at the jet flow exit was 8300. The fuel mixture consists of 50% C₂H₄, 46% N₂, and 4% Kr by volume, giving a stoichiometric mixture fraction, $Z_{st} = 0.128$. The addition of 4% Kr (by volume) was introduced in the fuel jet stream as the tracer for the PLIF measurements.

A schematic of energy level of two photon excitation process and subsequent decay and photon emission used in this study is shown in Fig. 13. This study follows the pump-detect strategy employed by Ref.[3]. The fluorescence of Kr is achieved by exciting the ground state ($4p^6 1S_0$) to the $5p[3/2]_2$ state transition, a transition accessible via two-photon absorption at 214.7 nm [Miller 1989] [4]. The resulting fluorescence is collected at 760.2 nm, arising from the decay of this upper state to the $5s[3/2]_2$ state [Miller 1989] [4]. The natural lifetime of this fluorescence is 26.4 0.5 ns [Whitehead et al. 1995] [5]. The 214.7 nm beam was produced by sum frequency generation method. The third harmonic (355 nm) of a Nd:YAG laser and output of a dye laser (544 nm) were combined in a Type I BBO crystal.

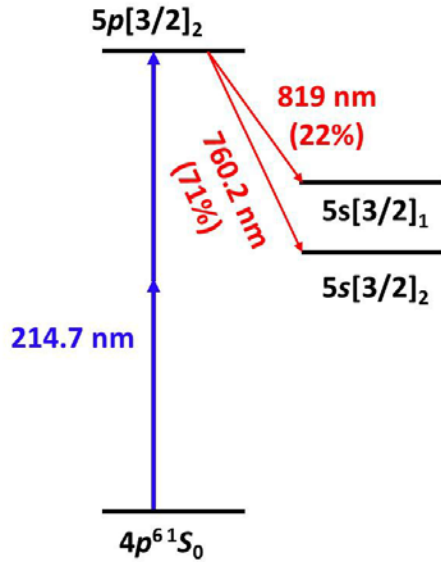
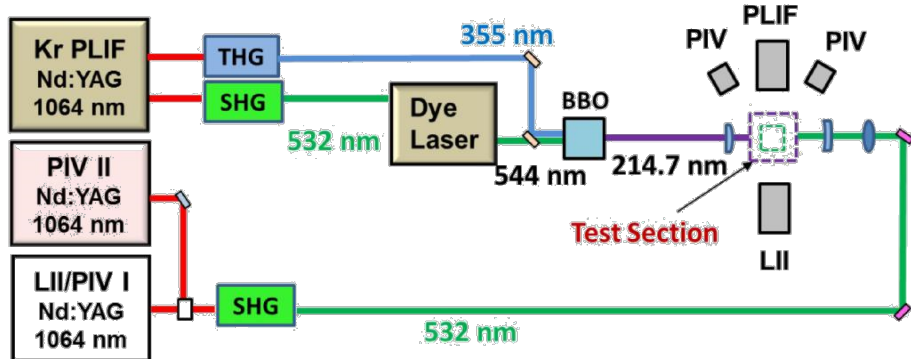


Figure 13: Energy level diagram for the two photon excitation of krypton.

Figure 14 shows simplified schematics of the laser and optical setup for the simultaneous LII/sPIV/Kr PLIF measurements. The 214.7 nm laser beam (2 mJ/pulse) was focused with a 500 mm fused silica cylindrical lens into a small sheet of height 4 mm and thickness 250 μm. The small sheet height was used to maintain high laser intensity since the two-photon signal scales as intensity squared. The fluorescence was imaged through a 760 nm bandpass filter (10 nm bandpass) to reject unwanted radiation. The intensified camera was gated to 50 ns. Note that the signal-to-noise ratio (SNR) is only sufficient over a small region near the peak of the laser sheet because the Kr PLIF signal is nonlinear; therefore, the data shown here were restricted to a height of only 1 mm.

Both the fuel-jet and co-flow were seeded with aluminum oxide (Al_2O_3) particles of nominal diameter 0.5-1.0 μm for PIV. The time-delay between the two PIV pulses was set to 32.5 microseconds. Two 2048x 2048 pixels CCD cameras were used in a stereoscopic configuration to capture the 3-component PIV images. The cameras were fitted with 105 mm focal length lenses mounted to Scheimpflug mounts. Both PIV cameras were on the same side of the light sheet and the angle between two cameras was 60 degrees. A 750 mm



SHG : Frequency doubling crystal
THG : Frequency tripling crystal

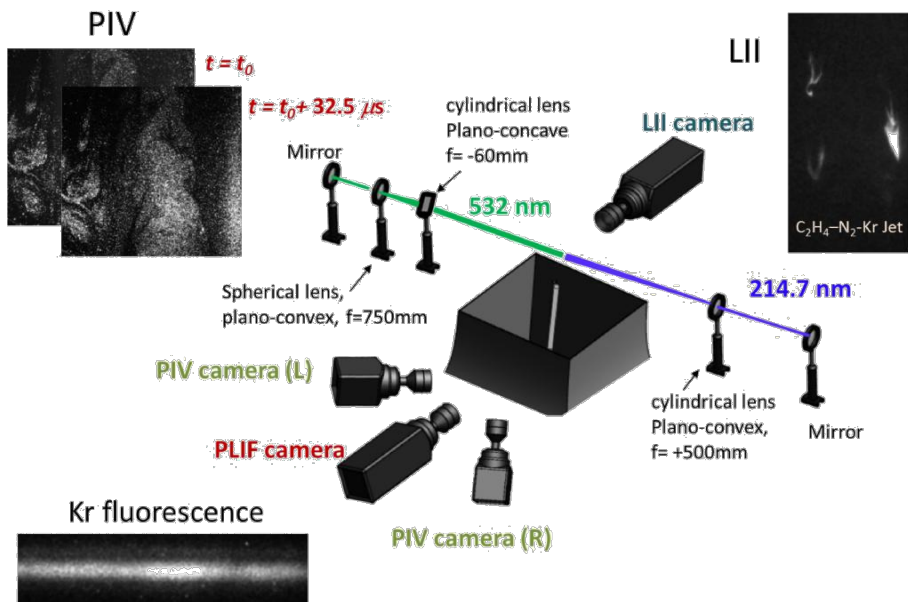


Figure 14: Simplified schematics of laser and optical setup for the simultaneous PLIF/PIV/LII measurements.

spherical lens and a negative focal length (-60 mm) cylindrical lens were used to form a sheet for both PIV and LII. The field of view was 3 cm x 3 cm and spatially overlapped with the fields of view of the PLIF and LII measurements. LaVision DaVis 7.2 was used for spatial image mapping for PIV, LII, and PLIF measurements and to process PIV images. An iterative, multi-pass, adaptive interrogation windowing algorithm was used for PIV image processing. The final iteration was 32x32 pixels with a 75% overlap between adjacent interrogation windows. Vectors with a magnitude greater than 3 times the standard deviation of the neighboring vectors were defined as spurious vectors and were replaced with the median of the valid neighboring vectors. The first pulse of 532 nm light was used for LII measurements. The 532 nm laser fluence was 0.2 J/cm² and the pulse duration was about 10 ns; therefore, the LII is in the plateau region. The laser pulse for the PLIF measurements was placed between the two PIV laser pulses, which was 10 s after the first PIV laser pulse.

An intensified CCD camera with resolution of 512x512 pixels was used for LII. The soot incandescence was imaged through a bandpass filter with a central wavelength of 400 nm and bandwidth of 40 nm (FWHM). The intensified camera for LII was gated to 500 ns.

Both soot extinction and LII measurements of C₂H₄/air premixed flat-flame using McKenna burner were performed by establishing various equivalence ratios of fuel-rich premixed flames to obtain the calibration constant for converting LII intensity counts to f_v . Extinction measurements were performed using a He-Ne laser at a wavelength of 632.8 nm.

The measurements were performed in the near-field of the ethylene jet flame (approximately 5-10 jet diameters downstream), where the yellow luminous region first appears in the flame as shown in the Fig. 15. The vertical center of the laser sheet was set to be 10 cm (10d) downstream of the jet exit. The approximate location is marked in the Fig. 15. The Kr PLIF signal was measured at the jet exit as well to get the reference krypton fluorescence signal where the mole fraction of krypton is known.

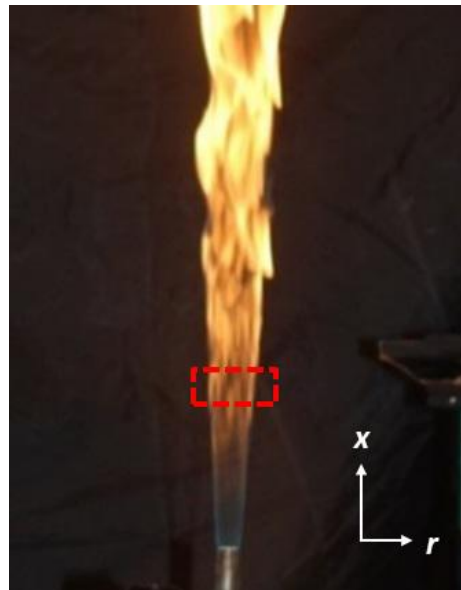


Figure 15: A photograph of the non-premixed ethylene-N₂-Kr-jet flame. The approximate location of the 10d downstream of the jet exit is marked by the red box.

Time-averaged temperature measurements were carried out using an unsheathed fine diameter (51 μm wire diameter) of Type R (Pt-Pt/13%Rh) thermocouple to compare with the Kr PLIF measurements. The thermocouple measurements were performed independently from the laser-based measurements. Studies have been reported that catalytic effects in the non-premixed flames are expected to be small due to low radical concentration [McEnally et al 1997 [6], Miller et al. 1993 [7]]. Measured temperatures were corrected for radiative heat losses (e.g., [McEnally et al. 1997 [6], Smyth et al. 1985 [8]]).

The uncertainty in the velocity from the PIV measurement is due to the particle inertia effects, thermophoretic velocity induced by temperature gradients, calibration procedure, and PIV processing algorithm and it is estimated as less than 0.2 m/s. For LII measurements, the minimum detectable soot volume fraction was 0.27 ppb. Uncertainties

in soot volume fraction measurements were estimated at 16%, mostly from the extinction measurements and the calibration process. Precision uncertainty in the Kr PLIF measurements were due primarily to shot noise and pulse-to-pulse variation in the intensity. The krypton concentrations were held low enough that no effects of stimulated emission could be discerned. The combined precision uncertainty is roughly 18% near the flame zone and 4% at the maximum Kr PLIF signal at $r/d = 0$. Uncertainties in the thermocouple measurements were determined by considering flow conditions, temperature reading device accuracy, radiation correction, and standard deviation of several sets of measurements. Note that the temperature validation from thermocouple measurements was used to help assess the accuracy of the Kr PLIF-based temperature measurements.

B-2.3 Methodology for Inferring Mixture Fraction and Temperature

Mixture fraction and temperature are determined from the Kr PLIF signals and an assumed state relationship. The Kr PLIF signals cannot be directly mapped to mixture fraction because the signals are influenced by density variations and fluorescence quenching effects, which are not known independently. However, if we start with an assumed state relationship, then it is possible to map from the Kr LIF signal (normalized by the jet exit value) to mixture fraction and temperature. The quenching effects are derived from the species mole fractions that are derived from the state relationship and quenching rates, which must be independently measured. In other words, we are assuming that $T=T(Z)$, $S_f/S_{f\max}=S_f;Kr/S_f;Kr;ref(Z)$ and $Q=Q(Z)$, where Z is mixture fraction, T is temperature, $S_f;Kr$ is the Kr fluorescence signal, $S_f;Kr;ref$ is the fluorescence signal measured at a known reference condition (e.g. jet exit), and Q is the fluorescence quenching rate. Since we can measure $S_f;Kr/S_f;Kr;ref$ then using the state relationship we can map to all other variables. Our assumed state relationship is derived from a laminar strained diffusion flame calculation. Such a state relationship has been shown to be quite accurate in low Reynolds number flames by using Raman scattering [Hsu et al. 2011] [3].

The 1D opposed jet code developed by [Kee et al. 1989] [9] was used to simulate non-premixed C₂H₄/N₂/Kr-air flames, where the fuel composition was 50% C₂H₄, 46% N₂ and 4% Kr by volume. USC Mech II [Hai Wang et al. 2007] [10] was used for the detailed kinetic mechanism. The simulation output provided the state relationship that enables us to map the measured Kr PLIF signal to Z and T , provided the quenching cross sections are known. Transport parameters and thermodynamic data in polynomial form for Kr were taken from the literature (Refs. [Herschfelder and Bird 1954] [11], [Burcat 2005] [12]), and combined with USC Mech II transport data and thermodynamic data. The specific Lennard-Jones parameters used were: potential well depth, $\epsilon/k_B =$

190.00 K and collision diameter, $\sigma = 3.61 \text{ \AA}$. Binary diffusion coefficients of Kr were re-evaluated by comparing with different literature values [Tee et al. 1966] [13] of Lennard-Jones parameters and the differences are negligible for temperature and species profiles. Multi-component transport coefficients and thermal diffusion were used in the simulation. The Lewis number effect by adding only 4% of Kr was negligible.

The resulting species mole fraction and temperature profiles were used to map the measured Kr PLIF signal to T and Z by accounting for collisional quenching rates of major

Table 1: The temperature dependence of quenching rates.

	$q(T) = q_0(T/T_0)^n$			
Species	q_0 (MHz/torr)	n	T_0	Ref
Kr-N ₂	6.5	-0.26	294	[10]
Kr-H ₂	18	-0.53	294	[10]
Kr-CO ₂	24	-0.78	294	[10]
Kr-O ₂	25	-0.64	294	[10]
Kr-CH ₄	17	-0.71	294	[10]
Kr-H ₂ O	47	-0.96	294	[10]
Kr-Kr	0.379	-0.0976	291	[15]
Kr-C ₂ H ₄	10.02	-0.4906	291	[15]

P

species. The total quenching rate is given by $Q = \sum_i q_i X_i$, where q_i is the Kr quenching rate for collision partner i and X_i is the collision partner mole fraction. The collisional partners considered were Kr, N₂, H₂, CO₂, CO, O₂, H₂O, CH₄, and C₂H₄. Table 1 shows the temperature dependent quenching rates of Kr with collisional partners of N₂, H₂, CO₂, O₂, H₂O, and CH₄ from Ref. [Hsu et al. 2011] [3] and quenching rates for Kr-Kr and Kr-C₂H₄ from Ref. [Burns 2014] [14]. Details of the quenching rates measurements are described in Refs. [Hsu et al. 2011] [3] and [Burns 2014] [14]. The quenching rate for CO is not available in the literature; however, a sensitivity analysis showed that the results were not sensitive to CO quenching, and so its quenching rate was assumed to be the same as that of CO₂.

B-2.4 Kr PLIF Results

The Kr PLIF images were background subtracted and low-pass filtered with a 3 3 kernel to reduce the influence of noise. To make the krypton PLIF technique quantitative it is necessary to calibrate the fluorescence signal. The Kr fluorescence signal, S_{f;Kr} is given by

$$S_{f;Kr} = c \frac{E_I}{a} \frac{\frac{2}{21} A_{21} \lambda^2}{4 \cdot 2 \cdot (\sim!)^2 n_{Kr}} \int F^2(t) dt \quad (1)$$

where c is the collection efficiency of the detector system, E_I is the pulse energy for the exciting radiation, A_{21} is the spontaneous emission rate for the transition in question, λ is the total decay rate of the excited state of krypton, $5p[3/2]_2$, λ^2 is the effective two-photon absorption cross section, n_{Kr} is the krypton number density, a is the exciting beam radius, $\sim!$ is the frequency of the exciting radiation, and $F(t)$ is the temporal profile of the exciting radiation pulse. The fluorescence quantum yield is given by A_{21}/λ where,

$$X = A + \sum_i q_i X_i \quad (2)$$

and A is the spontaneous emission rate for all transitions.

We can show that Z is related to ratios of several other variables:

$$Z = \frac{S_{f;Kr}}{S_{f;Kr;ref}} \frac{(Z; T)}{T_{ref}} \frac{W_{fuel}}{W_{mix}(Z)} X_{Kr;ref}; \quad (3)$$

where $S_{f;Kr}$ is Kr PLIF signal at the location of interest, $S_{f;Kr;ref}$ is Kr PLIF signal at the jet exit and W_{fuel} is the molecular weight of the fuel stream and W_{mix} is the local mixture molecular weight. In Eq. 3 “ref” refers to the value of the quantity in the fuel stream at the jet exit. The assumed state relationship allows us to create a mapping from the normalized PLIF signal to Z , T and X_i .

Figure 16 presents a flowchart that summarizes the procedure to determining the mixture fraction and temperature from the measured Kr PLIF signal.

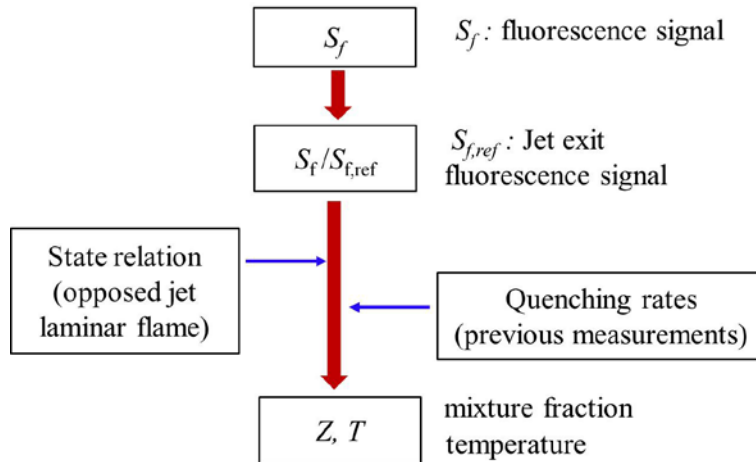


Figure 16: A flowchart for mapping Kr PLIF signal to mixture fraction.

Fig. 17 shows how the normalized Kr PLIF signal, temperature and Kr mole fraction vary with Z . These results were obtained using the state relationship inferred from the 1D opposed-jet simulation and collisional quenching data of major species. Temperature and species mole fraction from the simulation were taken at the local strain rates, K_{local} of 300 s^{-1} , 800 s^{-1} and 1000 s^{-1} , and compared. K_{local} was determined as the maximum velocity gradient along the center line just upstream of the flame in the opposed jet simulation. The Kr mole fraction and normalized Kr LIF signal did not vary with strain rate, but the temperature varied more significantly. These results show that the particular state relationship used will have relatively small effect on the Z inferred from the Kr PLIF data, but about a 10% effect on the inferred temperature. At these strain rates we expect the state relationship to be valid instantaneously, and Fig. 17 shows the mapping is single-valued. In this study, temperature and Z profiles were derived from a combination of the measured Kr PLIF and the state relationship based on the 800 s^{-1} strain rate. This strain rate was used because it is close to the actual strain rate measured near the reaction zone with PIV. In this near-field region ($x/d = 10$), the jet has not experienced significant mixing and so Z remains relatively high on centerline (about 0.87). Note that both Z and T are derived from the normalized fluorescence signal (and the state relationship) and so the

temperature field is not independent of Z.

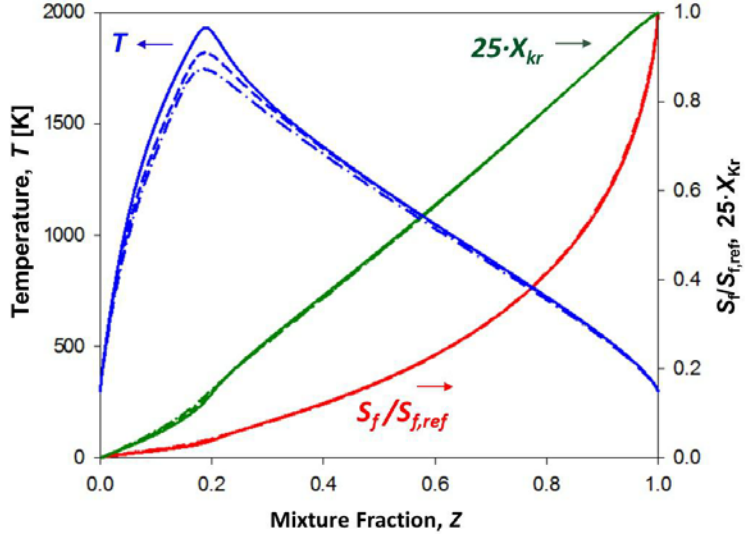


Figure 17: Temperature (left axis), Kr PLIF signal normalized to the reference signal, and mole fraction of Kr times 25 (right axis) against mixture fraction using OPPDIF simulation and collisional quenching rates for 50% C_2H_4 /46% N_2 /4%Kr (by volume) non-premixed flames depending on various strain rates. Solid line: $K_{\text{local}} = 300 \text{ s}^{-1}$; dashed line: $K_{\text{local}} = 800 \text{ s}^{-1}$; and dashed-dotted line: $K_{\text{local}} = 1000 \text{ s}^{-1}$.

The resulting LII intensity was mapped to f_v using the calibration constant [Bockhorn et al. 2002 [16], Zerbs et al. 2009 [17]], obtained from LII/extinction measurements of C_2H_4 /air premixed flat-flames generated in a flat-flame McKenna burner. The choice of the complex refraction index, m is critical for the accuracy of f_v measurement. A wide range of values for m have been reported in the literature (e.g., [Dalzell and Sarofim 1969] [18]), and differences of a factor of 2 in f_v can be obtained by using m between Refs. [Dalzell and Sarofim 1969] [18] and [Williams et al. 2007] [19]. In this study, the Ref. [Dalzell and Sarofim 1969] [18] values were used ($m = 1.57 - 0.56i$), since they have been widely used in the literature.

Figure 18 shows simultaneously-acquired instantaneous f_v , Z and T fields derived from Kr PLIF superimposed on the axial velocity field. Also shown is the stoichiometric velocity contour (white line), $U_{\text{stoic}} = (U_0 - U_{\text{co}})Z_{\text{st}} + U_{\text{co}}$ ($=2.2 \text{ m/s}$), which is known to correspond approximately with the location of the reaction zone [Han and Mungal 2003] [20], where, U_0 is the centerline velocity at the jet exit. $Z_{\text{st}}(0.128)$ is shown as the red contour and $Z=0.3$ is shown as yellow. We see that the U_{stoic} contour is just to the outside of Z_{st} and T_{max} . f_v tends to be found near the stoichiometric contour on the fuel-rich side and within the temperature band of about 1200–1600 K. This figure shows a soot structure with maximum soot volume fraction is 5.4 ppb at $x/d = 10$. The temperature peaks at $Z = 0.17$ on the lean side of the reaction zone, and the peak soot volume fraction $f_{v,\text{max}}$ is near the $Z = 0.35$, which is in the lower-temperature fuel-rich side of the reaction zone.

Figure 19(a) shows simultaneously-acquired instantaneous radial profiles of Z and axial

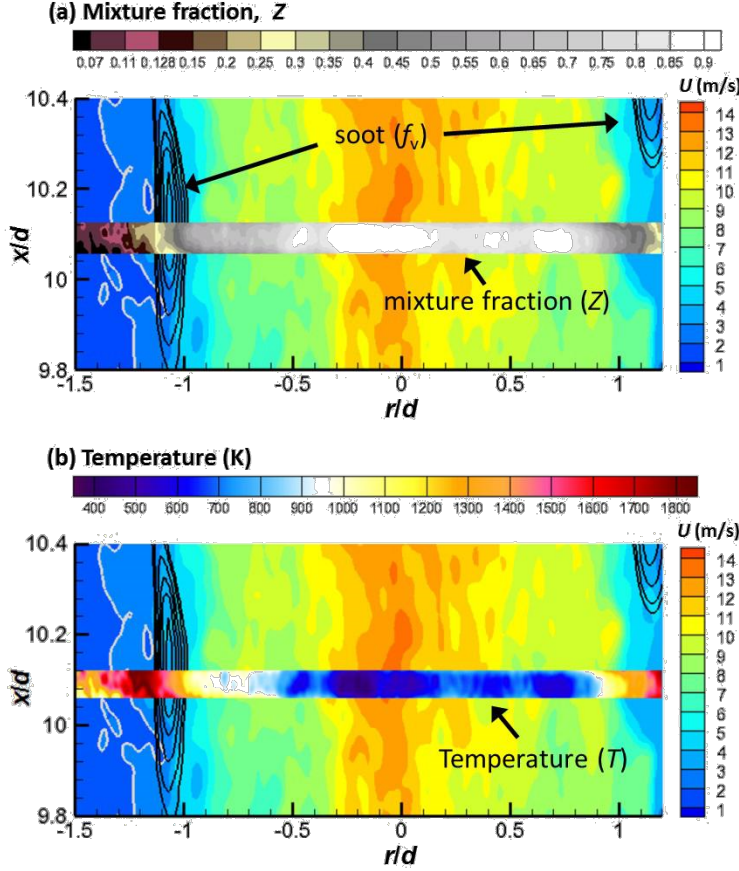


Figure 18: Instantaneous simultaneous f_v (gray-scale-contour line) and U_{stoic} (white line) derived from the PIV field. The (a) Z from the Kr PLIF, and (b) T from the Kr PLIF are superimposed on the axial velocity field. $f_{v,\max} = 5.4 \text{ ppb}$

velocity U . It is seen that Z and U have the same general shape, which is expected since they both have their peak value in the potential core and then reduce in value owing to mixing with the co-flow gas. The radial locations of Z_{st} and U_{stoic} at $10d$ above the jet exit are marked in Fig. 19(a). The profiles show that Z_{stoic} and U_{stoic} are nearly coincident, which is expected since U_{stoic} has been shown to mark the approximate location of the reaction zone.

Figures 19(b) and 19(c) shows simultaneously-acquired instantaneous radial profiles of T , Z , and f_v at the location of $10d$ above the jet exit. The radial profiles are obtained from a single row of pixels in the images. We see that the elevated temperature regions tend to be much broader than the soot, which is expected from previous studies [Atilli et al. 2014 [21], Mahmoud et al. 2015 [22]]. Although these profiles represent just a single instance, we see that the peak soot is associated with the rich side of the flame at a temperature of about 1200 K in Fig. 19(b) and 1400 K in Fig. 19(c). Additionally, we can see that the peak value of f_v occurs over the mixture fraction range Z 0.25 to 0.5 and Z 0.3, respectively as shown in Fig. 19(b) and 19(c) (red dashed lines mark $Z = 0.3$). References [Atilli et al 2014] [21] and [Kent and Wagner 1984] [23] indicate that the soot

is characterized by large positive growth over the range $0.25 < Z < 0.5$ and peaks at about $Z \approx 0.3$, which corresponds to the approximate peak in the soot precursor/growth species acetylene (and naphthalene) [Atilli et al. 2014 [21], Bisetti et al. 2012 [24]]. Note that the current opposed flow simulations of $50\%C_2H_4/46\%N_2/4\%Kr$ -air flames also show that the peak mass fraction for acetylene (C_2H_2) occurs at about $Z = 0.3$.

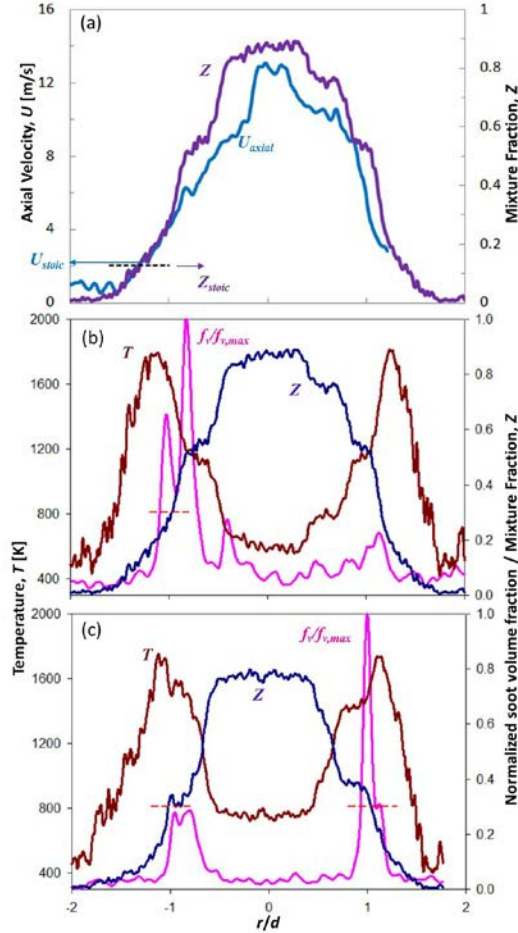


Figure 19: (a) Profiles of instantaneous Z by Kr PLIF ($Z_{st} = 0.128$) and axial velocity by PIV ($U_{stoic} = 2.2$ m/s) (b) and (c) Profiles of instantaneous temperature by Kr PLIF and soot volume fraction by LII. Measurements are made at $10d$ above the jet exit. Black dashed lines mark $Z_{st} = 0.128$ and red dotted lines mark $Z = 0.3$

Figure 20 shows mean temperature and Z profiles derived from the measured Kr PLIF and state relationship based on the 800 s^{-1} strain rate using 1280 instantaneous images. For validation of the technique, mean temperature profiles of non-premixed $C_2H_4/N_2/Kr$ flames were also measured using fine-wire thermocouples to compare with Kr PLIF experimental results. A comparison of mean temperature profiles derived from Kr PLIF and measured by R-type thermocouples with 51 μm wire diameter is shown in Fig. 20. The temperature values measured by the thermocouple were corrected for radiation effects. It is well known that thermocouple measurements can be affected by other sources

of error such as conduction along the thermocouple wire and potential catalytic effects due to the presence of the bare thermocouple wire. In addition, when a thermocouple is inserted into a sooting flame, soot particles will deposit on the junction and both the junction diameter and its emissivity will increase. These parameters are important to obtain the flame temperature and so the error in the temperature measurement can be significantly increased by soot deposition. Nevertheless, procedures have been suggested that enable accurate thermocouple-based flame temperature measurements to be made in sooting flames. In addition, there were no significant problems with soot deposition because the present measurements were made in regions of low soot concentration.

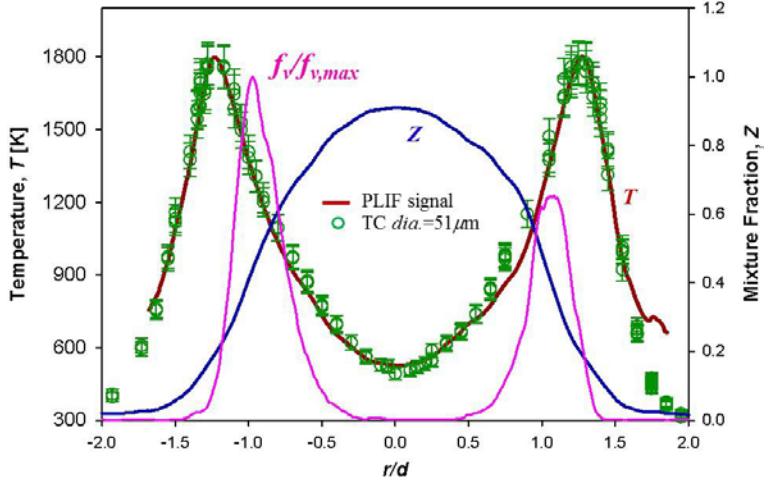


Figure 20: Profiles of mean temperature and mixture fraction by Kr PLIF, and normalized f_v by LII over 1280 instantaneous images at 10d above the jet exit. Comparisons of temperature profiles mapped from mixture fraction (red line) by the Kr PLIF signal and thermocouple measurements with 51 m wire diameter (symbols) along the radial direction at the location of 10d above the jet exit.

Figure 20 also shows the mean temperature profiles and mean f_v computed using the 1280 instantaneous images. Although the temperature and mixture fraction profiles from the PLIF showed symmetry along the radial direction, the shape of the mean soot volume fractions showed a slight asymmetry with greater soot concentrations on the left (laser entry) side. Asymmetric soot volume fraction profiles have been reported in several previous studies [Zerbs et al. 2009] [17]. Recent study by [Sun et al. 2015] [25] suggested that beam steering can alter the distribution of local fluence in the laser beam sheet and thus cause this asymmetry, although we can observe asymmetry in the visible luminosity at the flame base, which does suggest there is a natural asymmetry in the soot formation. Soot is predominantly formed within the temperature band of 1100-1500 K on the fuel-rich side and peak f_v is formed between the temperature bands of 1300-1400 K. Previous work by others in pure C₂H₄ jet flames has shown that soot exists in the temperature range of 1200-1800 K, with the peak f_v occurring in the temperature range of 1500-1600 K [Lee et al. 2009 [26], Coppalle and Joyeux 1994 [27]]. The peak soot thus occurs at a higher temperature than found in this study, but this is not unexpected since pure ethylene has a higher flame temperature than the mixture (50% C₂H₄) used in the current study. The

mean temperature peak corresponds to $Z = 0.16$, and peak f_v occurs at $Z \approx 0.4$. Although the temperature and Z profiles from the PLIF are symmetric, the shape of the mean f_v shows a slight asymmetry with greater soot concentration on the left (laser entry) side, which has been mentioned earlier for the mean profiles in Fig. 20.

Figure 21 shows the PDF of the streamwise velocity U conditioned on the stoichiometric mixture fraction (specifically, the PDF of U is compiled for the finite range $0.127 < Z < 0.129$). The PDF has a peak at just above 2 m/s, which shows that fluid at the stoichiometric mixture fraction has a preferential velocity that is near the stoichiometric velocity of 2.2 m/s and is consistent with observations made from the instantaneous images.

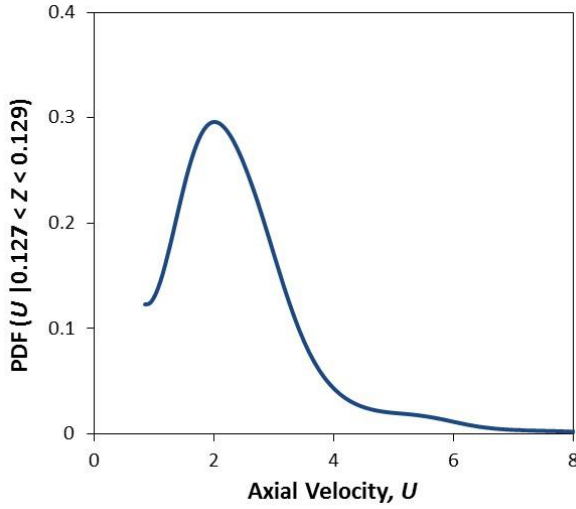


Figure 21: PDF of axial velocity U conditioned on Z_{stoic} ($0.127 < Z < 0.129$).

Figure 22 shows joint PDFs between the mixture fraction and soot volume fraction (left panel) and between the temperature and soot volume fraction (right panel). The statistics were compiled from all pixels along a radial line at $x/d = 10$. The figure shows that f_v is found for values of Z ranging from 0.15 to 0.65, but the peak soot volume fraction is found over the more restricted range of $Z = 0.3-0.4$. These observations are broadly similar to results of the DNS simulation of soot production in n-heptane flames [Bisetti et al. 2012] [24], although in the simulation the soot seems to be more broadly distributed in mixture fraction space. The joint PDF involving temperature shows that f_v is preferentially found over the range of temperature 1300–1500 K and peaks at $T \approx 1400$ K, which is consistent with the qualitative observations made above.

B-2.5 Summary

Simultaneous Kr PLIF, LII and PIV are used for the first time to obtain simultaneous measurements of mixture fraction, soot volume fraction and velocity in the soot inception region of an ethylene/N₂/Kr-air jet flame. Mixture fraction is inferred from the normalized PLIF signal, a state relationship derived from a strained flame simulation, and quenching cross-sections obtained from the literature. The inferred mixture fraction fields enable the

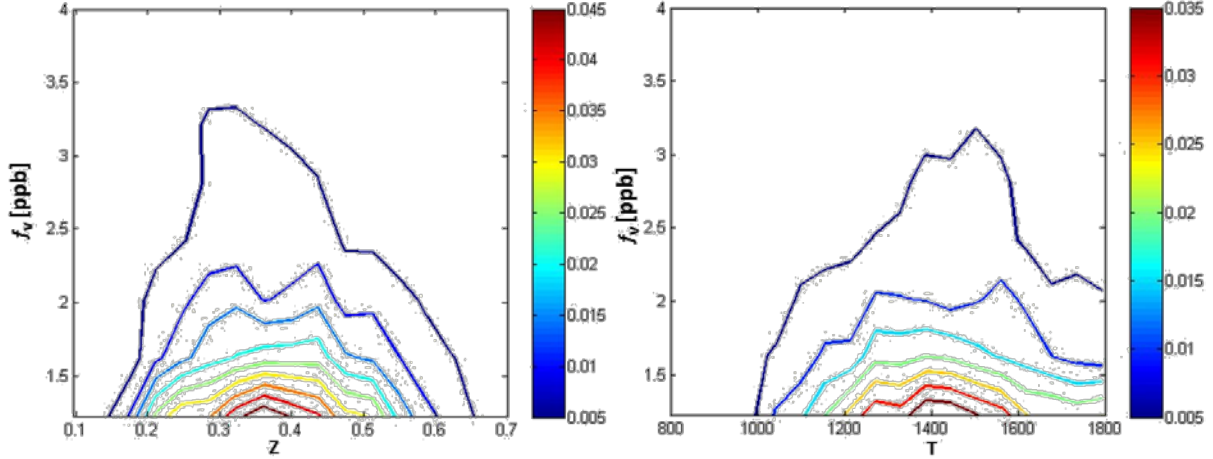


Figure 22: Joint PDFs of mixture fraction (left panel) and soot volume fraction, and temperature (right panel) and soot volume fraction at $x/d = 10$.

determination of the temperature, and possibly scalar dissipation and thermal dissipation fields if the signals are sufficiently high. For validation of the technique, PLIF-derived temperature profiles were compared to mean thermocouple measurements. The resulting radial profiles of temperature obtained from krypton PLIF and the thermocouple show excellent agreement. The data also showed that the stoichiometric velocity and stoichio-metric mixture fraction are nearly coincident, the mean soot peaks in the expected range of temperatures, and the soot peaks at a mixture fraction of 0.3–0.4, which is the location of peak soot precursors.

Overall, results show that the Kr PLIF technique can be used to make quantitative mixture fraction and temperature measurements in the soot inception region, and can be successfully combined with LII and PIV. However, this technique is likely to be less applicable farther downstream or in heavily sooting flames where stronger fluorescence interference is expected and where radiation cooling renders the state relationship invalid. Future work will focus on improving the quality of the measurements and to derive additional statistical correlations among the soot volume fraction, mixture fraction, temperature and velocity.

B-3 Soot Measurements in Surrogate-Fuel Jet Flames

B-3.1 Flow Facility

Experiments were performed in a turbulent non-premixed jet flame that was surrounded by a co-flow of air as shown in Fig. 23. The co-flow was generated using a nozzle with a contraction area ratio of 2.8:1, and which had a $36 \times 36 \text{ cm}^2$ exit area and a length of 76.2 cm. The co-flow air was driven by a centrifugal fan, and its velocity was about 0.7 m/s. The inlet co-flow was conditioned by a honeycomb, a perforated plate between the two screens. The length of the jet delivery tube is 130 cm and the jet nozzle diameter, d is 1 cm.

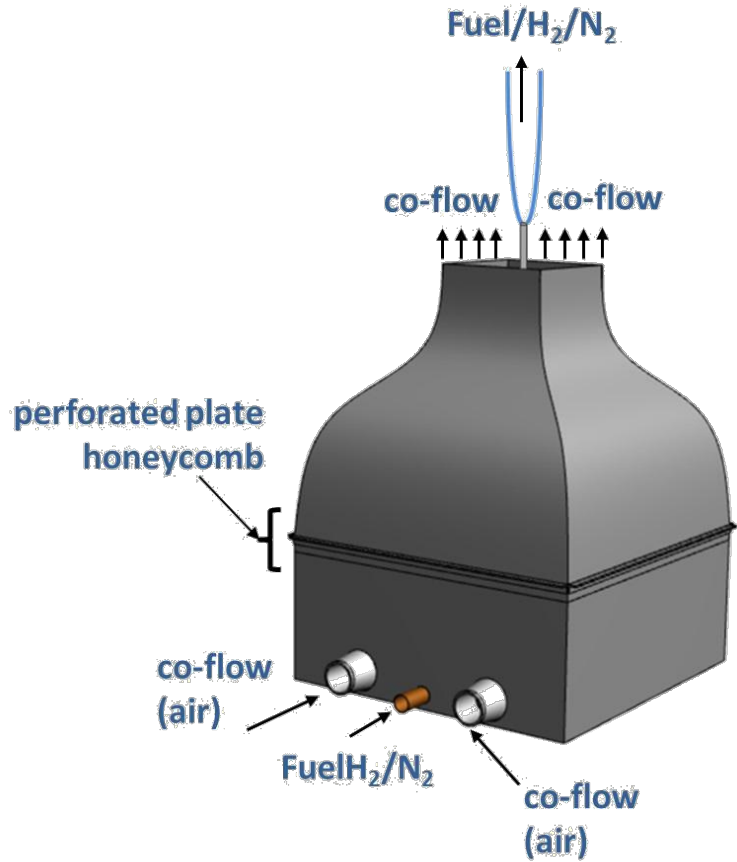


Figure 23: Experimental setup of a simple jet burner nozzle and co-flow system

B-3.2 Fuel vaporization system

Jet fuel and jet fuel surrogates are liquid at room temperature, but it is beneficial for the modeling and diagnostics to burn them in the gas phase. As a consequence, it was necessary to design and build a new fuel-vaporization system. The basic premise of the fuel vaporizer, was to inject a finely atomized spray of liquid fuel into a heated chamber, as shown in Fig. 24. To generate finely atomized spray of the liquid fuel, an atomizing nozzle was installed in the vaporization chamber. The liquid fuel was supplied to the atomizing nozzle under pressure. The liquid fuel and compressed N₂ were mixed internally in the atomizing nozzle to produce a completely atomized spray. Pressures of 30–40 psig of N₂ was used to drive the liquid through the spray nozzles. The fuel flow rate was accurately metered by a liquid flow sensor (OMEGA FLR1007D, max 1.4% error of full scale of 100 ml/min). The N₂ flow to the atomizer was preheated using an in-line gas heater. An additional N₂ stream was preheated, using another in-line gas heater, to a temperature that was above the boiling temperature of the fuel, and then flowed to the vaporization chamber. The gas temperature was monitored by a K-type thermocouple and kept approximately 30 K above the boiling point of the fuel to ensure complete vaporization. The vaporization chamber was heated by externally-mounted ceramic heating bands. Ther-

mal mass was added to the chamber by stuffing it with brass wool. The thermal mass is meant to help the chamber maintain a high temperature and thus assist in the vaporization of the fuel aerosol. The surface temperature of the vaporization chamber was monitored by K-type thermocouple and set to be 30 K above the boiling temperature of the fuel as well to keep the fuel from condensing on the walls. Downstream of the vaporization chamber, the stainless-steel tubing was heated by electrical heating tape and insulated to maintain the fuel and nitrogen mixtures at fixed temperatures at the burner exit and to prevent re-condensation of fuel vapors. The H₂ delivery line was wrapped with heating tape and teed into the tubing that exited the vaporization chamber. The jet was designed from a long straight stainless steel tube that was also heated by thin polyimide film insulated flexible heaters. The jet exit temperature was kept at 473 K, 443 K, and 413 K for n-dodecane, Jet Fuels (Jet-A and surrogate), and m-xylene respectively. A K-type thermocouple was used to monitor unburned reactant temperature at the center of the burner exit. The partial pressure of the fuel was kept below its vapor (saturation) pressure under all conditions.

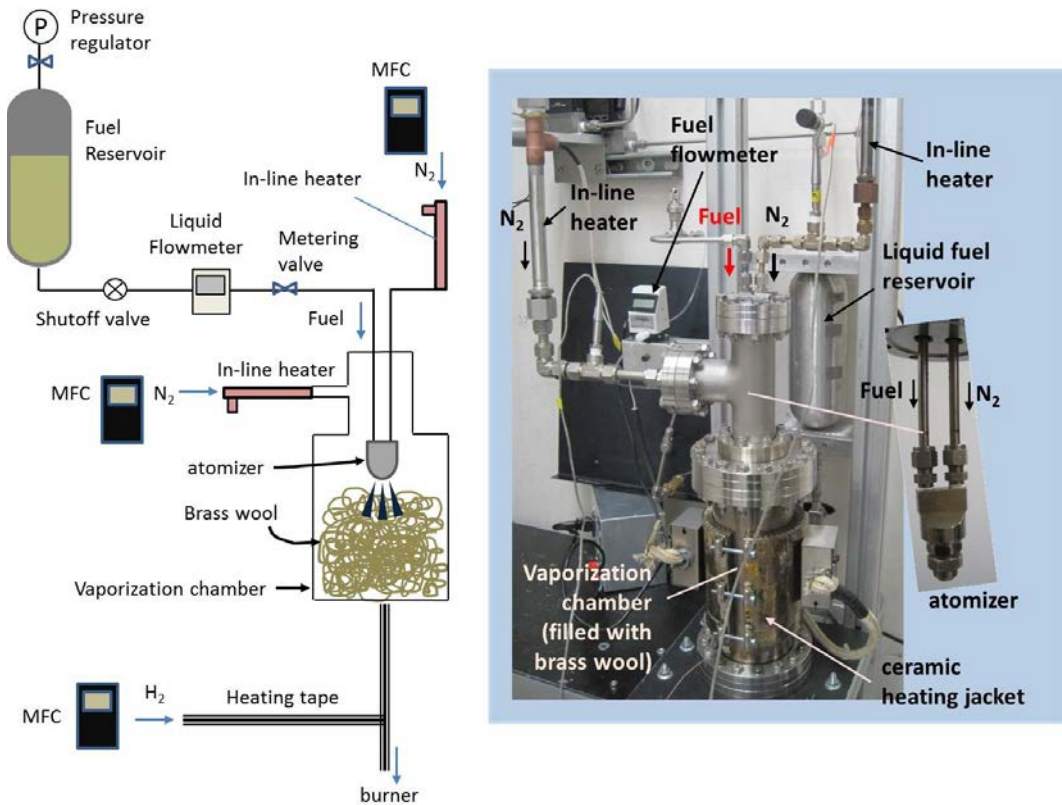


Figure 24: Fuel vaporization system.

B-3.3 Experimental Conditions

The soot-volume fraction fields and kinematics were investigated in the near-filed soot-inception region of non-premixed jet flames operating on different vaporized fuel mixtures. In particular, jets of n-dodecane ($n\text{-C}_{12}\text{H}_{26}$), m-xylene, Jet A, and a mixture of

Table 2: Fuel Properties

	n-dodecane	m-xylene	Jet A
Formula	$n\text{-C}_{12}\text{H}_{26}$	$C_8\text{H}_{10}$	-
			-
Molecular Weight	170.34 g/mol	106.16 g/mol	153 g/mol
Boiling Point	489.35 K (216.2 C)	412.15 K (139 C)	438-538 K (165 - 265 C)
Density	0.7495 g/cm ³ @ 20 C	0.864 g/cm ³ @ 20 C	0.775-0.840 g/cm ³ @ 20 C

Table 3: Chemicals used

Chemicals	Purity	Source
n-dodecane	Pure, >99.0% minimum purity	ACROS Organics
m-xylene	>99.0, Extra pure, >99.0%	ACROS Organics
Jet A	Jet A + Prist (anti-icing fuel additive)	Austin Executive Airport
Hydrogen	99.999% Ultra high purity grade	PRAXAIR

n-dodecane and m-xylene to represent JP-8 surrogates, were studied. The diagnostics used included particle image velocimetry (PIV) and laser-induced incandescence (LII). The surrogate composition of JP-8 in the present study was a mixture of 75% n-dodecane and 25% m-xylene by volume. Table 2 and 3 contain relevant information for all fuels considered in this investigation.

In this study, Jet-A (pre-blended with the Fuel System Icing Inhibitor) was used for the measurements instead of JP-8 owing to the difficulty we had in obtaining JP-8. Typically, petroleum-derived jet fuels consist of a hundred hydrocarbon components such as C₈-C₁₆ hydrocarbons including paraffins, naphthenes, and aromatics (e.g., [Colket et al. 2007 [28], Won et al. 2014] [29]). Jet A is the base fuel for the production of JP-8. Typical compositions of Jet A and JP-8 fuels are very similar [Colket et al. 2007] [28], with the primary difference being the freeze point. Jet A has the same flash point as JP-8 but a higher freeze point as shown in Table 4. JP-8 includes additives of the Corrosion Inhibitor/Lubricity Enhancer, the Fuel System Icing Inhibitor, and the Static Dissipater Additive to meet the requirement of the U.S. Military Specification MIL-DTL-83133G.

Table 4: Common characteristics of jet fuels

Name	Specification	Description	Flash point [C]	Freeze point [C]
Jet-A	ASTM D1655	U.S. domestic jet fuel	>38	<-40
Jet A-1	ASTM D1655, UK DefStan 91-91	Standard commercial jet fuel	>38	<-47
JP-8	MIL-DTL-83133	U.S. military jet fuel (Jet A-1 + 3 additives)	>38	<-47

Dryer and coworkers [Won et al. 2014] [29] indicated that extinction limits of JP-8 resulted in almost identical behavior to the Jet A as expected based on the similarity of their respective combustion targets. They also pointed out that the alternative jet fuels formed by similar feed stock and synthetic process exhibit similar behavior in terms of extinction limits as a function of transport-weighted enthalpy. It was shown that the high temperature reactivity for JP-8 and Jet A is very close.

Note that although our previously-studied ethylene(C_2H_4)/ N_2 flames were attached to the burner at $Re = 8300$, the flames of Jet A, n-dodecane ($n-C_{12}H_{26}$), and m-xylene (C_8H_{10}) remained attached only under laminar conditions (jet exit velocity of 3 m/sec, $Re = 2000$) with a 2 cm jet exit diameter burner. The first two photographs shown in Fig. 25 are Jet A and n-dodecane flames with fuel mole fraction, $X_{fuel} = 0.2$ and bulk velocity at the jet exit, $U_0 = 3$ m/s. It was shown that the soot inception zone for these laminar flames of Jet A/ N_2 and n-dodecane/ N_2 were less than 1 cm downstream of the jet for Jet A flames and 2.5 cm for n-dodecane, where the jet exit diameter was 2 cm. However, by adding hydro-gen (H_2) in the fuel stream, the flame was both attached to the fuel nozzle and we could obtain turbulent conditions. With the hydrogen-enriched flames, the soot began forming approximately 7d downstream for n-dodecane/ H_2/N_2 cases as shown in the third photographs in Fig. 25 (n-dodecane/ H_2/N_2 flames with composition of 0.15/0.07/0.77 by volume at $Re = 6700$ with burner exit diameter, $d = 1$ cm).

Table 5 listed mixture composition of fuel-mixtures used in the present study. The mixture composition of all flames was (15% Fuel + 15% H_2 + 70% N_2) by volume as listed in Table 5. The bulk flow velocity at the exit was 12 m/s for all conditions. The temperature of the fuel mixtures at the jet exit was set to 443.15K (170 C) for both Jet A and Surrogate, 473.15 K (200 C) for n-dodecane, and 413.15 K (140 C) for m-xylene.

A binary mixture of (75% n-dodecane+25% m-xylene)

Figure 26 depicts photographs of flame luminosity for n-dodecane/ H_2/N_2 , m-xylene/ H_2/N_2 ,

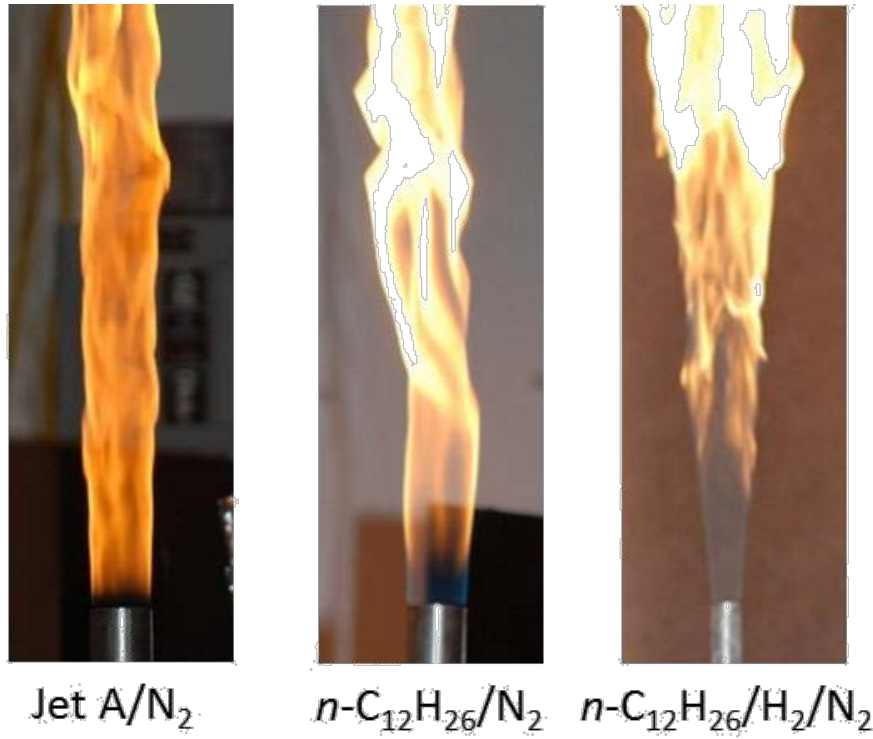


Figure 25: Photographs of Jet A/N₂ flame with $X_{fuel} = 0.2$, $U_0 = 3$ m/s, and $d = 2$ cm (left); n-dodecane/N₂ flame with $X_{fuel} = 0.2$, $U_0 = 3$ m/s, and $d = 2$ cm (middle); and n-dodecane/N₂/H₂ (0.15/0.07/0.77 by volume) flame with $U_0 = 10$ m/s and $d = 1$ cm (right).

Jet-A/H₂/N₂, and JP-8 surrogate/H₂/N₂ mixtures listed in the Table 5. As shown in Fig. 26, soot formation regions (where yellow color first appears in the flame) are different for each fuel mixture. The n-dodecane sooting region is delayed by about 10 jet diameters downstream, whereas m-xylene shows strong soot formation immediately out of the nozzle. The Jet-A and JP-8 surrogate flames have about a three diameter soot inception region. Hydrogen (H₂) in the fuel keeps the flame attached to the burner and helps to suppress polycyclic aromatic hydrocarbon (PAH) formation. The surrogate composition of JP-8 was a mixture of 75% n-dodecane and 25 % m-xylene by volume.

B-3.4 Soot Volume Fraction

Laser Induced Incandescence (LII) measurements were performed using an excitation wavelength of 532 nm. A long focal length of 750 mm spherical lens and a negative focal length (-60 mm) cylindrical lens were used to form a sheet for LII. The laser fluence was about 0.25 J/cm² and pulse duration was about 10 ns, therefore, the LII is in the plateau region. An intensified CCD camera (Princeton Instruments PI-Max 2) with resolution of 512x512 pixels was used for LII measurement. The soot incandescence was imaged through a bandpass filter with a central wavelength of 400 nm and bandwidth of 40 nm (FWHM). The intensified camera for LII was gated to 500 ns.

Table 5: Composition of fuel and operating conditions

Fuel	Fuel composition	Jet exit temperature	Jet exit velocity
n-dodecane	0.15% n-dodecane+15%H ₂ +70%N ₂	200 C	12 m/s
m-xylene	15% m-xylene+15%H ₂ +70%N ₂	140 C	12 m/s
Jet A	15% jet A+15% H ₂ +70% N ₂	170 C	12 m/s
Surrogate	15% surrogate +15% H ₂ +70% N ₂	170 C	12 m/s

A collage (composite) of instantaneous LII images of the turbulent Jet-A, JP-8 surrogate, m-xylene, and n-dodecane jet flame are presented in the Fig. 27 for the Re = 8000. Each collage is formed by images taken at different times and then assembled into the composite image. For n-dodecane flames, LII signal was first observed about 9 cm (9 diameters) downstream of the jet exit. Jet A showed LII intensity near 5 cm downstream of the jet exit but 10 times higher signal intensity than n-dodecane flames. Very strong LII signal was observed for m-xylene flames starting from 3 cm downstream of the jet exit. Signals for soot start to show around 3-4 jet diameter for Jet-A and surrogate. Similarly, as observed from the photographs of the flame luminosity in Fig. 26, the LII intensity signal for Jet-A and surrogate flames are similar but the surrogate fuel flame image shows slightly higher soot tendency.

LII/extinction measurements were performed to obtain the calibration constant to enable us to map the LII signal to soot volume fraction [Bockhorn et al. 2002] [16]. Extinction measurements were performed using He-Ne laser at a wavelength of 632.8 nm. The quantitative correlation between the LII signal $I_{LII}(x; h)$ and the soot volume fraction $f_v(x; h)$ is

$$f_v(x; h) = C_{cal} I_{LII}(x; h) \quad (4)$$

$$K_{ext}(x; h) = \frac{8^2 Im}{m^2 + 2} \frac{N_v(x; h)}{v} \int_0^v P(r) r^3 dr f_v(x; h) \quad (5)$$

where, m is the complex index of refraction of the soot particles at λ_{laser} , the wavelength of the laser light, $N_v(x; h)$ is the particle number density, x the propagation direction of the laser beam, and h the height above the burner.

By measuring the integral extinction and utilizing the Lambert-Beer formula

$$I_{hLaser} = I_{0Laser; h} \exp \int_0^h k_{ext}(x; h) dx ; \quad (6)$$

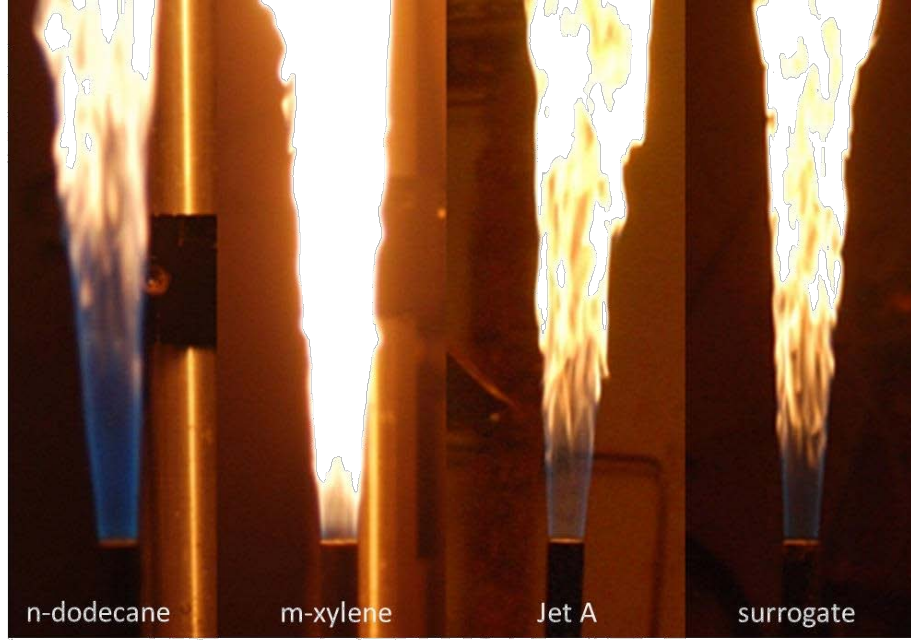


Figure 26: Photographs of n-dodecane, m-xylene, Jet-A, and JP-8 surrogate

the calibration constant can directly be derived for any height h above the burner using eqns. 4 and 5:

$$U_{\text{cal}} = \frac{\ln \frac{I_m}{I_h^{\text{Laser}}} + 2}{\int_0^L I_{\text{LI}}(x; h) dx} \quad (7)$$

In eqn. 7, $I_0^{\text{Laser},h}$ is the laser intensity of the incoming and I_h^{Laser} is the intensity behind the flame.

The choice of the complex refraction index, m is critical for the accuracy of a soot volume fraction measurement. A wide range of values for m have been reported in the literature. Table 6 listed widely used complex indices of refraction in the literature. $m = 1.57 - 0.56i$ is a widely used value in the visible spectrum by [Dalzell and Sarofim 1969] [18]. An-other popular value is $m = 1.90 - 0.55i$ by [Lee and Tien 1989] [30]. A number of recent studies have used refractive indices relation of wavelength dependence by [Chang and Charalampopoulos 1990] [31] for calculating m . In this study, the Ref [Dalzell and Sarofim 1969] [18] values were used: $m = 1.57 - 0.56i$.

Figure 28 shows collages of the averaged soot volume fraction, $\langle f_v \rangle$ and RMS f_v for Jet-A and surrogate fuel. Each distribution is composed of stacked slices at different heights. Approximately 700 instantaneous images were collected for each height, and were used for the statistical analysis. These collages are assembled to provide the axial and radial distributions of $\langle f_v \rangle$ and RMS f_v in the flame. The maximum locally-averaged soot vol-ume fraction, $\langle f_{v;\max} \rangle$ was found to be 28 ppb for Jet-A flames and 36 ppb for JP-8 sur-rogate.

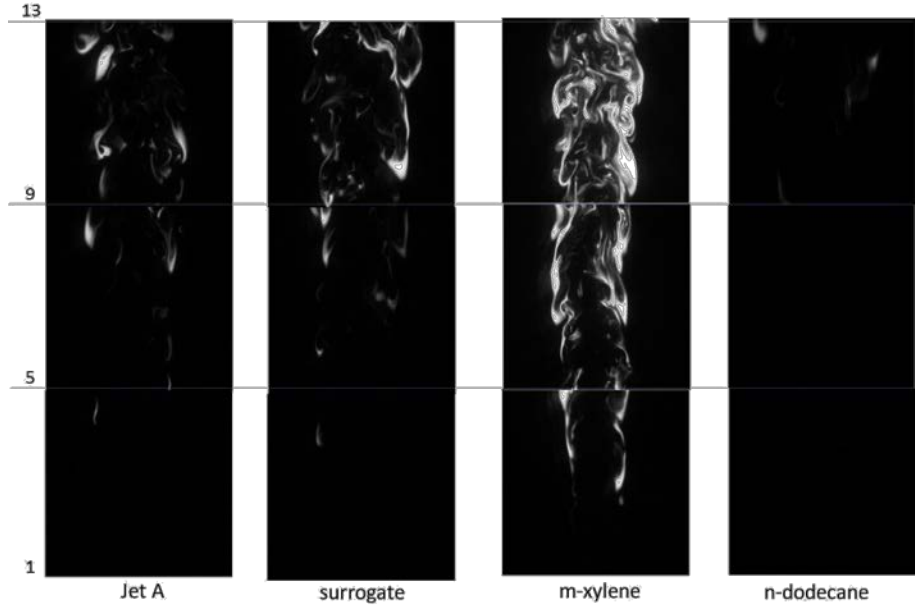


Figure 27: Instantaneous LII images of the turbulent JetA, JP-8 surrogate, m-xylene, n-dodecane jet flames. Each distribution is composed of stacked slices at different heights. Reynolds number, $Re = 8000$. Incident laser beam is coming from the RHS.

Table 6: Soot index of refraction

Refractive Indices, m	Ref.
1.57-0.56i	Dalzell and Sarofim [18]
1.90-0.55i	Lee and Tien [30]
1.755-0.576i (632.8 nm)	Change and Charalmpopoulos [31]
1.75-1.03i	Williams et al. [19]

Fig. 29 shows profiles of the mean soot volume fraction, f_v for Jet-A and JP-8 surrogate at $x/d = 7$ (top) and $x/d = 12$ (bottom) computed using the 700 instantaneous images. As mentioned earlier, mean soot volume fraction profiles showed that surrogate fuel produced slightly higher soot emission than Jet-A. The shape of the mean soot volume fractions showed a slight asymmetry with greater soot concentrations on the right (laser entry) side. It was observed from ethylene/ N_2 flames. Although the temperature and mixture fraction profiles from the PLIF showed symmetry along the radial direction, the shape of the mean soot volume fractions showed a slight asymmetry with greater soot concentrations on the laser entry side. Asymmetric soot volume fraction profiles have been reported in several previous studies [Zerbs et al. 2009 [17], Kohler et al. 2011 [32]]. Note that we can observe asymmetry in the visible luminosity at the flame base, which does suggest there is a natural asymmetry in the soot formation.

Figure 30 shows Probability density Functions (PDFs) of soot volume fraction of turbulent

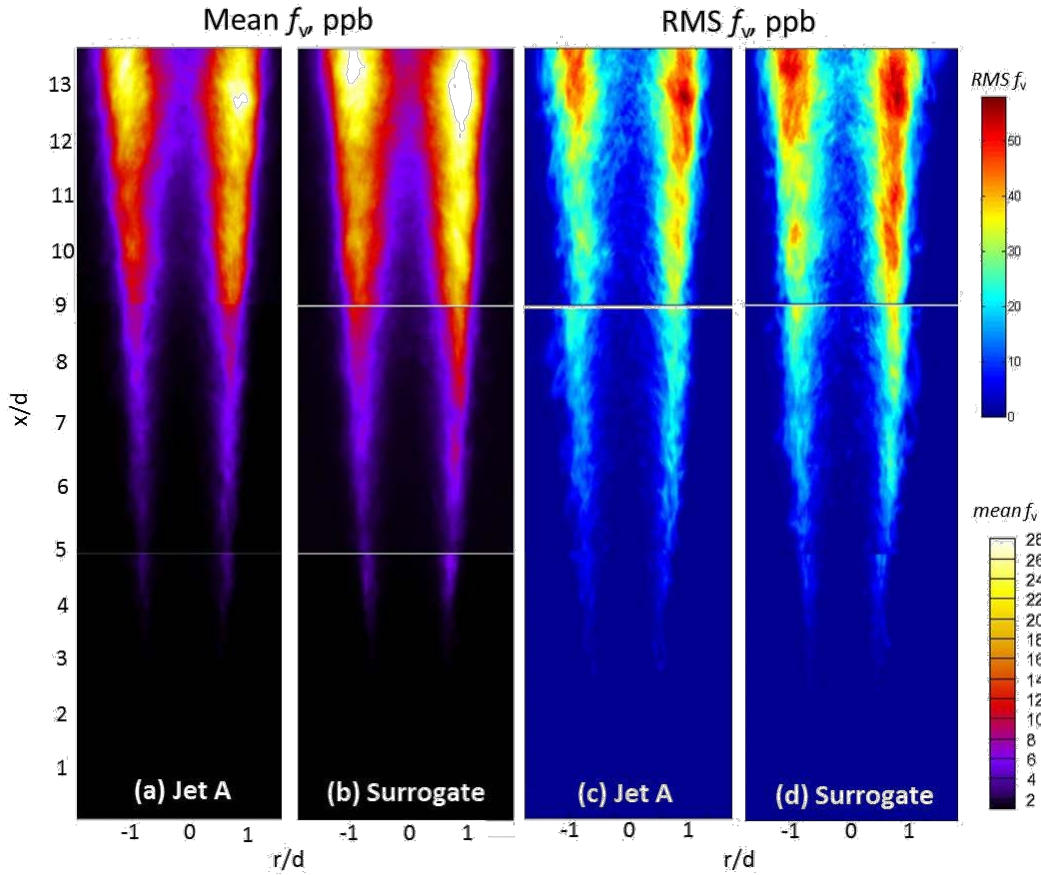


Figure 28: Mean (a,b) and RMS (c,d) soot volume fraction measured by LII imaging in a $Re = 8000$ turbulent non-premixed Jet A and JP-8 surrogate flames. The mean and RMS statistics are computed from 700 instantaneous images taken at each height. Max 36 ppb for JP-8 surrogate and 28 ppb for Jet A.

non-premixed surrogate fuel and Jet-A flames at $x/d = 7$ in a $Re = 8000$ conditioned on $0.95 < jr/dj < 1.05$. The statistics are computed from 500 instantaneous images. It is shown that the most probable soot volume fraction lies around 2 ppb for the surrogate. For Jet-A, PDF of soot volume fraction has significant zero-clipping. The zero-clipping continues to occur further downstream for the Jet-A flame as can be seen for the $x/d = 12$ data in Fig. 30. However, a scatter plot is shown for the $x/d=12$ location, and shows that the soot volume fraction values are fairly widely distributed at that location.

Figure 32 shows collages of the averaged soot volume fraction, $\langle f_v \rangle$ of m-xylene (left) and n-dodecane (right). 500 instantaneous images were collected for each height. As shown in the earlier photographs and instantaneous images, m-xylene soots significantly higher than other fuels with maximum $\langle f_v \rangle$ of 110 ppb. On the other hand, n-dodecane soots much less as the maximum $\langle f_v \rangle$ is 2.4 ppb. The asymmetric soot volume fraction tendency is consistently observed with the higher $\langle f_v \rangle$ on the laser beam entry side (right).

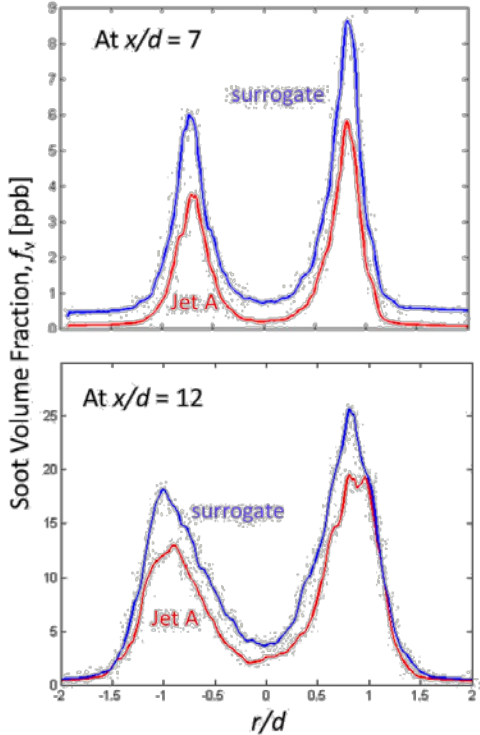


Figure 29: Mean profiles of soot volume fraction for Jet-A and JP-8 surrogate at $x/d = 7$ (top) and 12 (bottom).

B-3.5 Simultaneous LII and PIV

Simultaneous LII and PIV measurements were performed for n-dodecane/H₂, Jet A/H₂, and m-xylene/H₂ flames. Both the fuel-jet and coflow were seeded with aluminum oxide (Al₂O₃) particles of nominal diameter 0.5-1.0 μm for PIV. Separate N₂ and H₂ gases were passed through the main jet seeder to avoid fuel condensation in the seeder and wetting of the alumina particles. The time t between the two pulses was set to 50 s. A 2048x2048 pixels CCD camera was used to capture the PIV images. The cameras were fitted with 105 mm focal length and operated with an aperture of f/32. Bandpass filters were placed in front of the PIV cameras, which had a center wave length of 532 nm and a bandwidth of 10 nm. The first pulse of 532 nm light was used for the LII measurements. A 750 mm spherical lens and a slow negative focal length (-60 mm) cylindrical lens were used to form a sheet for both PIV and LII. The camera was fitted with a 105 mm focal length lens that was operated with an aperture of f/2.8. The field of view was 3 cm x 3 cm and spatially overlapped with the fields of view of the PLIF and LII measurements. LaVi-sion DaVis 7.2 was used for spatial image mapping for the PIV and LII and to process PIV images. An iterative, multi-pass, adaptive interrogation windowing algorithm was used for PIV image processing. The final iteration was 32x32 pixels with a 75% overlap between adjacent interrogation windows. Vectors with a magnitude greater than 3 times the standard deviation of the neighboring vectors were defined as spurious vectors and were replaced with the median of the valid neighboring vectors.

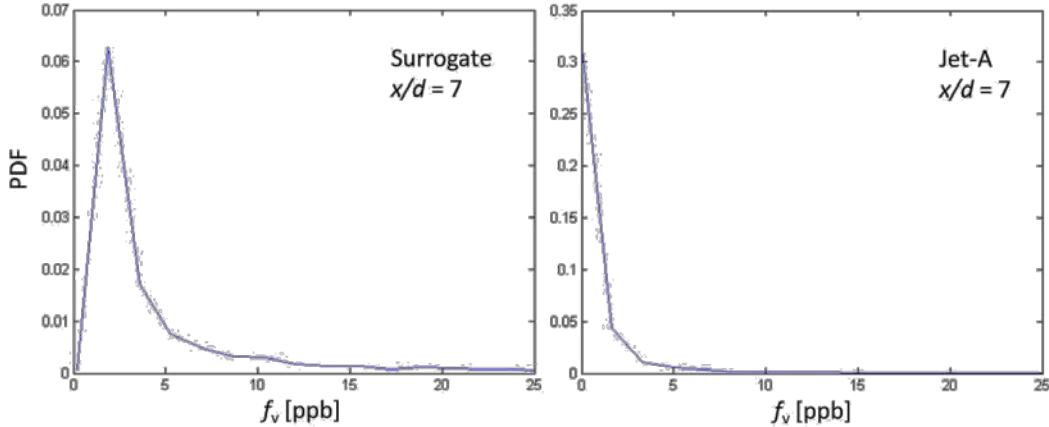


Figure 30: Probability Density Functions of soot volume fraction at $x/d = 7$ in a $Re = 8000$ turbulent non-premixed surrogate fuel (left) and Jet-A (right) flames conditioned on $0.95 < jr/dj < 1.05$. The statistics are computed from 500 instantaneous images.

Figures 33-35 depict simultaneously-acquired instantaneous f_v superimposed on the axial velocity field for Jet-A/ H_2/N_2 , m-xylene/ H_2/N_2 , and n-dodecane/ H_2/N_2 flames. Also shown is the stoichiometric velocity contour (black line), $U_{\text{stoic}} = (U_0 U_{\text{co}})Z_{\text{st}} + U_{\text{co}}$, which is known to correspond approximately with the location of the reaction zone [Han and Mungal 2003] [20], where, U_0 is the centerline velocity at the jet exit. Soot structures are found predominantly near the stoichiometric contour on the fuel-rich side. For the case of ethylene/ N_2/Kr flames, it was shown that the soot was predominantly formed within the temperature band of 1100-1500 K on the fuel-rich side and peak f_v is formed between the temperature bands of 1300-1400 K. The peak flame temperature of 50%ethylene/46% N_2 /4%Kr flame was approximately 1750 K.

Fig. 36 shows radial profiles of mean soot volume fraction and axial velocity for (a) Jet A/ H_2/N_2 flames, and (b) m-xylene/ H_2/N_2 flames at $x/d = 5.5$. At this location the m-xylene case is seen to exhibit substantial higher levels of soot than Jet A, as expected from the discussion above. The peak mean soot volume fraction is about 100 ppb and 10 ppb for m-xylene and Jet A, respectively. In both cases, however, the peak mean soot occurs in the low-velocity region of the jet where the velocity is about 2-4 m/s.

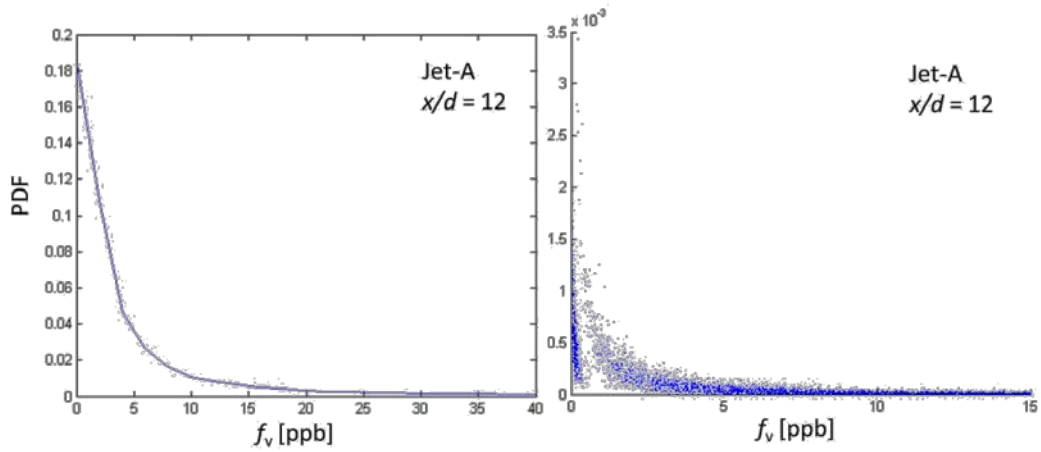


Figure 31: Probability density Function of soot volume fraction at $x/d = 12$ in a $Re = 8000$ turbulent non-premixed Jet-A flames conditioned on $0.95 < jr/dj < 1.05$. A scatter plot is shown on the right panel. The statistics are computed from 500 instantaneous images.

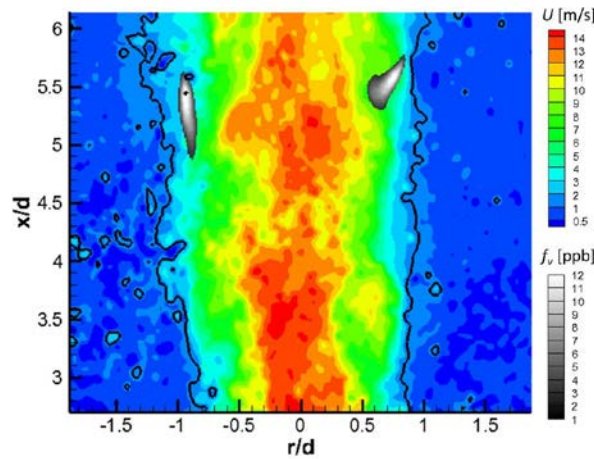


Figure 33: Instantaneous images of soot volume fraction fields of a Jet A/H₂ flame, $U_{st} = 1.5$ m/s.

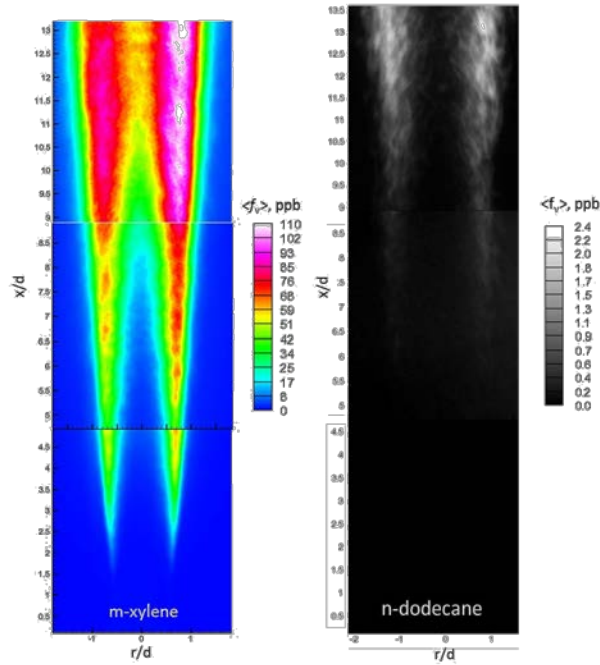


Figure 32: Mean soot volume fraction measured by LII imaging in a $Re = 8000$ turbulent non-premixed m-xylene and n-dodecane flames. The mean statistics are computed from 700 instantaneous images taken at each height.

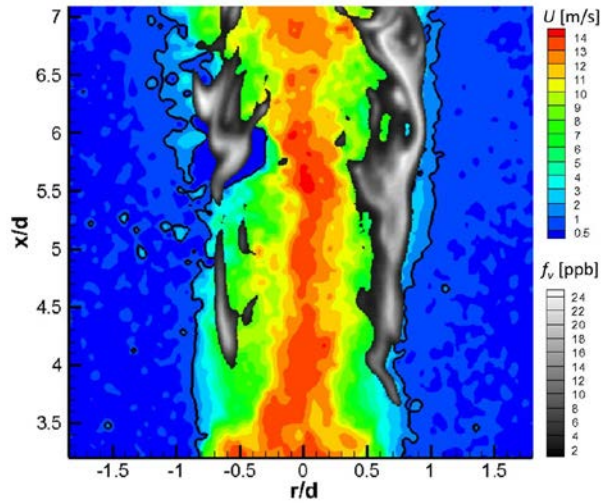


Figure 34: Instantaneous images of soot volume fraction fields of an m-xylene/H₂ flame.

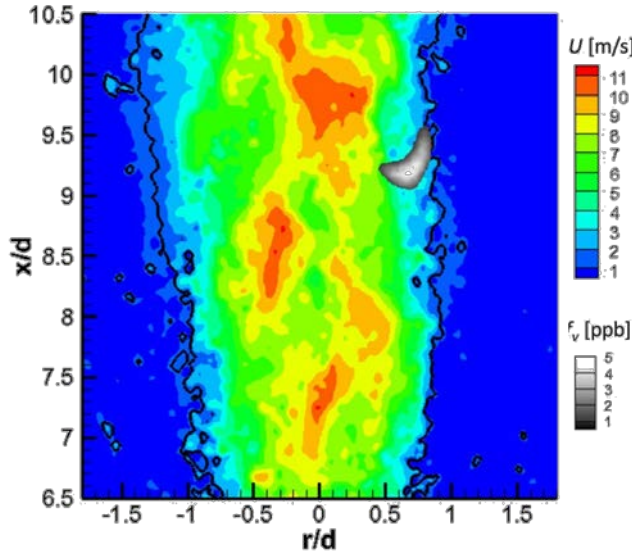


Figure 35: Instantaneous images of soot volume fraction fields of an n-dodecane/H₂ flame.

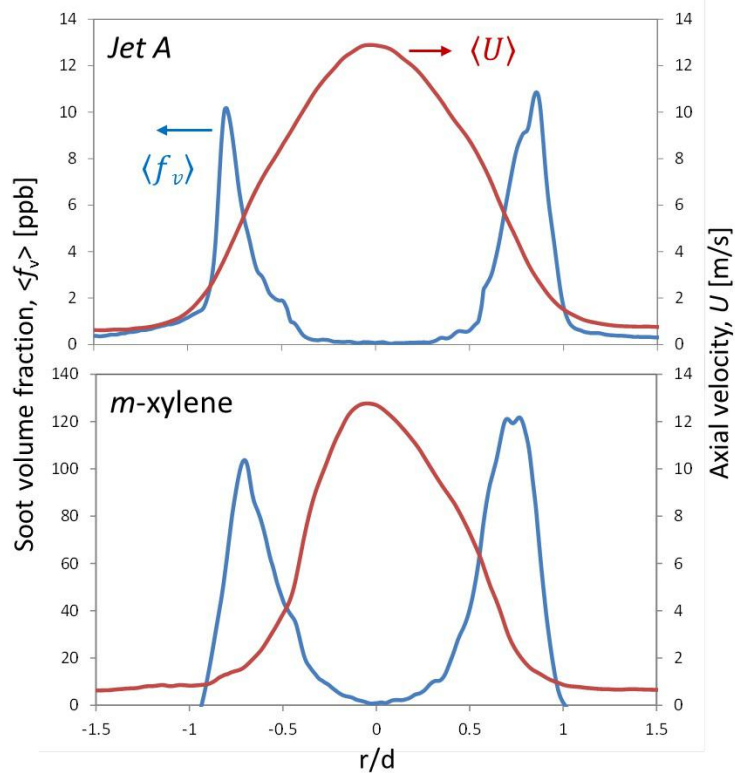


Figure 36: Radial profiles of mean soot volume fraction and axial velocity for (a) Jet A/H₂/N₂ flames and (b) m-xylene/H₂/N₂ flames at x/d = 5.5.

Table 7: Proposed vs Accomplished Tasks

Proposed Task	Accomplished Task
Velocity and emissions measurements in turbulent JFICF	Extensive measurements of velocity were made. Emission measurements were not pursued based on validation needs. New analysis techniques were developed to provide improved validation of turbulent statistical data.
Simultaneous LII+PIV Simultaneous LII+FRS+Kr-LIF	Extensive measurements of ethylene, jet fuel, and jet-fuel surrogates were performed using simultaneous LII and PIV. Simultaneous Kr LIF, LII and PIV were used to obtain simultaneous mixture fraction, temperature, velocity and soot volume fraction fields in ethylene jet flames. These data represent the first of their kind and present a new and unique validation data set.
Additional measurements dictated by the SAD procedure	The experimental approach was continuously evaluated to ensure it stayed relevant to validation needs. There were many instances where the approach needed to be modified as dictated by the SAD procedure. The most major example was the addition of measurements of jet fuel flames and jet fuel surrogates.

C. Fundamental Models for Emissions

The UCB objective was to develop reduce-order models for soot surface growth and oxidation. The strategy was to develop a detailed model of soot oxidation, validate it and combine with a detailed model of soot surface growth, and reduce the combined detailed surface chemistry model to a small mathematical form suitable for inclusion with CFD codes. All the objectives have been met, as detailed below.

C-1 Introduction

Oxidation of carbon by molecular oxygen has been studied for a long time, in various disciplines and contexts. One of the primary interests is mechanistic understanding of the process. It is not straightforward to decipher experimental observations into mechanistic details, and theoretical tools provide increasingly reliable approaches in this direction. Formation of carbon at high temperatures, such as soot formation in flames, is especially amenable to theoretical studies. Indeed, the overall reaction time at high temperatures is on the order of milliseconds and hence only fast reactions should be accounted for. Furthermore, at these conditions the gas-surface reactions follow the direct, Eley-Rideal mechanism [33] that allows a simpler theoretical treatment, as compared to the Langmuir-

Hinshelwood [33, 34] and mobile-precursor [35, 36] mechanisms at lower temperatures that increase the complexity of molecular interactions and enlarge the number of possible reactions. The past few decades of theoretical studies of high-temperature carbon growth have brought us to mechanistic understanding of the process [37] that is being currently exploited not only for combustion soot [38, 39] but also for carbon-black processes [40] as well as gas-phase synthesis of graphene [41]. These accomplishments motivate employing a similar strategy for unravelling details of carbon oxidation, and hence we begin with soot oxidation at high temperatures.

Oxidation of soot by molecular oxygen has received substantial attention over the years (see, e.g., a recent review [42] and accounts given in recent articles [43–48]). Early conception was based on an empirical model of Nagle and Strickland-Constable (NSC) [49], who represented the carbon surface by two empirical sites: less reactive and more reactive. In the early 1990’s, Frenklach and co-workers [37, 50, 51] suggested a physically-resolved model, postulating that oxidation by molecular oxygen occurs on radical sites of aromatic molecules comprising a soot particle, i.e.,



The rate coefficient of this reaction was assigned by analogy to phenyl oxidation [52]. This simple, one-step kinetic model has been broadly employed in numerical studies of soot formation in hydrocarbon flames.

While the simple reaction model based on chemical analogy, for both surface oxidation and growth, was successful in achieving an order-of-magnitude agreement with experiment [37, 51, 53, 54], the follow-up research revealed richer chemistry of the growth (see, e.g., [55–63] and references cited therein). One of the main features is surface migration of five-membered rings along zigzag edges of aromatics [55, 58]. Being in itself intriguing, this process opens numerous reaction possibilities [58, 59, 61–63]. Modeling that included all such identified different reactions exhibited curving of the initially planar aromatics [61]. Recent experimental studies suggested a substantial dependence of soot oxidation rate on soot particle curvature [43]. Clearly, a simple model such as Eq.8 is insufficient to explain this observation.

A more detailed look at soot and carbon oxidation has been given within the past decade (see, e.g., [46, 47, 64–74] and references cited therein). Some of the recent interest is motivated by the use of filters to capture soot from diesel engines and their regeneration through oxidation of the captured soot [47, 75]. The attention of the present study is on oxidation of soot at high temperatures, i.e., at conditions realized in flames of hydrocarbon fuels and inside combustion engines.

C-2 Methodology

The KMC methodology followed that used previously [61, 72, 76]. Briefly, the KMC simulations tracked a single graphene “molecule” evolving in a flame-like environment, but maintaining the gas phase in a constant state, i.e., at constant values of temperature, pres-

sure, and species mole fractions, which allowed us to investigate unambiguously the influence of individual factors on the simulation outcome. At each time step, a reaction event was selected stochastically and then applied.

The processes of surface growth and oxidation were modeled as a Markovian sequence of reaction events. There are two types of reactions that comprise the present model: bimolecular reactions between the gaseous species and surface sites, and unimolecular “decompositions” of surface species. All stochastic events were treated as first-order processes, with the respective per-site rates. The second-order reactions produced pseudo-first-order rate constants through multiplication of the gas-surface rate coefficient by the concentration of the gaseous reactant. The selection of the reaction event and specific graphene-edge site was done by application of the Gillespie algorithm [77, 78] adapted for surface processes [79, 80]. Briefly, given an instant of a current reaction event, t_n , the time of the next reaction event to occur at substrate site i is $t_{n+1;i} = t_n - (\ln u)/k_{\text{total};i}$, where u is a random number distributed uniformly from 0 to 1 and $k_{\text{total};i} = \sum_j k_j$; j is the sum of the per-site rates of reactions possible at site i . The smallest among the $t_{n+1;i}$ values, computed for all surface reaction sites, becomes the time instant of the next reaction event, t_{n+1} , and the particular reaction to occur at that time is chosen according its probability $p_j ;i = k_j ;i/k_{\text{total};i}$ upon drawing another random number u . Once a reaction event is implemented, the process repeats itself.

The set of surface reactions employed in the KMC model contains 45 growth and 45 oxidation reactions. The surface growth reactions and their corresponding rate coefficients are taken from Whitesides and Frenklach [61, 76] and 45 of the surface oxidation reactions and their corresponding rate coefficients are from our recent study [72]. This reaction mechanism is constructed for high temperatures, 1500–2500 K; in doing so, it has been presumed that active soot-particle surface is comprised of H-saturated graphene edges and an active, reactive site for the O₂ attack is an aromatic radical, created by H-atom abstraction [37, 51]. At high temperatures and gaseous environments containing hydrogen, the probability of having two adjacent radical sites is relatively low and hence we neglected reactions occurring on such diradical sites. Furthermore, considering the millisecond time scale of the high-temperature processes, we neglected slow reactions, such as edge reconstruction and nascent site deactivation [46, 81]. With these considerations, the primary product of carbon oxidation is CO [47, 71–73] and the O atoms released in the surface reactions enter into the gas phase. The gaseous concentration of O atoms and their contribution to soot oxidation is relatively low in flame environments [82, 83], as compared to OH and O₂, and hence the oxidative attack of graphene carbons by O atoms were not included in the present study. Also, the present simulations consider evolution of a single graphene “flake”, and hence no particle-dynamics processes, such as oxidation-induced particle fragmentation [83, 84], were included in the model.

To properly account for the evolving curvature, the KMC model was coupled to molecular-mechanics geometry optimization using the MM3 potential [85] with the TINKER molecular mechanics package [86]. The MM3 potential has been found to produce geometries for fullerenes in good agreement with the ab initio Hartree-Fock method [87] as well as experimental and DFT results for fullerene fragments [88]. Optimization of the structure

geometry was performed after each structure-changing event. The geometry optimization step properly accounted for substrate curvature while maintaining physically accurate bonding and geometric configuration of the evolving structures. A check was made after each geometry optimization to ensure that the geometry produced by the molecular mechanics code was consistent with the bonding implied by the KMC model. Specifically, the code tested if the geometry optimization left all carbon atoms within a specified distance of the other atoms to which they were bonded in the KMC description. If any two carbon bonds were found to be separated by more than two angstroms, the simulation was ended.

The evolution of the graphene structure, referred to hereafter as substrate, was monitored by computing the numbers of reaction events, instantaneous structure size, and its five-member ring fraction, f_{R5} , the latter defined as [76]

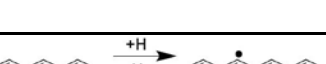
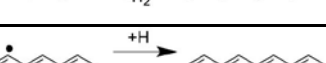
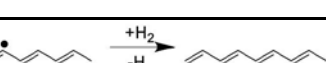
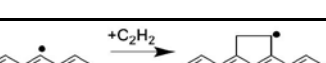
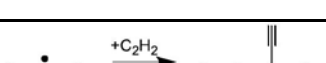
$$f_{R5} = \frac{32 N_{R5}}{12 N_{R5} + N_{R6}} ; \quad (9)$$

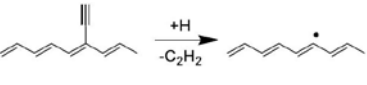
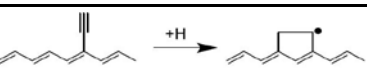
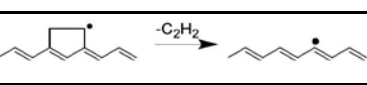
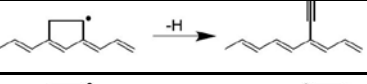
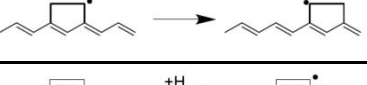
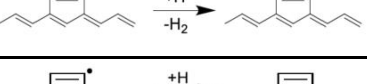
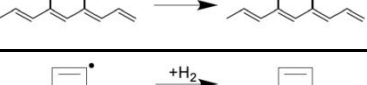
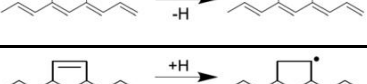
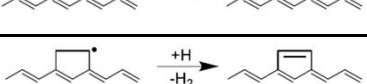
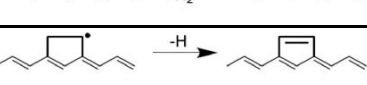
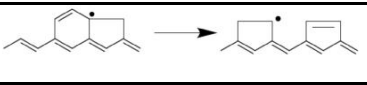
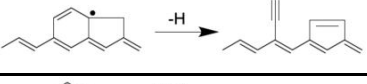
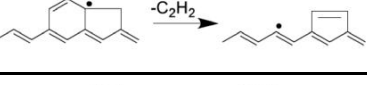
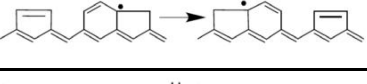
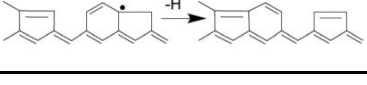
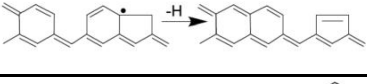
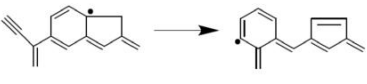
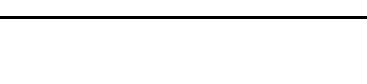
where N_{R5} and N_{R6} are the number of five- and six-member rings, respectively, and the 32/12 coefficient normalizes Eq. 9 to have $f_{R5} = 1$ for buckminsterfullerene, C_{60} .

The set of surface reactions employed in the current KMC model contains 45 growth and 59 oxidation reactions. The reaction model of soot surface growth and oxidation is presented in Table 8. The rates for each reaction (k 's) are pseudo-first order with units of s^{-1} .

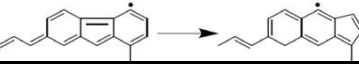
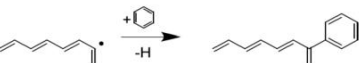
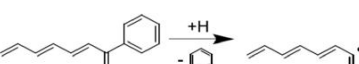
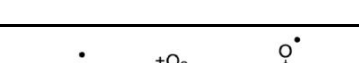
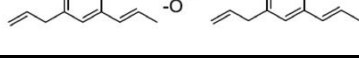
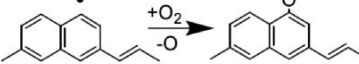
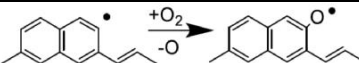
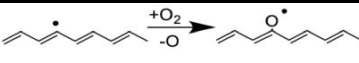
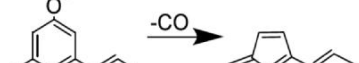
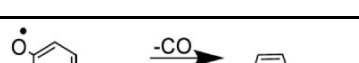
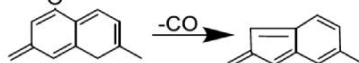
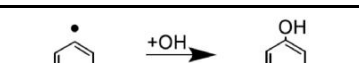
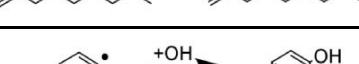
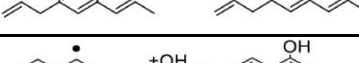
To collect better statistics, simulations for each set of initial conditions were repeated 100 times, each with a different starting random seed. The results reported in this work are averages over these ensembles of simulations. In the previous study [72] we repeated the entire sequence of calculations, comprised of the initial period of substrate growth followed by a period of substrate oxidation. With the primary focus on factors affecting oxidation, the present simulations all started with the same set of 100 grown substrates.

Table 8: KMC Reactions

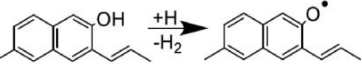
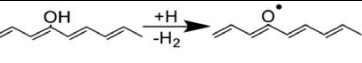
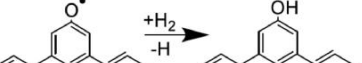
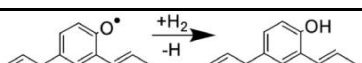
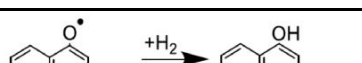
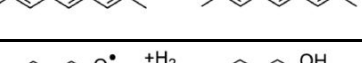
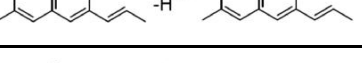
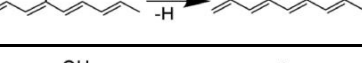
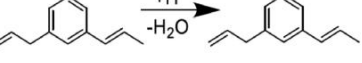
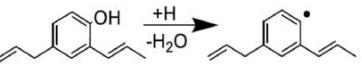
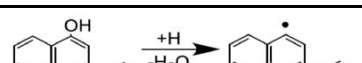
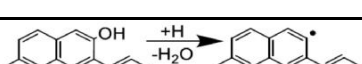
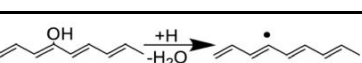
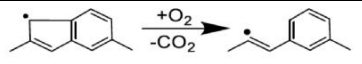
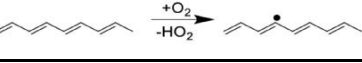
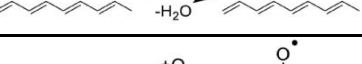
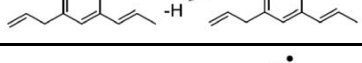
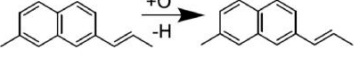
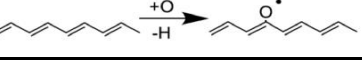
	reaction	per-site rate coefficient (s, mol/cm ³ , K)
1		$k_1 = 4.2 \cdot 10^{13} e^{-8052/T} [H]$
2a		$k_{2a} = 2 \cdot 10^{13} [H]$
2b		$k_{2b} = \frac{k_1}{7.59e^{2097/T}} \frac{[H_2]}{[H]}$
3		$k_3 = \frac{k_a k_b}{k_b + k_c + k_d} [C_2H_2]$
4		$k_4 = \frac{k_a k_d}{k_b + k_c + k_d} [C_2H_2]$

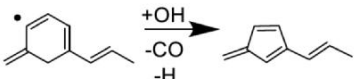
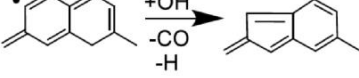
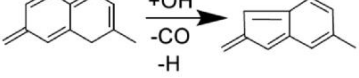
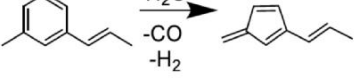
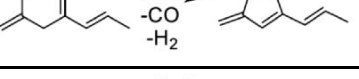
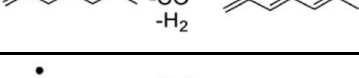
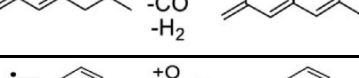
5		$k_5 = \frac{k_c k_e}{k_b + k_c + k_d} [H]$
6		$k_6 = \frac{k_b k_e}{k_b + k_c + k_d} [H]$
7		$k_7 = 3:1 10^{11} T^{0.87} e^{-37403/T}$
8		$k_8 = 6:7 10^{11} T^{0.84} e^{-35625/T}$
9		$k_9 = 1:3 10^{11} T^{0.16} e^{-23099/T}$
10		$k_{10} = 5:07 \quad 10^7 T^{1.93} e^{-6518/T} [H]$
11a		$k_{11a} = 6:08 \quad 10^{12} T^{0.27} e^{-141/T} [H]$
11b		$k_{11b} = 9:46 \quad 10^3 T^{2.56} e^{-2529/T} [H_2]$
12		$k_{12} = 5:40 \quad 10^{11} T^{0.45} e^{-916/T} [H]$
13a		$k_{13a} = 2 \cdot 10^{12} [H]$
13b		$k_{13b} = \frac{k_{12}}{1.791e17708-T}$
14		$k_{14} = 8:9 10^5 T^{2.28} e^{-30944/T}$
15		$k_{15} = 2:1 10^9 T^{1.14} e^{-41952/T}$
16		$k_{16} = 3:8 10^{10} T^{1.30} e^{-51929/T}$
17		$k_{17} = 4:0 10^{10} T^{1.53} e^{-57225/T}$
18		$k_{18} = k_{15}$
19		$k_{19} = k_{15}$
20		$k_{20} = k_{15}$
21		$k_{21} = k_9$
22		$k_{22} = k_{15}$
23		$k_{23} = \frac{k_9}{k_7+k_8+k_9} 1:3 \quad 10^{11} T^{1.08} e^{-35428/T}$

24		$k_{24} = \frac{k_8}{k_7+k_8+k_9} 1:3 \quad 10^{11} T^{1.08} e^{-35428/T}$
25		$k_{25} = \frac{k_7}{k_7+k_8+k_9} 1:3 \quad 10^{11} T^{1.08} e^{-35428/T}$
26		$k_{26} = \frac{k_{aKf}}{k_c+k_d+k_f} [C_2H_2]$
27		$k_{27} = 1:9 \quad 10^{10} T^{0.712} e^{-4893/T} [C_2H_2]$
28		$k_{28} = k_9$
29		$p_{29} = 0:5$
30		$p_{30} = 0:5$
31		$p_{31} = 2:3$
32		$p_{32} = 1:3$
33		$k_{33} = \frac{k_{17}}{3.24 \cdot 10^9 e^{-52539/T}} [C_2H_2]$
34		$k_{34} = k_{33}$
35		$k_{35} = 1:0 \quad 10^{10} T^{0.955} e^{-5326/T} [C_2H_2]$
36		$k_{36} = 7:0 \quad 10^{10} T^{0.018} e^{-6059/T} [H]$
37		$k_{37} = k_9$
38		$k_{38} = k_{15}$
39		$k_{39} = k_{33}$
40		$k_{40} = 3:49 \cdot 10^{12} T^{0.39} e^{-1228/T}$
41		$k_{41} = 3:86 \cdot 10^{11} T^{0.21} e^{-8908/T}$
42		$k_{42} = 1:0 \quad 10^{13} [CH_3]$

43		$p_{43} = 1:3$
44		$k_{44} = 1:9010^{76} T^{-18.90} e^{-19884/T} [A1]$
45		$k_{45} = \frac{k_{44}}{1:45 \cdot 10^{13} T^{3.23} e^{3998/T}} \frac{[H]}{[A1]}$
46		$k_{46} = 3:17 \cdot 10^{13} e^{-1017/T} [O_2]$
47		$k_{47} = k_{46}$
48		$k_{48} = 3:91 \cdot 10^{13} e^{-1496/T} [O_2]$
49		$k_{49} = k_{48}$
50		$k_{50} = k_{48}$
51		$k_{51} = 1:08 \cdot 10^2 T^{3.28} e^{-21866/T}$
52		$k_{52} = 4:02 \cdot 10^2 T^{4.38} e^{-24624/T}$
53		$k_{53} = 6:42 \cdot 10^{10} T^{1.00} e^{-29183/T}$
54		$k_{54} = k_{53}$
55		$k_{55} = 1:47 \cdot 10^{14} e^{-632/T} [OH]$
56		$k_{56} = k_{55}$
57		$k_{57} = k_{55}$
58		$k_{58} = k_{55}$
59		$k_{59} = k_{55}$

60		$k_{60} = 2:13 \cdot 10^{15} e^{-42305/T}$
61		$k_{61} = k_{60}$
62		$k_{62} = k_{60}$
63		$k_{63} = k_{60}$
64		$k_{64} = k_{60}$
65		$k_{65} = 4:34 \cdot 10^{14} e^{-984/T} [H]$
66		$k_{66} = k_{65}$
67		$k_{67} = k_{65}$
68		$k_{68} = k_{65}$
69		$k_{69} = k_{65}$
70		$k_{70} = 2:14 \cdot 10^{16} e^{-52988/T}$
71		$k_{71} = k_{70}$
72		$k_{72} = k_{70}$
73		$k_{73} = k_{70}$
74		$k_{74} = k_{70}$
75		$k_{75} = 1:14 \cdot 10_{12} \frac{T}{300}^{2.117} e^{-5603/T} [H]$
76		$k_{76} = k_{75}$
77		$k_{77} = k_{75}$

78		$k_{78} = k_{75}$
79		$k_{79} = k_{75}$
80		$k_{80} = 1:70 \quad 10^{14} e^{-9635=T} [H_2]$
81		$k_{81} = k_{80}$
82		$k_{82} = k_{80}$
83		$k_{83} = k_{80}$
84		$k_{84} = k_{80}$
85		$k_{85} = 2:00 \quad 10^{14} e^{-2670=T} [H]$
86		$k_{86} = k_{85}$
87		$k_{87} = k_{85}$
88		$k_{88} = k_{85}$
89		$k_{89} = k_{85}$
90		$k_{90} = 3:45 \quad 10^{11} e^{-13422=T} [O_2]$
91		$k_{91} = 1:05 \quad 10^{13} e^{-30190=T} [O_2]$
92		$k_{92} = 3:88 \quad 10^3 T^{2.683} e^{-369=T} [OH]$
93		$k_{93} = 4:0 \quad 10^{12} e^{-2328=T} [O]$
94		$k_{94} = k_{93}$
95		$k_{95} = k_{93}$
96		$k_{96} = 1:0 \quad 10^{14} [OH]$

97		$k_{97} = k_{96}$
98		$k_{98} = k_{96}$
99		$k_{99} = k_{96}$
100		$k_{100} = 1:0 \cdot 10^{12} [\text{H}_2\text{O}]$
101		$k_{101} = k_{100}$
102		$k_{102} = k_{100}$
103		$k_{103} = k_{100}$
104		$k_{104} = 6:29 \quad T \frac{0.505}{298} e \frac{306-T}{306} [\text{O}]$

For reactions 3 – 6 and 26: $k_a = 1:1 \cdot 10^7 T^{1.71} e^{1960=T}$, $k_b = 6:8 \cdot 10^{11} e^{11084=T}$, $k_c = 1:3 \cdot 10^{14} e^{21025=T}$, $k_d = 4:8 \cdot 10^{12} e^{16875=T}$, $k_e = 1:5 \cdot 10^{10} T^{0.85} e^{601=T}$, $k_f = 2:5 \cdot 10_{12} T^{0.13} e^{7902=T}$

Reactions 1 – 45. The surface growth reactions and their corresponding rate coefficients are taken from Whitesides and Frenklach [61, 76] and further discussion of those reactions can be found in those studies. Reactions 2, 11, and 13 each occur in two different ways and are expressed as parts (a) and (b) in Table 8.

Reactions 46 – 50. The calculation of rate coefficients for the oxidation of six-member rings by O_2 is discussed in detail in Chapter 3. Reactions 46 and 47 were assigned the high-pressure-limit rate coefficients computed for the prototype reaction of phenyl + O_2 ! phenoxy + O. The rate coefficients for reactions 48, 49, and 50 are taken from the calculation of pyrenyl + O_2 ! pyrenoxy + O.

Reactions 51 – 54. The rates of thermal decomposition of oxyradicals were taken from the RRKM-ME calculations performed by Edwards et al. [68] for the decomposition of graphene armchair oxyradicals. The study found that the rate coefficients depended on the position of the radical site could affect product yields. Reaction 51 was given the high-pressure-limit rate coefficients of (R1) from Edwards et al. [68]. Reaction 52 corresponds with (R2), and reactions 53 and 54 were assigned the rate coefficients for (R3).

Reactions 55 – 59. The attack of OH on a radical site to form an R-OH site was taken from the RRKM-ME calculations of rate coefficients for the reaction phenanthryl + OH performed by Edwards et al. [69].

Reactions 60 – 64. The elimination of H from R-OH to form an oxyradical is also taken from Edwards et al. [69].

Reactions 65 – 69. The rate for H addition to an oxyradical was computed using the rate coefficients for reactions 60 – 64 and the corresponding equilibrium constants of reactions 65 – 69 which are published in [69].

Reactions 70 – 74. The rates for the reverse of reactions 55 – 59 are taken from Edwards et al. [69].

Reactions 75 – 79. The rate coefficients for the reaction R-OH + H ! R-O + H₂were taken from the calculations performed by Meana-Paneda et al. [89] for the reaction CH₃OH + H ! CH₃O + H₂.

Reactions 80 – 84. The rate coefficients for the reverse of reactions 75 – 79 were found by taking the forward rate for the reaction CH₃OH + H ! CH₃O + H₂ calculated in [89] and multiplying it by the equilibrium constants calculated by Jodkowski et al. [90].

Reactions 85 – 89. The rate of H addition to produce H₂O and form a radical site is taken from shock tube measurements of the thermal decomposition of methanol performed by Hidaka et al. [91].

Reaction 90. Present study. The high-pressure-limit rate is used in the KMC model.

Reaction 91. The rate coefficient for hydrogen abstraction by O₂ utilizes the per-site rate coefficient for the reaction of benzene + O₂ ! phenyl + HO₂ determined in shock tube experiments performed by Asaba and Fujii [92].

Reaction 92. The rate coefficient for hydrogen abstraction by OH is the per-site rate coefficient of benzene + OH ! phenyl + H₂O as determined by Seta et al. [93].

Reactions 93, 94, and 95. The rate coefficient for R-H + O ! R-O + H is the per-site rate coefficient for benzene + O ! phenoxy + H from a study by Leidreiter and Wagner [94].

Reactions 96 – 99. The rate coefficient for six-member ring oxidation by OH was calculated to be 1 10¹⁴ cm³ mol⁻¹ s⁻¹ in the high-pressure limit in [69].

Reactions 100 – 103. The rate coefficient for six-member ring oxidation by H₂O was estimated to be 1 10¹² cm³ mol⁻¹ s⁻¹ in the high-pressure limit based on the results of a mechanistic study by Dong et al. [95].

Reaction 104. Present study.

C-3 Detailed Kinetic Monte Carlo Simulations of Graphene-Edge Oxidation by Molecular Oxygen

KMC simulations were performed at temperatures of 1500, 2000, and 2500 K. Two scenarios were simulated: one with pure oxidation and one where oxidation competes with

growth. In the latter scenario, the graphene layer was first grown from an initial coronene substrate for 5 ms and then O_2 was added to the gaseous environment to simulate oxidation that accompanies growth. The temperature was held constant in each simulation run. The pressure was held constant at 1 atm and the gas-phase composition was held constant with mole fractions $x_{C_2H_2} = x_{H_2} = 0.1$ and $x_H = 0.01$. After O_2 was added, its concentration was also held constant. The pure oxidation scenario was similar to the oxidation-and-growth one, except that when O_2 was added after the initial 5 ms of growth, acetylene was removed, i.e., $x_{C_2H_2}$ was set to 0. The two scenarios were designed to cover conditions encountered in hydrocarbon flames.

Time evolution of the substrate size and five-member ring fraction for a range of oxygen concentrations are depicted in Fig.37 for each temperature. The results computed for the substrate size, shown in the left-hand panels of Fig.37, demonstrate that as oxygen is added, oxidation begins to compete with growth, increasingly so with an increase in the amount of oxygen added and an increase in temperature. For instance, at the same level of O_2 added (e.g., $x_{O_2} = 1 \times 10^{-3}$), the growth of the graphene layer is only inhibited at 1500 and 2000 K but at 2500 K the layer decreases in size.

The computed five-member ring fractions, depicted in the right-hand panels of Fig.37, reveal that the addition of O_2 promotes the formation of five-member rings embedded in the graphene layer. Analysis of the computed reaction fluxes indicated that the increase in the five-member rings is primarily due to their formation via thermal decomposition of oxyradicals (reactions 51–54). Excluding oxidation of five-member from the model results in faster saturation of the graphene edge with five-member rings, which prevents the graphene edge from further degradation (or growth).

The KMC results obtained in this oxidation-and-growth simulations revealed two major, competing pathways for an oxyradical originating in O_2 reaction with a surface radical. In the first pathways, the oxyradical undergoes thermal decomposition to form a five-member ring and expel CO—the actual oxidation step. In the second one, a neighboring-site H adds to the oxyradical forming OH, to which another H atom adds to expel H_2O and regenerate a new aromatic radical site—a pathways recycling the aromatic-radical site. Fig.37 shows a schematic diagram of the two pathways and Fig.39 quantifies the competition between these two pathways by comparing numbers of reaction events for the attack of O_2 on a radical site (reactions 46–50), thermal decomposition of an oxyradical (reactions 51–54), and regeneration of an aromatic radical site (reactions 85–89). For all three temperatures, the number of oxyradicals formed increases with an increase in oxygen concentration. At 1500 K, the regeneration pathway is dominant over the thermal-decomposition pathway. As the temperature increases to 2000 K, thermal decomposition begins to compete with regeneration, and at 2500 K thermal decomposition is the dominant pathway. This switch is a result of thermal decomposition being a higher activation-energy process than regeneration.

Carbon is removed from the graphene edge either by thermal desorption (reactions 5, 7, 17, 25, and 45) or by oxidation (reactions 51–54). For all three temperatures studied, the reaction statistics show that as the concentration of oxygen increases, the frequency of oxidation reactions increases while the frequency of thermal desorption reactions decreases,

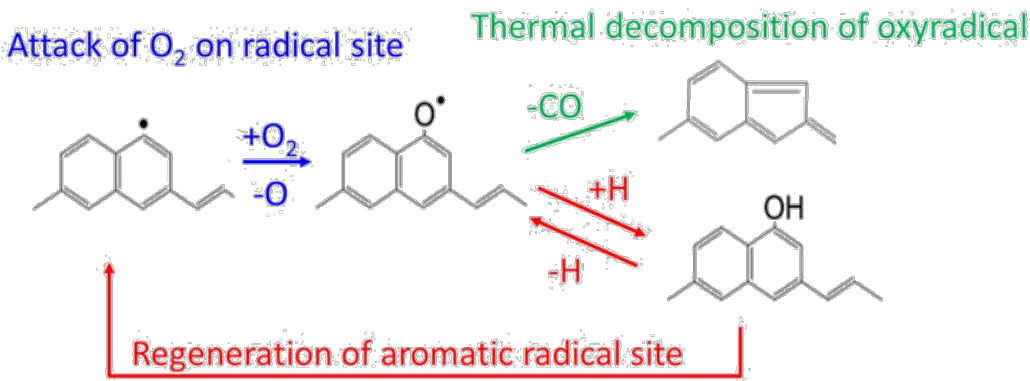


Figure 37: Diagram of two major pathways: Thermal decomposition of oxyradicals (green) and regeneration of an aromatic radical site (red).

indicating that competition exists between the two types of reactions. Although the frequency of thermal desorption decreased with an increasing oxygen concentration, the thermal desorption pathway still remained dominant over the oxidation pathway for all oxygen concentrations and temperatures tested. This result indicates that when growth reactions (3, 4, 26, 27, 33, 34, 35, 39, 42, and 44) added carbon atoms to the graphene layer, they were more likely to be removed by thermal desorption than oxidation, even for the highest oxygen concentrations.

A set of KMC simulations was performed at exactly the same conditions as the previous one, except that acetylene was removed from the gaseous environment at the time oxygen was added. Fig.40 displays the time evolution of the substrate size and five-member ring fraction for each temperature and for a range of oxygen concentrations. There is no growth to compete with oxidation in these simulations, so the addition of any amount of oxygen leads to a decrease in the size of the graphene layer. Other than that, the results displayed in Fig.41 are similar to those of the discussed above oxidation-and-growth case. Also similar are the major competition pathways of thermal decomposition and regeneration, as shown in Fig.37 and exemplified by reaction-event counts in Fig.41, as well as the relative frequency of reaction 90.

In the pure oxidation simulations, the frequency of thermal-desorption reactions was over an order of magnitude lower than in the oxidation-and-growth cases because acetylene was not present in the gaseous environment during oxidation and hence lower occurrence on the graphene edge of lone adsorbates able to desorb. Unlike for the oxidation-and-growth cases, at 1500 K the oxidation pathway became dominant over thermal desorption for the highest oxygen concentration, $x_{O_2} = 0.1$. At 2000 K, oxidation dominated thermal desorption for $x_{O_2} > 10^{-4}$. Still, similar to the oxidation-and-growth cases, at 2500 K, the thermal desorption reactions were dominant over the oxidation ones for all concentrations of oxygen studied.

Similarly to the oxidation-and-growth case, the graphene edge became “non-reactive” quicker when the five-member-ring oxidation was excluded from the simulation. Such

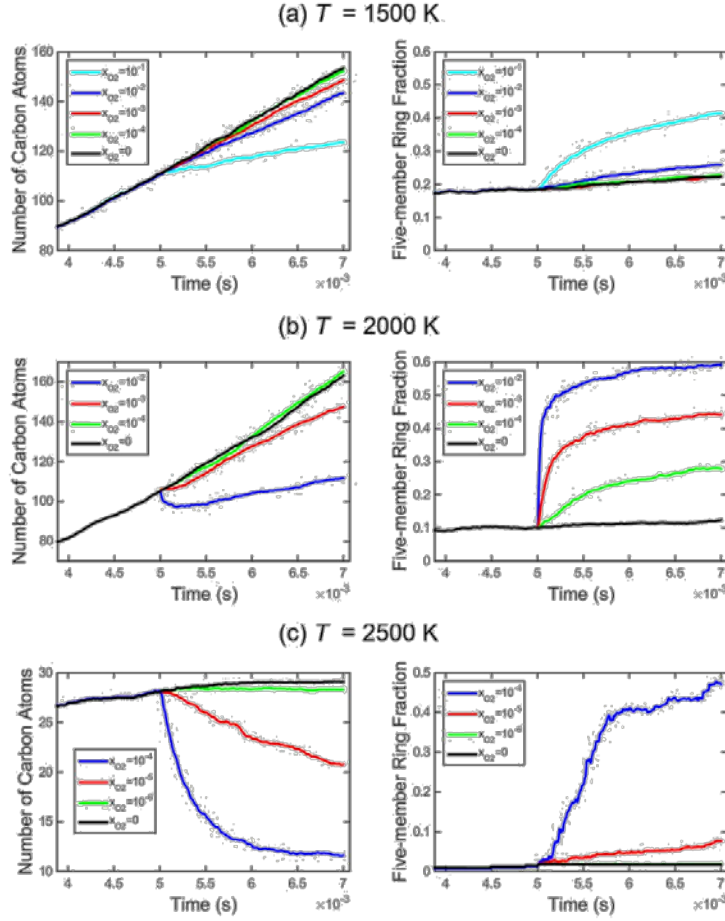


Figure 38: Substrate size (left) and five-member ring fraction (right) for the oxidation-and-growth simulations at temperatures (a) 1500 K, (b) 2000 K, and (c) 2500 K.

“non-reactive” sites are illustrated in Fig.42, which displays two snapshots from an oxidation-only KMC simulation at 2000 K and $x_{O_2} = 0.001$. The snapshot shown on the left-hand side of the figure is taken at a simulation time of 5 ms, at the instant when C_2H_2 is removed from and O_2 is added to the gaseous environment. The green box exemplifies that before the oxidizer is added, the edge consists of six-member rings with a “free” corner thus enabling a zipper oxidation [67, 68]. The right-hand side of the figure depicts a structure formed after 1.8 ms of the oxidation period. The red pentagons drawn over the structure highlight some of the five-member rings of the graphene edge. If not removed, the highlighted five-member rings prevent further oxidation from occurring. Even when the five-member-ring oxidation reaction is included, its rate is relatively low and hence may not prevent the buildup of five-member rings.

The oxidation and regeneration pathways were said to compete for oxyradicals formed by the attack of O_2 on surface radical sites. While the relative rates of the two pathways switch dramatically in the temperature range studied, the influence of the regenerative pathway on the overall, bulk oxidation rate is not very large. Table 9 reports the bulk ox-

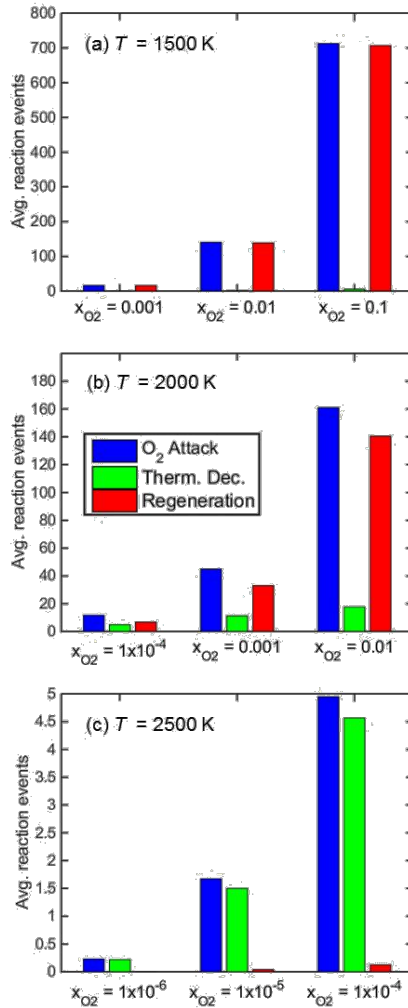


Figure 39: Reaction-event counts for O_2 attack on a radical site (blue), thermal decomposition of an oxyradical (green), and regeneration of an aromatic radical (red) for the oxidation-and-growth simulations.

idation rates obtained in additional KMC runs but with regeneration pathways excluded from the simulations.

At 1500 K, the initial oxidation rates increase by up to 12 % when regeneration was excluded. In spite of the dominant pathway for oxyradicals at 1500 K being the regeneration pathway, excluding the regeneration reactions leads only to a marginal increase in the frequency of oxidation of six- and five-member rings and hence only a marginal increase in the oxidation rates. In other words, at these conditions the fast regeneration reactions simply recycle the aromatic oxyradicals. The results at 2000 K are similar to those at 1500 K with the oxidation rates increasing by up to 21 % for the simulations without regeneration. At 2500 K, there is no change in the oxidation rates when regeneration reactions are excluded, because the oxidation pathway is already completely dominant over the regeneration pathway at this high temperature.

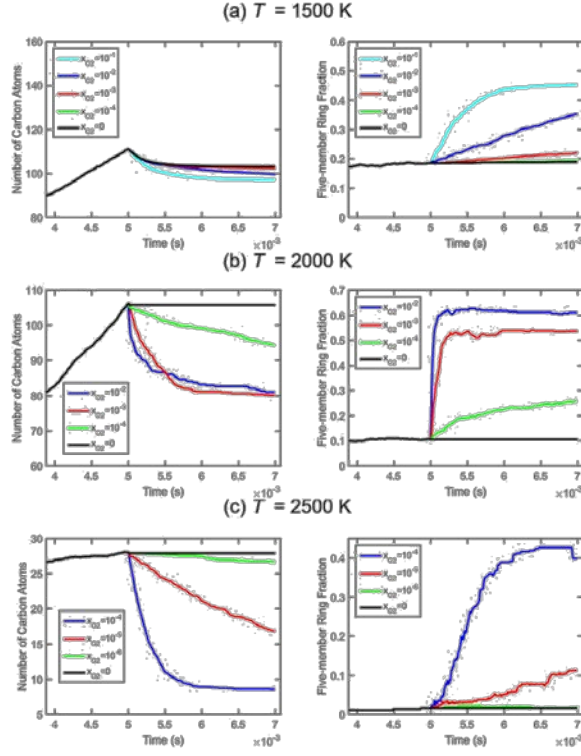


Figure 40: Substrate size (left) and five-member ring fraction (right) for the oxidation-only simulations at temperatures (a) 1500 K, (b) 2000 K, and (c) 2500 K.

The fact that regeneration does not affect greatly the bulk oxidation rate may help in developing reduced models of soot oxidation at flame conditions.

C-4 Reactivity of Graphene Edges with Embedded Five-Member Rings

The above results indicate that accumulation of five-member rings at the graphene edge leads to its reduced reactivity. This is manifested by the decaying rates of graphene-edge oxidation. Indeed, as can be seen in Fig.40 the profiles of the substrate size during the oxidation are non-linear in time, implying time-varying—decaying—rates of oxidation. Since the gaseous environment is maintained unchanged during an individual simulation, the only varying property affecting the rate of oxidation is the edge density of reac-

Table 9: Oxidation rates (C-atom/ms) computed with and without regeneration pathway included

Temperature (K) 1500				2000			2500		
X_{O_2}	10^{-3}	10^{-2}	10^{-1}	10^{-4}	10^{-3}	10^{-2}	10^{-6}	10^{-5}	10^{-4}
With	24.5	26.6	36.4	15.3	45.0	54.1	7.0	10.2	49.7
Without	27.2	29.8	36.4	18.6	53.8	54.1	7.0	10.2	49.7

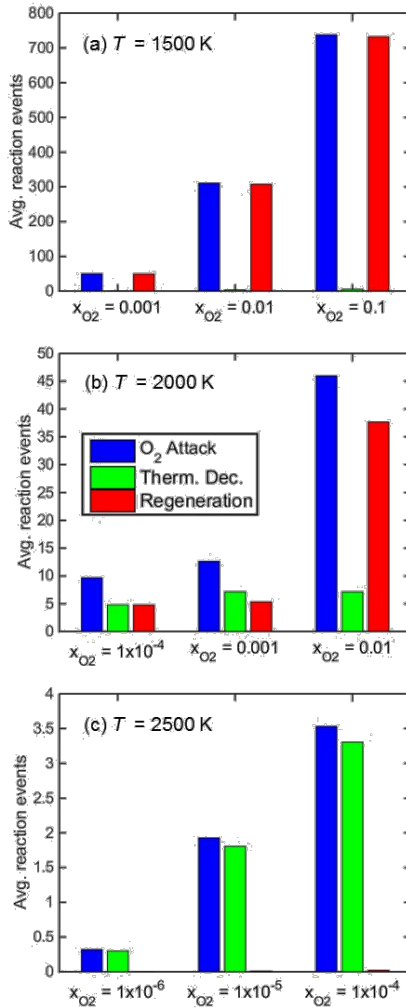


Figure 41: Reaction-event counts for O_2 attack on a radical site (blue), thermal decompo-sition of an oxyradical (green), and regeneration of an aromatic radical site (red) for the oxidation-only simulations.

tive sites and their reactivity towards oxidation.

The notion that incorporation of five-member rings into graphene edges makes it less reactive is counter intuitive at first, as five-member rings are usually considered to be less stable [21, 81, 84]. To explain the computed behavior, one must consider the morphology of the graphene edge. Fundamentally, a graphene edge can be in two forms, armchair and zigzag. At combustion conditions it is presumed that all edge sites are saturated with H atoms and reaction is initiated by abstracting an H atom forming a surface radical [11, 13, 14, 85]. Left to growth only, a finite-size armchair edge evolves quickly into zigzag edges [47]. Zigzag edges can also grow, rate-limited by surface nucleation occurring either at edge corners or though chemisorbed and migrating five-member rings [53], both slower than the growth of armchair edges (via the HACA mechanism [11, 85], for example).

Oxidation is essentially controlled by decomposition of surface oxyradicals. A six-member-

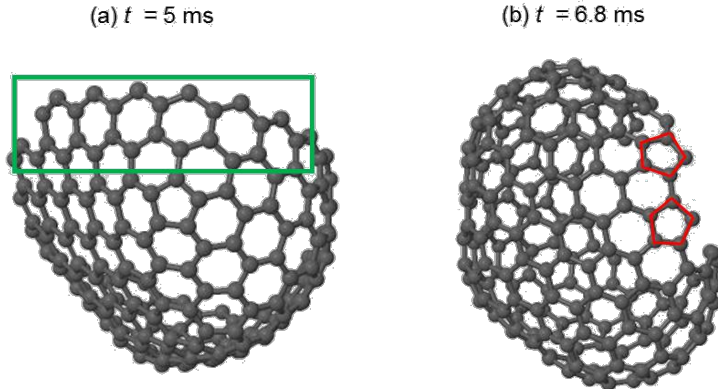


Figure 42: Representative structures seen in the oxidation-only simulations. The displayed snapshot are from a KMC simulation at 2000 K and $x_{O_2} = 0.001$: (a) at the end of the growth period and just before the onset of oxidation, (b) after 1.8 ms of the oxidation. The H atoms saturating the edge carbon atoms are not shown for clarity.

ring oxyradical decomposes by expelling CO and forming a five-member ring [58]. Recent theoretical studies of elementary reactions concluded that inner zigzag oxyradical sites decompose much slower, if at all, than corner zigzag and armchair sites at combustion conditions [67, 68]. These results imply that armchair-edge oxidation should proceed as random removal of individual edge sites while that of zigzag edges as a zipper-type reaction process. Literature is rather conflicting on comparison of armchair and zigzag oxidation reactivity. For instance, the early microscopy work of Thomas and Hughes [86] reported slightly higher recession rates of zigzag than armchair edges, yet more recent consensus is that armchair carbon atoms are more reactive than zigzag ones [87]. Also, the close proximity in numerical measures of reactivity (e.g., those observed by Thomas and Hughes) for the two edges could be consistent with the theoretical predictions that the oxidation (and growth [85]) rates of armchair and corner zigzag sites are close to each other, and the difference in experimentally observed edge evolution is due to cooperative phenomena of elementary reaction steps and edge geometry.

Returning to the present simulations, graphene edges formed in the growth period are both zigzag and armchair, as illustrated in Fig.43 (a). When the oxidation period begins, the zigzag sites remain largely intact and the armchair sites convert into five-member rings, as can be seen by comparison between the edge fragment enclosed in the green box in Figure 6a with the corresponding red-marked edge fragment in Fig.43 (b).

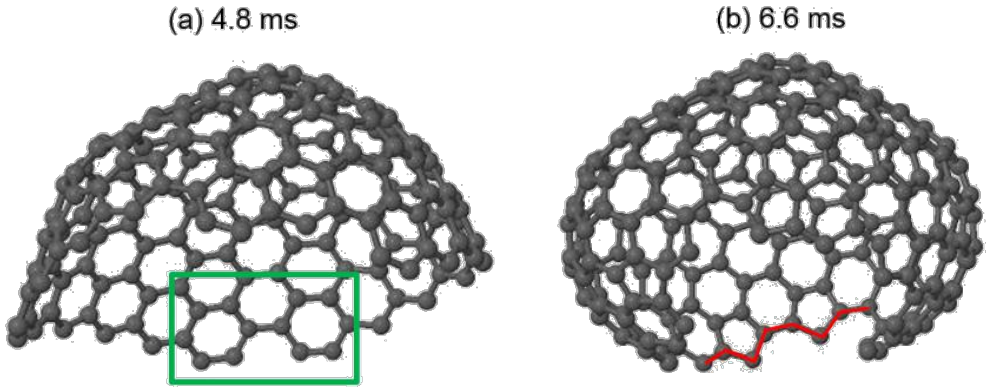


Figure 43: Graphene structures obtained in a KMC simulation at 2000 K and $x_{O_2} = 0.001$ (a) toward the end of the growth period, just before the onset of oxidation, and (b) after 1.6 ms of oxidation. The H atoms saturating the edge carbon atoms are not shown for clarity.

While the emerged red-marked fragment with embedded five-member rings is not a zigzag edge fragment, it is also not an armchair. Analysis of oxidation pathways for such embedded five-member rings yielded rates substantially higher than those of inner zigzag sites [68] but much (over four orders of magnitude) lower than those for six-member rings of an armchair edge [81, 82].

The phenomenon of decreasing oxidative reactivity of soot over time has been observed experimentally. In a study by Vander Wal and co-workers [88], soot samples were collected from diesel particulate filters after different kinds of engine testing, and the nanostructure of primary particles within the aggregates was observed using HRTEM imaging. They found that samples with longer exposure to oxidation conditions had a higher fraction of densified particles than samples collected over limited-time low-load conditions. The authors [88] explained that the densification occurred because oxidation preferentially removed amorphous carbon relative to graphitic carbon causing a decrease in the number of reactive edge-site carbon atoms relative to the number of more stable basal-plane carbon atoms and, hence, a decrease in oxidative reactivity. Similar observations were reported by Jaramillo et al. [89] and Fang and Lance [90].

In the present KMC simulations, a similar decrease was observed in the ratio of reactive edge sites to basal-plane carbon atoms during oxidation, as evidenced by the computed ratios depicted in Fig.44.

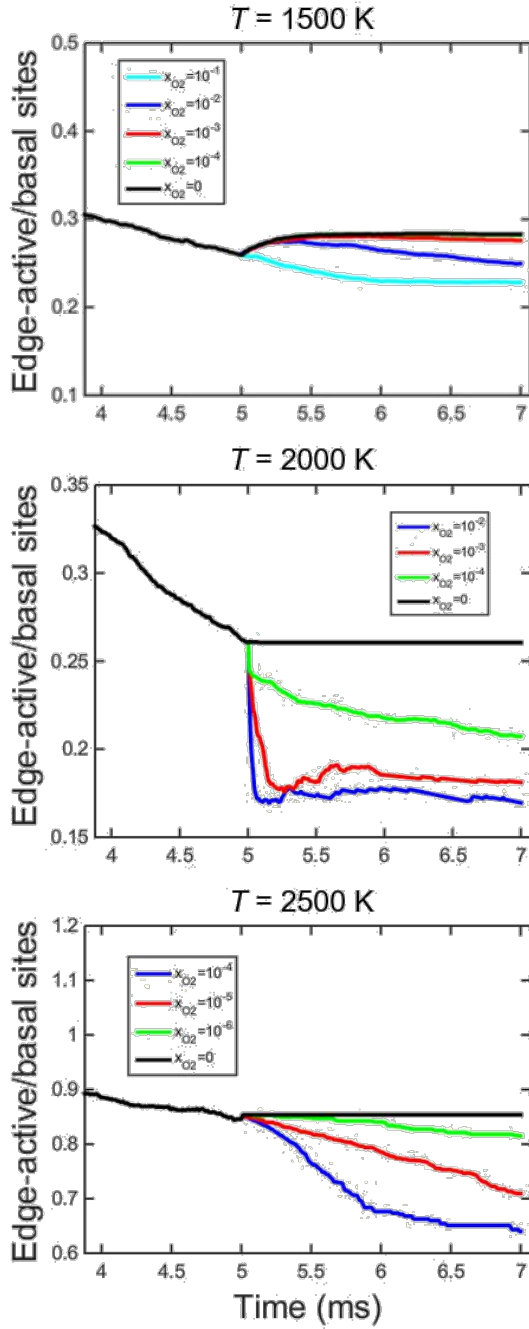


Figure 44: $C_{\text{edge}}\text{-H}/C_{\text{basal}}$ site ratio versus time.

At all temperatures the ratio is decreasing during the growth period of the simulation. This is readily understood: carbon addition reactions reproduce edge sites while incorporating the carbon atoms of the preceding reactive sites into the basal plane. One would expect a reverse outcome in oxidation: removal of peripheral edge carbons would leave behind reactive sites while decreasing the number of inner, basal-plane carbons. However, the simulations showed that the $C_{\text{edge}}\text{-H}/C_{\text{basal}}$ site ratio is decreased during oxida-

tion. The results at 1500 K, displaying an initial increase in this site ratio, may seem con-tradictory to this assessment. A closer examination, adding an annealing period between growth an oxidation, revealed that the rise in the site ratio is due to thermal desorption of carbon, but the oxidation keeps decreasing it, as demonstrated in Fig.44. The reason for the site ratio decrease, as explained above, is the formation of five-member rings that ac-cumulate and create less-reactive zigzag edges. These considerations lead me to conclude that the observed decrease in reactivity over time seen in my results is in accord with the phenomena observed in experiment [88-90].

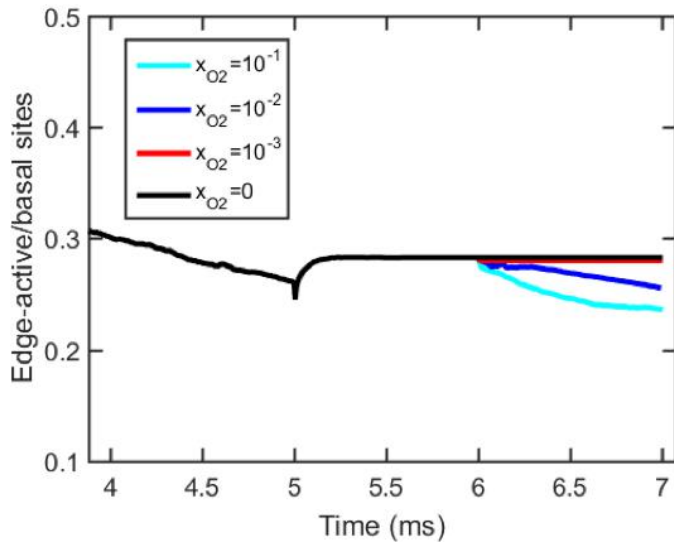


Figure 45: Cedge-H/Cbasal site ratio computed at the same conditions as those of upper left corner of Figure 3 with the addition of 1 ms annealing period between growth and oxidation.

Effect of Graphene Curvature on the Rate of Oxidation

In an earlier experimental study, Vander Wal and Tomasek [91] investigated the dependence of oxidation rates on particle nanostructure. Soot was synthesized using three different fuels (acetylene, benzene, and ethanol) to achieve different nanostructures. Burnout rates were measured for the initial stage of oxidation, when less than 25 % of the initial mass was lost. The authors [91] found that the burnout rates for ethanol- and benzene-derived soot were higher than those for acetylene-derived soot by nearly a factor of five. Fringe lattice analysis revealed that the fringe length distribution of benzene-derived soot indicated shorter, unaligned graphene segments, which is indicative of a high ra-tio of edge-site carbon atoms to basal-plane carbon atoms and, therefore, higher reactiv-ity. However, ethanol-derived soot had longer graphene segments, like acetylene-derived soot but still had much higher burnout rates. Examination of the HRTEM images showed that ethanol-derived soot had much greater curvature than acetylene-derived soot. Van-der Wal and Tomasek conjectured that a higher degree of curvature increases the imposed bond strain between C-C bonds thereby decreasing their resistance toward oxidation and

thus explained why the ethanol-derived soot had higher burnout rates than the acetylene-derived soot despite having a similar fringe length distribution.

The numerical prediction that incorporation of five-member rings into graphene edges causes the decay in the oxidation rate could be seemingly perceived as contradictory to the experimentally derived conclusion of Vander Wal and Tomasek [91] that graphene curvature increases the oxidation rate of soot. Yet, further analysis revealed not only that there is no controversy but identified an additional feature of the graphene oxidation.

This next set of tests was performed by starting oxidation with graphene structures of differing curvature. Such two different nanostructures were obtained in KMC simulations of graphene growth at two different temperatures, 1500 and 2000 K. The degree of curvature was quantified by the five-member ring fraction, f_{R5} . The substrates grown at 1500 K had an average f_{R5} of 0.18, while those grown at 2000 K had an average f_{R5} of 0.10, thus indicating a higher degree of curvature for the substrates grown at 1500 K. Fig.46 illustrates the differences in curvature by showing representative structures after 5 ms of growth at each temperature.

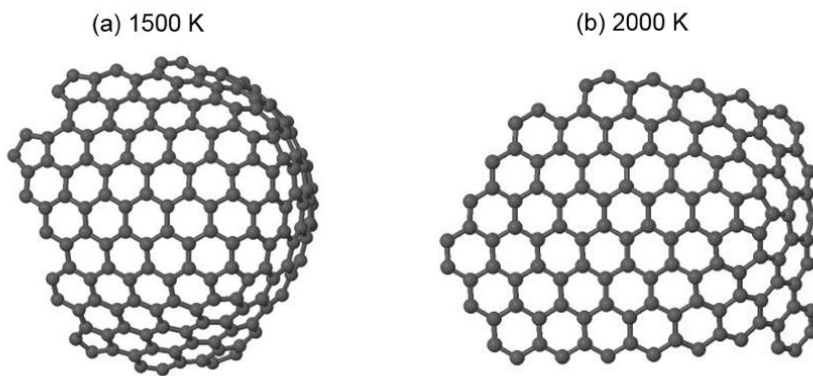


Figure 46: Snapshots of substrates grown at (a) 1500 K and (b) 2000 K at 5 ms. The H atoms saturating the edge carbon atoms are not shown for clarity.

The two graphene structures were subjected to oxidation at different oxygen concentrations, each substrate at three different temperatures: 1500, 2000, and 2500 K. The KMC simulations were now performed in three stages: growth, annealing, and oxidation. Like in prior simulations, the graphene sheet was grown for 5 ms starting with an initial coronene substrate. After that, the grown graphene structure underwent an annealing period for 1 ms, during which C_2H_2 and H were removed from the gaseous environment and O_2 was not yet added. The purpose of the annealing period was to allow for radical sites that existed at 5 ms to thermally decompose. At 6 ms, molecular oxygen and atomic hydrogen were added to the gaseous environment for 2 ms of oxidation. The temperature and pressure remained unchanged throughout the simulation. To stay closer to the experimental procedure of Vander Wal and Tomasek [91], we examined here the initial rates of oxidation. The obtained results are reported in Table 10.

Table 10: Initial oxidation rates (C-atom/ms) for substrates with different curvature.

Oxidation T (K)		1500		2000			2500			
	x_{O_2}	10^{-3}	10^{-2}	10^{-1}	10^{-4}	10^{-3}	10^{-2}	10^{-6}	10^{-5}	10^{-4}
Growth T (K)	T_{R5}									
1500	0.18	24.5	26.6	36.4	48.8	77.6	82.1	42.2	44.3	59.7
2000	0.10	6.4	9.1	21.2	15.3	45.0	54.1	9.3	10.7	29.0

Inspection of the results reported in Table 10 indicates that in all nine cases tested the oxidation rates were higher, by a factor of 1.5 to 4.6, for graphene with larger starting curvature. This comparison shows that our KMC model does reproduce the phenomenon seen in the experiments of Vander Wal and Tomasek [91]. Then how can it be that the same mechanistic feature—incorporation of five-member rings into a growing edge of graphene—explains both the decay of the oxidation rate in time and the faster initial oxidation of a more curved graphene.

In the KMC model, in addition to carbon being removed from the graphene edge by oxidation, reactions 51–54 and 90, it is also eliminated by thermal desorption.

In these simulation tests, the frequency of oxidation reactions 51–54 was approximately the same for substrates grown at 1500 and 2000 K. However, the thermal desorption reactions, primarily reactions 5 and 7, occurred between two to four times as often for the substrates grown at 1500 K as for those grown at 2000 K during the first 0.2 ms of oxidation (Figure 47). Therefore, it is the thermal desorption that accounts for the difference in the oxidation rates.

Further examination of the data displayed in Figure 47 shows that the difference in frequency of thermal desorption reactions between the two sets of substrates is much smaller after the initial 0.2 ms of oxidation for all simulations conditions. This suggests that the difference in oxidation rates between substrates with different curvature occurs primarily at the beginning of oxidation and happens because substrates with higher curvature form a larger number of sites that can potentially desorb.

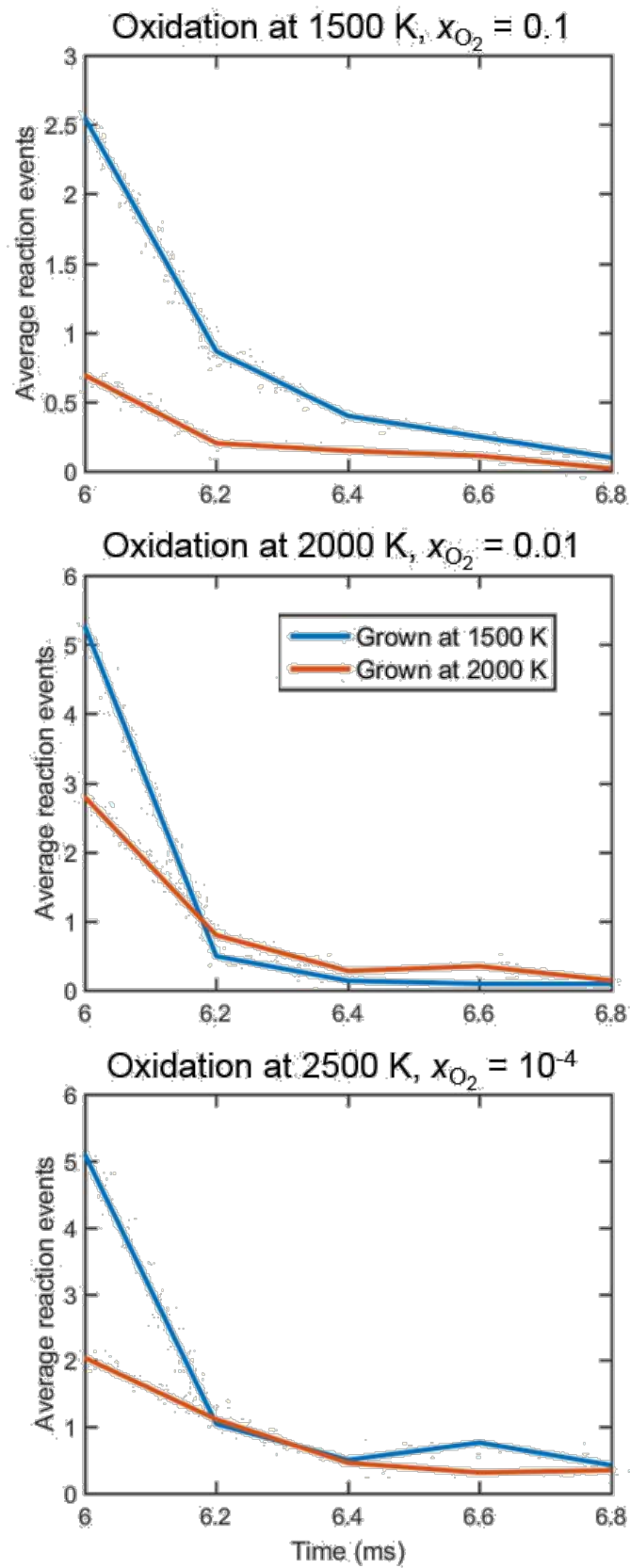


Figure 47: Event counts for thermal desorption reactions versus time for substrates oxidized at three sets of conditions.

The reaction count statistics indicate that the metric of curvature is more complex than simply knowing the fraction of five-member rings in the graphene sheet. Five-member rings can affect oxidation differently, depending on their location in the graphene sheet, i.e., if they are on an edge or embedded. The time evolution of the different types of five-member rings is plotted in Figure 48. Inspection of these results indicates that at the beginning of oxidation substrates grown at 1500 K have a higher number of free five-member rings (red lines in Figure 48) that can be thermally desorbed compared to substrates grown at 2000 K, thus explaining the difference in the reaction counts presented earlier. As oxidation progresses, the free five-member rings are thermally desorbed and their number decreases close to zero for the substrates grown at both temperatures. The number of five-member rings at armchair sites (blue lines) increases for both substrates due to thermal decomposition of oxyradicals to form five-member rings. These latter five-member rings form zigzag edges that lead to a decrease in oxidative reactivity. The number of bay-capped five-member rings (black lines) decrease only slightly for the substrates at both temperatures and do not seem to affect the oxidation rate.

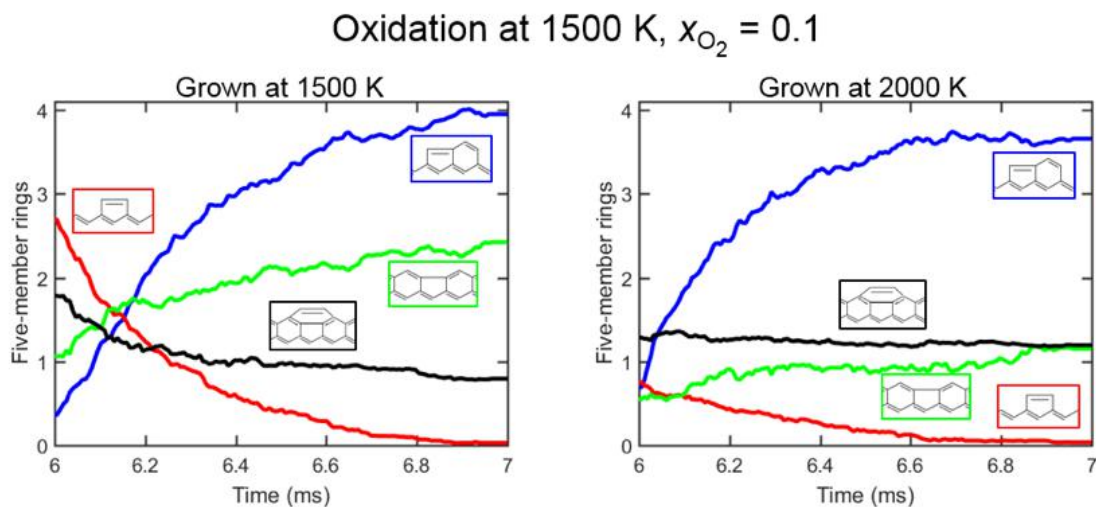
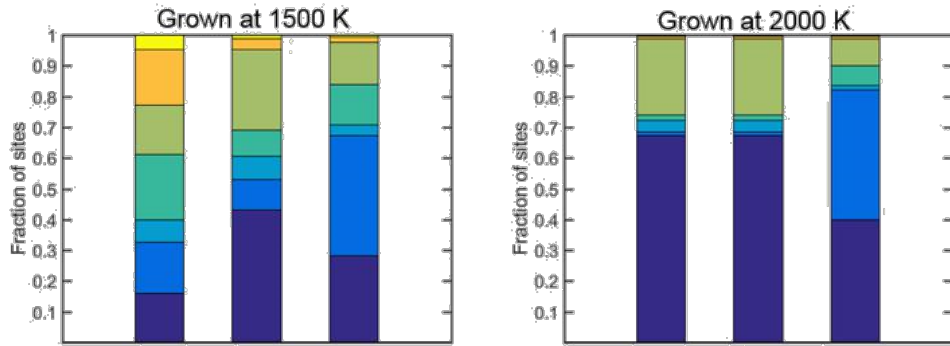


Figure 48: Number of five-member rings versus time for substrates grown at 1500 (left) or 2000 K (right), and oxidized at 1500 K with $x_{O_2} = 0.1$.

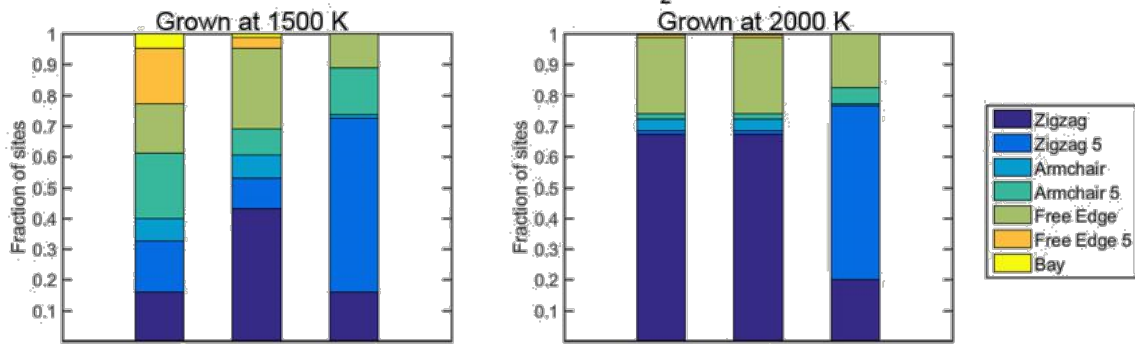
Thus, while the total number of five-member rings increases during oxidation for the substrates grown at 1500 and 2000 K, their individual histories vary and have different effects on the oxidation rate. Analysis of the graphene-edge site distribution over time further supports this conclusion. Figure 49 displays population of pertinent edge sites at several instances of reaction; the sites are identified in Figure 50. Inspection of these results indicates that the fraction of free-edge sites decreases during the oxidation stage for both substrates. The substrates grown at 1500 K have a significant fraction of free-edge-5 sites, five-member rings that thermally desorb, which is evidenced by a substantial decrease in these sites during the annealing period. By contrast, such five-member rings

barely appear on substrates grown at 2000 K. This discrepancy in free-edge-5 sites further illuminates that a higher oxidation rate of more curved graphene is due to the presence of five-member rings that can thermally desorb. At the same time, the total number of zigzag sites, the sum of zigzag and zigzag-5 sites, increases as oxidation progresses at both temperatures. Accumulation of such less-reactive-to-oxidation sites causes the decrease in the oxidation rate over time. These distinct aspects of graphene edge morphology reconcile the two seemingly contradictory conclusions about curvature effects on oxidation rates.

Oxidation at 1500 K, $x_{O_2} = 0.1$



Oxidation at 2000 K, $x_{O_2} = 0.01$



Oxidation at 2500 K, $x_{O_2} = 10^{-4}$

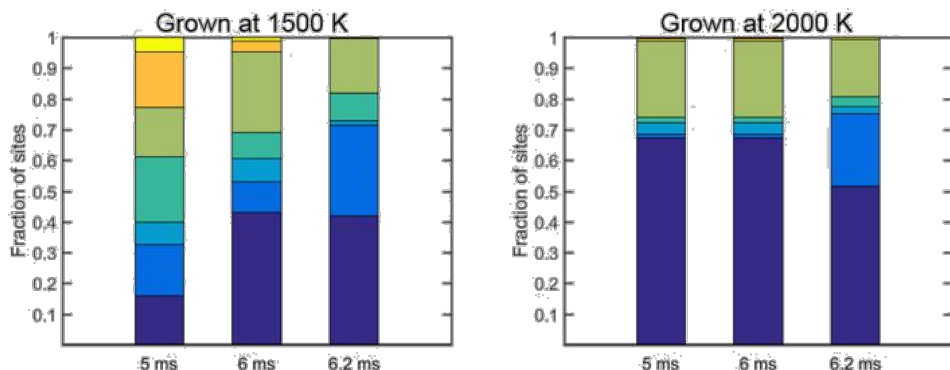


Figure 49: Site distribution at 5 ms (start of annealing), 6 ms (start of oxidation), and 6.2 ms (after 0.2 ms of oxidation) for substrates grown and oxidized under different conditions.

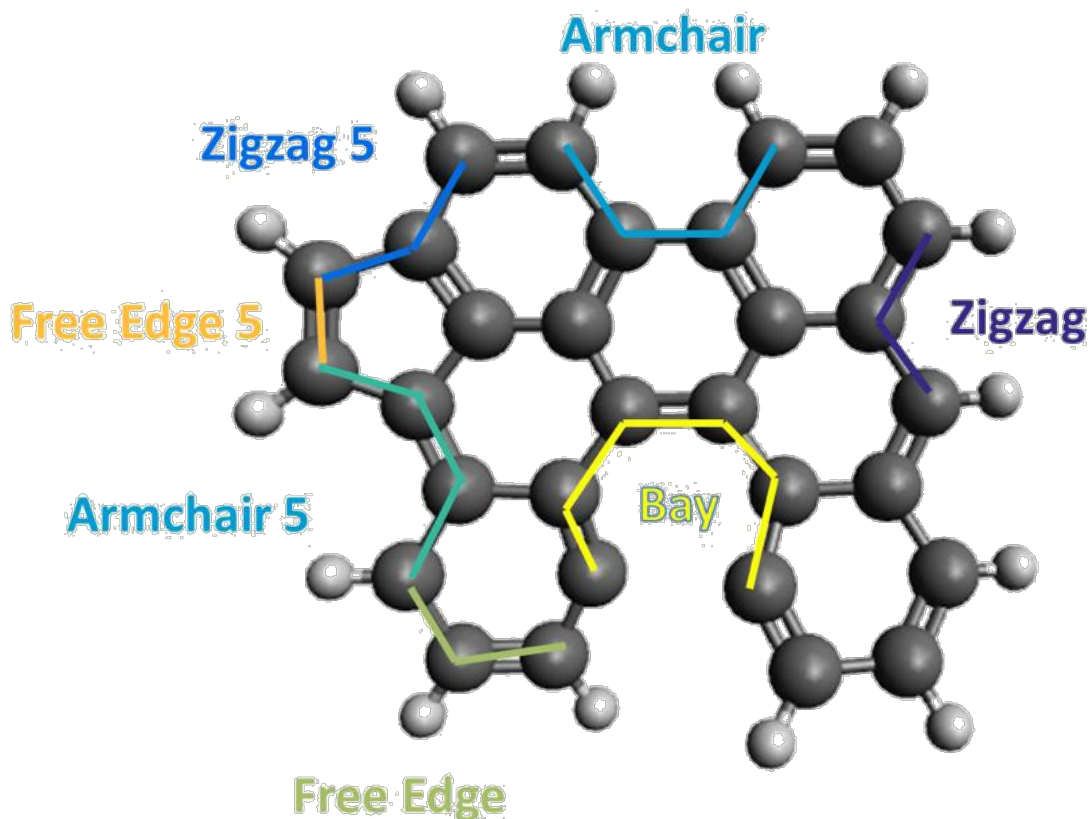


Figure 50: Diagram of sites used in Figure 12.

Thus, the Kinetic Monte-Carlo simulations of the graphene-edge evolution in combustion-like environments revealed that oxidation by molecular oxygen exhibits two principal pathways: thermal decomposition of oxyradicals and regeneration of aromatic radical sites. Their competition is temperature dependent, with former dominating at higher and the latter at lower temperatures. Yet, the overall oxidation rate at the conditions tested is not substantially affected by presence or absence of the regeneration pathway. This may help in developing reduced models of soot oxidation at flame conditions.

The overall oxidation rate of the graphene substrate was computed to be time dependent, with reactivity decreasing over time as the ratio of reactive edge sites decreases relative to the number of basal-plane carbon atoms. At the same time, the oxidation rate was found to be higher for graphene with a higher initial curvature. Both results are in accord with experimental observations [88, 91]. Analysis showed that distinct aspects of graphene-edge morphology are responsible for curvature either raising or reducing the oxidative reactivity of the graphene edge.

C-5 KMC Simulations of High-Temperature Oxidation of Soot Particles in an H₂/O₂ Mixture

The next step for testing the model was to test it quantitatively by comparing to experimentally-measured oxidation rates. While many studies [94-106] have measured the oxidation rates of carbon species including chars, coals, or solid graphite, there have been considerably fewer studies [93, 107-109] directly measuring the oxidation rate of soot, especially at temperatures relevant to combustion. The most recent experiments to measure soot oxidation rates at high temperatures were performed by Paul Roth and co-workers [93, 107, 108]. In these studies, Roth and co-workers conducted shock tube experiments in which soot particles suspended in O₂/H₂/Ar gas mixtures were oxidized at high temperature conditions (1652 – 3130 K). A rapid tuning IR diode laser was employed to measure time-resolved CO/CO₂ concentration profiles and in situ laser light extinction measurements were performed to find particle size and number density. The particles were assumed to be spherical and the size distribution was assumed monodisperse. This allowed them to calculate the total intrinsic surface area per cm³ (a_{pi}). Oxidation rates (g cm⁻² s⁻¹) were calculated by dividing the rate of CO formation by the total intrinsic surface area per cm³. They found that for experiments in which soot particles were dispersed in Ar containing diluted stoichiometric H₂/O₂ mixtures, CO was the main gas phase reaction product.

In order to validate the KMC model of graphene-edge oxidation against their experimental results, we needed to modify the KMC code so that it could account for an evolving gas phase composition, and we needed to couple the surface chemistry to the gas phase chemistry, so that species consumed or produced through surface reactions could be added or subtracted from the gas phase.

KMC simulations have been augmented include coupling between surface chemistry and gas phase chemistry. A Matlab model of a Plug Flow Reactor (PFR) developed by the Frenklach group [110] was chosen to simulate the gas phase chemistry of H₂/O₂ combustion. The gas phase mechanism of 10 species and 22 reactions is taken from You et al. [111] and is shown in Table 11.

At the start of oxidation ($t_0 = 0$ ms), the KMC and PFR is initialized in parallel with the gas phase conditions (T, P, x_{O_2} , x_{H_2}) from Roth et al. [93]. $x_{C_2H_2}$ and x_H are assumed to be 0 at the onset of oxidation. The KMC model begins with an initial substrate. The surface chemistry starts with the first KMC reaction taking place over the interval t_{KMC}, described below. The most basic way to couple the KMC and PFR would be for the PFR to be simulated for t_{PFR} = t_{KMC}, and for the gas phase environment of the KMC to be updated after every KMC time step. However, this method would be computationally expensive as KMC time steps can be on the order of 10⁻⁷ s. Instead, a fixed time step of 10 s was selected for t_{PFR}. The time step was large enough to reduce computational time and small enough so that further reductions in t_{PFR} did not affect the simulation results.

Using this method with different step sizes for the PFR and KMC, the gas phase evolution is simulated for a residence time of t_{PFR}, and the surface chemistry is simulated in the KMC model for a duration of t_{PFR}. During this time, the gas phase environment

Table 11: H₂/O₂ combustion mechanism employed in coupled KMC/PFR simulation

	Reaction	Reference
G1	O + O + M \$ O ₂₊ M	[112]
G2	O + H + M \$ OH + M	[113]
G3	O + H ₂ \$ H + OH	[112]
G4	O + HO ₂ \$ OH + O ₂	[112]
G5	O + H ₂ O ₂ \$ OH + HO ₂	[112]
G6	H + O ₂ + M \$ HO ₂₊ M	[114, 115]
G7	H + O ₂ \$ O + OH	[112]
G8	H + H + M \$ H ₂₊ M	[112]
G9	H + OH + M \$ H ₂ O + M	[112]
G10	H + HO ₂ \$ O + H ₂ O	[112]
G11	H + HO ₂ \$ O ₂ + H ₂	[116]
G12	H + HO ₂ \$ OH + OH	[112]
G13	H + H ₂ O ₂ \$ HO ₂₊ H ₂	[112]
G14	H + H ₂ O ₂ \$ OH + H ₂ O	[112]
G15	OH + H ₂ \$ H + H ₂ O	[112]
G16	OH + OH + M \$ H ₂ O ₂₊ M	[117, 118]
G17	OH + OH \$ O + H ₂ O	[112]
G18	OH + HO ₂ \$ O ₂₊ H ₂ O	[119]
G19	OH + H ₂ O ₂ \$ HO ₂ + H ₂ O	[117]
G20	HO ₂₊ HO ₂ \$ O ₂₊ H ₂ O ₂	[112]
G21	O + OH + M \$ HO ₂₊ M	[120, 121]
G22	OH + CO \$ H + CO ₂	[122]

remains constant with the gas phase conditions from $t_0 = 0$. The reaction counts during this time interval are recorded in order to calculate how many molecules are added to or removed from the gas phase by surface reactions. For example, when reaction $R + O_2 \rightarrow R-O + O$ occurs, one O_2 molecule is removed from the gas phase and one O atom is added.

At $t_1 = t_0 + t_{PFR}$, the gas phase concentrations from the PFR simulation are updated based on the change in gas phase species (H , H_2 , O , O_2 , OH , H_2O , HO_2 , CO , and CO_2) due to surface reactions. The following equation is used to calculate the change in concentrations,

$$[H] = \frac{\text{net H atoms produced in KMC}}{1} \cdot \frac{1}{N_{\text{sites}}} \cdot \frac{2.3 \cdot 10^{15} \text{ sites}}{\text{cm}^2} \cdot \frac{1 \text{ mol}}{N_A \text{ H atoms}} \cdot \frac{a_p \text{ cm}^2}{1 \text{ cm}^3} \quad (10)$$

where N_{sites} is the number of active edge sites of the KMC substrate, $2.3 \cdot 10^{15}$ is the number density of C-H sites on soot surfaces as estimated in [46], N_A is Avogadro's number, and a_p is the reacting particle area specified in [93]. The updated gas phase conditions (T , P , x_H , x_{H_2} , x_O , x_{O_2} , x_{OH} , and x_{H_2O}) are set as the new gas phase environment for the KMC simulation for the next t_{PFR} . They are also used as the initial values for the next PFR step. Fig.51 shows a diagram of the coupling between the PFR and KMC simulations.

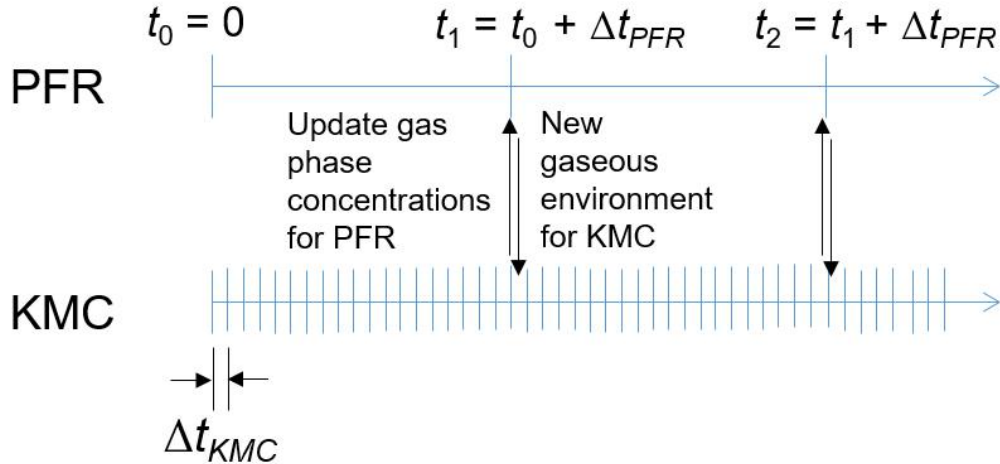


Figure 51: Diagram of the coupling between gas phase and surface chemistry.

For some gas phase compositions, it is possible that the time steps for the KMC could exceed the time step for the PFR. As a contingency for those cases, if $t_{KMC} > t_{PFR}$, then the gas phase is simulated for t_{PFR} , the KMC gaseous environment is updated with PFR results from $t_0 + t_{PFR}$, and the KMC simulation is advanced to $t_0 + t_{PFR}$ without a KMC reaction occurring at that step. The KMC reaction counts are reset to zero at the start of each t_{PFR} interval. The coupling process is repeated until the end of the

KMC simulation. During oxidation, when the substrate is oxidized down to one ring, the substrate is instantly regrown to the initial substrate and the one ring is assumed to instantly fall apart and produce 6 CO molecules and 6 H atoms while consuming 3 O₂ molecules.

To see how the assumption of the final ring falling apart would affect the results, two test cases were performed with an initial substrate of circumcoronene, one where the final ring was assumed to fall apart, and one where it did not fall apart. Fig.52 shows time-dependent [CO] and [CO₂] profiles for the test cases and reveals that the concentrations of these species changed by less than 5 % meaning that this assumption has little effect on the results.

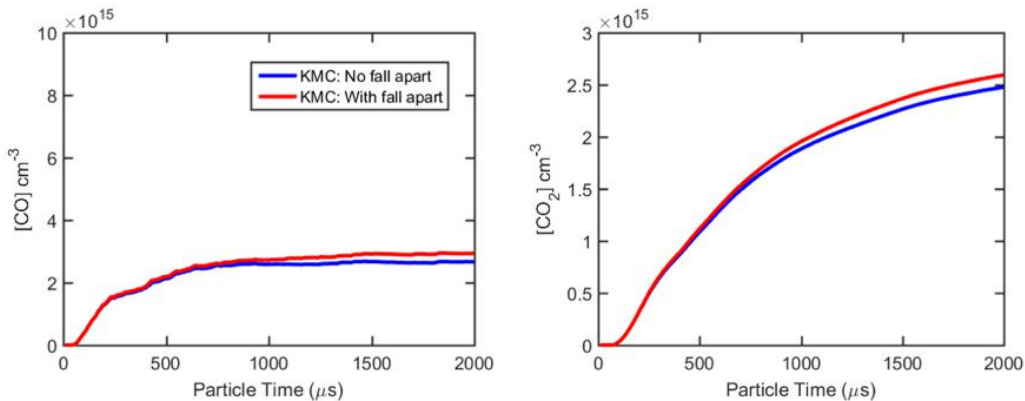


Figure 52: [CO] and [CO₂] versus time for test cases where the final ring can either fall apart to produce CO and H or not.

The set of surface reactions employed in the KMC model has been augmented from the 45 growth and 45 oxidation reactions to include reactions 91 – 104. Reactions 2, 11, and 13 were split into two separate reactions to account for the two ways that each of those reactions consumes or produces gas phase species.

KMC simulations were performed using the gas phase conditions specified in Fig.44 of Roth et al. [93] for a soot/O₂/H₂/Ar mixture: T = 1990 K, P = 0.72 bar, P_{O2} = 8 10³ bar, P_{O2}/P_{H2} = 0.5, and a_p = 0.23 cm²/cm³. This set of conditions was chosen because Roth et al. [93] provided the most results for this particular experiment. Each numerical simulation lasted for 2 ms, and t_{PFR} was selected to be 10 s.

A set of simulations was also performed for only the gas phase reactions occurring in the PFR. In these simulations, benzene acts as soot instead of the graphene substrates used in the coupled KMC/PFR simulations. The benzene can undergo hydrogen abstraction to produce phenyl, which can in turn be oxidized to form C₅H₅. As soon as the five-member ring is formed, the molecule is immediately transformed back to benzene and the oxidation process can start over. By modeling the instant refreshing of C-H sites, the PFR model neglects steric effects and thus oxidation can only be limited by a decrease in the concentration of oxidizers (O₂, OH, O). Therefore, the uncoupled PFR simulations

can be thought of as an upper limit on the oxidation rate. The coupled KMC/PFR model takes into account steric effects and the changing of the gas phase composition, which causes it to have a lower oxidation rate.

Five initial substrates were studied to determine the effects of substrate size and shape: coronene (7 rings), circumcoronene (19 rings), circumcircumcoronene (37 rings), circum-circumcircumcoronene (61 rings), and a 5 5 ring rhombus (25 rings). The five substrates are shown in Figure 16.

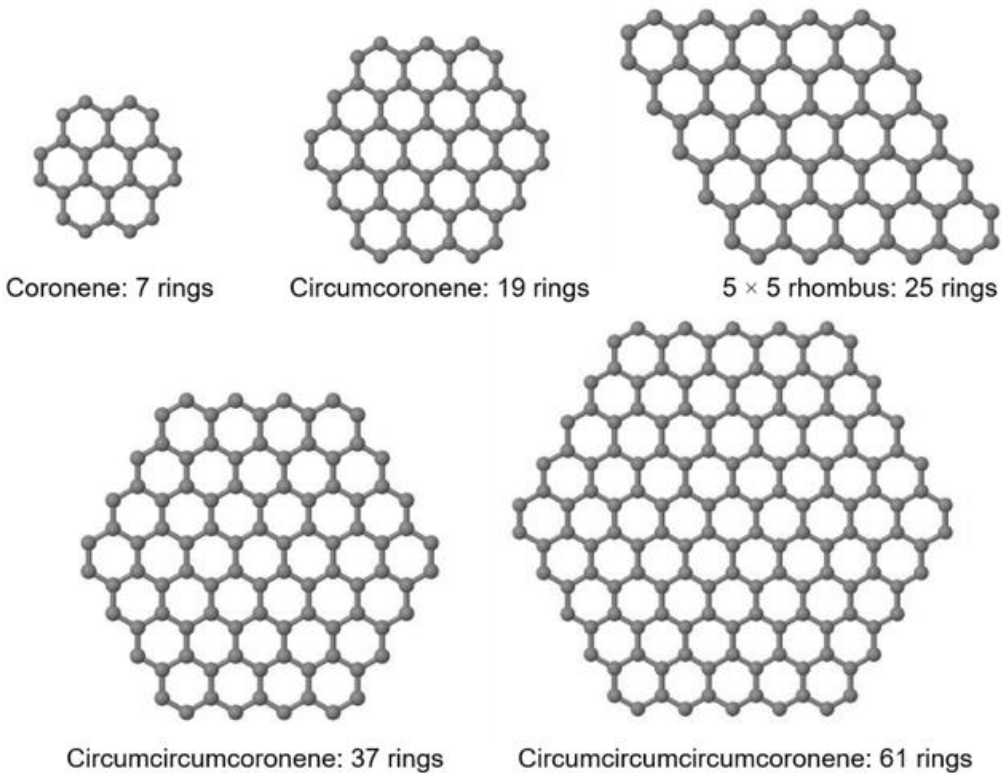


Figure 53: Initial substrates for KMC simulations. The H atoms saturating the edge carbon atoms are not shown for clarity.

Gas phase concentration profiles of each of the 10 species were computed from a series of 50 simulation runs performed with different seeds for the random number generator for each substrate. Fig.54 shows the effect of initial substrate size on CO and CO₂ concentration profiles. The black line in Fig.54 comes from PFR simulations that are not coupled to surface chemistry. The black markers in Fig.54 are experimentally-measured data points from Fig.44 of Roth et al. [93].

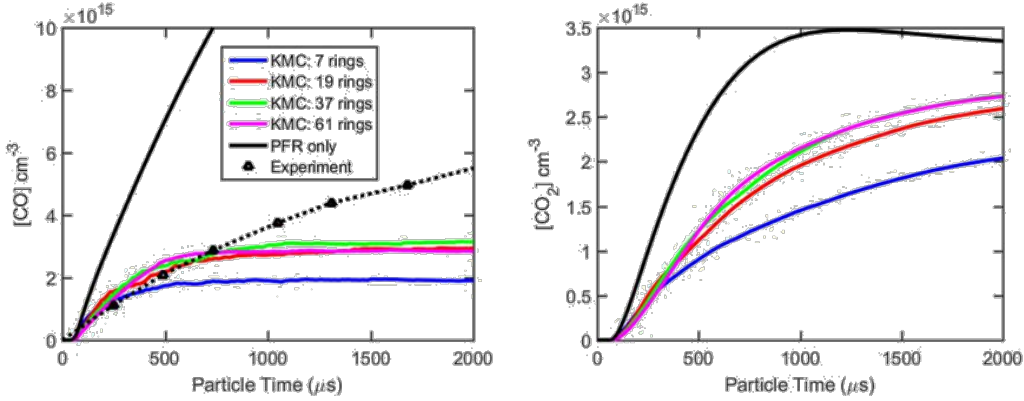


Figure 54: CO and CO_2 concentration versus time for KMC simulations with different initial substrate sizes.

Fig.54 shows the effects on the magnitude and shape of the CO and CO_2 concentration profiles by changing the initial substrate size. Although the production of CO and CO_2 increase as the substrate size increases from seven rings to 19, further increases to substrate size have no significant effect on formation rates of CO or CO_2 . Based on the concentration profiles alone, it is tempting to assume that the oxidation behavior is the exactly the same for the cases with the three largest initial substrate sizes. However, one must look at the underlying reaction statistics in order to get a more detailed understanding of the oxidation kinetics.

In the current KMC model, carbon can be removed from the graphene edge via oxidation by O_2 (reactions 51-54 and 90), OH (reactions 96-99), H_2O (reactions 100-103), O (reaction 104), or via thermal desorption (reactions 5, 7, 17, 25, and 45). The reaction statistics for oxidation and thermal desorption reactions illustrated in Fig.55 and presented in Table 12 provide insight into how the kinetics are affected by initial substrate size.

Table 12: Event counts for oxidation and thermal desorption reactions for KMC simulations with different initial substrate sizes

	Initial substrate size (rings)			
Reactions	7	19	37	61
Oxidation by O ₂ : R51 – R54, R90	7.2	17.0	21.7	33.0
Oxidation by OH: R96-R99	5.0	13.9	18.5	29.7
Oxidation by H ₂ O: R100- R103	0.5	1.5	1.6	2.7
Oxidation by O: R104	6.5	15.8	24.1	41.0
Thermal desorption: R5, R7, R17, R25, R45	9.0	24.7	24.3	31.9

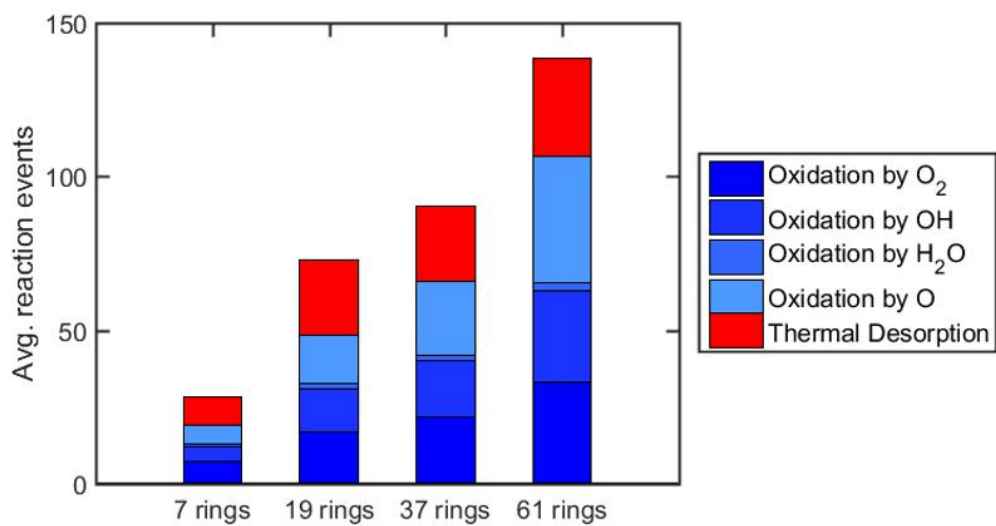


Figure 55: Event counts for oxidation and thermal desorption reactions for KMC simulations with different initial substrate sizes.

The reaction counts in Table 12 show that as the initial substrate size increases, the frequency of oxidation and thermal desorption reactions increases. This result is expected due to an increase in the number of edge carbon sites and does not reveal much on its own. To gain a better understanding of the relationship between the reactions that remove carbon, the data from Table 12 can be recast in terms of the share of carbon atoms removed by each type of reaction as shown in Fig.56 and Table 13.

Table 13: Share of carbon atoms removed from the substrate by oxidation and thermal desorption reactions for KMC simulations with different initial substrate size

	Initial substrate size (rings)			
Reactions	7	19	37	61
Oxidation by O ₂ : R51 – R54, R90	16%	17%	19%	19%
Oxidation by OH: R96-R99	11%	14%	16%	17%
Oxidation by H ₂ O: R100- R103	1%	1%	1%	2%
Oxidation by O: R104	15%	16%	21%	24%
Thermal desorption: R5, R7, R17, R25, R45	57%	53%	43%	38%

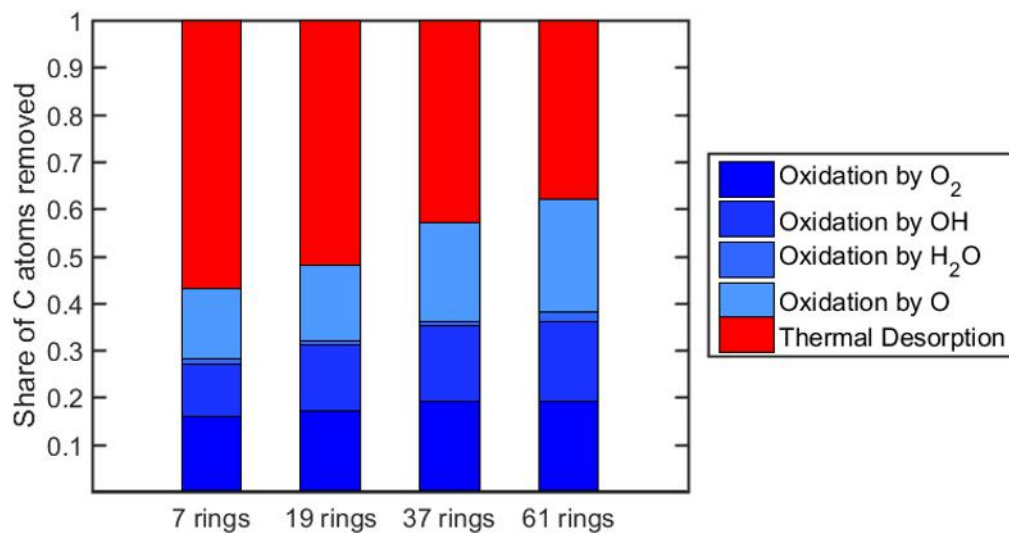


Figure 56: Share of carbon atoms removed from the substrate by oxidation and thermal desorption reactions for KMC simulations with different initial substrate size.

The data in Table 13 show that the oxidation behavior does change slightly as the initial substrate size increases. A tradeoff occurs between thermal desorption reactions, which account for 57 % of the carbon atoms removed for the smallest initial substrate case, and oxidation reactions which remove 62 % of the carbon atoms for the largest initial substrate case. While the oxidation behavior is not exactly the same for the different cases, the shift between relative frequencies of oxidation and thermal desorption reactions does not manifest in different CO and CO₂ concentration profiles indicating that the oxidation rate

is not very sensitive to initial substrate size.

KMC simulations were also performed using a rhombus-shaped graphene substrate in order to see if substrate shape would affect the results. Fig.57 shows a comparison of CO and CO₂ concentration profiles between simulations using the rhombus substrate and simulations with circumcoronene and circumcircumcoronene. The species concentration profiles are similar for all three sets of simulations indicating that CO and CO₂ formation are not significantly affected by the shape of the initial substrate. Fig.58 and Table 14 show the share of carbon atoms removed by oxidation and thermal desorption for these simulations.

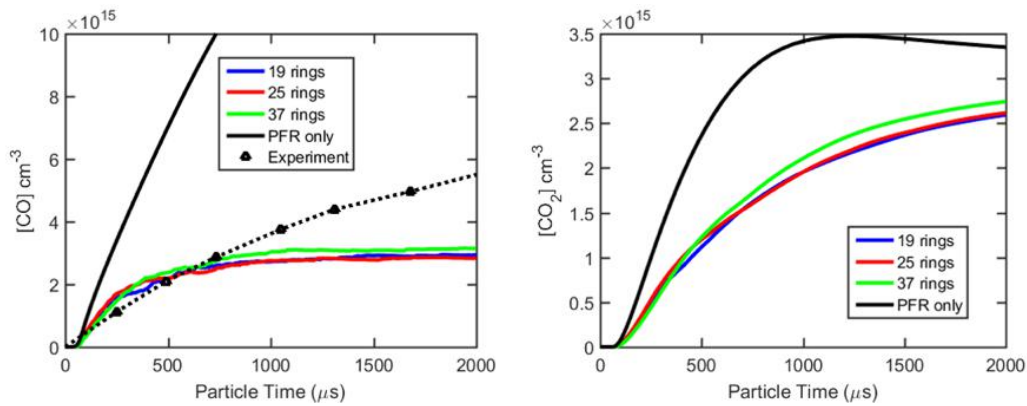


Figure 57: CO and CO₂ concentration versus time for KMC simulations with different initial substrate shapes.

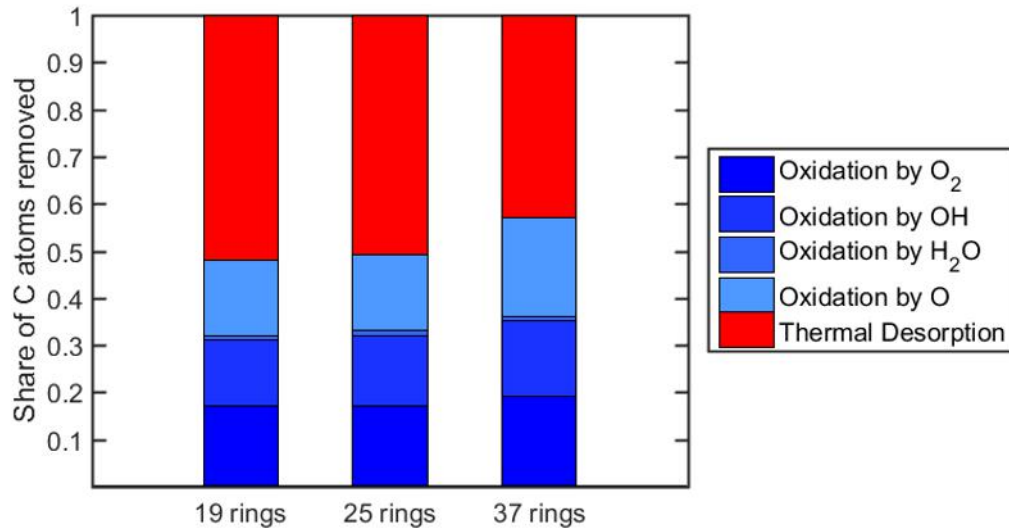


Figure 58: Share of carbon atoms removed from the substrate by oxidation and thermal desorption reactions for KMC simulations with different initial substrate shape.

Table 14: Share of carbon atoms removed from the substrate by oxidation and thermal desorption reactions for KMC simulations with different initial substrate shape

	Initial substrate size (rings)		
Reactions	19	25	37
Oxidation by O ₂ : R51 – R54, R90	17%	17%	19%
Oxidation by OH: R96-R99	14%	15%	16%
Oxidation by H ₂ O: R100- R103	1%	1%	1%
Oxidation by O: R104	16%	15%	21%
Thermal desorption: R5, R7, R17, R25, R45	53%	52%	43%

The oxidation behavior shown in Fig.58 and Table 14 for the case with the rhombus sub-strate is similar to the kinetics exhibited by the cases with substrates of 19 and 37 rings. The fact that the oxidation rate is not highly dependent on either substrate size or shape justifies the choice of using circumcoronene as the initial substrate for the rest of the simulations.

In the simulations discussed above, the initial substrate was oxidized down to one ring before it was replaced by a new substrate. However, the reality may be that the outermost layer of the soot surface would not have to be completely oxidized before oxidation would start to take place at the next layer. To test the sensitivity of CO formation to the extent of oxidation allowed before continuing on to the next substrate, different lim-its of oxidation were implemented beyond which oxidation would continue with a new substrate. For example, if the initial substrate was circumcoronene ($C_{54}H_{18}$) and the ex-tent of oxidation allowed was set at 50 %, whenever the substrate size would decrease to less than 27 C atoms, a new circumcoronene substrate would be instantly regenerated. Thresholds of 5, 10, 25, 50, and 100 % were tested and the initial substrate was chosen to be circumcoronene. The scenario of 100 % oxidation allowed corresponds with oxida-tion continuing until one ring remains, and that ring is assumed to fall apart instantly as shown in the previous results.

Fig.59 shows that CO and CO₂ formation increase as the extent of oxidation allowed be-fore creating a new substrate decreases. This result is consistent with the analysis pre-sented above that states that oxidation rate decreases over time. By limiting the extent of oxidation allowed and regenerating a new substrate earlier in the oxidation process, the overall oxidation rate will be higher and more product formation will occur. Fig.45 shows that as the extent of oxidation allowed is decreased towards 5 %, the CO concen-tration profile moves closer to the PFR profile. This result is expected as the PFR scenario assumes a constant replenishment of C-H sites for any amount of oxidation and is essen-tially a minimum case for the extent of oxidation allowed.

Table 15: Event counts for oxidation and thermal desorption reactions for KMC simulations with different extents of oxidation allowed

		Extent of oxidation allowed (%)				
Reactions	5	10	25	50	100	
Oxidation by O ₂ : 51 – 54, 90	132.4	99.7	57.9	43.1	17.0	
Oxidation by OH: 96 – 99	118.2	89.8	50.4	36.8	13.9	
Oxidation by H ₂ O: 100 – 103	22.0	13.6	6.4	5.3	1.5	
Oxidation by O: 104	42.1	48.1	42.7	33.7	15.8	
Thermal desorption: 5, 7, 17, 25, 45	0.8	3.3	26.3	45.0	24.7	

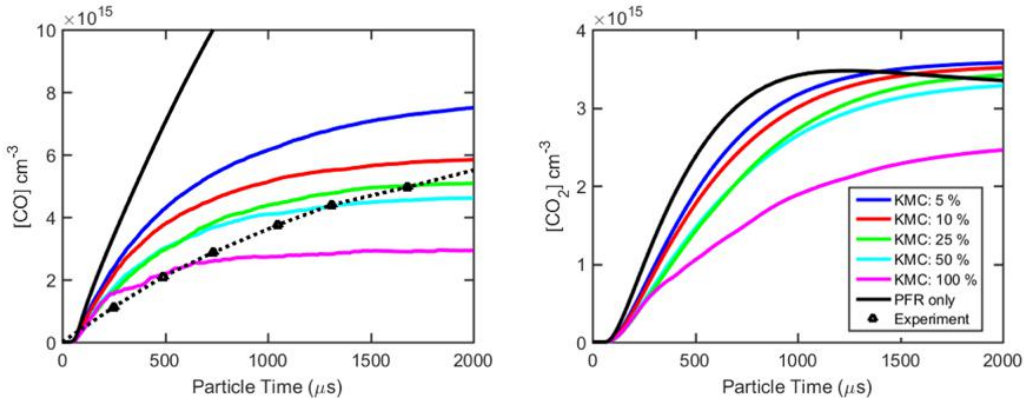


Figure 59: CO and CO₂ concentration versus time for KMC simulations with different extents of oxidation allowed. Circumcoronene was the initial substrate.

The reaction counts for oxidation and thermal desorption reactions for each of the simulations are shown in Table 15 and Fig.60. As the extent of oxidation allowed decreases, the number of event counts for oxidation reactions increases with the majority of oxidation occurring by O₂ and OH. In contrast to the trend for oxidation reactions, the number of thermal desorption reactions decreases sharply as the extent of oxidation is decreased. The tradeoff between oxidation and thermal desorption is made even clearer when looking at the share of carbon atoms removed by each type of reaction as shown in Fig.61 and Table 16.

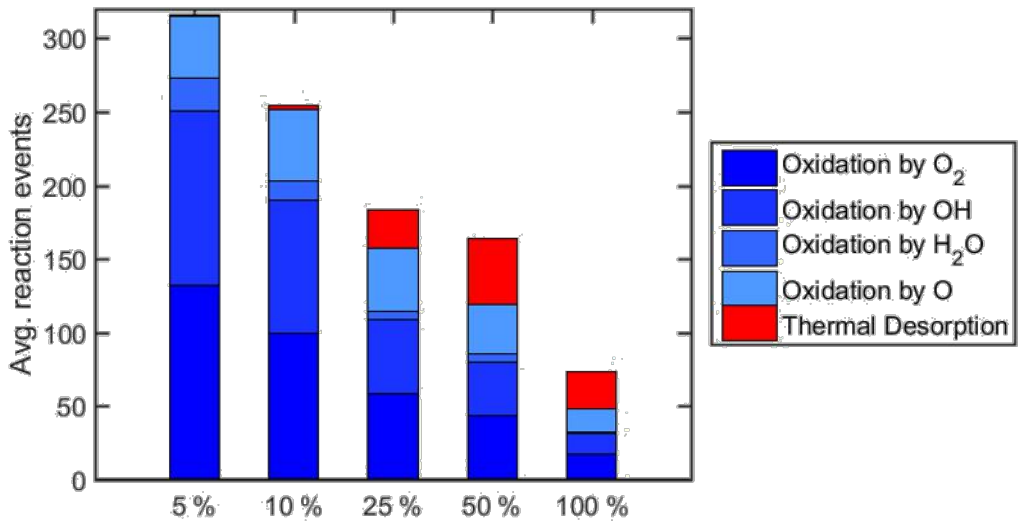


Figure 60: Event counts for oxidation and thermal desorption reactions for KMC simulations with different extents of oxidation allowed.

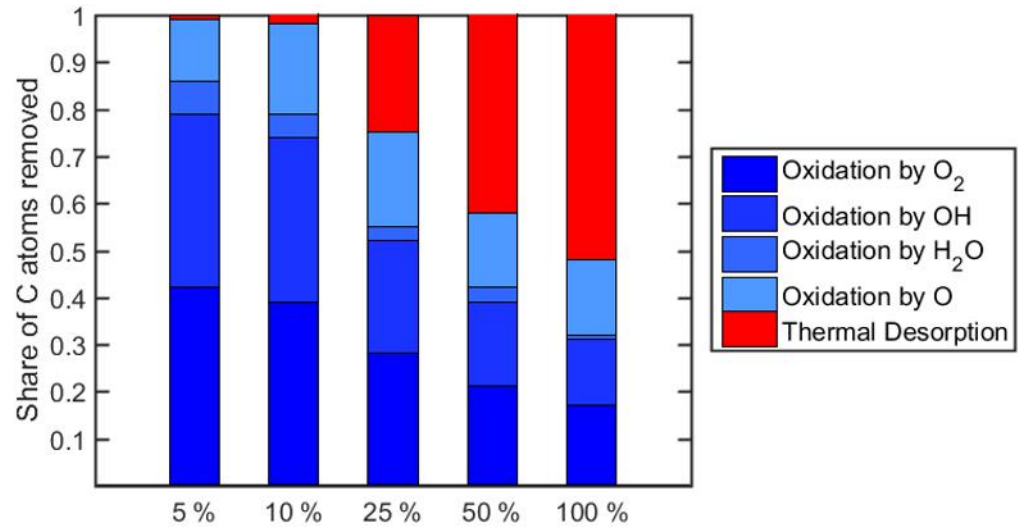


Figure 61: Share of carbon atoms removed by oxidation and thermal desorption reactions for KMC simulations with different extents of oxidation allowed.

Fig.61 reveals the relative order of the mechanisms which remove carbon. Oxidation of six-member rings by O₂ and OH occurs at the onset of oxidation followed by oxidation of five-member rings by O which precedes thermal desorption reactions. These results are

Table 16: Share of carbon atoms removed by oxidation and thermal desorption reactions for KMC simulations with different extents of oxidation allowed

		Extent of oxidation allowed (%)				
Reactions	5	10	25	50	100	
Oxidation by O ₂ : 51 – 54, 90	42%	39%	28%	21%	17%	
Oxidation by OH: 96 – 99	37%	35%	24%	18%	14%	
Oxidation by H ₂ O: 100 – 103	7%	5%	3%	3%	1%	
Oxidation by O: 104	13%	19%	20%	16%	16%	
Thermal desorption: 5, 7, 17, 25, 45	0%	3%	25%	43%	53%	

consistent with the earlier findings that the oxidation behavior of graphene edges changes over time.

C-5.0.1 Effect of Atomic Hydrogen Production In the shock tube experiments conducted by Roth et al. [93], the concentration of atomic hydrogen was not measured. It is known that minute quantities of impurities adsorbed to the walls of a shock tube can generate a non-negligible amount of hydrogen atoms upon shock heating, and the additional hydrogen atoms can greatly affect the kinetics of the mixture being tested [123, 124]. Roth et al. did not measure hydrogen atom concentration, so it is possible that hydrogen atoms could have been produced by this mechanism. To simulate this phenomenon, a source term was added to Equation 3 which would allow for a constant rate of production of hydrogen atoms. Equation 4 shows the modified expression for updating the hydrogen concentration.

$$[H] = \frac{\text{net H atoms produced in KMC}}{1} \frac{1}{N_{\text{sites}}} \frac{2:3 \cdot 10^{15} \text{ sites}}{\text{cm}^2} \frac{1 \text{ mol}}{N_A \text{ H atoms}} \frac{a_p \text{ cm}^2}{1 \text{ cm}^3} + H_{\text{prod}} ; \quad (11)$$

Values of $1 \cdot 10^{-10}$, $3 \cdot 10^{-10}$, and $5 \cdot 10^{-10}$ mol/cm³ for the H_{prod} parameter were tested, meaning that the concentration of hydrogen atoms was increased by that value every 10 s. The initial substrate was chosen to be circumcoronene and oxidation was allowed to continue until the substrate reached one ring before creating a new substrate.

Fig. 62 shows CO and CO₂ concentration profiles for different rates of hydrogen atom production. For simulations in the previous sections, the formation of CO was seen to taper off at later oxidation times. Here though, the production of hydrogen atoms allows for CO formation to continue at its initial rate. When $H_{\text{prod}} = 3 \cdot 10^{-10}$ mol/cm³, the CO concentration profile shows good agreement with the magnitude and shape of the experimentally-measured CO concentration profile. The increase in CO concentration when H_{prod} increases is directly linked to the decrease in CO₂ concentration seen at later oxidation times. When H concentration is higher due to hydrogen atom production

(as seen in Fig.63), the reverse of the reaction $\text{CO} + \text{OH} \rightarrow \text{CO}_2 + \text{H}$ becomes favorable and CO_2 goes back to CO .

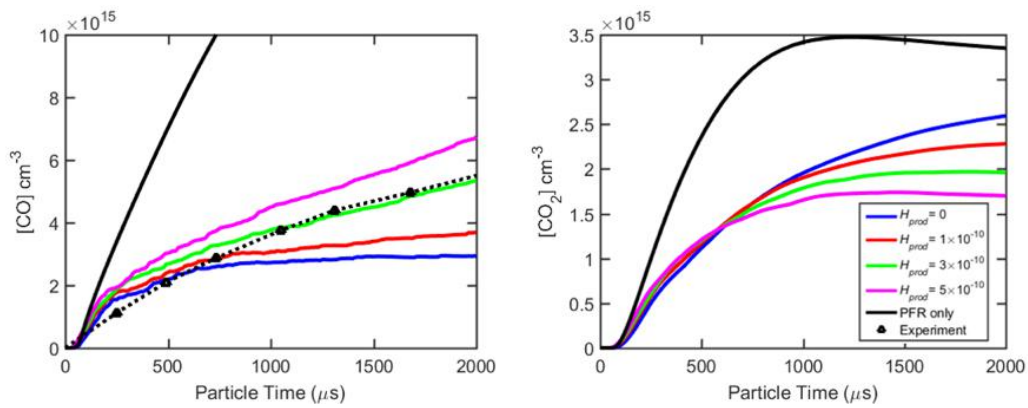


Figure 62: CO and CO_2 concentration versus time for KMC simulations with different levels of atomic hydrogen production. Circumcoronene was the initial substrate and the extent of oxidation allowed was 100 %.

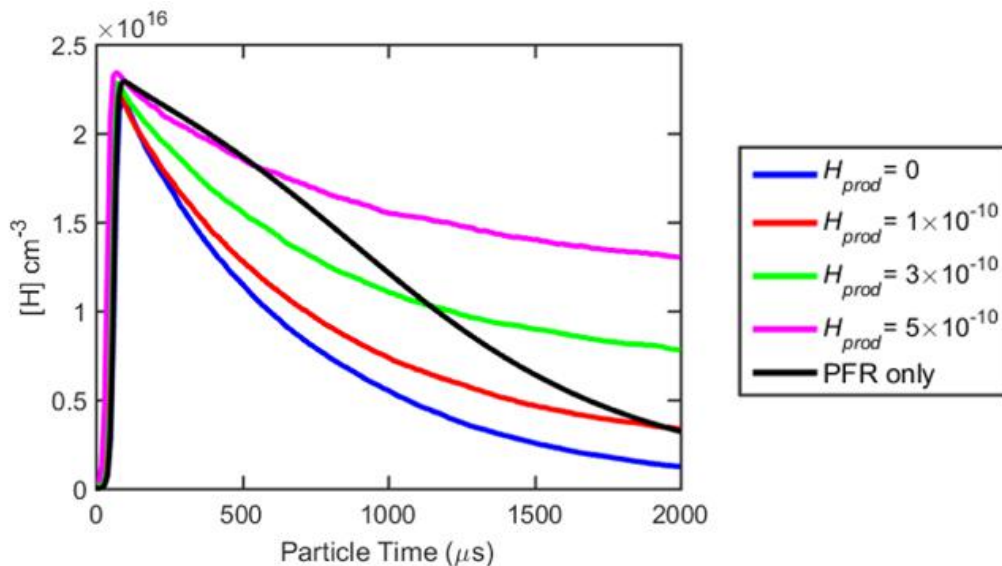


Figure 63: $[\text{H}]$ versus time for KMC simulations with different rates of atomic hydrogen production. Circumcoronene was the initial substrate and the extent of oxidation allowed was 100 %

While the frequency of reactions that form radical sites via hydrogen abstraction (reactions 1, 10, 13a, and 92) increased with increasing production of atomic hydrogen, the frequency of radical site deactivation reactions also increased (reactions 2a, 2b, 11a). The net effect was a modest increase in the event counts for oxidation and thermal desorption

reactions as hydrogen production increased, as can be seen in Fig.64 and Table17. Presenting the data in terms of the share of carbon atoms removed by oxidation and thermal desorption (Fig.65 and Table18) illustrates that increasing hydrogen production had only a marginal effect on the surface reaction oxidation behavior. The share of carbon atoms removed by each type of reaction remained roughly the same for all four cases. These simulations demonstrate that atomic hydrogen production leads to significant changes in the gas phase concentrations of CO, CO₂, and H, but these changes have a smaller effect on the surface oxidation and thermal desorption reaction event counts.

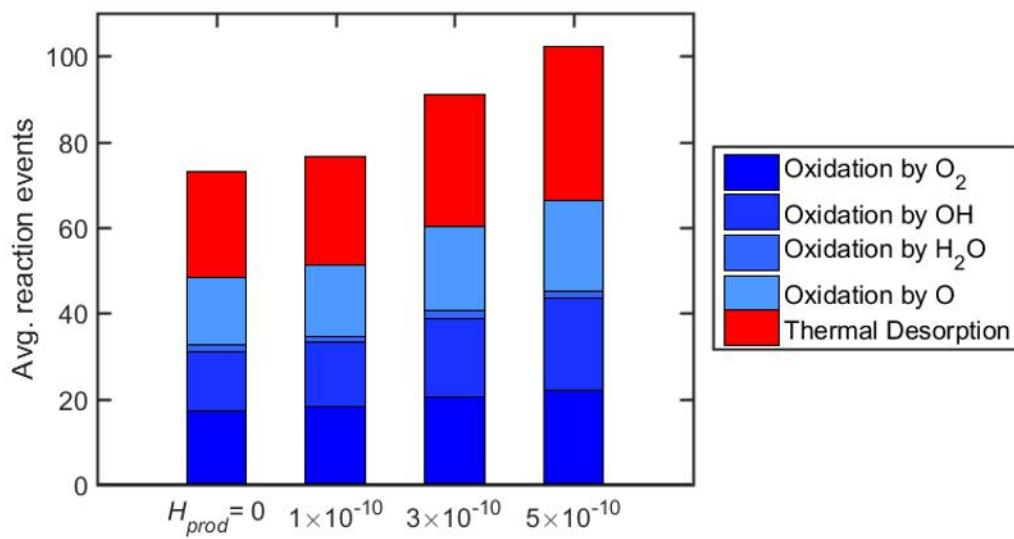


Figure 64: Event counts for oxidation and thermal desorption reactions for KMC simulations with different rates of atomic hydrogen production.

Table 17: Event counts for oxidation and thermal desorption reactions for KMC simulations with different rates of atomic hydrogen production

	$H_{prod} 10^{10}$ cm^{-3}	(mol)		
Reactions	0	1	3	5
Oxidation by O_2 : R51 – R54, R90	17.0	18.0	20.4	22.0
Oxidation by OH: R96-R99	13.9	15.1	18.4	21.5
Oxidation by H_2O : R100- R103	1.5	1.4	1.9	1.7
Oxidation by O: R104	15.8	16.6	19.3	20.9
Thermal desorption: R5, R7, R17, R25, R45	24.7	25.3	30.9	36.2

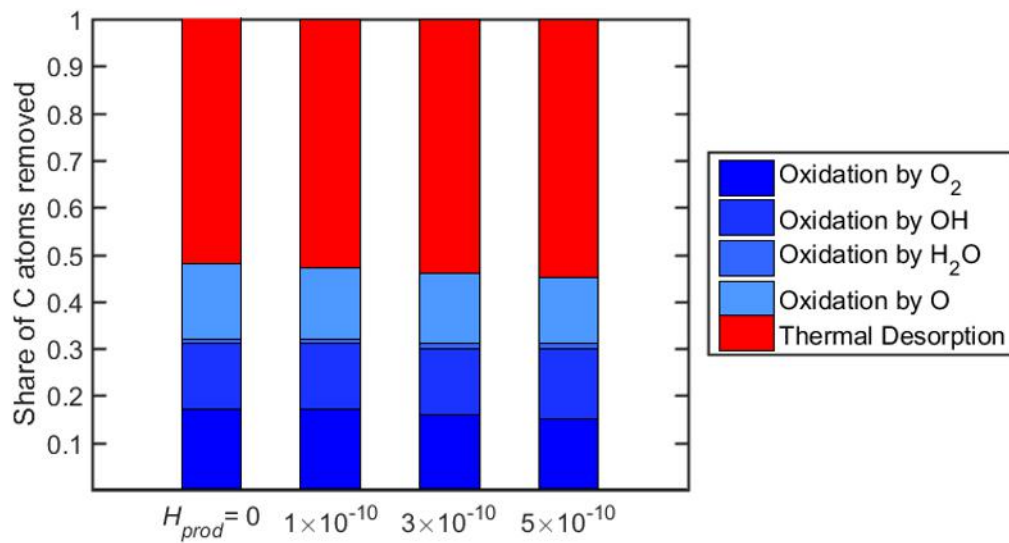


Figure 65: Share of carbon atoms removed by oxidation and thermal desorption reactions for KMC simulations with different rates of atomic hydrogen production.

C-6 Summary

It was initially determined that the primary pathway for the attack of O_2 on the surface radical site of a graphene-edge six-member ring was the elimination of O and the formation of an oxyradical. The oxyradical could then thermally decompose into a five-member ring and eliminate CO. The computed rate coefficients showed a slight dependence on the number of free edges and size of the PAH, with the rates increasing as the former increases and decreasing as the latter increases. Oxidation of a graphene-edge five-member ring by

Table 18: Share of carbon atoms removed by oxidation and thermal desorption reactions for KMC simulations with different rates of atomic hydrogen production.

	$H_{prod} \cdot 10^{10}$ (mol cm ⁻³)			
Reactions	0	1	3	5
Oxidation by O ₂ : R51 – R54, R90	17.0	18.0	20.4	22.0
Oxidation by OH: R96-R99	13.9	15.1	18.4	21.5
Oxidation by H ₂ O: R100- R103	1.5	1.4	1.9	1.7
Oxidation by O: R104	15.8	16.6	19.3	20.9
Thermal desorption: R5, R7, R17, R25, R45	24.7	25.3	30.9	36.2

O₂ was shown to have a slower rate than oxidation of a six-member ring by several orders of magnitude. Oxidation of a graphene-edge five-member ring with atomic oxygen was found to be a possible pathway to explain how five-member rings are removed from the substrate. The rate coefficient for oxidation by atomic oxygen exceeded that of oxidation by molecular oxygen by several orders of magnitude. The oxidation reactions examined in the present study and their corresponding rate coefficients were incorporated into a de-tailed model of elementary reactions of graphene-edge oxidation. This model was added to a detailed model of soot surface growth.

The combined model of surface growth and oxidation reactions were implemented into KMC simulations of graphene-edge oxidation by O₂ at high-temperature. Two principal oxidation pathways were found: thermal decomposition oxyradicals and regeneration of aromatic radical sites. Their competition is temperature-dependent with the former dominating at higher and the latter dominating at lower temperatures. Yet, the overall oxidation rate at the conditions tested was not substantially affected by the presence or absence of the regeneration pathway. This may help in developing reduced models of soot oxidation at flame conditions.

The overall oxidation rate of the graphene substrate was computed to be time-dependent, with reactivity decreasing over time as the ratio of reactive edge sites decreases relative to the number of basal-plane carbon atoms. At the same time, the oxidation rate was found to be higher for graphene with a higher initial curvature. Both results are in accord with experimental observations [88, 91]. Analysis showed that distinct aspects of graphene-edge morphology are responsible for curvature either raising or reducing the oxidative reactivity of the graphene-edge.

Finally, the KMC simulations were performed in an evolving gas-phase environment that was coupled to the surface chemistry for conditions of high-temperature shock-tube experiments of soot oxidation performed by Roth et al. [93]. The formation rate of CO was found only to depend on substrate size if the substrate was very small (seven rings). In-

creasing the initial substrate size beyond coronene did not affect the production of CO and CO₂. The substrate shape did not appear to have a significant effect on CO and CO₂ formation either. Decreasing the extent of oxidation allowed before moving on to a new platelet led to increased rates of CO formation and produced CO profiles closer to the PFR-only scenario in which steric effects were not accounted for. The formation of CO was also shown to be sensitive to production of H atoms. Increasing H production led to an increase in CO and a decrease in CO₂ due to the reverse of the reaction CO + OH ! CO₂ + H becoming more favorable for higher H concentration. By adjusting modeling parameters (initial substrate, extent of oxidation allowed, and hydrogen production) within reasonable limits, the model did a good job of reproducing the experimental oxidation rates. This analysis shows that the soot oxidation rate depends on gas phase kinetics, steric effects, and how the structure of the soot surface is approximated in models.

Publications

Presentations

M. Frenklach, "Mechanism of Soot Formation: Oxidation," Multiagency Coordination Committee for Combustion Research (MACCCR)—5th Annual Fuels Research Review, Sandia National Laboratory, Livermore, CA, September 17-20, 2012.

D. E. Edwards, D. Yu. Zubarev, W. A. Lester, Jr., and M. Frenklach, "Oxidation of Phenanthrene Radicals by OH," 8th U.S. National Combustion Meeting, University of Utah, May 19-22, 2013, Paper No. 2B14.

D. E. Edwards, D. Yu. Zubarev, W. A. Lester, Jr., and M. Frenklach, "Products and Path-ways for the Reaction of OH with Phenanthrene Radicals", 8th International Conference on Chemical Kinetics, Seville, Spain, July 8-12, 2013, Paper No. c-43.

M. Frenklach, "Mechanism and Kinetics of Soot Oxidation," 2nd International Workshop on Flame Chemistry, San Francisco, CA, August 2-3, 2014.

R. Singh and M. Frenklach, "Oxidation of soot: Kinetic Monte Carlo simulations of graphene-edge growth and oxidation," 35th International Symposium on Combustion, San Francisco, CA, August 3-8, 2014, Work-in-Progress Poster W4P093.

R. Singh, A. M. Mebel, and M. Frenklach, "Kinetics of oxidation of graphene edges," 9th U.S. National Combustion Meeting, Cincinnati, Ohio, May 17-20, 2015, Paper 114RK-0269.

D. DNS-based analysis of emissions modeling

D-1 Introduction

The LES soot modeling framework [96] that is analyzed in this project is made up of a number of components that can be thought of as the basic ingredients of the soot prediction model. These component models fall into two major categories. The first category of models parameterize physico-chemical processes and necessary ingredients from this category include a gas-phase combustion model, a model for soot precursor species evo-

lution (assumed to be polycyclic aromatic hydrocarbons or PAH), and models for the evolution of the soot particle population. The second category of models, called subgrid or, more precisely, subfilter models, account for the loss of information at scales smaller than the LES filter scale. This is typically accomplished using one-point statistical closures for the joint subfilter distributions of the scalar variables required by the physicochemical process models [97].

The use of data from direct numerical simulation (DNS) of turbulent flows to develop and validate LES subfilter models is well established. However, it is important to recognize the potential pitfalls of this approach when applied to soot modeling. First, DNS is only able to fully resolve the gas-phase flow. Soot must still be represented in a statistical sense as a population of particles, and the evolution of the soot population must be described using simplified, approximate models for complex processes of nucleation, growth, and oxidation. In this study, the hybrid method of moments (HMOM) [98] is used to de-scribe a bimodal soot particle population in terms of the number, volume, and surface area of small and large mode particles. Secondly, because soot particles are non-diffusive, the finest scales of the soot moment fields are much smaller than those of gas-phase turbulence and are necessarily under-resolved. Furthermore, it is critical to note that the spatial distribution of the soot moments are determined by the Lagrangian trajectories of soot motion relative to the gas-phase flow. While soot particles form at somewhat rich mixture fractions, DNS studies find soot at much richer mixture fractions [99, 100], sug-gesting the particles move extensively in the gas-phase composition space. Thus, they move across large scales of the flow, which are dependent on the specific flow configu-ration. It is necessary to evaluate to what extent subfilter modeling can disregard this history, which can only be done by evaluating data from a variety of cases with different geometries and compositions. Finally, LES predictions of soot depend not only on the accuracy of the soot model, but are also contingent upon accurate prediction of gas-phase combustion. These factors complicate the development of generically applicable subfilter models for soot.

The factors mentioned above acquire even greater significance in light of the high computational demands of DNS of sooting turbulent flames, which strongly limits the variety and scope of such simulations that can feasibly be performed. As an indication of these demands, it should be noted that a minimal realistic representation of the chemistry of gas-phase soot precursors requires tens of chemical species to be considered [99]. Further-more, long simulation run times are needed to capture the slow formation and growth of soot. Therefore, such simulations are necessarily restricted to rather idealized flow con-figurations, such as temporal planar jets [99–102] , that are able to exploit periodicity to limit the size of computational domain required. This leads to uncertainty in extrapolat-ing soot subfilter models from these relatively simple turbulent flows to more complex flows of practical significance.

Therefore, a hierarchical approach to using DNS is developed in this study. The first step in this approach is to validate models for predicting gas-phase soot precursors. This is done by comparing a “reduced-order DNS” simulation performed with full resolution of the turbulent fields, but using an LES-appropriate combustion model, to a conventional

DNS performed with detailed, finite-rate chemistry. It is this first step in the approach that is the primary focus of this report. Because the reduced-order DNS approach has a moderate computational cost, it can be used to simulate more challenging flow configurations. The data from these simulations can be used to develop widely applicable subfilter models for soot. Some preliminary work in developing analysis methods for investigating subfilter models will also be reported.

With the conceptual outline of the study's methodology in place, the next section reviews the essential features of the models for gas-phase combustion, PAH, and soot.

D-2 Modeling background

Soot is modeled using the hybrid method of moments (HMOM) [98], which combines features of two other moment methods, direct quadrature method of moments (DQMOM) [103] and method of moments with interpolative closure (MOMIC) [104]. HMOM is constructed to capture the characteristically bimodal soot particle population, with a nucleation mode of small, spherical particles of assumed size and number N_0 and an accumulation mode of large, irregularly shaped soot aggregates described by a set of bi-variate moments $M_{x;y}$ in the internal coordinates of surface area and volume. The set of moments $M_{x;y}$ and weight N_0 evolve by turbulent transport and source terms resulting from interactions between the soot particles and gas-phase and between the soot particles themselves. In particular, soot particle nucleation is modeled as resulting from collisions between dimers of the PAH species naphthalene , while collisions of PAH dimers with existing soot particles produces soot particle growth. Thus the source terms

M_i^- for the soot scalars M_i (the moments $M_{x;y}$ and weight N_0) can be written as

$$M_i^- = S(M_i; \cdot) \quad (12)$$

where \cdot is any thermochemical variable such as density, temperature, or species mass fractions and S represents the functional form of the soot source term models [96].

Gas-phase combustion is modeled using a flamelet modeling approach. Several varieties of flamelet models exist [97]. All are based on the basic idea that a turbulent flame can be approximated as an ensemble of laminar flamelets, but differ in the set of flamelet solutions included in the ensemble and the parameters used to access individual members of the ensemble. Here, because radiative losses are negligible, the flamelet progress variable (FPV) approach [105] is used. This type of flamelet model takes as its ensemble solutions of the steady flamelet equation computed across a range of scalar dissipation rates and is parameterized by the mixture fraction, Z , and progress variable, C , defined as the sum of the mass fractions of major products of combustion. Mathematically, the FPV model can be summarized by

$$= F(Z; C) \quad (13)$$

where F is the functional relationship obtained from the solution of the steady flamelet equations.

In sooting flames, slight modifications to the conventional definitions of Z and C are needed to account for the loss of carbon atoms from the gas-phase to the solid phase [96].

PAH molecules develop more slowly than other gas-phase species. The study of Bisetti et al. [99] found that naphthalene mass fractions roughly follow flamelet model predictions but show significant scatter due to unsteady turbulent mixing effects. Therefore, it is proposed to model a lumped PAH mass fraction with the properties of naphthalene using a transport equation model where the source terms are taken from the flamelet model but modified according to the local amount of PAH. A similar method was previously used for the prediction of NOx [106]. The modified PAH source term for the transport equation model \dot{Y}_{PAH} is given by

$$\dot{Y}_{PAH} = \dot{Y}_{PAH}^f + \dot{Y}_{PAH}^f - \frac{\dot{Y}_{PAH}^f}{\dot{Y}_{PAH}^f} + \dot{Y}_{dimer}^f - \frac{\dot{Y}_{PAH}^f}{\dot{Y}_{PAH}^f} : \quad (14)$$

In this expression, \dot{Y}_{PAH}^f is the positive source term for PAH from gas-phase reactions given by the flamelet model, \dot{Y}_{PAH}^f is the negative sink term for PAH from gas-phase reactions given by the flamelet model, and \dot{Y}_{dimer}^f is the dimerization sink term for PAH, again as given by the flamelet model. Here, \dot{Y}_{PAH} denotes the PAH mass fraction obtained from solution of the transport equation model, while \dot{Y}_{PAH}^f is the PAH mass fraction predicted by the flamelet model.

Thus, returning to Eq. 12, the source terms of the soot scalars can be found from

$$M_i = S(M_i; F(Z; C); \dot{Y}_{PAH}) : \quad (15)$$

Written in this way, it can readily be seen that the relevant quantity for LES subfilter modeling associated with this soot model is the joint probability density function (PDF) of M_i , Z , C , and \dot{Y}_{PAH} .

D-3 Reduced-order DNS Simulation

Recently, a three-dimensional DNS of soot formation in a turbulent temporal jet flame was carried out by Attili and co-workers [100]. It is to this simulation that the reduced-order DNS simulation will be compared in Section D-3.2.

D-3.1 Flow specifications

The temporal jet geometry consists of a slab of fuel with counterflowing oxidizer streams on either side. The flow is periodic in the two horizontal dimensions while the top and bottom boundaries are open. Here, the fuel stream consists of nitrogen-diluted n-heptane (15% C_7H_{16} , 85% N_2 by volume) at 400 K while the oxidizer is air (21% O_2 , 79% N_2 by volume) at 800 K. To provide a burning initial condition, the equilibrium chemistry solution is assumed to hold in the transition region between the fuel and air streams. This also avoids introducing soot precursors as part of the initial condition.

The velocity difference between the fuel and air streams is 17.48 m/s. Fluctuations are imposed on the initial jet core velocity using the results of a turbulent channel flow simulation at $Re = 390$. These fluctuations are mirrored on each side in the co-flowing air streams.

The initial width of the jet, H , is 15 mm. The computational domain extends 105 mm by 47 mm by 23.5 mm in the cross stream, streamwise, and spanwise directions, respectively. The spacing between grid points is isotropic and equal to 91 m. Since the minimum estimated Kolmogorov scale is 110 m, the turbulent velocity field is well resolved. Additionally, the OH layer of the flame is spanned by at least 10 grid points, showing that the flame structure is also well resolved.

These specifications are matched as closely as possible in the reduced-order DNS simulation. The initial velocity, mixture fraction, and density fields are matched exactly. The initial values of the progress variable are determined by matching to the mixture fraction and density values.

D-3.2 Results

In this section, the predictions of gas-phase chemistry from the reduced-order DNS are compared to those obtained in the finite-rate chemistry DNS of Attili et al. [100].

Figure 66 shows conditional means of temperature and OH mass fraction, conditioned on mixture fraction, at four times in the simulation. At all four times, the peak value of conditional mean temperature is slightly higher for the reduced-order DNS and is located at a lower value of mixture fraction. However, for values of mixture fraction richer than about $Z = 0.2$, the finite-rate chemistry DNS shows notably warmer temperatures. There is rather little change in the conditional temperature profiles across the four times considered. The results for OH show more distinct temporal trends than do the temperature results. The reduced-order DNS results show a higher peak value of the conditional mean at 5 and 10 ms, but by 15 ms the maximum values attained by the reduced-order and finite-rate chemistry DNS are nearly equal. By 20 ms, the peak values of OH mass fraction are higher for the finite-rate chemistry DNS. Similarly to the temperature results, the finite-rate chemistry DNS shows greater amounts of OH present at rich values of mixture fraction. Together, these results suggest that the flame in the reduced-order DNS, as modeled using the FPV approach, is more intense, at least for the first 15 ms its evolution, and distributed across a narrower range of mixture fraction values. The finite-rate chemistry DNS shows more reactivity at richer values of mixture fraction at all four times.

Because the soot model used in this study assumes that soot nucleates and grows from collisions of PAH dimers, with naphthalene ($C_{10}H_8$) taken as the representative PAH species, accurate prediction of the PAH mass fraction Y_{PAH} is a precondition for accurate prediction of soot. Figure 67 compares the conditional means of PAH mass fractions obtained from the finite-rate chemistry DNS and reduced-order DNS. Two options are considered for the reduced-order DNS. In the first option, the value of Y_{PAH} is evaluated directly from the FPV model, i.e. it is equivalent to Y_{PAH}^f in Eq. 14. In the second option, the transport equation model for Y_{PAH} that was discussed in Sec. D-2 is used. The transport equation model predictions of Y_{PAH} remains related to the FPV chemistry parameterization through the modified source term expression, Eq. 14.

Predictions of PAH mass fraction are shown in the left column of Figure 67. Early in the simulation, the finite-rate chemistry results show a high PAH mass fraction that is

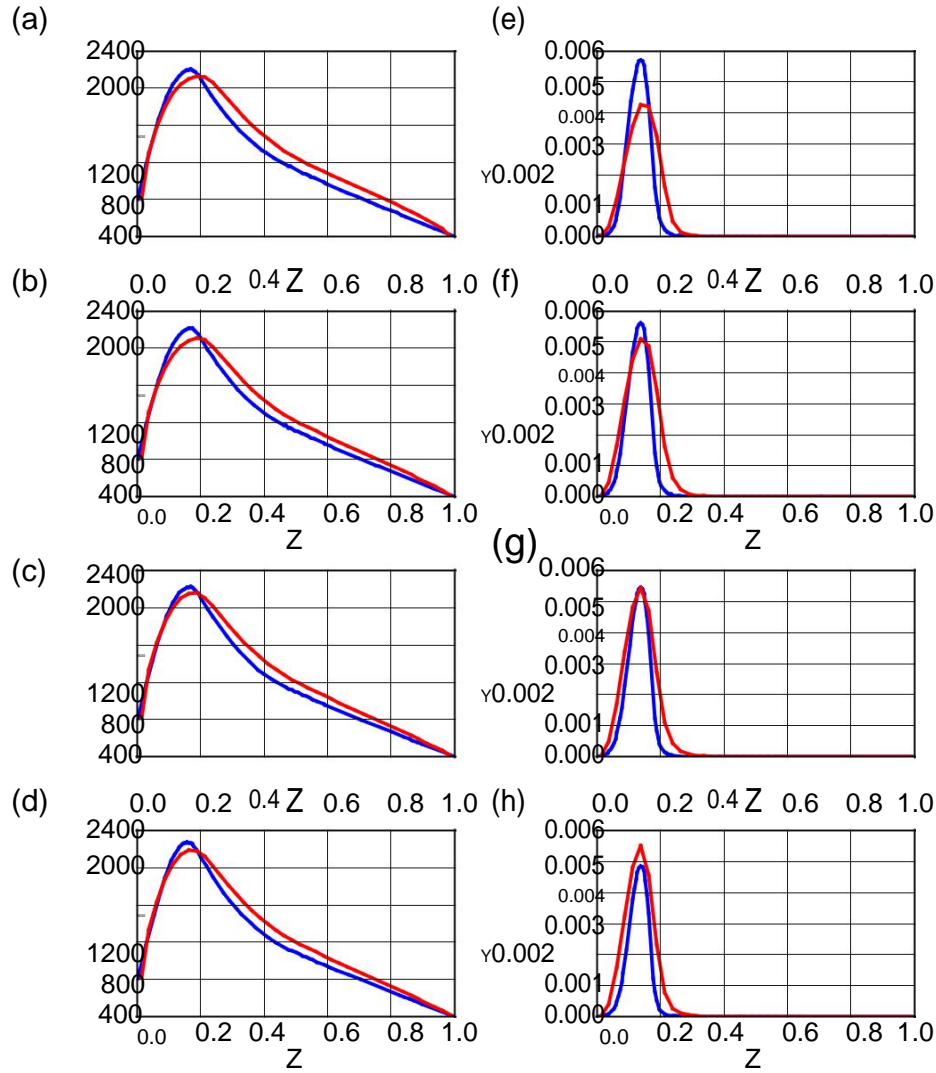


Figure 66: Comparison of mean statistics, conditioned on mixture fraction Z , of the finite-rate chemistry DNS (red) and reduced-order DNS using the FPV model (blue). The left column shows results for temperature T (in Kelvin) at (a) 5 ms (b) 10 ms (c) 15 ms (d) 20 ms. The right column shows results for the mass fraction of OH, Y_{OH} , at (e) 5 ms (f) 10 ms (g) 15 ms (h) 20 ms.

not reproduced in either of the reduced-order DNS results. This may be an artifact of the initially specified equilibrium chemistry profile. However, this appears to be a transient effect, since by 10 ms the peak PAH mass fraction has fallen by more than fifty percent. While the transport equation model underpredicts the magnitude of PAH mass fraction, it is successful at qualitatively capturing the conditional relationship between PAH amount and mixture fraction. This is a highly significant finding, as it strongly argues that reduced-order DNS data can inform subfilter model development. It is also notable than the relationship between PAH and mixture fraction is not adequately reproduced by the FPV model alone.

The chemical source term (combination of $\mathbf{!}$ and $\mathbf{!}_+$ in Eq. 14) and dimerization sink term ($\mathbf{!}_{\text{dimer}}$ in Eq. 14) are shown in the right column of Figure 67. Both the original FPV chemical source and rescaled transport equation model chemical source show net formation of PAH occurring over mixture fraction values between about 0.25 and 0.45. Between $Z = 0:25$ and $Z = 0:15$, where the latter is the stoichiometric mixture fraction value, PAH is consumed by gas-phase reactions. Thus, PAH that is transported towards mixture fraction values richer than 0.25 persists until it is either transported toward leaner mixture fraction values or forms soot. This helps to explain the model's better agreement with DNS results at later times in the simulation. Because they depend on the square of the PAH mass fraction, dimerization rates are more strongly peaked for the basic FPV model than for the transport equation model over the first 15 ms of the simulation. This result reverses by 20 ms. Furthermore, because Y_{PAH} is higher at very rich mixture fraction, the dimerization rate is also higher. This indicates that soot can form and grow across a broad range of mixture fraction values. In contrast, the FPV model alone will predict that soot nucleation and growth occurs over a much narrower interval of mixture fraction values. Again, this is a significant result for the development of subfilter models.

Confirming the impressions given by these results, Figure 68 shows snapshots of the PAH mass fraction fields predicted directly from the FPV model (the plot on the left-hand side) and from the PAH transport equation model (the plot on the right hand side). For reference, the black lines indicate isolines of $Z = 0:2$ and $Z = 0:6$. While thinner structures of maximum PAH mass fraction are apparent in the field obtained from the FPV model, considerable fine structure is evident in the PAH field obtained from the transport equation model, especially at mixture fraction values greater than 0.6. This fine structure exists despite the very smooth conditional mean, $hY_{PAH}|Z_i$ for the transport equation model shown in Figure 67(c). Since the rate of PAH dimerization is directly related to the second moment of Y_{PAH} , Figure 68 suggests subfilter modeling of the variability of Y_{PAH} may be important for accurate prediction of soot using LES.

D-4 Subfilter Modeling of Soot

Mueller and Pitsch [107] proposed a double-delta subfilter PDF model for soot moments and performed a priori tests on this model using the two-dimensional DNS of Bisetti et al. [99]. The model has subsequently been used in three-dimensional LES computations of sooting flames [96], but the interactions of many different modeling assumptions and numerical approximations in these results preclude attributing any aspect of the simu-

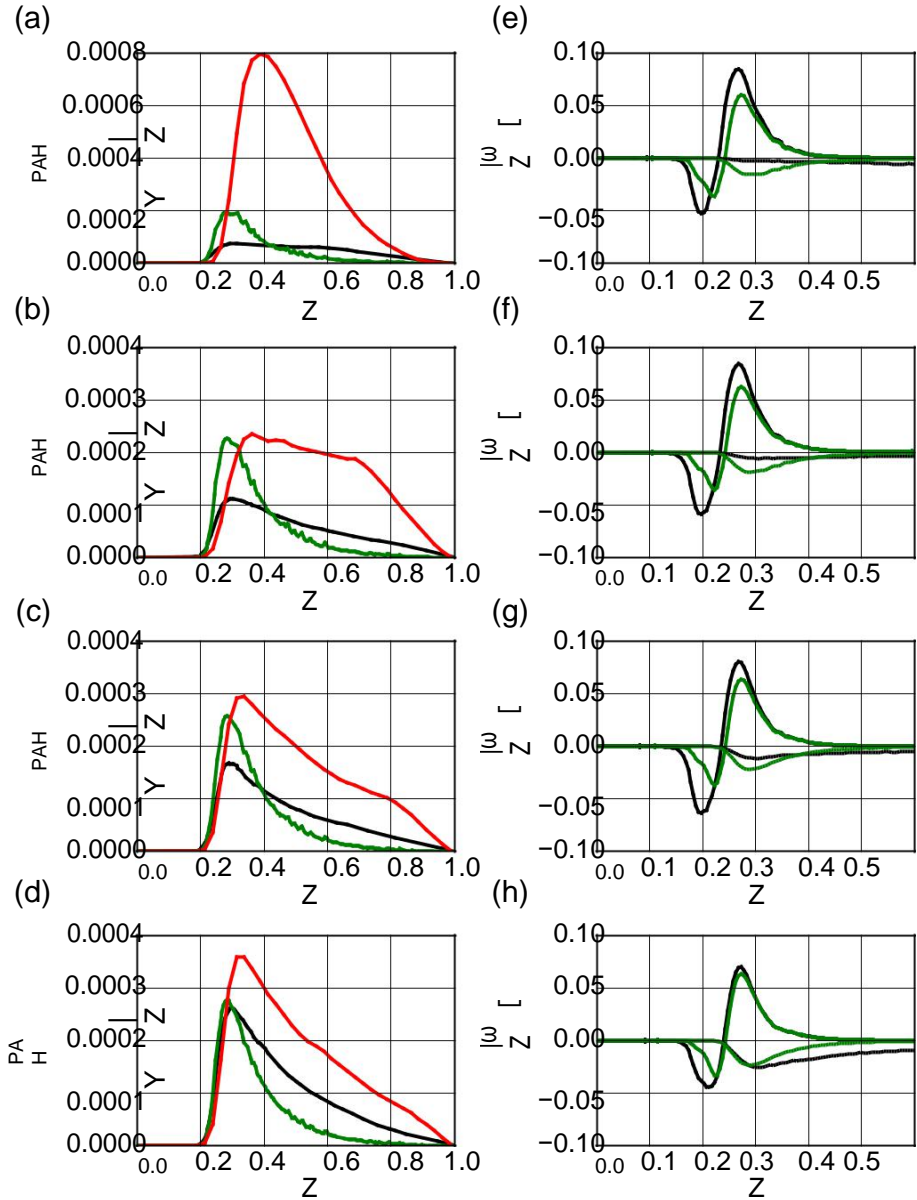


Figure 67: Comparison of mean statistics, conditioned on mixture fraction Z , of the finite-rate chemistry DNS (red) and reduced-order DNS directly using the FPV model (green) and using the PAH transport equation model (black). The left column shows results for PAH mass fraction Y_{PAH} (equivalent to naphthalene mass fraction in the finite-rate chem-istry DNS) at (a) 5 ms (b) 10 ms (c) 15 ms (d) 20 ms. The right column shows results for chemical reaction rate (solid lines) and dimerization rate (dashed lines), both in units of $\text{kg}=\text{m}^3=\text{s}$ at (e) 5 ms (f) 10 ms (g) 15 ms (h) 20 ms.

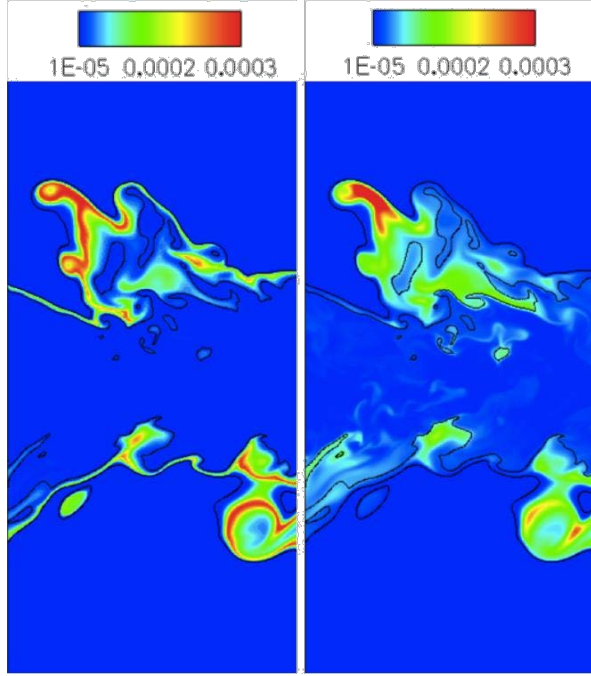


Figure 68: Contour plots of PAH mass fraction from the reduced-order DNS simulation at 15 ms. (Left) direct evaluation of Y_{PAH} from the FPV model (Right) Y_{PAH} obtained using the PAH transport equation model. The black lines indicate isolines of $Z = 0:2$ and $Z = 0:6$.

lation results to the soot subfilter model. Given the lack of conclusive evidence from LES-based testing of the model and noting the significant dissimilarities in the physics of two-dimensional and three-dimensional turbulence, it is important to re-evaluate the model using three-dimensional DNS data.

The results shown in this section use reduced-order DNS data, but the simulation differs slightly from that discussed in Section D-3. A temporal jet configuration is again considered, but the fuel stream is composed, by volume, of seventy-five percent n-heptane and twenty-five percent toluene (a single ring aromatic with chemical formula C_7H_8), rather than diluted n-heptane as in the previously discussed simulation. The lack of nitrogen dilution and the presence of a significant amount of an aromatic species results in higher soot yields. Both the fuel and air streams are initially at 300 K. Additionally, the change in fuel composition reduces the stoichiometric mixture fraction from approximately $Z = 0:15$ to $Z = 0:06$. This means that stoichiometric mixture fraction contour is shifted within the jet shear layer, affecting the intensity of the turbulence “seen” by the soot particles as they reside at various values of mixture fraction. This has potentially interesting implications since different values of mixture fraction can be associated with the dominance of different soot growth mechanisms.

The initial velocity difference between the fuel and air streams is 10 m/s. Initial velocity fluctuations are imposed on the jet core based on an isotropic turbulence spectrum and

are smoothly filtered to zero in the oxidizer stream. The simulation domain is 12H 12H 6H in the streamwise, cross-stream, and spanwise directions, respectively, where H is the jet width. It was verified that this domain size was several times larger than the integral length scale of the turbulence and five to six of the largest turbulence structures could be accommodated by the streamwise domain extent. This attention to domain size was motivated by the importance of ensuring that a too-small domain did not impose an effective two-dimensionality on the nominally three-dimensional flow.

D-4.1 Double-delta PDF model

The relevant aspects of the formulation of the double-delta PDF model are briefly reviewed here, with complete details given in the original source [107].

If the LES soot model computes the soot moment source terms based on the filtered values of the moments, this can be viewed as the no subfilter model case or, alternatively, as a model in which the subfilter PDF is presumed to be a delta function. This can be expressed symbolically as

$$P(M_i) = M_i \ M_i^g : \quad (16)$$

Mueller and Pitsch [107] instead assume a bimodal distribution using two weighted delta functions. This subfilter model can be written as

$$P(M_i) = ! (M_i) (1 - !) (M_i - M_i) : \quad (17)$$

where $!$ is here the probability of the nonsooting mode and should not be confused with the source terms discussed in Section D-3. Using the definition of M_i^g as the mean value of M_i associated with the subfilter PDF, the location of the sooting mode M_i is found to be

$$M_i = M_i = (1 - !) \quad (18)$$

using the definition of the second subfilter moment, $!$ is determined from

$$\text{Then } ! = 1 - \frac{\frac{g}{M_{xy}^2}}{\frac{g}{M_{xy}}} : \quad (19)$$

Any of the soot population moments solved for by HMOM (and the second moment [with respect to the subfilter PDF] of that soot moment) could be used for computing $!$, but using M_{00} , the total number density, appears to give the best results [107]. However, the assessment of the best choice for computing to $!$ may depend on the quantities being considered and whether they are most sensitive to the total number, total volume, or total surface area of soot particles.

D-4.2 A priori evaluation results

The double-delta PDF model given by Eqs. 17-19 is evaluated by filtering the soot moment fields obtained from the reduced-order DNS simulation using a box filter. The box

filter halfwidth is eight times the grid spacing and the data is accordingly spatially down-sampled in the ensuing analysis. Additionally, filter volumes where the total amount of soot is negligibly small are not considered in the analysis. However, this still leaves a large number of data points in the analysis so to enhance the clarity of the figures the data is further randomly downsampled in the construction of the scatter plots. The results shown here are for the option of computing \bar{I} based on the total number density moment, M_{00} . Results are shown at two different times in the simulation, 7 ms and 14 ms.

Figure 69 compares the subfilter intermittency predicted by the double-delta model to the exact value computed from the DNS. The subfilter soot intermittency \bar{I} is a quantity defined as the probability of finding a volume fraction of soot lower than 0.1 parts per billion (ppb) within the filter volume [107, 108]. Thus, it is closely related to the conceptual picture of a sooting and non-sooting mode on which the double-delta subfilter model is based.

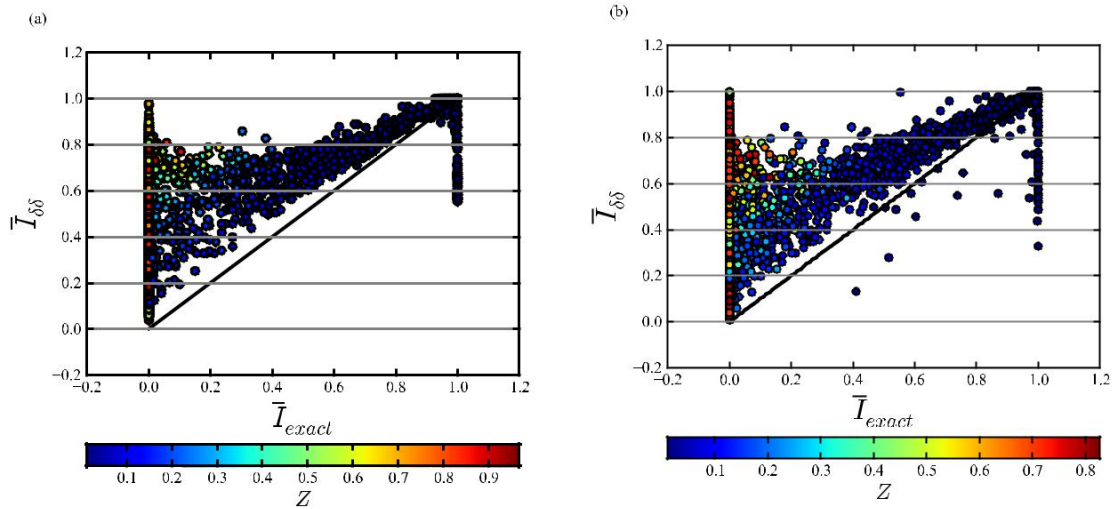


Figure 69: Comparison of soot intermittency using the double-delta model to the exact value at (a) 7 ms (b) 14 ms. Markers are colored by the value of mixture fraction. The solid line indicates a 1:1 relationship.

The results in Figure 69 show that at both 7 ms and 14 ms the double-delta model has a strong bias towards overprediction of the subfilter intermittency except when true subfilter intermittency is close to one. This can be associated with a situation in which the entire filter volume has a distribution of volume fraction values everywhere close to, but below, the intermittency threshold of 0.1 ppb and not totally uniform. Thus, \bar{I} is nonzero and the double-delta model forces some of the probability weight to be associated with the non-sooting mode. To maintain the correct prediction of the filtered moments, the location of the sooting mode is forced to a higher value exceeding the intermittency threshold. The filter volumes associated with this behavior are located at low values of mixture fraction, at or below the stoichiometric value of $Z = 0.06$. At these mixture fraction values, soot overwhelmingly tends to be destroyed through oxidation rather than to grow, so this

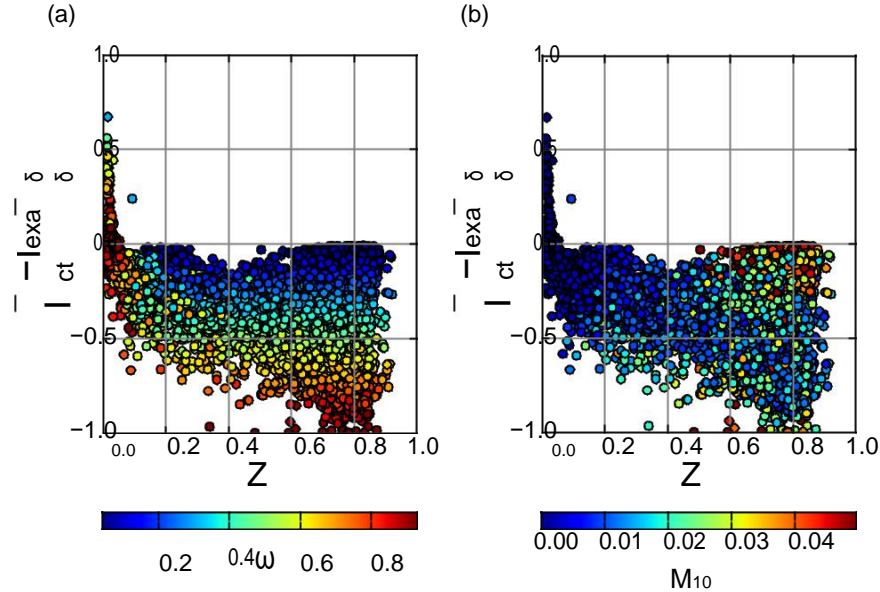


Figure 71: Same as Figure 70, but for results at 14 ms.

ranging from zero to nearly one were found across almost the entire range of mixture fraction values. This result appears to contrast with that of Mueller and Pitsch [107], whose analysis found the single-delta model to give clearly inferior predictions of intermittency. While part of the difference in the results could be explained by differences in the analysis method and filterwidths analyzed, it seems likely that significant differences exist between the structure of the soot moment fields in two- and three-dimensional turbulence. Further analysis is needed, looking at the source terms of the soot moments themselves and considering a broader range of filterwidths, flow geometries, and fuel compositions, but these preliminary results intriguingly suggest that the choice of soot subfilter model presumed form might itself need to be conditioned on the mixture fraction value or on quantities like omega, with a blend of the single and double delta models perhaps giving better performance than either model alone can yield.

A few comments are needed before leaving this section. First, the overprediction of intermittency by the double-delta model may actually be less severe than it appears if we consider physical soot fields rather than those obtained from DNS. As remarked in Section D-1, the soot moments are high Schmidt number scalars that are inevitably some-what underresolved on a DNS mesh geared towards resolution of the gas-phase. We are investigating the ability of Lagrangian particle-based numerical methods [100] to alleviate this problem. Second, issues of computational convenience strongly influence the kinds of subfilter PDF models that can feasibly be used for the soot moments. For gas-phase scalars in LES, the convolution of the flamelet solutions with the scalar subfilter PDFs (such as the beta PDF for mixture fraction) can be performed during the construction of the flamelet lookup table, allowing arbitrarily complex PDFs to be used. However, the convolution of the soot moment source terms and subfilter PDFs cannot be easily pre-

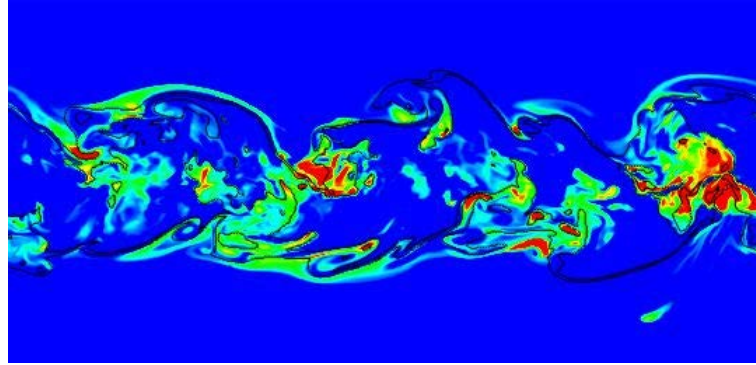


Figure 72: Contour plot of volume fraction, with red areas corresponding to volume fractions greater than 0.5 parts per million. Isolines are shown for mixture fraction values of $Z = 0:6$ and $Z = 0:8$.

computed making simple PDFs based on delta functions highly attractive. Nevertheless, it may be possible to use PDF forms from the exponential family of distributions by exploiting properties of the corresponding families of orthogonal polynomials, similar to the method used in the recently developed Extended Quadrature Method of Moments [109].

E. Large Eddy Simulation of Soot Formation in Model Aircraft Combustors

Modern aircraft combustors operate at pressures ranging from 20 atm (civilian) to 40 atm (military) [110], with a gradual push towards higher operating pressures to increase efficiency. Due to increasing environmental concerns of particulate emissions as well as the tactical risk of detection posed by these particles, there is a need to understand the basic soot evolution mechanisms in such gas turbines. In laminar diffusion flames, soot yield is known to scale as P^n , where n can be 1-3 based on the fuel used. McCrain and Roberts [111] show that for ethylene/air flames, the peak soot volume fraction scales with pressure as $P^{1:7}$. Prior studies have mostly concluded that increase in density and accelerated fuel pyrolysis due to air entrainment near the burner are the main causes for increase in soot formation [110, 112, 113]. Simulations show that the dominant mechanism for soot generation changes with pressure, with surface condensation the main contributor at low pressures and surface growth becoming more important beyond pressures of 6 atm [114]. While these studies explore the influence of soot kinetics on particulate generation, modern gas turbines operate predominantly in the turbulent flow mode, where a large range of length and time scales impact soot processes. Under these conditions, it is important to determine the combined effects of hydrodynamics and soot kinetics. The objective of this work is to use high fidelity and fully validated numerical tools to understand the flow dynamics that impact soot formation inside a model combustor at elevated pressures.

In aircraft engines, soot particles arise predominantly from inefficiencies in fuel-air mixing. In liquid-fueled gas turbines, the nonuniform dispersion and evaporation of droplets

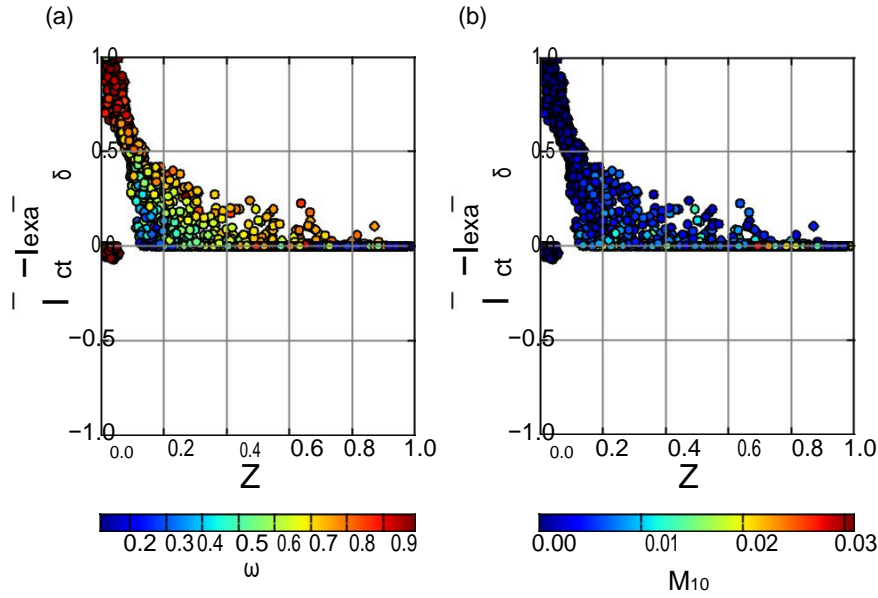


Figure 73: Error in soot intermittency prediction using the single-delta () subfilter pdf for the soot moments plotted against the mixture fraction value Z . The same points are shown in both plots, but different variables are used to color the points: (a) ! (from the double-delta model) (b) M_{10} . Results are shown at 7 ms.

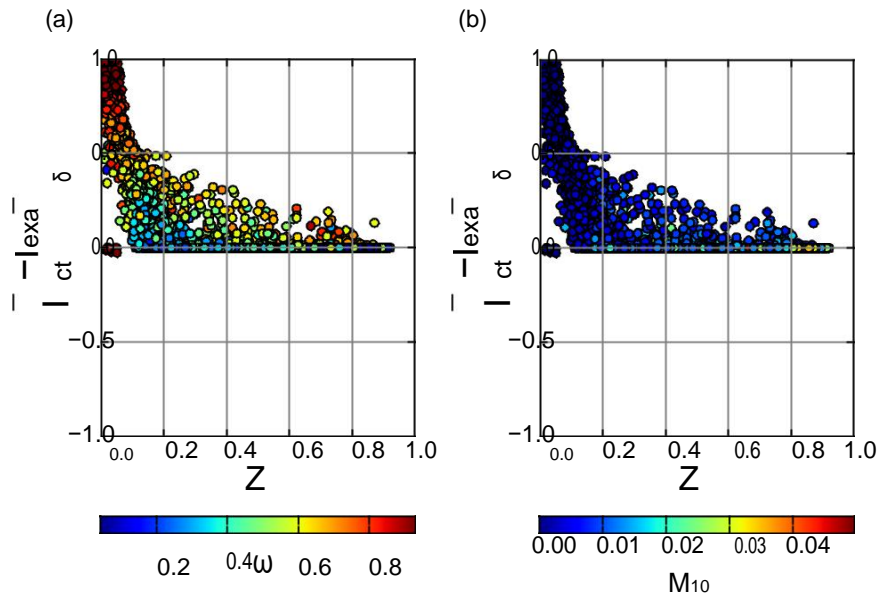


Figure 74: Same as Figure 73, but for results at 14 ms.

can create locally fuel-rich zones that promote soot generation. However, most of these combustors operate at globally lean conditions, and the presence of excess and high-

temperature air can quickly oxidize soot particles. Due to the chaotic nature of the turbulent flow, neither the formation of fuel-rich pockets nor soot oxidation can be fully controlled, leading to particulates exiting the combustor. Most gas turbines use swirl-stabilized primary combustion zones that contain a large recirculating core flow. These zones are also associated with long residence times compared to the mean flow-through time through the combustor. Since carbon conversion scales with residence time due to the slow nature of soot-related processes, the presence of such regions is thought to aid particulate formation. For instance, Mueller and Pitsch [115] show that soot formation occurs in the vortex core of such combustors, where inhomogeneous fuel entrainment leads to fuel-rich pockets.

Another defining feature of soot generation in engines is intermittency [116]. Since soot precursors are extremely sensitive to local strain rates [117], inception of soot is a sporadic event that depends on the time-history of the fluid element. The effect of hydrodynamics in the subsequent growth and oxidation processes is more complex. If particle growth is through condensation, the availability of gas-phase PAH molecules will also be affected by local strain variations. On the other hand, acetylene-based surface growth is not as sensitive to strain [117], but the concentrations of the gas-phase species still depend on the trajectory of the soot particles. This is similar to oxidation, which again depends on the soot particles being transported through fuel-lean mixtures. In general, only a very limited region of the gas-phase composition space promotes soot growth (as will be shown later here also). Consequently, only trajectories that spend an appreciable time in this region lead to significant soot mass. Since turbulent flow generates a large number of such trajectories, the probability of traversing a soot-favorable path is rather low. This effect is seen in experiments, where the average soot volume fraction (time-averaged) is much lower than instantaneous values [1, 118, 119]. In these experiments, an intermittency factor has been defined, which has a value of 1 when there is no soot. For example, in one turbulent jet sooting flame [118], time-averaged intermittency was reported to be 0.97, implying that only 3 frames out of 100 contained appreciable soot volume fraction in the LII measurements.

In the context of elevated pressure operations, the impact on hydrodynamics is dependent on the flow features of interest. Increase in pressure increases chemical reaction rates and will change the location and shape of the primary combustion zone. In addition, the concomitant increase in Reynolds number will affect turbulent mixing and flow structure, thereby altering soot particle trajectories inside the combustor. Increase in Reynolds number is also associated with increase in small-scale strain rates, which could affect soot precursor concentrations [117]. Based on this discussion, it can be inferred that soot formation in engines involves a complex interaction between hydrodynamics and soot physics.

To understand such complex systems, a combination of high-fidelity experiments and simulations is needed. In this regard, the use of large eddy simulation (LES) for such unsteady and complex reacting flows has been found to be useful in understanding the key physical interactions. LES has been applied to a number of simulations of gas turbines [115, 120–122]. Similarly, LES combined with detailed soot models has been shown to

predict canonical laboratory flames reasonably well [119, 123–125]. On the experimental side, Geigle et al. [1, 126–128] have studied gas turbine combustors experimentally with high-fidelity diagnostics for a range of operating pressures, referred to as DLR combustor here. The flow conditions have been chosen such that the increase in pressure increases Reynolds number and the soot as well as gas-phase kinetic rates, but the large scale strain rates are preserved by retaining the same inflow velocities for the different cases. This configuration provides an ideal flow system for understanding pressure effects in aircraft-like combustors. Previously, Eberle et al. [129] have conducted unsteady-RANS calculations of the same geometry using detailed models for PAH and soot formation. They simulated a 3-bar case and showed that soot volume fractions were overpredicted, but the overall gas-phase fields were captured reasonably accurately.

With this background, the focus of this work is to understand the predictive capability of LES-based soot models for the DLR combustor, focusing on the interaction between the turbulent flow field and soot evolution. For this purpose, the models developed by Mueller and co-workers [130–132] will be used in the simulations. Two different pressure conditions will be considered. Additionally, the impact of mesh resolution on capturing key flow field dynamics will be evaluated. The effect of flow structure and intermittency on soot formation will be studied.

E-1 DLR atmospheric pressure swirl combustor

E-1.1 Simulation Configuration and Numerical Details

The experimental configuration [1] replicates an aircraft engine by fuel being introduced between swirled oxidizer jets. Further, a set of injection ports located on the side walls is used to replicate secondary air injection in rich-quench-lean type aircraft engines. The ethylene-based combustor operates at a global equivalence ratio of roughly 1:5, which, for this fuel, is located very close to the maximum soot forming region. The use of the secondary injection ports reduces the global equivalence ratio to 1:15. Three cases are studied: a non-reacting flow case, and a case with and one without secondary injection.

Figure 75 shows the computational mesh used in this work, and is similar to the mesh used in [121]. The number of computational volumes was 5-7 million based on the cases studied, with the secondary injection grid requiring refined grid near the injection ports. The main combustor itself is geometrically simple, but the inflow ducts that pass through the swirler require detailed calculations. It was found that the flow profile at the exit of the inflow nozzles into the combustor directly affects the size of the recirculation zone and the stability of the combustion processes. For this reason, several grids were used to understand the impact of numerical discretization on the spatial evolution of the swirling flow. The computational mesh used here was found to provide the best performance with minimal grid resolution.

The mesh quality is further assessed and plotted in Fig. 75 using Pope's criterion [133, 134]. Here, M is defined as the ration between the residual (sub-filter) kinetic energy and

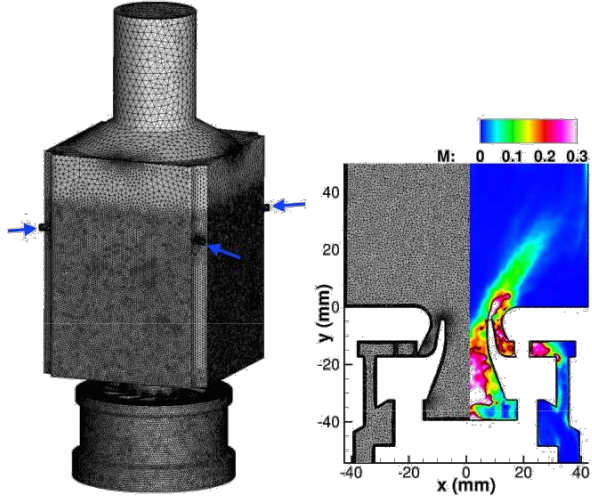


Figure 75: (Left) Full three-dimensional grid with secondary inlets marked, (right) The center plane mesh with Pope's criterior. $M = 0:2$ along the solid lines.

the total kinetic energy.

$$M = \frac{k_{\text{resid}}}{k_{\text{resol}} + k_{\text{resid}}} ; \quad (20)$$

where the residual kinetic energy is obtained using the scaling relations provided in [133]. While some portions of the inflow region is not adequately resolved, the mesh quality is acceptable in the primary flame region. More importantly, further refinement did not affect the statistics of the gas-phase flow field. Hence, it is argued that this mesh is adequate for the purposes intended in this work.

The combustion chamber is 110 mm in length, and spans a cross-section of 85 mm 85 mm. The inflow air swirls through the complex passages in the injector section, and mixes with fuel in the chamber. The fuel is injected through a round-shape slit with a size of 0.347 mm between air streams that pass through two different swirlers. The air mass flow rate incoming from the bottom swirlers is 3.2267 g/s, and the fuel stream mass flow rate is 0.3283 g/s. Secondary oxidizer streams are injected with a mass flow rate of 0.96667 g/s through four 3.5 mm diameter additional ducts at two-thirds the height of the chamber. Reactants are finally exhausted through a circular tube at the top to atmospheric pressure.

The detailed chemical mechanism of Blanquart et al. [135] extended by Narayanaswamy et al. [136] is used to construct the flamelet library. Some of the parameters required to calculate soot moment sources are also stored in the library. Locations of the progress variable and several coefficients of soot evolution sources are plotted in mixture fraction (Z) and progress variable (C) space in Fig. 76. Soot production through dimer occurs at a fuel rich condition, and so does the growth through surface reaction. Meanwhile, soot oxidation is maximized in fuel lean regions. Note here that stoichiometric condition is at $Z = 0:064$ for an ethylene-air combustion. The LES computations are performed on

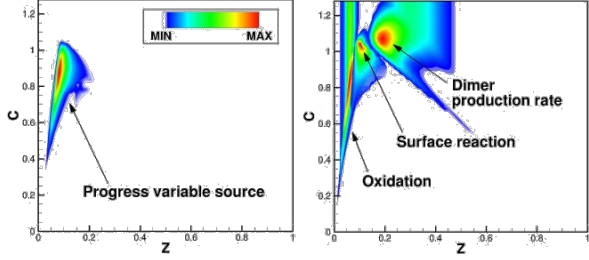


Figure 76: Flamelet solutions showing (left) progress variable source term and (right) key soot chemistry source terms.

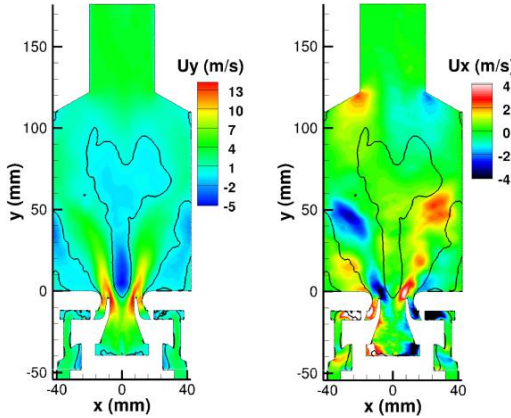


Figure 77: Mean axial (U_y) and tangential (U_x) velocity contours from LES. The axial velocity is zero along the solid lines.

512 cores, with each simulation taking roughly 200 hours. With a maximum allowed CFL of 1.5, the time-step size is approximately 1.5 s. Statistics were collected over ten flow-through times, defined based on the inflow bulk jet velocity and the chamber height. Soot statistics presented in the results section are averaged in the four homogeneous directions from the centerline normal to the side walls.

E-1.2 Non-reacting Flow Case

To ensure that the LES solver captures the general flow structure reasonably well, a non-reacting flow simulation was conducted. The corresponding experimental conditions are provided in [137]. The air mass flow rate is 4.68 g/s at the bottom of the swirlers, with air being injected through the fuel injection slit with a mass flow rate of 0.362 g/s. The upstream temperature of the fluid maintained at 330K [138]. The experimental data includes statistical averages of axial and tangential velocity measurements.

Figure 77 shows mean axial and tangential velocity contours. The algorithmic modifications made in this work led to tangential swirl angles that were consistent with experimental data. In particular, the injection angle was higher than corresponding angle in our earlier work [121]. Similarly, the axial velocities provide the high velocity region near

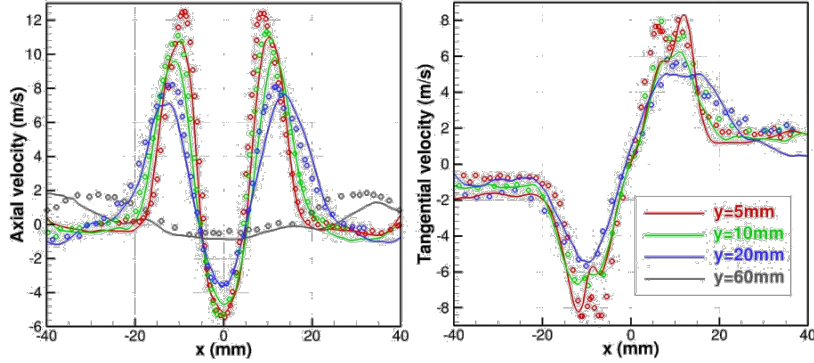


Figure 78: Mean axial and tangential velocities from LES (solid lines) compared to experimental data (circles) at different axial locations.

the walls that is essential for separating the inner recirculation region (located near the center of the combustor) and the outer recirculation zone (between the high-velocity region and the wall). This structure is also important for predicting the flame stabilization process (discussed below). Direct comparison with PIV data is shown in Figure 78, where line data extracted from the 2D images shown in Fig. 77 are compared with PIV data. It is seen that the simulations predict very well the flow structure found in experiments. In particular, the sharp peaks in velocity profiles (both components) are well captured, providing high confidence in the accuracy of the solver.

E-1.3 Reacting Flow Cases

The reacting flow cases comprise of two simulations, with and without secondary air injection. Below, gas phase data is analyzed first followed by the soot data.

E-1.3.1 Gas Phase Results Figure 79 shows the axial velocity comparison for the two cases (with and without secondary injection). As seen, the simulations are able to predict the flow structure reasonably well, including the injection velocity angle from the swirl nozzles. Similar agreement was found for the tangential component (not shown here). It should be noted that the inner recirculation region has expanded due to the heat release from combustion. For the case with secondary injection, the simulations predict a weaker inner recirculation region, but the overall structure is roughly the same as in the case without secondary injection.

Figure 80 shows the time-averaged mixture fraction and temperature fields. Stoichiometric mixture fraction for this fuel is roughly $Z_{st} = 0:064$. Without secondary air injection, the mixture fraction values in the inner recirculation zone are much higher than this value, promoting the formation of soot. In the case with secondary injection, the soot-favorable mixture fraction is confined to the narrow shear layers between the inner and outer recirculation zones. The temperature profiles show that the bulk of the combustor exhibits near-uniform temperature in the case without secondary injection. But with the secondary jets, the temperature profile exhibits “cool” spots where the side jets interact.

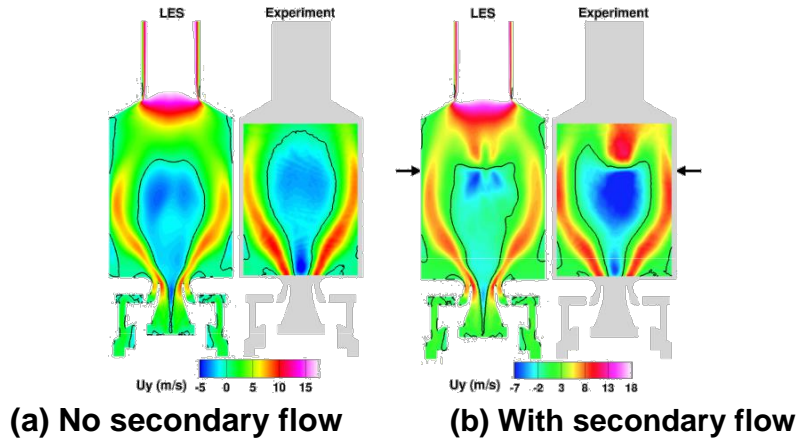


Figure 79: Mean axial velocities for the case with and without secondary injection, compared to the experimental PIV data [1]. The axial velocity is zero along the solid lines.

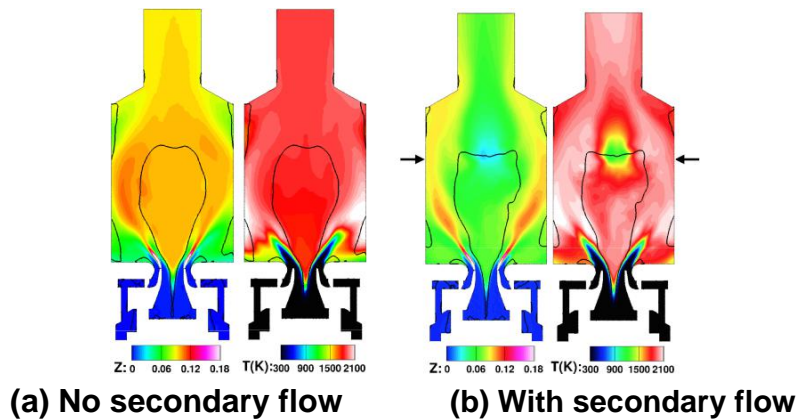


Figure 80: Mean mixture fraction and temperature fields.

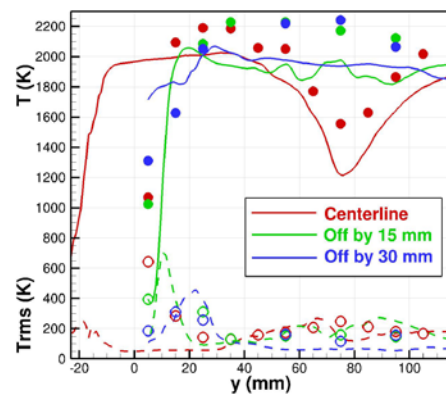


Figure 81: Mean and RMS temperature profiles along the centerline and two off-center axial lines for the case with secondary air injection. Solid lines and filled circles are mean temperature profiles, while dashes and empty circles are RMS values, respectively.

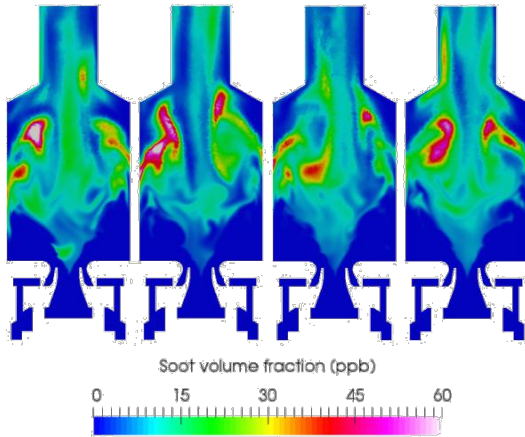


Figure 82: Instantaneous soot volume fraction snapshots at the center plane every 8 ms for the case without secondary injection.

The time-averaged mean and RMS temperature profiles are compared to experiments in Fig. 81. It is seen that the simulations predict the drop in temperature near the centerline due to the secondary air jets. However, the centerline temperature profile shows higher peak near the burner surface, indicating that the inner recirculation zone anchors the flame. However, in the experiments, the temperature drops significantly close to the nozzle exit, implying that the flame location is lower than in the experiment due to the stronger vortex near the bottom wall. The RMS profiles are predicted at levels close to the experiment, but with the reduced mean temperature profiles, this actually implies a higher level of turbulent fluctuations than in the experiments. Regardless, considering experimental uncertainties as well as the non-density weighted experimental data, the agreement is reasonably accurate.

E-1.3.2 Soot Volume Fraction Results Figures 82 and 83 show instantaneous soot volume fraction contours at several different time instances. Soot exhibits highly intermittent behavior, with peak soot values observed only sporadically. These sporadically-formed soot structures in Figs. 82 and 83 are qualitatively similar to the small scale soot filaments reported in the experiment [1]. Note that the inner recirculation region has the right gas phase conditions to generate soot almost continuously, and thus provides a baseline soot generation region. However, the majority of the soot is generated in regions close to the wall where the inner and outer recirculation zones merge. Here, low strain rates combined with low velocities and high temperatures promote soot growth. When secondary jets are present, soot production is significantly reduced. This is due to two reasons. First, the mixture fraction in the inner recirculation region falls below the critical value needed to generate soot. At the same time, presence of excess oxygen quickly oxidizes soot at these high temperatures.

Comparison of soot volume fraction statistics (Figs. 84 and 85) show that the simulations are able to predict the sooting tendencies of both cases reasonably accurately. Compared to canonical jet flame calculations [139, 140], the level of agreement is very good in this

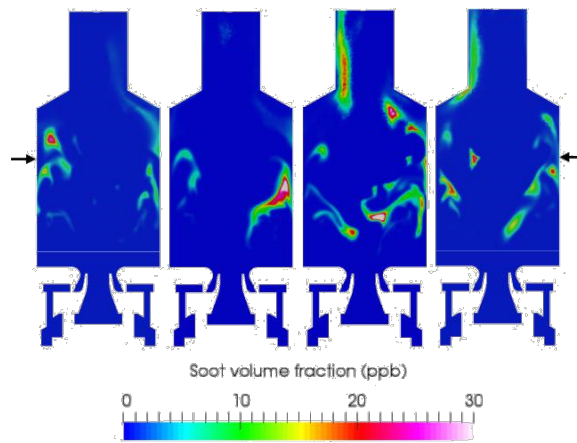


Figure 83: Instantaneous soot volume fraction snapshots at the center plane every 8 ms for the case with secondary injection.

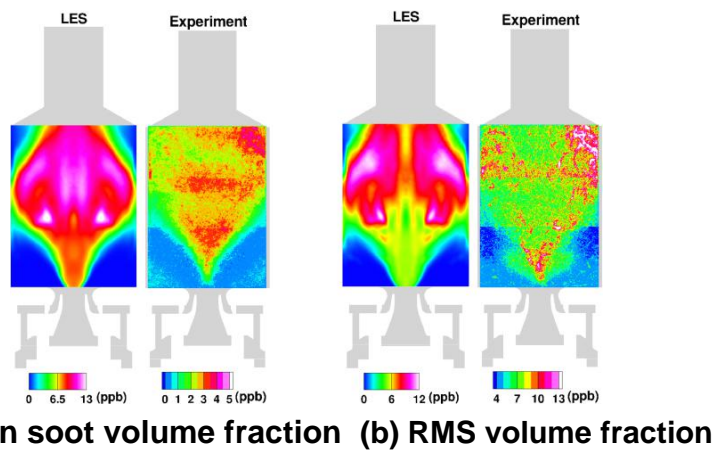


Figure 84: Soot volume fraction statistics for the case without secondary air injection com-pared to the experiment.

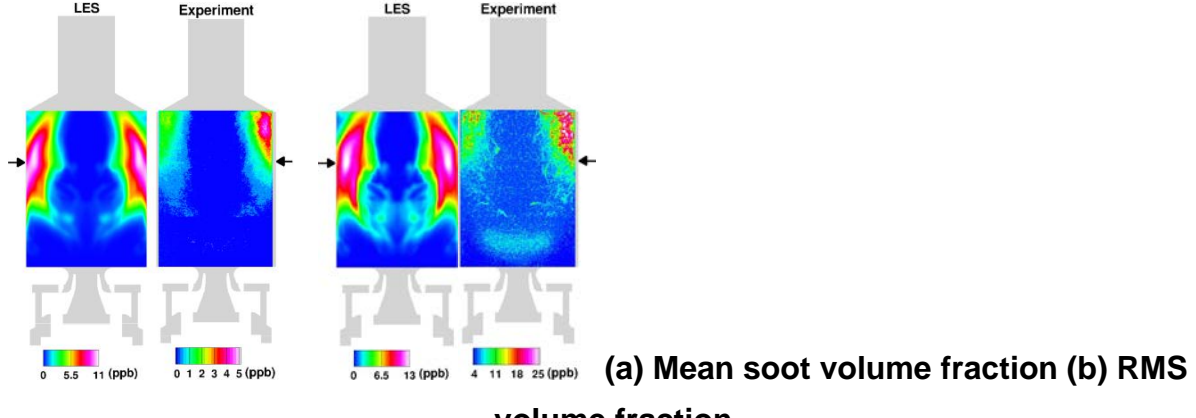


Figure 85: Soot volume fraction statistics for the case with secondary air injection compared to the experiment.

geometry. In particular, the ability to predict RMS soot distribution is very promising. As expected, soot volume fraction decreases substantially when the secondary jets are present. This is a combined effect of a lower equivalence ratio and the jet momentum of the secondary air flows. In both cases, the RMS soot volume fraction is comparable in magnitude to the mean, further emphasizing the role of intermittent soot generation. In the case with secondary injection, there is an asymmetry in soot profiles due to the placement of the secondary jets on the side walls, which is also captured well by the experiments. In the case with no secondary injection, the inner recirculation zone appears to be the main source of soot generation. It is unclear if such a large variation in the flame structure is present in practical gas turbines as well.

E-2 DLR High Pressure Combustor Configuration

The ethylene fueled DLR model aircraft combustor configuration is shown schematically in Fig. 86 [126, 127]. The oxidizer air is introduced in two streams, through a central nozzle with a diameter of 12.3 mm and a ring injector with inner and outer diameters of 14.4 mm and 19.8 mm. The inflow consists of an intricate set of swirlers to inject both oxidizer jets with tangential velocities. The fuel ports consist of 60 straight channels ($0.5 \times 0.4 \text{ mm}^2$) and are located between these two streams. A set of injection ports are located on the sidewalls that introduce secondary air similar to the rich-quench-lean design for air-craft combustors. For the studies discussed below, only experiments with no secondary air injection are considered. The main combustion chamber measures 120 mm in height and has a square cross-section of $68 \times 68 \text{ mm}^2$.

Two different cases are discussed in this work and correspond to the flow conditions provided in Table E-2. The two cases correspond to pressures of 3 and 5 bar with increasing mass flow rates of fuel and oxidizer. The ratio of mass flow rate between the central and ring air inlets was fixed at 3/7. However, the velocities of all the streams (including the fuel) are roughly unchanged for the different pressure cases, which implies that the large scale strain rates are similar but the Reynolds number increases across the cases. Broadly

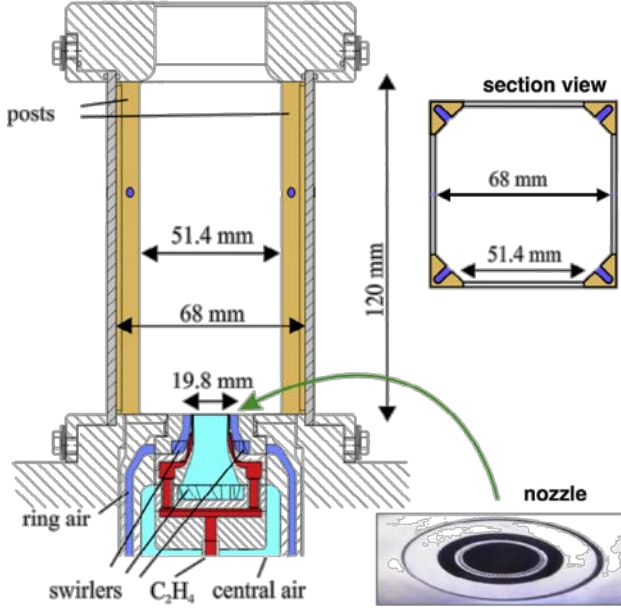


Figure 86: Burner geometry, nozzle details, and cross sections at the height of oxidation air injection and the middle of the chamber.

speaking, this retains the integral time scale that controls residence time in the reactor but reduces the small-scale mixing time scale. Detailed experimental data is available for the cases considered here.

P (bar)	$Q_{\text{central air}}$ (slpm)	$Q_{\text{ring air}}$ (slpm)	Q_{fuel} (slpm)	global
3	140.8	328.5	39.3	1.2
5	234.2	546.2	65.4	1.2

Table 19: Flow parameters used for the simulations. global indicates the global equivalence ratio for these inflow conditions.

E-2.1 Model and Simulation details

The DLR combustor is computed using the LES approach. The gas-phase combustion is described using a flamelet-progress variable approach [141], where a set of unsteady one-dimensional flamelets are tabulated for look-up in the computation. To account for radiation effects, enthalpy loss is also included in the flamelet approach [130]. A bivariate distribution with volume and surface as the internal coordinates is used to track the soot population. The evolution equations and associated rates are based on the model developed by Mueller [131, 132, 142]. The number density is described in terms of a finite set of moments [131], which are solved in the filtered form along with the gas-phase mass, momentum, and flamelet-related variables. The nucleation model is based on dimerization

[143], while soot growth is through surface growth [144] as well as PAH condensation [131].

The LES equations for soot moments and scalar fields are implemented in OpenFOAM [145]. OpenFOAM is an operator-based C++ codebase for solving partial differential equations, which has been applied to a number of combustion systems [146–148]. However, the baseline codebase had to be substantially modified to ensure accurate evolution of the LES equations. Due to the low speeds within the combustor, a low-Mach number assumption is used [149], which requires solution of a pressure Poisson equation at each time-step. Further, it decouples the influence of pressure from the energy field. Consequently, even when primary variables such as mass and momentum are conserved, derived quantities such as kinetic energy may not be conserved in the limit of zero viscosity. In structured-grid solvers that use staggered positioning of velocity and pressure variables, secondary conservation can be ensured by specific choice of divergence and gradient operators [150–152]. In fully unstructured mesh solvers, such as the one used here, a collocated variable approach is used, which prevents exact secondary conservation of kinetic energy. In general, minimally dissipative schemes are sought in order to reduce the effect of kinetic energy loss on flow evolution. Here, the variable density scheme of Morinishi [153] is used. The fluxes at the cell faces are computed using a second-order interpolation scheme. The governing equations are solved using a semi-implicit approximation that is second-order in time. This approach directly relates energy conservation to temporal convergence of the numerical scheme. To ensure second-order accuracy, a PISO (pressure-implicit second order) scheme is used [154] with at least two inner iterations. This solver was found to provide equal rate of energy dissipation as other staggered-mesh unstructured flow solvers [147]. This new variable density solver, umFlameletFoam [147, 148, 155] is used for all the simulations discussed below.

The gas-phase combustion and PAH formation are handled through a flamelet library using a detailed chemical mechanism including PAH chemistry [135, 136]. The flamelet library was constructed separately for each pressure, and soot source terms related to nucleation, surface growth, condensation, and oxidation were parametrized in terms of the rate coefficients and stored [130]. Figure 87 shows the source term for the reaction progress variable and the dimer production rates at three different pressure including two pressures considered in this study and the atmospheric condition for comparison. It is seen that the progress variable source term scales approximately as $P^{0.65}$, while the dimer production rate, which is a direct indicator of soot nucleation rate, scales approximately as $P^{1.57}$. Other soot related source terms show nearly linear increase with pressure. The pressure sensitivity of dimer concentration is higher than that of [114], where A4 (pyrene) concentration scales as $P^{1.14}$, which is roughly similar to the behavior of nucleation rates in that model. Hence, the current model shows a higher pressure dependence than the mechanism used in [114].

The computational mesh used for this study is shown in Fig. 88. A fully unstructured mesh with tetrahedral cells is used. Near the walls, five layers of prism-shaped pentahedrons are used to capture the boundary layers. The mesh is refined close to the jet exit but is coarser further downstream where the gradients are also smaller. Two mesh resolutions

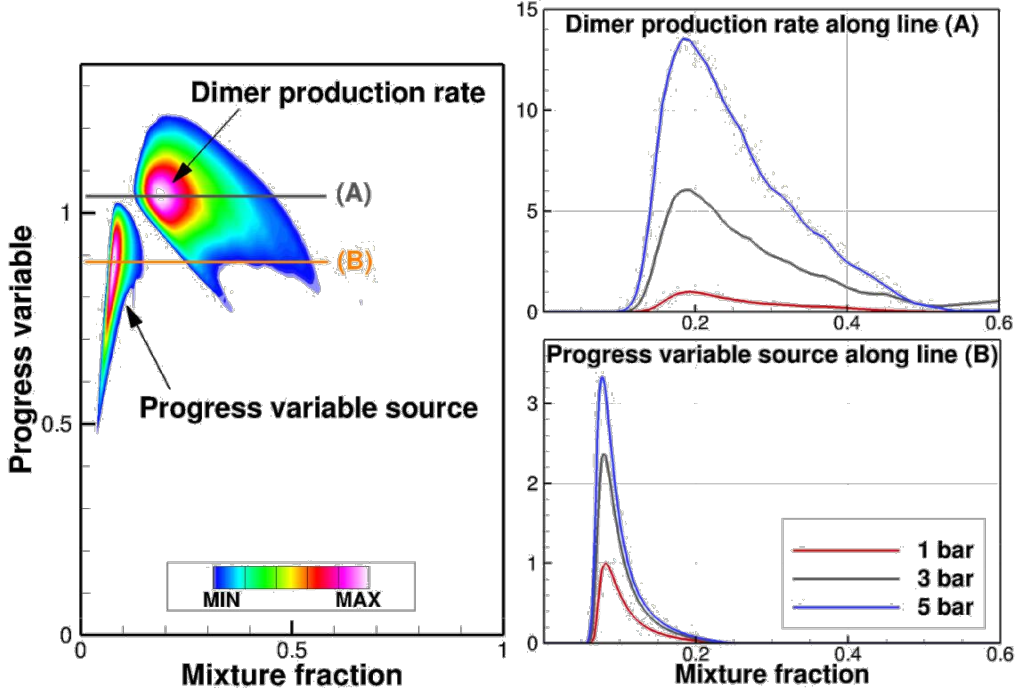


Figure 87: (Left) Dimer production rate and progress variable source from flamelet library; (right) same quantities along lines (A) and (B) normalized by corresponding peak value at 1 bar pressure.

are tested (Fig. 89). On the denser mesh, a refined zone is added on the lower part where flow experiences high shear from multiple inlet ports. The mesh quality is assessed using Pope's criterion [133, 134] and plotted in Fig. 89. While further mesh resolution might be needed along the central air passage below the fuel nozzle, the denser mesh significantly improves the resolution in the primary flame and soot nucleating region. Further refinement did not produce significant change in results. The total number of computational cells was 4.7 and 6.0 millions for the two resolutions.

The LES computations were performed on 512 cores, with each simulation starting from a non-reacting steady state and requiring roughly 100 wall-clock hours to reach steady state. Following this, statistics were collected for roughly 10 flow-through times, computed based on the inflow velocity and the length of the domain. It should be noted that this averaging time is sufficient for gas-phase statistics, such as those related to velocity and thermochemical state, but soot fields take much longer to converge. Consequently, soot statistics provided in the result section (Sec. E-2.2.2) are averaged in the four homogeneous directions from the centerline to the side walls.

E-2.2 Results and Discussion

In this section, gas-phase flow structure is first presented before discussing the soot evolution process.

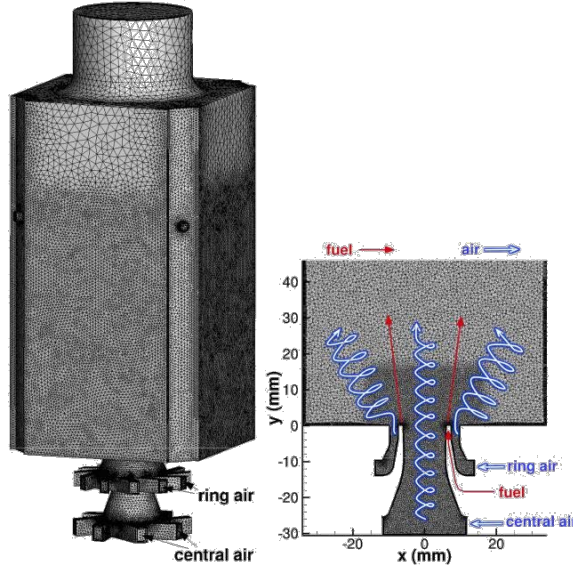


Figure 88: 3D view and a plane view of the lower half of the computational mesh.

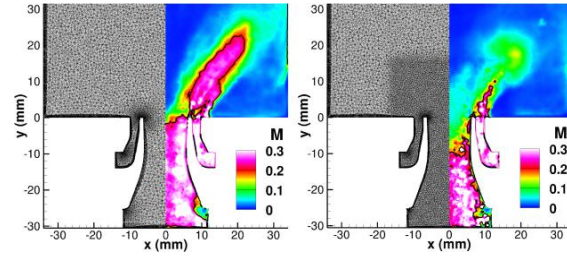
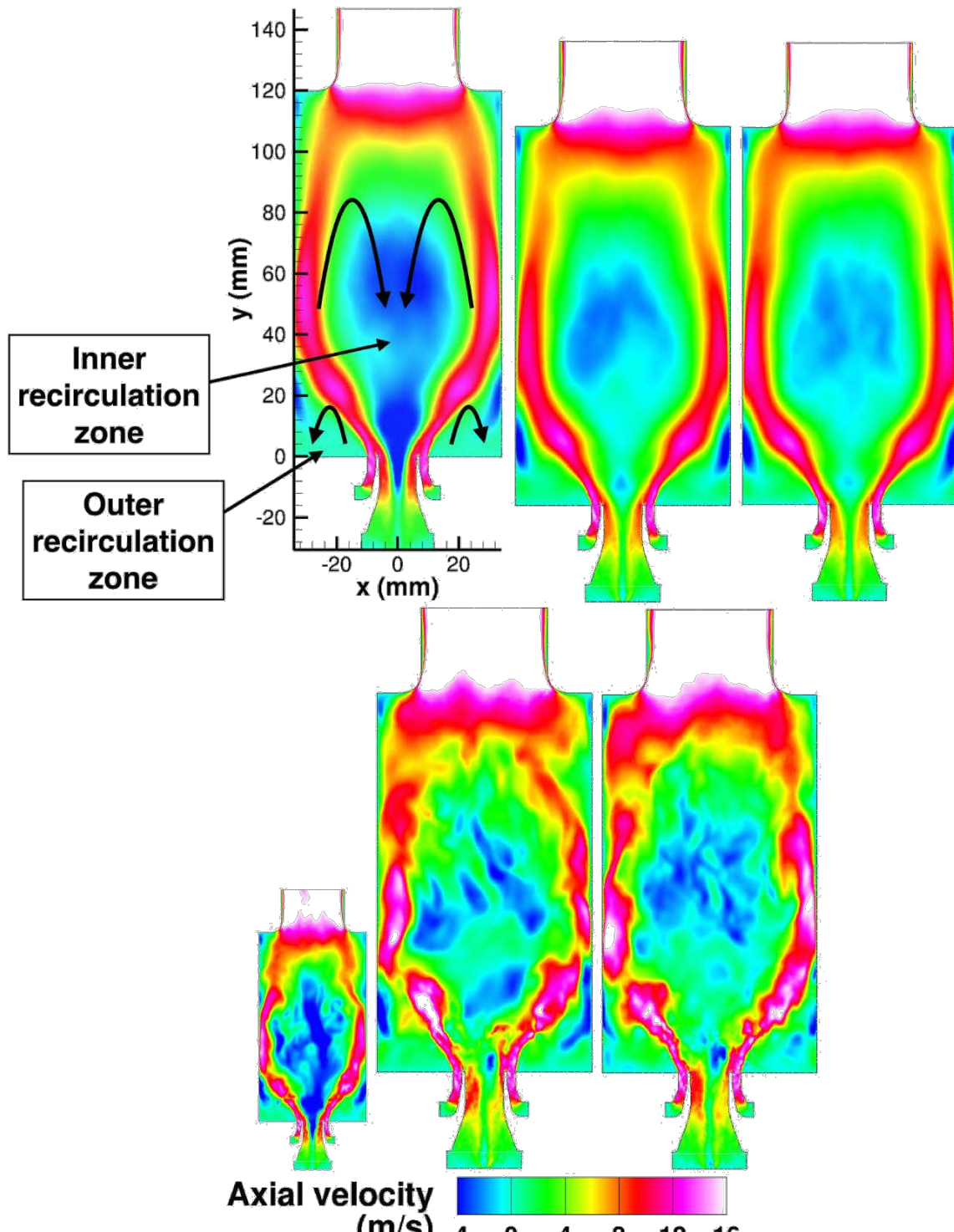


Figure 89: Center plane view of the two resolutions (coarse on the left, dense on the right) with the Pope's criterion. $M=0.2$ along the solid lines.

E-2.2.1 Gas-Phase Results Figure 90 shows both the time-averaged and instantaneous profiles of axial velocity for the two different pressure cases. For the lower pressure case, effect of mesh resolution is also revealed in Fig. 90. Due to the near-constant inflow velocity, the two pressure cases produce similar velocity profiles, albeit with some subtle but important differences. The instantaneous pictures demonstrate that, as the mesh resolution increases, the inner recirculation zone becomes highly unsteady and significantly weaker than the coarse mesh case. In the coarse mesh, the negative axial velocity zone extends below the fuel injection plane with strong but nearly steady vortical structure. This also causes the shear layers generated by the fuel and ring air injection to extend, nearly unbroken, further downstream from the injection plane. Therefore, the dense mesh is required to capture the correct flow features including increased unsteadiness of the inner recirculation region as well as a breakdown of the vortical structure from the central swirling air inflow. While the suppressed turbulence in the coarse mesh is a numerical artifact due to poor mesh resolution, soot turns out to be significantly affected by turbulence and mesh resolution. Hence, coarse mesh results are presented in this paper for



(a) 3 bar, coarse (b) 3 bar, dense (c) 5 bar, dense

Figure 90: (Top) Time-averaged and (bottom) instantaneous snapshots of the axial velocity for the two pressure cases and two mesh resolutions for the 3 bar case.

discussing model capability. Once the dense mesh is used, the pressure effect is not seen.

Figure 91 shows comparison of the experimental and LES velocity profiles for the 3 bar case. The computations are able to reproduce the shear layers accurately and also match the strength of the recirculation zone. While the coarse mesh appears to capture the downstream velocity profiles slightly better, the upstream recirculation zone was found to be critical for the soot evolution, which is far better with the dense mesh. It is important to note this agreement is a direct result of the numerical schemes that minimize kinetic energy dissipation and hence preserve the turbulent flow structures. Similar agreement is found for comparisons at other locations as well, and these are not shown here. Of particular interest is the separation of the axial velocity peaks, which indicates the size of the inner recirculation zone.

Fuel dispersion inside the combustor is heavily dependent on the structure and unsteady dynamics of the inner recirculation zone. Figure 92 shows the time-averaged mixture fraction contours for the 3 bar and 5 bar cases. It can be seen that, in the lower resolution case, the strong vortical structure near the center of the central air inlet draws fuel from the shear layers. In the dense mesh cases, this vortical structure is not present due to a weaker recirculating core, leading to fuel-lean structures near the central air inlet plane. Overall, most of the inner recirculation zone is slight fuel-rich ($Z_{st} = 0.064$ for ethylene/air flames), and the outer recirculation zone is fuel-lean. As will be discussed below, the most important feature of this mixture fraction plot is the thicker fuel jet near the injection zone. The 3 bar, coarse mesh case shows very thin regions of high mixture fraction as compared to the denser mesh cases. In Sec. E-2.2.2, it will be shown that this thick dispersion zone is at the root of intermittency in soot generation in this combustor.

Figure 93 shows the axial temperature profile along the centerline of the combustor and off-center profiles from the centerline, both from the 3 bar results. Temperature profiles match peak temperatures and flame location accurately, at both centerline and off-center locations. The only deviation is the coarse mesh simulation that predicts the inner core extending to the base of the combustor. As discussed before, this is caused by the under-prediction of vortical core unsteadiness.

OH mass fraction is compared to further evaluate the combustion fields. Laser-induced fluorescence (LIF) is used to measure OH mass fraction on the center plane in the experiment. In Fig. 94, thin and small instantaneous flame structures are reproduced in LES, similar to what are observed in the experiment. However, statistical profiles provided in Fig. 95 indicate that reaction implied by OH contours appears to delay in LES. Along the jet, simulations show a clear OH-free area that is missing in the averaged experimental data. Since flame location referred from the centerline temperature profile matches well (Fig. 93), subtle difference in the species definition is assumed to be responsible for the discrepancy in Fig. 95.

E-2.2.2 Statistics and Dynamics of Soot The experiments used laser-induced incandescence (LII) to measure soot volume fraction profiles. Figures 96 and 97 compare soot fields from experiment and simulation for the 3 bar and 5 bar cases. In both cases, the simulations predict most of the soot along the jet closer to the inner recirculation zone,

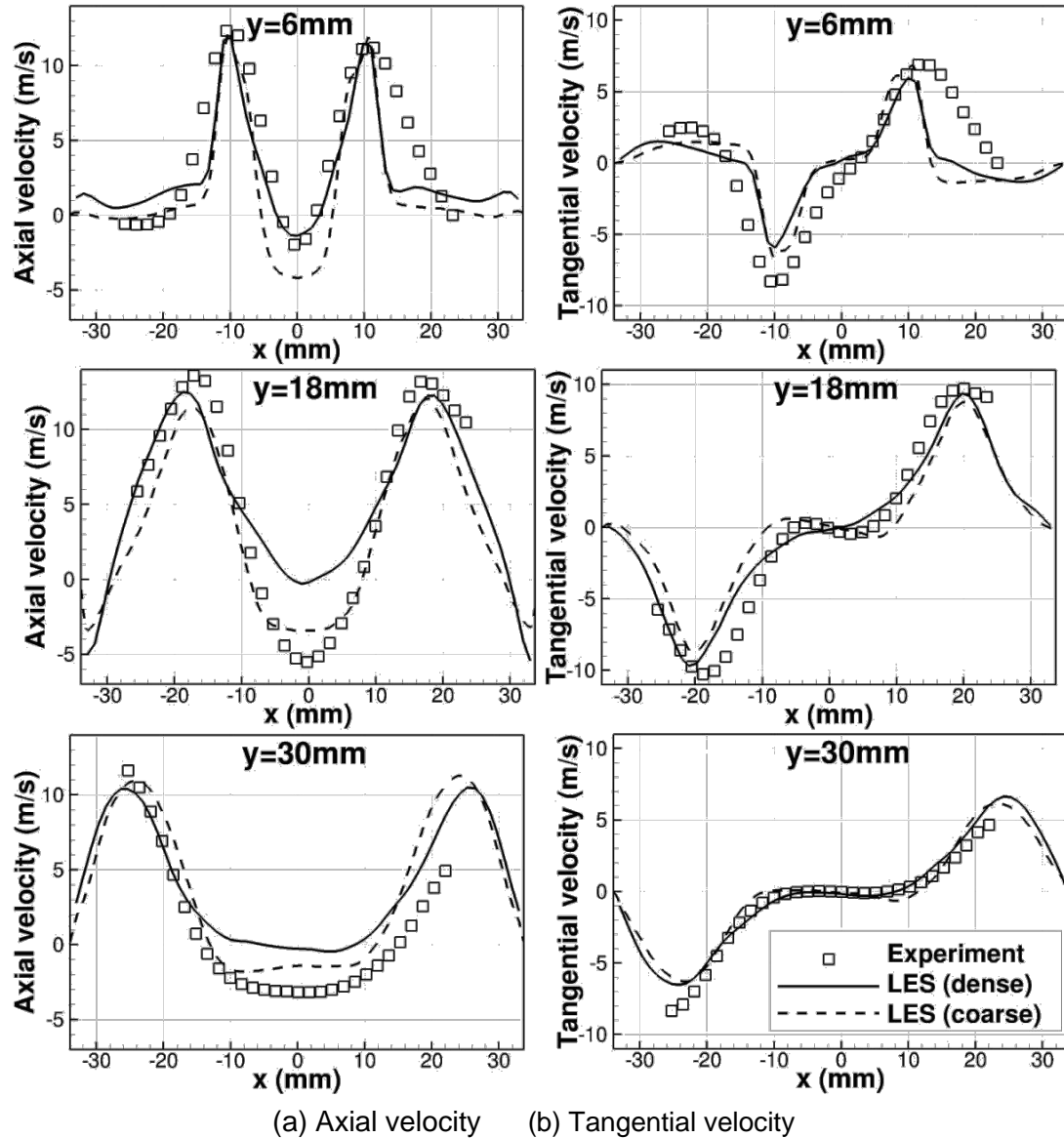
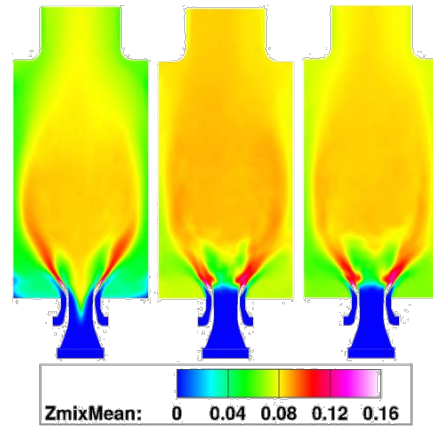


Figure 91: Axial and tangential velocity profiles at selected axial locations obtained from the 3 bar case compared to the corresponding experiment data, for coarse and dense mesh resolution cases.



(a) 3 bar, coarse (b) 3 bar, dense (d) 5 bar, dense

Figure 92: Time-averaged mixture fraction fields for the two pressure cases and two mesh resolutions for 3 bar case.

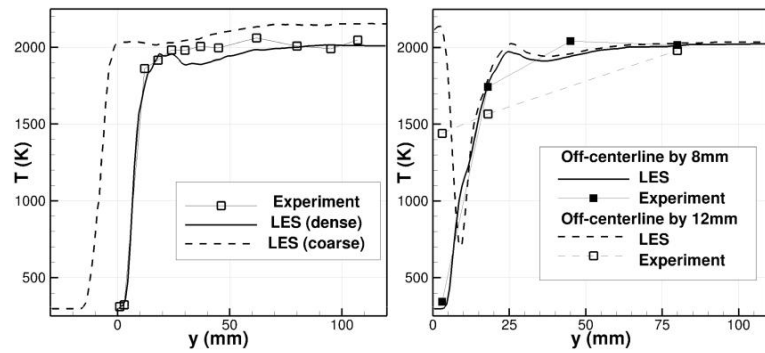
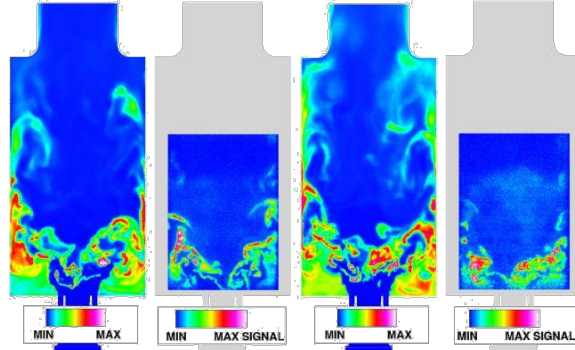
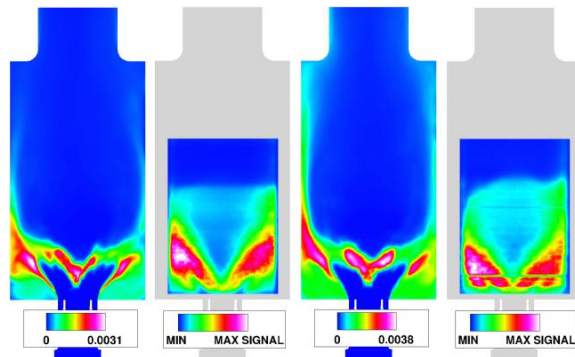


Figure 93: (Top) Axial and (bottom) off-center temperature profiles compared to the experimental data obtained at 3 bar conditions. Only dense mesh results are shown for the off-center profiles.



(a) 3 bar (b) 3 bar, exp. (c) 5 bar (d) 5 bar, exp.

Figure 94: Instantaneous OH mass fractions from dense grid LES compared to the experiment signal.

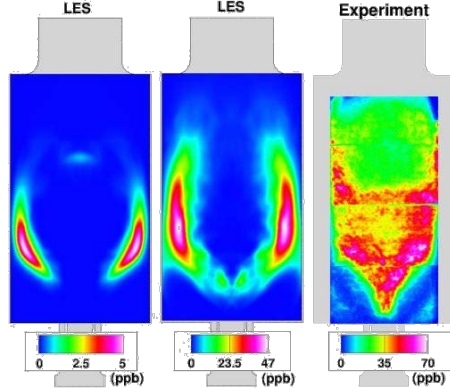


(a) 3 bar (b) 3 bar, exp. (c) 5 bar (d) 5 bar, exp.

Figure 95: Time-averaged OH mass fractions from dense grid LES compared to the experiment signal.

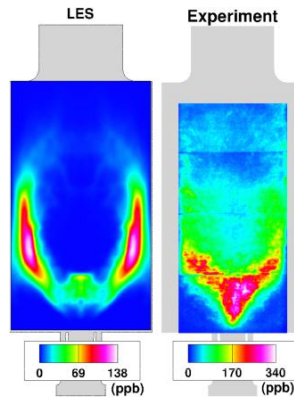
which is characterized by fuel entrainment and large recirculation times. Additionally, the lower part of the inner recirculation zone at the center of the central air inlet shows small amount of soot. Those two soot regions are denoted as “the jet” and “the lower center”, respectively. The experiments show soot along the jet, but also significant volume fraction at the lower center. It should be noted that the coarser simulation completely misses soot at the lower center while the denser resolution captures some soot albeit not as large as that along the jet (Fig. 96). Radial soot volume fraction profiles are plotted in Fig. 98. LES under-predicts lower center soot and misses soot inside the inner recirculation zone. However, at downstream locations along the jet, magnitude of soot volume fraction matches closely with the experimental data.

Another important aspect of these results is the pressure dependency of soot volume fraction. As expected, soot volume fraction increases with pressure, but the scaling factors are different from those associated with laminar flames. From this data and comparing to other DLR combustor experiments [1, 126], the pressure scaling of the peak mean soot



(a) LES, coarse (b) LES, dense (c) experiment

Figure 96: Mean soot volume fraction compared to the experiment for the 3 bar case.



(a) LES, dense (c) experiment

Figure 97: Mean soot volume fraction compared to the experiment for the 5 bar case.

volume fraction is roughly $P^{3:1}$. The computed LES scaling is lower, approximately 2.1. We caution that these are based on measurements at only two different pressure conditions. Nevertheless, these exponents are larger than the observed pressure dependencies for laminar flames (roughly 1.7 [111]). As will be discussed below, soot formation in such gas turbines is intricately linked to hydrodynamic intermittency at energetic scales of the turbulence spectrum.

As seen in Fig. 92, fuel-rich conditions appear along the jet with fuel-lean conditions at the lower center part. This implies that the soot evolution process is different between those two sooting regions. To further discuss soot evolution, time-averaged soot source terms are plotted in Fig. 99 for the 5 bar case. The 3 bar soot source results are omitted here due to high similarity with the 5 bar case. The four processes are considered that add or subtract soot mass: nucleation, condensation, surface reaction, and oxidation. The sources are plotted along the approximated jet and the centerline in Fig. 100. Along the jet, peak sources of the four processes occur one by one, similar to a laminar sooting jet.

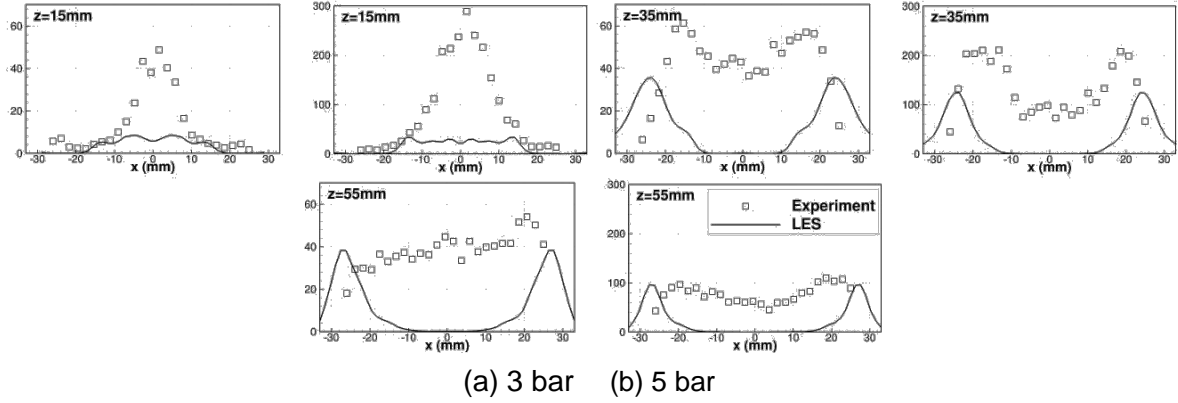


Figure 98: Radial soot volume fraction profiles of dense mesh LES results compared to the experiment.

However along the centerline, the four sources collapse to each other, indicating that the evolution has not been persistent throughout the simulation. On the lower center region, unsteady transport of fuel-rich pockets is attributed to the soot evolution.

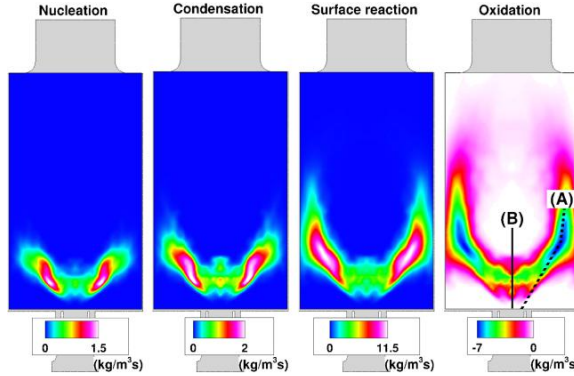


Figure 99: Four soot evolution sources of the 5 bar case.

To further understand the soot formation process, instantaneous soot volume fraction from the simulations at different times is shown for the 3 bar and 5 bar cases (Fig. 101). It is striking that the instantaneous values are nearly an order of magnitude higher than the time-averaged values. Also, soot formation happens very sporadically with highly inter-mittent spatio-temporal profiles. This sparse soot presence is confirmed by experimental data, which also shows very large but spatially concentrated soot volume fractions [126]. Further, the peak soot levels are much higher in the 5 bar case as compared to the 3 bar case. The instantaneous soot volume fraction contours further verify that soot at the lower center occurs through strong intermittent behavior of fuel-rich patches. 12.5 ms is enough for the jet to reach the exit, while a soot pocket at the lower center (denoted by a white arrow) surrounded by high mixture fraction flow moves very slowly. Since the center soot pocket moves horizontally, orderless profile between the soot sources in Fig. 100 is not surprising.

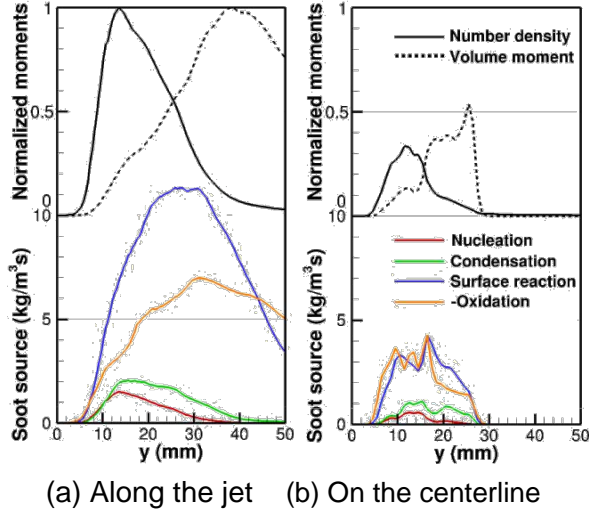


Figure 100: Soot evolution sources of the 5 bar case plotted along the jet (following line A marked at Fig. 99) and the centerline (line B). Moments are normalized by maximum values obtained in the simulation.

To understand the source of this intermittency, it is important to look at the dynamics of the mixture fraction field. In particular, it is seen that the fuel jet experiences a flapping motion due to the shear layers arising from the central and ring air inlets. Figure 102 shows mixture fraction contours near the fuel jet inlet with the jet at extreme locations in the horizontal direction. In the dense mesh case, it is seen that, at certain times, the jet breaks down immediately after entering the combustor, leading to fuel-rich pockets that are entrained by the recirculation zone. This shearing motion is amplified by the highly unsteady transverse motions of the recirculation zone. The jet-flapping is the main source of intermittency in this combustor. It is also seen that soot nucleation is dominant in these fuel-rich pockets as evidenced in the overlaid number density contours. Unlike intermit-tency due to small scales [117], soot intermittency in such gas turbines are driven by large scale hydrodynamic motions. The sporadic soot generation is the result of such large scale motions introducing fluid trajectories that pass through soot-favored regions in compo-sition space. In the coarse mesh case where turbulence is suppressed, such shearing mo-tion is largely absent, as is also seen in the velocity plots (Fig. 90). Consequently, the jet breakdown is similar to canonical turbulent jets, and intermittency is dominated here by small-scale strain effects. The primary soot nucleation region is removed from the jet inlet, and the frequency with which soot-rich regions are generated is dictated by the spectral content of the inflow turbulence. This scenario is similar to the turbulent jet flame exper-iments, where very high level of intermittency is observed [116, 118]. With the absence of jet fluctuation, the coarse mesh case fails to predict soot at the lower center and results in much lower soot volume fraction, by an order of magnitude. Therefore, capturing unsteadiness is important in soot prediction on this configuration. Note that unsteady-RANS computation was also unsuccessful in reproducing soot at the lower center [129], similar to the coarse mesh LES result.

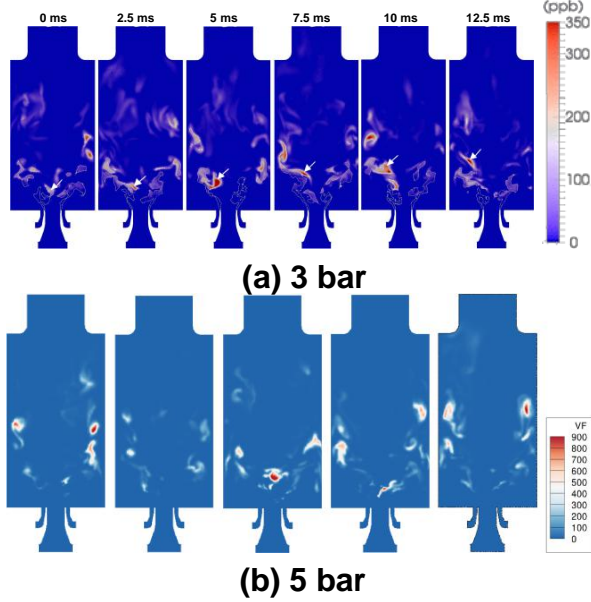


Figure 101: Instantaneous soot volume fraction snapshots separated by 2.5 ms, and over-laid with isocontour of equivalence ratio, $= 1:5$. White arrows follow a soot pocket generated on the lower center part.

Figure 103 shows the RMS of soot volume fraction for the 3 and 5 bar cases. Consistent with the high intermittency and the presence of very high local soot volume fractions, the RMS values are nearly twice the mean values. However, it is interesting to note that the RMS peaks are roughly in the same location as the peak mean values as well. In other words, soot growth takes finite residence time inside the combustor, and most of these trajectories pass through similar regions in physical space. Consequently, peak soot volume fractions are observed only in the regions that also have high mean values. Conversely, there exists no region of persistent but low soot volume fractions. This confirms an inherent hydrodynamic effect in soot formation inside gas turbines, which is different from canonical laminar flames.

However, despite all these efforts, maximum soot volume fraction is 2-3 times lower than the experimental data (Figs. 96 and 97). While the lower center soot is underpredicted, it is still encouraging that soot volume fraction along the jet matches closely to the experiment (Fig. 98). With improved mesh, the soot profile and the magnitude improve by a lot, mostly due to the capturing of the jet unsteadiness. However, further refinement did only slightly improved result, indicating that this configuration has limited range of sensitivity to the mesh resolution.

E-3 Conclusions

The evolution of soot for a range of pressures in a model gas turbine combustor was studied using LES. The LES approach included extensive details about PAH formation and transport, soot evolution, and gas-phase turbulent combustion. Comparison with

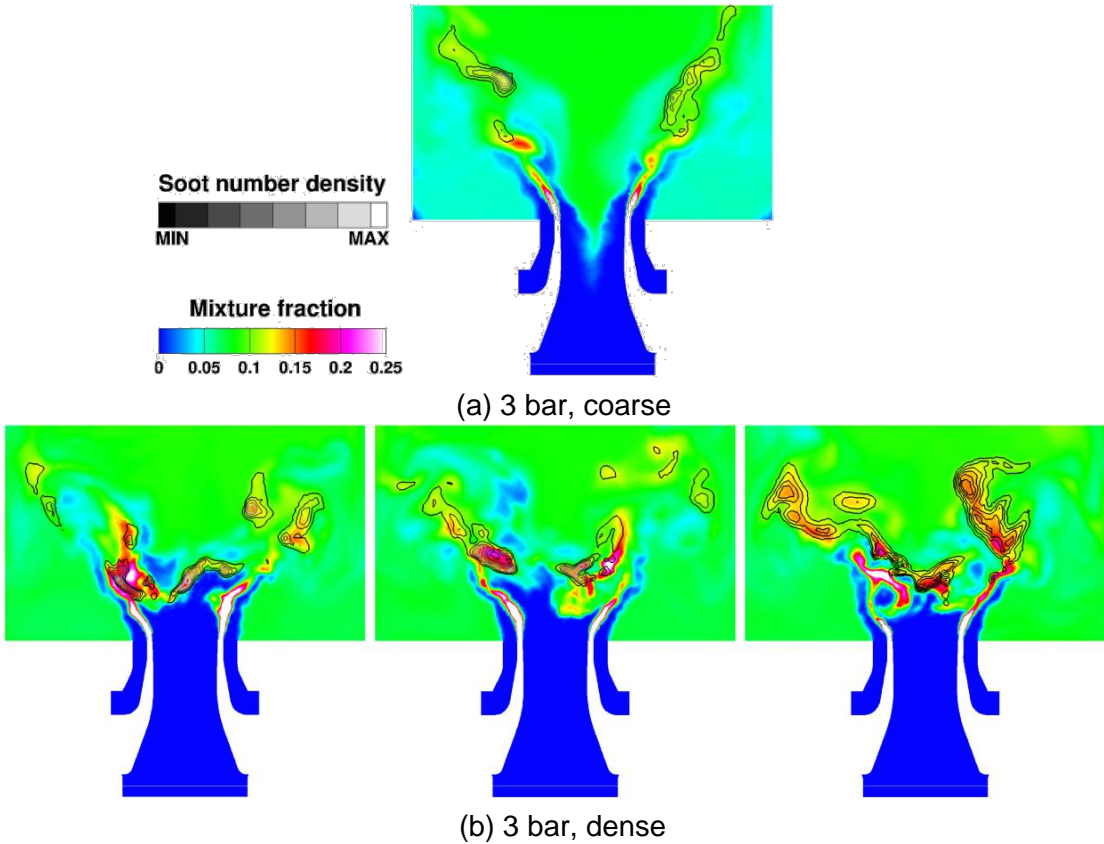


Figure 102: Instantaneous snapshots of mixture fraction near the fuel inlet overlaid with soot number density isocontours: (a) 3 bar result on the coarse mesh, (b) 3 bar dense mesh case at different times showcasing the jet-flapping process.

experiments show that the simulations are able to predict the gas phase properties very well. While soot volume fractions are underpredicted, the overall pressure tendencies are adequately represented. Much of the sooting region in the experiments and simulations match, except for the near-jet region, where the simulations underpredict soot formation. Further, the simulations replicate the intermittent nature of the soot formation found in the experiments.

These simulations, combined with detailed experimental measurements, demonstrate the influence of hydrodynamics on the production of soot inside gas turbines at elevated pressures. The pressure scaling of peak soot volume fraction is much higher than in corresponding ethylene/air laminar flames. The main cause of this high scaling coefficient is the presence of fuel-jet dynamics driven by the unsteadiness of the main recirculation zone within the combustor. Consequently, fuel-rich pockets are able to reside for long times in high-temperature recirculation zones within the combustor. In the high-pressure case, this hydrodynamic intermittency is not driven by small-scale strain effects but through intermediate and large scale motion of the jet and the recirculation zone. This points to the possibility that soot formation can be highly design dependent, where specific fuel port design choices can influence the nature of jet breakdown and soot forma-

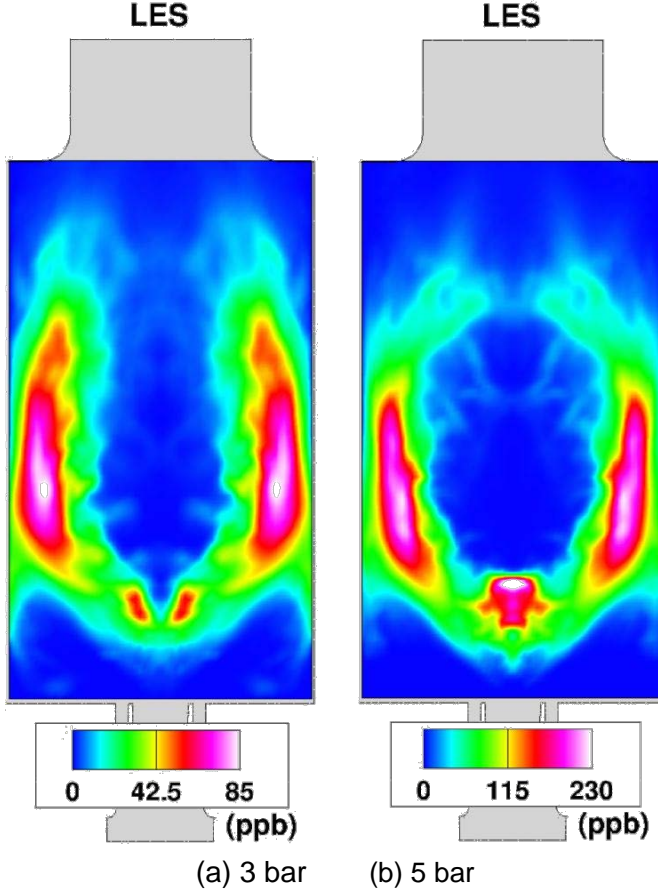


Figure 103: RMS of soot volume fraction for the two pressure cases.

tion. Further, this study demonstrates a much more intricate coupling between unsteady turbulent flow and soot formation than previously understood, indicating the need for carefully designed canonical test cases to fully assess such multi-scale intermittency effects.

F. Simulation Tools

F-1 Low Dissipation LES Solver in OpenFOAM

In this section, we focus on the kinetic energy conservation properties of the LES solver. As discussed in the introduction, preserving or minimizing discrete kinetic energy loss is essential for the robust solution of a turbulent flow field. The LES implementation is based on a low-Mach number formulation [156–158], which uses pressure to enforce the filtered continuity equation. In this sense, density changes directly affect the pressure field, leading to dilatation of the velocity field applied as a correction to an intermediate velocity solution.

In the OpenFOAM code base, a new solver was created to handle variable-density, flamelet-

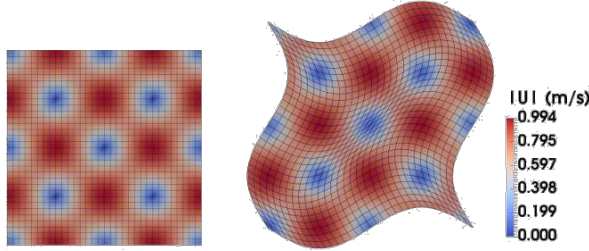


Figure 104: Velocity magnitude contours after 1 second of simulation time, for orthogonal and skewed meshes.

based LES computations [159]. The energy-conservation strategy is based on the scheme proposed by Morinishi [160]. This scheme reduces to the approach of Ham and Iaccarino [2] in the limit of constant density flows. The OpenFOAM solver uses a collocated variable placement, where fluxes are obtained by interpolation to cell faces. This interpolation as well as the required pressure gradient at the cell faces are computed using a second-order linear interpolation. For a uniform mesh, the linear interpolation reduces to a mid-point interpolation scheme that minimizes an energy loss [161].

The mid-point interpolation is also applied in the time direction, where the momentum transport equations are evolved from time n to $n + 1$, while the individual terms in the equation are evaluated at time $n + \frac{1}{2}$ obtained using interpolation method. This implicit formulation is crucial for the conservation of kinetic energy. In other words, ensuring convergence of the time discretization is important to minimizing discrete energy loss. In the OpenFOAM solver, this is ensured using PISO (pressure-implicit second order) iterations [154]. It has been shown that two PISO iterations are sufficient to achieve second order convergence in time [154]. This strategy is targeted towards statistically stationary flow problems since PISO procedure introduces a stronger coupling and allows a larger time step. For a more general tool, fractional time-step procedure can be utilized [162]. With the goal of capturing the flame location accurately, a stronger coupling between the scalar and density fields is introduced. The velocity at time $n + 1$ is used in the scalar transport equation rather than the velocity at time $n + \frac{1}{2}$. Second, the time-rate of change of density, which is needed to update pressure, uses a second-order Crank-Nicholson scheme rather than a first-order Euler scheme.

To demonstrate the energy conservation properties of this solver, verification studies using canonical flow configurations were considered (similar to that in [152]). A Taylor-Green vortex with no density change was computed on orthogonal and skewed meshes. Figure 104 shows the solution on these two grids at the same computed time. It can be seen that the solver preserves the vortical structures even in a skewed mesh representation, which is important for application to complex geometries. Figure 105 shows the decay of kinetic energy for this test case. Not only the implemented approach is unaffected by mesh skewness, it shows comparable amounts of energy loss to Ham and Iaccarino's formulation [2]. As mentioned earlier, exact conservation cannot be achieved in a collocated mesh scheme. Instead, energy dissipation is minimized using the procedure

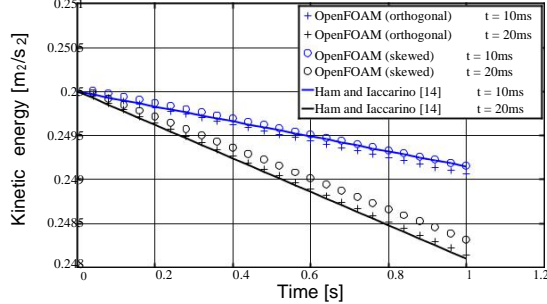


Figure 105: Temporal kinetic energy decay between different numerical approaches for orthogonal and skewed meshes, for two different timestep sizes. Ham and Iaccarino (solid lines,[2]) correspond to both orthogonal and skewed mesh cases.

described above. The truncation error of kinetic energy evolution is $O(\Delta t^2)$, implying that a smaller time step ensures better conservation properties as well. The extension to variable density is based on the scheme of Morinishi [160], which enforces kinetic energy conservation through a strictly skew-symmetric form of the convection terms but is not predicated on the simultaneous conservation of mass. This is difference from the conventional low-Mach number approaches [163] in ensuring that no additional error is introduced in the kinetic energy conservation. Note that compared to icoFOAM, one of the conventional OpenFOAM solvers, the implemented approach reduces kinetic energy loss by 16% and 94% for the orthogonal and skewed meshes, respectively. For the orthogonal case, the difference mostly rely on the semi-implicit coupling of timesteps. For the skewed case, the kinetic energy conservative spatial discretization schemes become effective and explain the larger discrepancy. This improved LES solver for unstructured grids is then used for the simulations described below.

F-2 Adjoint approach for flames

F-2.1 Background

An important component of this work is the development of a demonstrably predictive computational model. The accuracy of a model is often established through comparisons with experimental data. However, simulations of even the simplest turbulent flame experiments involve a host of models. Consequently, it is not possible to determine the role of a particular model in the simulation result. In order to determine the relative importance of models, we need additional tools beyond the normal computational method for simulating flames. The adjoint-based sensitivity approach to be discussed here is one such powerful method that provides the ability to isolate the performance of individual models.

Adjoint-based tools have other important applications as well. Design and control of reliable combustion devices requires planning for every possible hazard. For example, in the case of gas turbine combustors, blow out of the flame may happen in extreme operating conditions. When such a difficulty occurs, an ignition source must be placed back into

the flowfield of the combustor in order to reinitiate the flame. While this reignition may occur given a powerful ignition source in many locations within the combustor, it can occur faster and more efficiently in certain regions of the combustor. Those regions can be determined by knowledge of the sensitivity of reignition to the placement of an ignition source. This concept can be abstracted to a general idea. One can define key quantities, such as temperature profile at exit, soot emission, or the average NO_x concentration as the primary targets of the simulation, and call them quantities of interest (QoIs). In this context, knowledge of the sensitivity of QoIs to changes of the combustor's conditions can lead to improved design and control.

Generally, the sensitivity of QoIs to parameters can be computed using one of two methods: forward sensitivity equations or adjoint equations. The relative advantage of the method depends on the nature of the simulations. Any combustion simulation will involve a host of model parameters (e.g., Arrhenius rate coefficients). Similarly, depending on the flow configuration, a number of QoIs may be necessary. The forward sensitivity method of solution is best suited to situations which involve small numbers of parameters and multiple QoIs since each parameter adds an additional partial differential equation to be solved. An alternative method for sensitivity determination uses the adjoint method. This method is well suited to applications that involve few QoIs and many parameters since each QoI, not each parameter, adds additional equations to be solved.

Adjoint methods have been used in several aerospace-related applications including aerodynamic shape optimization, flow control, and acoustic noise reduction. Optimization of airfoil and aerodynamic shapes has been the focus of many studies [164–169]. These applications used adjoint methods to optimize shape parameters and improve certain aspects of performance, such as drag. Airfoil optimization has been carried out both using continuous adjoint derivations, in which the adjoint equations are derived and then discretized, and using discrete adjoint equations, in which the adjoint equations are derived from the already-discretized governing equations [170]. In the realm of flow control, adjoints have been used to reduce drag over bodies and in channels [171, 172]. Further applications of adjoints have aimed at the reduction of acoustic production [173, 174] in unsteady Direct Numerical Simulation (DNS) and Large Eddy Simulation (LES). Adjoint methods have also been used in the realm of chemical kinetics as it relates to atmospheric pollution. Sensitivity of output variables to kinetics parameters has been derived and implemented for the adjoint method alongside the direct decoupled method [175], and subsequently been applied to air pollution models [176, 177].

In the context of flame simulations, adjoint methods can be used to determine the sensitivity of various QoIs to chemistry, combustion, turbulence, or turbulence-chemistry interaction model parameters. In addition to this capability, adjoint methods also can be used to determine the sensitivity of QoIs to perturbations of the governing equations. Any number of perturbations may affect the chosen QoIs in the combustor. Here, we consider the situation where small changes to local scalar values are introduced. In a practical configuration, this could be the result of a spark ignition source placed in the flow or a minor modification of inlet conditions. Typically, the flow would need to be solved repetitively with the perturbed values in order to determine the effects of local

scalar changes on Qols in the flame. With the use of adjoints, no additional flow solve is necessary for each scalar value perturbation. Only an additional solution of the set of adjoint equations for each specified Qol is required in order to give the sensitivity of that Qol to the perturbations. In this way the effect of changes to the state of the flow within the combustor have been determined for NOx concentrations.

F-2.2 Computational Methodology

Computation of the sensitivity of the Qols to perturbations of upstream properties is desired. The determination of the sensitivities requires the steady state solution of the primal problem, which is the laminar reacting flow, and the subsequent solution of the dual problem, which is the set of adjoint equations. From these solutions the sensitivity of important quantities in the flame can be calculated. The primal problem consists of steady-state laminar incompressible variable density reacting flow. Reactions are handled with a multistep kinetics approach for laminar reactions. As a result, a reacting scalar for each chemical species will be carried in the flow. The dual problem involves the solution of the adjoint equations for a specific Qol. Starting with the defined Qol, the adjoint equations can be derived through the use of Lagrange multipliers.

A Qol Q can be selected which is impacted through the governing equations by flowfield properties. Perturbations to the properties can be effected by adding an additional term to the governing equations which acts as a source. For example if the Qol could be affected by OH radicals in the flow, then a source for OH can be introduced upstream of the flame. The added source term can be treated as a parameter in the governing equations. The solution to the governing equations can proceed with the parameterized source term set to zero; however, the sensitivity to that source term nonetheless can be calculated.

F-2.3 Results

A laminar hydrogen diffusion flame simulation and its corresponding adjoint solution have been developed to demonstrate the capabilities of the adjoint method. The flame includes a jet of pure hydrogen with a coflow of air. Figure 106 shows a schematic of the domain of the simulation with the inlet sections labeled. Table 20 lists the inlet flow properties. For this application a detailed kinetics model for hydrogen with NOx formation [178] has been used. This model includes 32 species and 172 reactions. The next two sections will include first a brief description of the flame simulation results and second a description of the sensitivity results calculated using the adjoint solution.

F-2.3.1 Laminar flame simulation results Figure 107 displays the temperature field from the solution of the primal problem. The peak flame temperature reaches 2214K along the centerline at 0.099m downstream of the inlet. The NOx mass fraction fields are plotted in Fig. 108. Nitric oxide peaks in the region just downstream of peak temperature. Although its peak value decreases as the flow cools downstream, NO remains in the flow. Nitrogen dioxide peaks in the downstream area of the flow at the edge of the hot

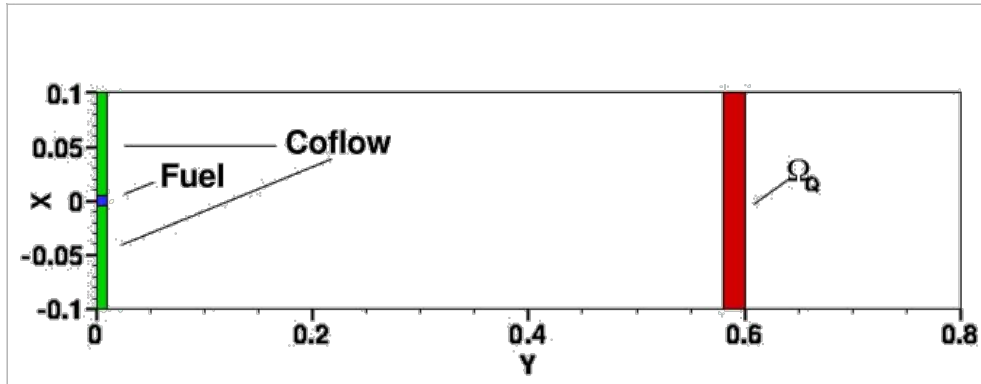


Figure 106: Simulation domain

Table 20: Inlet flow properties

Property nStream	Fuel stream	Coflow stream
Temperature (K)	293.0	293.0
Y_{H_2}	1.0	0.0
Y_{O_2}	0.0	0.232
Y_{N_2}	0.0	0.768
U (m/s)	0.05	0.25

combustion products. Here, the NO formed in the higher temperature regions combines with the cool coflow and reacts to form NO₂.

F-2.3.2 Laminar flame sensitivity results Although control of ignition can be a goal of adjoint-based sensitivity methods, control of pollutant emissions from combustion devices also is desired. The study of the sensitivity of pollutants to the state of the flow inside the combustor is a step towards that control. Combustion pollution includes such chemicals as unburned hydrocarbons, carbon monoxide, carbon dioxide, and NOx. NOx for instance contributes to the formation of acid rain and smog. Determination and minimization of the level of pollutant output is a driving factor in the development of simulation techniques used in the combustor design cycle. Here the sensitivity of NOx levels in a laminar flame are considered.

For this reason, NOx concentration is used as the QoI for the analyses below. The QoI

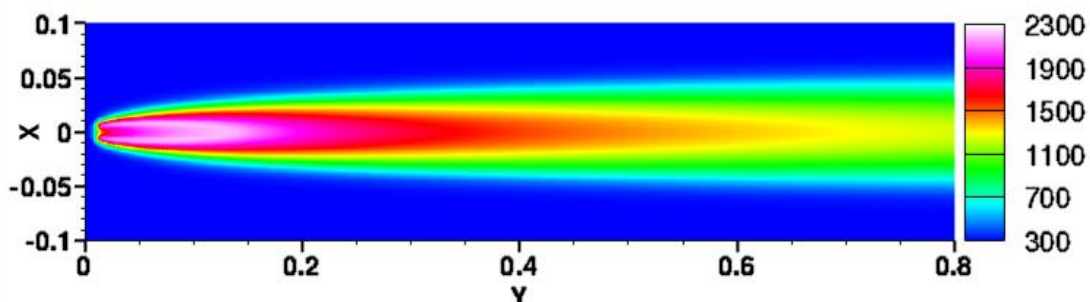


Figure 107: Temperature (K)

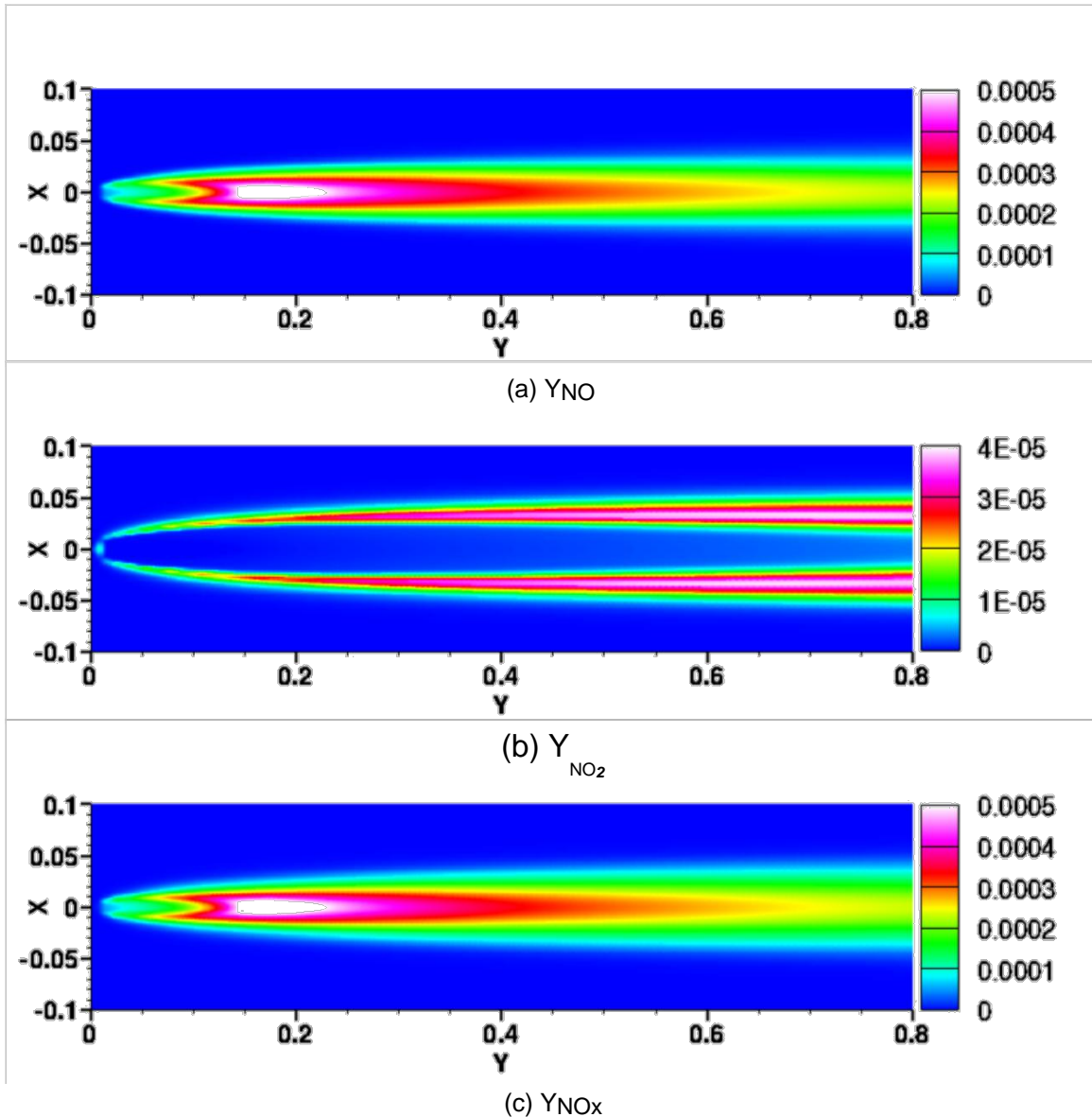


Figure 108: NOx fields

thus can be written in the following manner:

$$Z = \int_Q (Y_{NO} + Y_{NO_2}); \quad (21)$$

where Q refers to the region over which the NOx has been calculated. Figure 106 shows Q , the rectangular region downstream of the flame in which the NOx has been calculated. The region occupies the full width of the domain and extends from 0.58m to 0.6m.

Source perturbations can be applied anywhere within the domain. Since the sensitivity value is a summation of the adjoint solution over the source-perturbed region, plots of the adjoint variables themselves depict where the source perturbations most affect the QoI.

The adjoint variable solutions for Y_{H_2} , Y_{O_2} , and Y_{N_2} are displayed in Fig. 109. The regions near the inlet of the domain and just outside of the fuel jet show the greatest sensitivity. Additionally, the region of the flame itself shows sensitivity to H_2 , O_2 , and N_2 . For H_2 increases to its source decrease the QoI, while for O_2 and N_2 increases increase the QoI.

Figure 110 shows the adjoint variable solutions for Y_{OH} , Y_O , and Y_N . The adjoint solutions for OH and O indicate regions near the inlet 0.04m to either side of the core fuel jet where the NOx concentration is sensitive for which increases to Y_{OH} and Y_O decrease the QoI. These regions continue downstream with a lower magnitude flanking either side of the high temperature combustion products. Additionally for O, two small regions of sensitivity exist immediately to either side of the fuel jet in which increases to Y_O will increase NOx. For Y_N a region of high sensitivity exists near the inlet for the majority of the span of the domain. Continuing downstream, a lower sensitivity region encompasses the region of higher temperature combustion products.

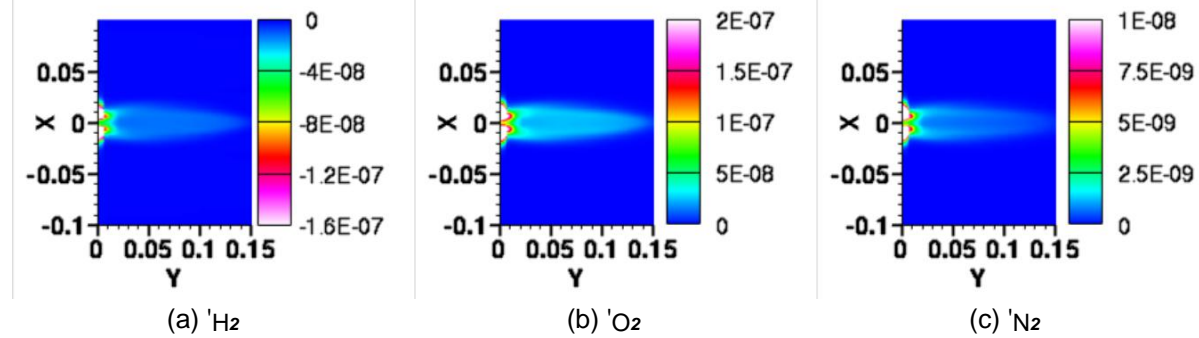


Figure 109: Adjoint variable fields for H_2 , O_2 , and N_2

F-2.4 Conclusions

The adjoint equations have been derived for steady state laminar variable density reacting flow. A laminar hydrogen flame simulation has been developed to demonstrate the capabilities of the adjoint method in determining sensitivity of the NOx production of the flame to perturbations of the state variables via source terms. The adjoint solutions show that the NOx levels are sensitive to H_2 and O_2 in the region of the flame itself and near the inlet where they would be transported into the flame. Additionally, the NOx levels

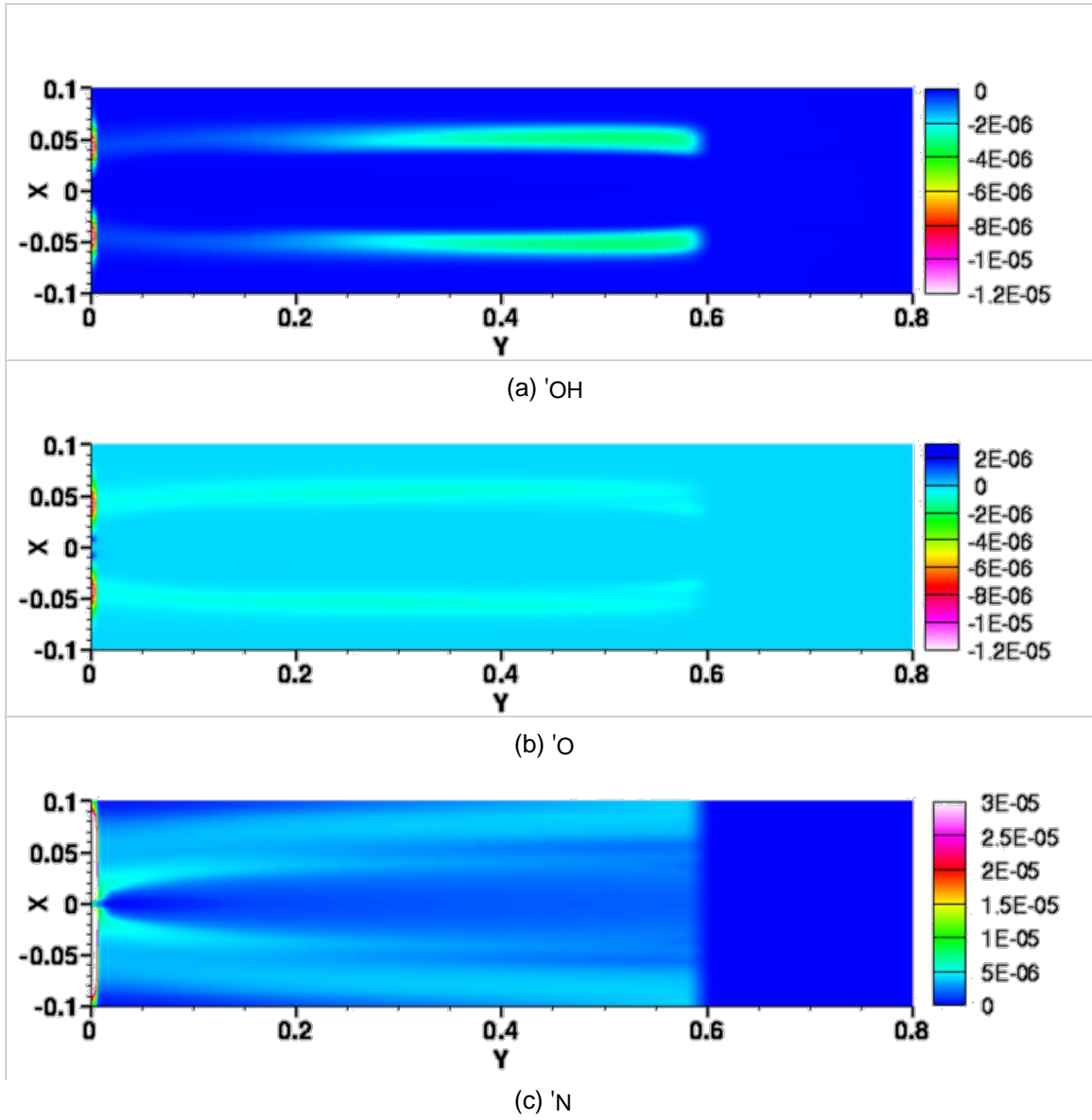


Figure 110: Adjoint variable fields for OH, O, and N

are sensitive to addition of radicals in the region bordering the hot combustion products, and again at the inlet where they would be transported into those regions.

G. Conclusions and Implications for Future Research

This research program significantly advanced fundamental understanding of emissions from aircraft engines burning alternative fuels. The tools and databases generated here could serve as a starting point for future programs focusing on aircraft fuels. In particular, the National Jet Fuels Certification Program (NJCFP) has many of the same elements that have been covered in this program, and the tools used there have evolved from this study. From this vantage point, we see a need for continued research investment on this topic. Below, some key questions that remain unsolved are listed.

From a fuel composition perspective, a rigorous analysis of the surrogate-fuel based model for a range of fuel chemical structures and compositions is necessary. In particular, it is important to consider oxygen-containing fuel components (which will affect the formation and oxidation mechanisms of particulates). Further, considering fuel mixtures that exhibit similar thermophysical properties but different oxidation pathways will be useful in understanding the limitations of surrogate-based modeling.

The present work identified a more complex mechanism of soot oxidation, with an implication that current soot modeling in combustion substantially overpredicts the rate of soot oxidation and hence underpredicts the amount of soot formed. The problem originates from two factors: (a) unforeseen development of low-reactivity edges due to oxidation, and (b) unaccounted-for coupling between gas and surface reactions. Hence, the following actions are suggested:

- explore further the oxidation mechanisms and kinetics of soot oxidation for various soot-surface patterns and a wide range of temperature
- establish relationships between initial fuel structure and oxidation mechanisms, focusing especially on oxygen-containing alternative fuels
- establish a database of validation experiments for soot oxidation
- challenge the validation experiments to measure time-resolved evolution of soot particles and gaseous environment, both in non-intrusive manner, including high-accuracy resolution of concentrations of H, O, OH, O₂, CO, and CO₂, as a minimum
- validate the oxidation model using the new experiments
- test the combined growth-oxidation model in realistic combustion environments
- subject the model to rigorous validation thorough uncertainty-quantification analysis

A comprehensive analysis of soot formation in turbulent flames identified two different mechanisms: a) a small-scale dominated soot formation process that is present in jet flames, and high-Reynolds number flows, and b) a large-scale dominated soot formation process that is more critical in flows with large recirculation zones such as that in modern aircraft combustors. The latter processes are dominated by intermittency associated with integral-scale dynamics of recirculating flows. Understand the interaction between these low-Reynolds number regions, and the high-Reynolds number inflow region of the combustor is important for estimating not just the soot mass but also soot number density and size distribution.

Experimental techniques for measuring soot in turbulent flames have focused mainly on soot volume fraction (which relates to mass) but not so much on the soot number density distribution, which will produce the distribution of particle sizes. As regulations increasingly target both size and total mass, it becomes imperative that models are accurate at estimating these quantities. For this purpose, experimental measurements in engine-relevant conditions (recirculating flows, high Reynolds numbers, higher pressures) are important. Here, new diagnostic tools that can operate at extreme conditions as well as provide detailed soot distributions are needed.

Overall, simulation tools have to evolve to take advantage of the emergence of data sciences. In particular, estimation of uncertainty with regard to models and operating/input conditions, as well as the assimilation of experimental and engine-relevant data directly into models will be necessary. Moreover, as a wide variety of alternative fuels become available, this notion of fuel-specific model development will become inefficient. Instead, a broader learning-based approach that uses machine-learning as well as probabilistic techniques to identify chemistry models will become attractive. A broad program to take advantage of these rapidly developing tools will be of great benefit to the engine development community.

H. References

References

- [1] Geigle, K. P., Zerbs, J., Kohler, M., Stohr, M., and Meier, W., "Experimental analysis of soot formation and oxidation in a gas turbine model combustor using laser diagnostics," *Journal of Engineering for Gas Turbines and Power*, Vol. 133, 2011, pp. 121503.
- [2] Ham, F. and Iaccarino, G., "Energy conservation in collocated discretization schemes on unstructured meshes," *CTR Annual Research Briefs*, 2004.
- [3] Hsu, A., Narayanaswamy, V., Clemens, N., and Frank, J., "Mixture fraction imaging in turbulent non-premixed flames with two-photon LIF of krypton," *Proceedings of the Combustion Institute*, Vol. 33, No. 1, 2011, pp. 759–766.
- [4] Miller, J. C., "Two-photon resonant multiphoton ionization and stimulated emission in krypton and xenon," *Physical Review A*, Vol. 40, No. 12, 1989, pp. 6969.
- [5] Whitehead, C., Pournasr, H., Bruce, M., Cai, H., Kohel, J., Layne, W., and Keto, J. W., "Deactivation of two-photon excited Xe (5p56p, 6p, 7p) and Kr (4p55p) in xenon and krypton," *The Journal of chemical physics*, Vol. 102, No. 5, 1995, pp. 1965–1980.
- [6] McEnally, C. S., Koylu, U. O., Pfefferle, L. D., and Rosner, D. E., "Soot volume fraction and temperature measurements in laminar nonpremixed flames using thermo-couples," *Combustion and Flame*, Vol. 109, No. 4, 1997, pp. 701–720.
- [7] Miller, J. H., Elreedy, S., Ahvazi, B., Woldu, F., and Hassanzadeh, P., "Tunable diode-laser measurement of carbon monoxide concentration and temperature in a laminar methane-air diffusion flame," *Applied optics*, Vol. 32, No. 30, 1993, pp. 6082–6089.
- [8] Smyth, K. C., Miller, J. H., Dorfman, R. C., Mallard, W. G., and Santoro, R. J., "Soot inception in a methane/air diffusion flame as characterized by detailed species profiles," *Combustion and flame*, Vol. 62, No. 2, 1985, pp. 157–181.
- [9] Kee, R. J., Miller, J. A., Evans, G. H., and Dixon-Lewis, G., "A computational model of the structure and extinction of strained, opposed flow, premixed methane-air flames," *Symposium (International) on Combustion*, Vol. 22, Elsevier, 1989, pp. 1479–1494.

- [10] Wang, H., You, X., Joshi, A. V., Davis, S. G., Laskin, A., Egolfopoulos, F., Law, C. K., and Version II, U. M., "High-temperature combustion reaction model of H₂," Tech. rep., CO/C1-C4 Compounds, 2007.
- [11] Hirschfelder, J. O., Curtiss, C. F., Bird, R. B., and Mayer, M. G., Molecular theory of gases and liquids, Vol. 26, Wiley New York, 1954.
- [12] Burcat, A. and Ruscic, B., Third millenium ideal gas and condensed phase thermochemical database for combustion with updates from active thermochemical tables, Argonne National Laboratory Argonne, IL, 2005.
- [13] Tee, L. S., Gotoh, S., and Stewart, W. E., "Molecular parameters for normal fluids. Lennard-Jones 12-6 Potential," Industrial & Engineering Chemistry Fundamentals, Vol. 5, No. 3, 1966, pp. 356–363.
- [14] Burns, R. A., Development of scalar and velocity imaging diagnostics for supersonic hy-permixing strut injector flowfields, Ph.D. thesis, 2014.
- [15] Lee, S., Turns, S., and Santoro, R., "Measurement of soot, OH and PAH concentrations in turbulent ethylene/air jet flames," Combust. Flame, Vol. 156, 2009, pp. 2264– 2275.
- [16] Bockhorn, H., Geitlinger, H., Jungfleisch, B., Lehre, T., Schon," A., Streibel, T., and Suntz, R., "Progress in characterization of soot formation by optical methods," Physical Chemistry Chemical Physics, Vol. 4, No. 15, 2002, pp. 3780–3793.
- [17] Zerbs, J., Geigle, K., Lammel, O., Hader, J., Stirn, R., Hadef, R., and Meier, W., "The influence of wavelength in extinction measurements and beam steering in laser-induced incandescence measurements in sooting flames," Applied Physics B, Vol. 96, No. 4, 2009, pp. 683–694.
- [18] Dalzell, W. and Sarofim, A., "Optical constants of soot and their application to heat-flux calculations," Journal of Heat Transfer, Vol. 91, No. 1, 1969, pp. 100–104.
- [19] Williams, T. C., Shaddix, C., Jensen, K., and Suo-Anttila, J., "Measurement of the dimensionless extinction coefficient of soot within laminar diffusion flames," International Journal of Heat and Mass Transfer, Vol. 50, No. 7, 2007, pp. 1616–1630.
- [20] Han, D. and Mungal, M., "Simultaneous measurements of velocity and CH distributions. Part 1: jet flames in co-flow," combustion and flame, Vol. 132, No. 3, 2003, pp. 565–590.
- [21] Attili, A., Bisetti, F., Mueller, M. E., and Pitsch, H., "Formation, growth, and transport of soot in a three-dimensional turbulent non-premixed jet flame," Combustion and Flame, Vol. 161, No. 7, 2014, pp. 1849–1865.
- [22] Mahmoud, S., Nathan, G., Medwell, P., Dally, B., and Alwahabi, Z., "Simultaneous planar measurements of temperature and soot volume fraction in a turbulent non-premixed jet flame," Proceedings of the Combustion Institute, Vol. 35, No. 2, 2015, pp. 1931–1938.

- [23] Kent, J. H. and Wagner, H. G., "Who do diffusion flames emit smoke," *Combustion science and technology*, Vol. 41, No. 5-6, 1984, pp. 245–269.
- [24] Bisetti, F., Blanquart, G., Mueller, M. E., and Pitsch, H., "On the formation and early evolution of soot in turbulent nonpremixed flames," *Combustion and Flame*, Vol. 159, No. 1, 2012, pp. 317–335.
- [25] Sun, Z., Alwahabi, Z., Gu, D., Mahmoud, S., Nathan, G., and Dally, B., "Planar laser-induced incandescence of turbulent sooting flames: the influence of beam steering and signal trapping," *Applied Physics B*, Vol. 119, No. 4, 2015, pp. 731–743.
- [26] Lee, S.-Y., Turns, S. R., and Santoro, R. J., "Measurements of soot, OH, and PAH concentrations in turbulent ethylene/air jet flames," *Combustion and Flame*, Vol. 156, No. 12, 2009, pp. 2264–2275.
- [27] Coppalle, A. and Joyeux, D., "Temperature and soot volume fraction in turbulent diffusion flames: measurements of mean and fluctuating values," *Combustion and flame*, Vol. 96, No. 3, 1994, pp. 275–285.
- [28] Colket, M., Edwards, T., Williams, S., Cernansky, N. P., Miller, D. L., Egolfopoulos, F., Lindstedt, P., Seshadri, K., Dryer, F. L., Law, C. K., et al., "Development of an experimental database and kinetic models for surrogate jet fuels," 45th AIAA Aerospace Sciences Meeting and Exhibit, 2007, pp. 8–11.
- [29] Won, S. H., Dooley, S., Veloo, P., Santner, J., Ju, Y., and Dryer, F. L., "Characterization of global combustion properties with simple fuel property measurements for alternative jet fuels," 50th AIAA/ASME/SAE/ASEE Joint Propulsion Conference, 2014, p. 3469.
- [30] Lee, S. and Tien, C., "Optical constants of soot in hydrocarbon flames," *Symposium (international) on combustion*, Vol. 18, Elsevier, 1981, pp. 1159–1166.
- [31] Chang, H. and Charalampopoulos, T., "Determination of the wavelength dependence of refractive indices of flame soot," *Proceedings of the Royal Society of London A: Mathematical, Physical and Engineering Sciences*, Vol. 430, The Royal Society, 1990, pp. 577–591.
- [32] Kohler, M., Geigle, K., Meier, W., Crosland, B., Thomson, K., and Smallwood, G., "Sooting turbulent jet flame: characterization and quantitative soot measurements," *Applied Physics B*, Vol. 104, No. 2, 2011, pp. 409–425.
- [33] Boudart, M. and Djega-Mariadassou, G., *Kinetics of heterogeneous catalytic reactions*, Princeton University Press, 2014.
- [34] Steinfeld, J. I., Francisco, J. S., and Hase, W. L., *Chemical kinetics and dynamics*, Vol. 3, Prentice Hall Englewood Cliffs (New Jersey), 1989.
- [35] Carmer, C., Weiner, B., and Frenklach, M., "Molecular dynamics with combined quantum and empirical potentials: C₂H₂ adsorption on Si (100)," *The Journal of chemical physics*, Vol. 99, No. 2, 1993, pp. 1356–1372.

- [36] Harris, J. and Kasemo, B., "On precursor mechanisms for surface reactions," *Surface Science*, Vol. 105, No. 2, 1981, pp. L281–L287.
- [37] Frenklach, M., "Reaction mechanism of soot formation in flames," *Physical Chemistry Chemical Physics*, Vol. 4, No. 11, 2002, pp. 2028–2037.
- [38] Wang, H., Abid, A., Bockhorn, H., DAnna, A., Sarofim, A., and Wang, H., "Combustion generated fine carbonaceous particles," *Proceedings of an International Workshop held in Villa Orlandi, Anacapri (May 13–16, 2007)*, Karlsruhe University Press, Karlsruhe, 2009, pp. 367–384.
- [39] Wang, H., "Formation of nascent soot and other condensed-phase materials in flames," *Proceedings of the Combustion Institute*, Vol. 33, No. 1, 2011, pp. 41–67.
- [40] Balthasar, M., Mauss, F., Knobel, A., and Kraft, M., "Detailed modeling of soot formation in a partially stirred plug flow reactor," *Combustion and Flame*, Vol. 128, No. 4, 2002, pp. 395–409.
- [41] Dato, A. and Frenklach, M., "Substrate-free microwave synthesis of graphene: experimental conditions and hydrocarbon precursors," *New Journal of Physics*, Vol. 12, No. 12, 2010, pp. 125013.
- [42] Stanmore, B. R., Brilhac, J.-F., and Gilot, P., "The oxidation of soot: a review of experiments, mechanisms and models," *Carbon*, Vol. 39, No. 15, 2001, pp. 2247–2268.
- [43] Vander Wal, R. L. and Tomasek, A. J., "Soot oxidation: dependence upon initial nanostructure," *Combustion and Flame*, Vol. 134, No. 1, 2003, pp. 1–9.
- [44] Vander Wal, R. L., Yezerets, A., Currier, N. W., Kim, D. H., and Wang, C. M., "HRTEM Study of diesel soot collected from diesel particulate filters," *Carbon*, Vol. 45, No. 1, 2007, pp. 70–77.
- [45] Ma, X., Zangmeister, C., and Zachariah, M., "Soot oxidation kinetics: a comparison study of two tandem ion-mobility methods," *The Journal of Physical Chemistry C*, Vol. 117, No. 20, 2013, pp. 10723–10729.
- [46] Radovic, L. R., "Active sites in graphene and the mechanism of CO₂ formation in carbon oxidation," *Journal of the American Chemical Society*, Vol. 131, No. 47, 2009, pp. 17166–17175.
- [47] Raj, A., Yang, S. Y., Cha, D., Tayouo, R., and Chung, S. H., "Structural effects on the oxidation of soot particles by O₂: Experimental and theoretical study," *Combustion and Flame*, Vol. 160, No. 9, 2013, pp. 1812–1826.
- [48] Jaramillo, I. C., Gaddam, C. K., Vander Wal, R. L., and Lighty, J. S., "Effect of nanos-tructure, oxidative pressure and extent of oxidation on model carbon reactivity," *Combustion and Flame*, Vol. 162, No. 5, 2015, pp. 1848–1856.

- [49] Nagle, J. and Strickland-Constable, R., "Oxidation of Carbon between 1000-2000 C," Proceedings of the fifth carbon conference, Vol. 1, Pergamon Oxford, 1962, p. 154.
- [50] Tarter, J. C., Chang, S., and Defrees, D. J., "Carbon in the Galaxy: Studies from Earth and Space," 1990.
- [51] Frenklach, M. and Wang, H., "Detailed modeling of soot particle nucleation and growth," Symposium (International) on Combustion, Vol. 23, Elsevier, 1991, pp. 1559– 1566.
- [52] Yu, T. and Lin, M., "Kinetics of the C₆H₅+ O₂ reaction at low temperatures," Journal of the American Chemical Society, Vol. 116, No. 21, 1994, pp. 9571–9576.
- [53] Frenklach, M. and Wang, H., "Detailed mechanism and modeling of soot particle formation," Soot formation in combustion, Springer, 1994, pp. 165–192.
- [54] Appel, J., Bockhorn, H., and Frenklach, M., "Kinetic modeling of soot formation with detailed chemistry and physics: laminar premixed flames of C₂ hydrocarbons," Combustion and Flame, Vol. 121, No. 1, 2000, pp. 122–136.
- [55] Frenklach, M., Schuetz, C. A., and Ping, J., "Migration mechanism of aromatic-edge growth," Proceedings of the Combustion Institute, Vol. 30, No. 1, 2005, pp. 1389–1396.
- [56] Violi, A., "Cyclodehydrogenation reactions to cyclopentafused polycyclic aromatic hydrocarbons," The Journal of Physical Chemistry A, Vol. 109, No. 34, 2005, pp. 7781– 7787.
- [57] Tokmakov, I. V., Kim, G.-S., Kislov, V. V., Mebel, A. M., and Lin, M. C., "The reaction of phenyl radical with molecular oxygen: a G2M study of the potential energy surface," The Journal of Physical Chemistry A, Vol. 109, No. 27, 2005, pp. 6114–6127.
- [58] Whitesides, R., Domin, D., Salomon'-Ferrer, R., Lester, W. A., and Frenklach, M., "Embedded-ring migration on graphene zigzag edge," Proceedings of the Combustion Institute, Vol. 32, No. 1, 2009, pp. 577–583.
- [59] Whitesides, R., Domin, D., Salomon'-Ferrer, R., Lester, W. A., and Frenklach, M., "Graphene layer growth chemistry: five-and six-member ring flip reaction," The Journal of Physical Chemistry A, Vol. 112, No. 10, 2008, pp. 2125–2130.
- [60] Whitesides, R., Kollas, A. C., Domin, D., Lester, W. A., and Frenklach, M., "Graphene layer growth: Collision of migrating five-member rings," Proceedings of the Combustion Institute, Vol. 31, No. 1, 2007, pp. 539–546.
- [61] Whitesides, R. and Frenklach, M., "Detailed kinetic Monte Carlo simulations of graphene-edge growth," The Journal of Physical Chemistry A, Vol. 114, No. 2, 2009, pp. 689–703.

- [62] Raj, A., Man, P. L., Totton, T. S., Sander, M., Shirley, R. A., and Kraft, M., "New polycyclic aromatic hydrocarbon (PAH) surface processes to improve the model prediction of the composition of combustion-generated PAHs and soot," *Carbon*, Vol. 48, No. 2, 2010, pp. 319–332.
- [63] You, X., Whitesides, R., Zubarev, D., Lester, W. A., and Frenklach, M., "Bay-capping reactions: Kinetics and influence on graphene-edge growth," *Proceedings of the Combustion Institute*, Vol. 33, No. 1, 2011, pp. 685–692.
- [64] Sendt, K. and Haynes, B. S., "Density functional study of the chemisorption of O₂ on the armchair surface of graphite," *Proceedings of the Combustion Institute*, Vol. 30, No. 2, 2005, pp. 2141–2149.
- [65] Sendt, K. and Haynes, B. S., "Density functional study of the chemisorption of O₂ on the zig-zag surface of graphite," *Combustion and flame*, Vol. 143, No. 4, 2005, pp. 629–643.
- [66] You, X., Zubarev, D. Y., Lester Jr, W. A., and Frenklach, M., "Thermal decomposition of pentacene oxyradicals," *The Journal of Physical Chemistry A*, Vol. 115, No. 49, 2011, pp. 14184–14190.
- [67] Zubarev, D. Y., Robertson, N., Domin, D., McClean, J., Wang, J., Lester Jr, W. A., Whitesides, R., You, X., and Frenklach, M., "Local Electronic Structure and Stability of Pentacene Oxyradicals," *The Journal of Physical Chemistry C*, Vol. 114, No. 12, 2009, pp. 5429–5437.
- [68] Edwards, D. E., You, X., Zubarev, D. Y., Lester, W. A., and Frenklach, M., "Thermal decomposition of graphene armchair oxyradicals," *Proceedings of the Combustion Institute*, Vol. 34, No. 1, 2013, pp. 1759–1766.
- [69] Edwards, D. E., Zubarev, D. Y., Lester Jr, W. A., and Frenklach, M., "Pathways to soot oxidation: reaction of OH with phenanthrene radicals," *The Journal of Physical Chemistry A*, Vol. 118, No. 37, 2014, pp. 8606–8613.
- [70] Zhou, C.-W., Kislov, V. V., and Mebel, A. M., "Reaction Mechanism of Naphthyl Radicals with Molecular Oxygen. 1. Theoretical Study of the Potential Energy Surface," *The Journal of Physical Chemistry A*, Vol. 116, No. 6, 2012, pp. 1571–1585.
- [71] Kislov, V., Singh, R., Edwards, D., Mebel, A., and Frenklach, M., "Rate coefficients and product branching ratios for the oxidation of phenyl and naphthyl radicals: A theoretical RRKM-ME study," *Proceedings of the Combustion Institute*, Vol. 35, No. 2, 2015, pp. 1861–1869.
- [72] Singh, R. I., Mebel, A. M., and Frenklach, M., "Oxidation of graphene-edge six- and five-member rings by molecular oxygen," *The Journal of Physical Chemistry A*, Vol. 119, No. 28, 2015, pp. 7528–7547.

- [73] Raj, A., da Silva, G. R., and Chung, S. H., "Reaction mechanism for the free-edge oxidation of soot by O₂," *Combustion and Flame*, Vol. 159, No. 11, 2012, pp. 3423– 3436.
- [74] Xu, K. and Ye, P. D., "Theoretical study on the oxidation mechanism and dynamics of the zigzag graphene nanoribbon edge by oxygen and ozone," *The Journal of Physical Chemistry C*, Vol. 118, No. 19, 2014, pp. 10400–10407.
- [75] Hernandez'-Gimenez, A., Castello, D., and Bueno-Lopez, A., "Diesel soot combustion catalysts: review of active phases," *Chemical Papers*, Vol. 68, No. 9, 2014, pp. 1154–1168.
- [76] Whitesides, R. and Frenklach, M., "Effect of reaction kinetics on graphene-edge morphology and composition," *Zeitschrift fur Physikalische Chemie*, Vol. 229, No. 4, 2015, pp. 597–614.
- [77] Gillespie, D. T., "Exact stochastic simulation of coupled chemical reactions," *The journal of physical chemistry*, Vol. 81, No. 25, 1977, pp. 2340–2361.
- [78] Gillespie, D., "Markov Processes: An Introduction for Physical Scientists (Academic, San Diego)," 1992.
- [79] Frenklach, M., "Monte Carlo simulation of diamond growth by methyl and acetylene reactions," *The Journal of chemical physics*, Vol. 97, No. 8, 1992, pp. 5794–5802.
- [80] Frenklach, M., "Monte Carlo simulation of hydrogen reactions with the diamond surface," *Physical Review B*, Vol. 45, No. 16, 1992, pp. 9455.
- [81] Radovic, L. R., Silva-Villalobos, A. F., Silva-Tapia, A. B., and Vallejos-Burgos, F., "On the mechanism of nascent site deactivation in graphene," *Carbon*, Vol. 49, No. 11, 2011, pp. 3471–3487.
- [82] Neoh, K., Howard, J., and Sarofim, A., "Soot oxidation in flames," *Particulate Carbon*, Springer, 1981, pp. 261–282.
- [83] Neoh, K., Howard, J., and Sarofim, A., "Effect of oxidation on the physical structure of soot," *Symposium (International) on Combustion*, Vol. 20, Elsevier, 1985, pp. 951– 957.
- [84] Sirignano, M., Kent, J., and DAnna, A., "Modeling formation and oxidation of soot in nonpremixed flames," *Energy & Fuels*, Vol. 27, No. 4, 2013, pp. 2303–2315.
- [85] Allinger, N. L., Yuh, Y. H., and Lii, J. H., "Molecular mechanics. The MM3 force field for hydrocarbons. 1," *Journal of the American Chemical Society*, Vol. 111, No. 23, 1989, pp. 8551–8566.
- [86] Ponder, J. W. et al., "TINKER: Software tools for molecular design," Washington University School of Medicine, Saint Louis, MO, Vol. 3, 2004.

- [87] Murry, R. L., Colt, J. R., and Scuseria, G. E., "How accurate are molecular mechanics predictions for fullerenes? A benchmark comparison with Hartree-Fock self-consistent field results," *The Journal of Physical Chemistry*, Vol. 97, No. 19, 1993, pp. 4954–4959.
- [88] Schulman, J. M. and Disch, R. L., "Bowl-shaped hydrocarbons related to C₆₀," *Journal of computational chemistry*, Vol. 19, No. 2, 1998, pp. 189–194.
- [89] Meana-Paneda, R., Truhlar, D. G., and Fernandez-Ramos, A., "High-level direct-dynamics variational transition state theory calculations including multidimensional tunneling of the thermal rate constants, branching ratios, and kinetic isotope effects of the hydrogen abstraction reactions from methanol by atomic hydrogen," *The Journal of chemical physics*, Vol. 134, No. 9, 2011, pp. 094302.
- [90] Jodkowski, J. T., Rayez, M.-T., Rayez, J.-C., Berces, T., and Dob'e, S., "Theoretical study of the kinetics of the hydrogen abstraction from methanol. 3. Reaction of methanol with hydrogen atom, methyl, and hydroxyl radicals," *The Journal of Physical Chemistry A*, Vol. 103, No. 19, 1999, pp. 3750–3765.
- [91] Hidaka, Y., Oki, T., Kawano, H., and Higashihara, T., "Thermal decomposition of methanol in shock waves," *The Journal of Physical Chemistry*, Vol. 93, No. 20, 1989, pp. 7134–7139.
- [92] Asaba, T. and Fujii, N., "High temperature oxidation of benzene," *Proc. Int. Symp. Shock Tubes Waves*, Vol. 8, 1971, pp. 1–12.
- [93] Seta, T., Nakajima, M., and Miyoshi, A., "High-temperature reactions of OH radicals with benzene and toluene," *The Journal of Physical Chemistry A*, Vol. 110, No. 15, 2006, pp. 5081–5090.
- [94] Leidreiter, H. and Wagner, H. G., "An investigation of the reaction between O (3P) and benzene at high temperatures," *Zeitschrift fur Physikalische Chemie*, Vol. 165, No. Part 1, 1989, pp. 1–7.
- [95] Dong, H., Ding, Y.-h., and Sun, C.-c., "Radical-molecule reaction C₃H+ H₂O: a mechanistic study," *The Journal of chemical physics*, Vol. 122, No. 6, 2005, pp. 064303– 064303.
- [96] Mueller, M. E. and Pitsch, H., "LES model for sooting turbulent nonpremixed flames," *Combust. Flame*, Vol. 159, 2012, pp. 2166–2180.
- [97] Pitsch, H., "Large-Eddy Simulation of turbulent combustion," *Ann. Rev. Fluid Mech.*, Vol. 38, 2006, pp. 453–482.
- [98] Mueller, M. E., Blanquart, G., and Pitsch, H., "Hybrid Method of Moments for modeling soot formation and growth," *Combust. Flame*, Vol. 156, 2009, pp. 1143–1155.
- [99] Bisetti, F., Blanquart, G., Mueller, M. E., and Pitsch, H., "On the formation and early evolution of soot in turbulent nonpremixed flames," *Combust. Flame*, Vol. 159, 2012, pp. 317–335.

- [100] Attili, A., Bisetti, F., and Mueller, M. E., "DNS of soot formation and growth in turbulent non-premixed flames: Damkohler number effects and Lagrangian statistics of soot transport," Proceedings of the Summer Program, Center for Turbulence Research, 2012, pp. 409–418.
- [101] Lignell, D. O., Chen, J. H., Smith, P. J., Lu, T., and Law, C. K., "The effect of flame structure on soot formation and transport in turbulent nonpremixed flames using direct numerical simulation," Combust. Flame, Vol. 151, 2007, pp. 2–28.
- [102] Lignell, D. O., Chen, J. H., and Smith, P. J., "Three-dimensional direct numerical simulation of soot formation and transport in a temporally evolving nonpremixed ethylene jet flame," Combust. Flame, Vol. 155, 2008, pp. 316–333.
- [103] Marchisio, D. L. and Fox, R. O., "Solution of population balance equations using the Direct Quadrature Method of Moments," J. Aerosol Sci., Vol. 36, 2005, pp. 43–73.
- [104] Frenklach, M., "Method of moments with interpolative closure," Chemical Engineering Science, Vol. 57, 2002, pp. 2229–2239.
- [105] Pierce, C. D. and Moin, P., "Progress variable approach for Large Eddy Simulation of non-premixed turbulent combustion," J. Fluid Mech., Vol. 504, 2004, pp. 73–97.
- [106] Ihme, M. and Pitsch, H., "Modeling of radiation and nitric oxide formation in turbulent nonpremixed flames using a flamelet/progress variable formulation," Phys. Fluids, Vol. 20, 2008, pp. 055110.
- [107] Mueller, M. E. and Pitsch, H., "LES subfilter modeling of soot-turbulence interactions," Phys. Fluids, Vol. 23, 2011, pp. 115104.
- [108] Qamar, N. H., Alwahabi, Z. T., Chan, Q. N., Nathan, G. J., Roekaerts, D., and King, K. D., "Soot volume fraction in a piloted turbulent jet non-premixed flame of natural gas," Combust. Flame, Vol. 156, 2009, pp. 1339–1347.
- [109] Yuan, C., Laurent, F., and Fox, R. O., "An extended quadrature method of moments for population balance equations," J. Aerosol Sci., Vol. 51, 2012, pp. 1–23.
- [110] Karatas, A. E. and Gulder, O. L., "Soot formation in high pressure laminar diffusion flames," Progress in Energy and Combustion Science, Vol. 38, No. 2, 2012, pp. 818–845.
- [111] McCrain, L. L. and W.L.Roberts, "Measurements of the soot volume field in laminar diffusion flames at elevated pressures," Combustion and Flame, Vol. 140, 2005, pp. 60– 69.
- [112] Liu, F., Thomson, K. A., Guo, H., and Smallwood, G. J., "Numerical and experimental study of an axisymmetric coflow laminar methane?air diffusion flame at pressures between 5 and 40 atmospheres," Combustion and Flame, Vol. 146, No. 3, 2006, pp. 456–471.

- [113] Charest, M. R. J., Joo, H. I., Gulder, O. L., and Groth, C. P. T., "Experimental and numerical study of soot formation in laminar ethylene diffusion flames at elevated pressures from 10 to 35 atm," *Proceedings of the Combustion Symposium*, Vol. 33, No. 1, 2011, pp. 549–557.
- [114] Consalvi, J.-L. and Liu, F., "Numerical study of the effects of pressure on soot formation in laminar coflow n-heptane/air diffusion flames between 1 and 10 atm," *Proceedings of the Combustion Institute*, Vol. 35, No. 2, 2015, pp. 1727–1734.
- [115] Mueller, M. E. and Pitsch, H., "Large eddy simulation of soot evolution in an aircraft combustor," *Physics of Fluids*, Vol. 25, 2013, pp. 110812.
- [116] Raman, V. and Fox, R. O., "Modeling of fine-particle formation in turbulent flames," *Annual Review of Fluid Mechanics*, Vol. 48, 2016, pp. 159–190.
- [117] Attili, A., Bisetti, F., Mueller, M. E., and Pitsch, H., "Formation, growth, and transport of soot in a three-dimensional turbulent non-premixed jet flame," *Combustion and Flame*, Vol. 171, No. 7, 2014, pp. 1849–1865.
- [118] Qamar, N., Alwahabi, Z., Chan, Q., Nathan, G., Roekaerts, D., and King, K., "Soot volume fraction in a piloted turbulent jet non-premixed flame of natural gas," *Combustion and Flame*, Vol. 156, No. 7, 2009, pp. 1339–1347.
- [119] Mueller, M. E., Chan, Q. N., Qamar, N. H., Dally, B. B., Pitsch, H., Alwahabi, Z. T., and Nathan, G. J., "Experimental and computational study of soot evolution in a turbulent nonpremixed bluff body ethylene flame," *Combustion and Flame*, Vol. 160, 2013, pp. 1298–1309.
- [120] Poinsot, T. and Veynante, D., *Theoretical and Numerical Combustion*, R. T. Edwards, Philadelphia, USA, 2001.
- [121] Koo, H., Raman, V., Mueller, M. E., and Geigle, K. P., "Large-eddy simulation of a turbulent sooting flame in a swirling combustor," 53rd AIAA Aerospace Science Meeting, No. AIAA 2015-0167, 2015.
- [122] di Mare, F., "LES of a gas turbine combustor," *The Combustion Institute - British Section Autumn Research Meeting*, 2002.
- [123] Xuan, Y. and Blanquet, G., "Effects of aromatic chemistry-turbulence interactions on soot formation in a turbulent non-premixed flame," *Proceedings of the Combustion Institute*, Vol. 35, No. 2, 2015, pp. 1911–1919.
- [124] Chittipotula, T., Janiga, G., and Thevenin, D., "Optimizing soot prediction models for turbulent non-premixed ethylene/air flames," *Chemical Engineering Science*, Vol. 70, 2012, pp. 67–76.
- [125] El-Asrag, H. and Menon, S., "Large eddy simulation of soot formation in a turbulent non-premixed jet flame," *Combustion and Flame*, Vol. 156, 2009, pp. 385–395.

- [126] Geigle, K. P., Hadef, R., and Meier, W., "Soot Formation and Flame Characterization of an Aero-Engine Model Combustor Burning Ethylene at Elevated Pressure," *Journal of Engineering for Gas Turbines and Power*, Vol. 136, 2014, pp. 021505.
- [127] Geigle, K. P., Kohler, M., O'Loughlin, W., and Meier, W., "Investigation of soot formation in pressurized swirl flames by laser measurements of temperature, flame structures and soot concentrations," *Proceedings of the Combustion Symposium*, Vol. 35, 2015, pp. 3373–3380.
- [128] Geigle, K. P., O'Loughlin, W., Hadef, R., and Meier, W., "Visualization of soot inception in turbulent pressurized flames by simultaneous measurement of laser-induced fluorescence of polycyclic aromatic hydrocarbons and laser-induced incandescence, and correlation to OH distributions," *Applied Physics B*, Vol. 119, No. 4, 2015, pp. 717–730.
- [129] Eberle, C., Gerlinger, P., Geigle, K. P., and Aigner, M., "Soot Predictions in an Aero-Engine Model Combustor at Elevated Pressure Using URANS and Finite-Rate Chemistry," *50th AIAA/ASME/SAE/ASEE Joint Propulsion Conference*, No. AIAA 2014-3472, 2014.
- [130] Mueller, M. E. and Pitsch, H., "LES models for sooting turbulent nonpremixed flames," *Combustion and flame*, Vol. 159, 2012, pp. 2166–2180.
- [131] Mueller, M. E., Blanquart, G., and Pitsch, H., "Hybrid Method of Moments for Modeling Soot Formation and Growth," *Combustion and Flame*, Vol. 156, 2009, pp. 1143– 1155.
- [132] Mueller, M. E., Large eddy simulation of soot evolution in turbulent reacting flows, Ph.D. thesis, Stanford University, 2012.
- [133] Pope, S. B., *Turbulent Flows*, Cambridge University Press, 2000.
- [134] Pope, S. B., "Ten Questions Concerning the Large-Eddy Simulation of Turbulent Flows," *New Journal of Physics*, Vol. 6, No. 35, 2004.
- [135] Blanquart, G., Pepiot-Desjardins, P., and Pitsch, H., "Chemical mechanism for high temperature combustion of engine relevant fuels with emphasis on soot precursors," *Combustion and Flame*, Vol. 156, No. 3, 2009, pp. 588–607.
- [136] Narayanaswamy, K., Blanquart, G., and Pitsch, H., "A Consistent Chemical Mechanism for Oxidation of Substituted Aromatic Species," *Combustion and Flame*, Vol. 157, 2010, pp. 1879–1898.
- [137] Widenhorn, A., Noll, B., Stohr, M., and Aigner, M., "Numerical characterization of the non-reacting flow in a swirled gasturbine model combustor," *High Performance Computing in Science and Engineering*, 2008, pp. 431–444.
- [138] Widenhorn, A., Noll, B., and Aigner, M., "Numerical Characterization of a Gas Turbine Model Combustor," *High Performance Computing in Science and Engineering*, 2010, pp. 179–195.

- [139] Donde, P., Raman, V., Mueller, M. E., and Pitsch, H., "LES/PDF based modeling of soot-turbulence interactions in turbulent flames," Proceedings of the Combustion Institute, Vol. 34, 2013, pp. 1183–1192.
- [140] The second international sooting flame workshop, 2014.
- [141] Pierce, C. D. and Moin, P., "Progress-variable Approach for Large-Eddy Simulation of Non-Premixed Turbulent Combustion," Journal of Fluid Mechanics, Vol. 504, 2004, pp. 73–97.
- [142] Mueller, M. E. and Pitsch, H., "Large eddy simulation subfilter modeling of soot-turbulence interactions," Physics of fluids, Vol. 23, 2011, pp. 115104.
- [143] Blanquart, G. and Pitsch, H., Combustion Generated Fine Carbonaceous Particles, Karl-sruhe University Press, 2009.
- [144] Frenklach, M. and Wang, H., "Detailed modeling of soot particle nucleation and growth," Proceedings of the Combustion Institute, Vol. 23, 1991, pp. 1559–1566.
- [145] "The Open Source CFD Toolbox," OpenCFD Inc. <http://www.openfoam.com/>.
- [146] Chapuis, M., Fedina, E., Fureby, C., Hannemann, K., Karl, S., and Schramm, J. M., "A computational study of the HyShot II combustor performance," Proceedings of the Combustion Institute, Vol. 34, 2013, pp. 2101–2109.
- [147] Koo, H., Hassanaly, M., Raman, V., Mueller, M. E., and Geigle, K. P., "Large-eddy simulation of soot formation in a model gas turbine combustor," ASME Turbo Expo 2016, No. GT2016-57952, 2016.
- [148] Lietz, C., Heye, C., Raman, V., and Blunck, D., "Flame Stability Analysis in an Ultra Compact Combustor Using Large-Eddy Simulation," 52nd AIAA Aerospace Science Meeting, No. AIAA 2014-1022, 2014.
- [149] Kim, J., Moin, P., and Moser, R. D., "Turbulence Statistics in Fully Developed Channel Flow at low Reynolds Number," Journal of Fluid Mechanics, Vol. 177, 1987, pp. 133–166.
- [150] Desjardins, O., Moureau, V., and Pitsch, H., "An accurate conservative level set/ghost fluid method for simulating turbulent atomization," Journal of Computational Physics, Vol. 227, 2008, pp. 8395–8416.
- [151] Ferziger, J. H. and Peric, M., Computational Methods for Fluid Dynamics, Springer, 3rd ed., 2002.
- [152] Mahesh, K., Constantinescu, G., and Moin, P., "A Numerical Method for Large-Eddy Simulation in Complex Geometries," Journal of Computational Physics, Vol. 197, 2004, pp. 215–240.

- [153] Morinishi, Y., Lund, T. S., Vasilyev, O. V., and Moin, P., "Fully conservative higher order finite difference schemes for incompressible flow," *Journal of Computational Physics*, Vol. 143, No. 1, 1998, pp. 90–124.
- [154] Issa, R. I., "Solution of the Implicitly Discretised Fluid Flow Equations by Operator-Splitting," *Journal of Computational Physics*, Vol. 62, 1985, pp. 40–65.
- [155] Lietz, C. and Raman, V., "Large Eddy Simulation of Flame Flashback in Swirling Premixed CH₄/H₂-Air Flames," 53rd AIAA Aerospace Science Meeting, No. AIAA 2015-0844, 2015.
- [156] Kim, J. and Moin, P., "Application of a fractional-step method to incompressible Navier-Stokes equations," *Journal of Computational Physics*, Vol. 59, No. 2, 1985, pp. 308–323.
- [157] Akselvoll, K. and Moin, P., "Large Eddy Simulation of Turbulent Confined Coannular Jets," *Journal of Fluid Mechanics*, Vol. 315, 1996, pp. 387–411.
- [158] Pierce, C. D., Progress-variable approach for large-eddy simulation of turbulence combustion, Ph.D. thesis, Stanford University, 2001.
- [159] Lietz, C., Tang, Y., Koo, H., Hassanaly, M., and Raman, V., "Large eddy simulation of a high-pressure multi-jet combustor using flamelet modeling," 10th OpenFOAM Workshop, 2015.
- [160] Morinishi, Y., "Skew-symmetric form of convective terms and fully conservative finite difference schemes for variable density low-Mach number flows," *Journal of Computational Physics*, Vol. 229, 2010, pp. 276–300.
- [161] Felten, F. N. and Lund, T. S., "Kinetic energy conservation issues associated with the collocated mesh scheme for incompressible flow," *Journal of Computational Physics*, Vol. 215, 2006, pp. 465–484.
- [162] Kravchenko, A. G. and Moin, P., "On the Effect of Numerical Errors in Large Eddy Simulations of Turbulent Flows," *Journal of Computational Physics*, Vol. 131, 1997, pp. 310–322.
- [163] Nicoud, F., "Conservative High-order Finite-difference Schemes for Low-Mach Number Flows," *Journal of Computational Physics*, Vol. 158, 2000, pp. 71–97.
- [164] Jameson, A., "Aerodynamic design via control theory," *Journal of Scientific Computing*, Vol. 3, 1988, pp. 233–260.
- [165] Baysal, O. and Eleshaky, M. E., 29th Aerospace Sciences Meeting and Exhibit, No. AIAA 92-0471, American Institute of Aeronautics and Astronautics, 1991.
- [166] Jameson, A., Pierce, N., and Martinelli, L., 35th Aerospace Sciences Meeting and Exhibit, No. AIAA 97-0101, American Institute of Aeronautics and Astronautics, 1997.

- [167] Reuther, J., Alonso, J., Rimlinger, M., and Jameson, A., "Aerodynamic shape optimization of supersonic aircraft configurations via an adjoint formulation on distributed memory parallel computers," *Computers & Fluids*, Vol. 28, No. 45, 1999, pp. 675 – 700.
- [168] Giles, M. and Pierce, N., "An Introduction to the Adjoint Approach to Design," *Flow, Turbulence and Combustion*, Vol. 65, 2000, pp. 393–415.
- [169] Kim, S., Alonso, J., and Jameson, A., 40th Aerospace Sciences Meeting and Exhibit, No. AIAA 2002-0844, American Institute of Aeronautics and Astronautics, 2002.
- [170] Nadarajah, S. and Jameson, A., 38th Aerospace Sciences Meeting and Exhibit, No. AIAA 2000-0667, American Institute of Aeronautics and Astronautics, 2000.
- [171] Gunzburger, M., Hou, L., and Svobodny, T., "Boundary velocity control of incompressible flow with an application to viscous drag reduction," *SIAM J. Control Optim.*, Vol. 30, No. 1, Jan. 1992, pp. 167–181.
- [172] Bewly, T., Moin, P., and Temam, R., "DNS-based predictive control of turbulence: an optimal benchmark for feedback algorithms," *Journal of Fluid Mechanics*, Vol. 447, 10 2001, pp. 179–225.
- [173] Wei, M. and Freund, J. B., "A noise-controlled free shear flow," *Journal of Fluid Mechanics*, Vol. 546, Dec. 2005, pp. 123.
- [174] Freund, J., Kim, J., and Bodony, D., "Adjoint-Based Optimal Control of a Mach 1.3 Turbulent Jet for Noise Reduction," 49th AIAA Aerospace Sciences Meeting including the New Horizons Forum and Aerospace Exposition, American Institute of Aeronautics and Astronautics, 2011.
- [175] Sandu, A., Daescu, D., and Carmichael, G. R., "Direct and adjoint sensitivity analysis of chemical kinetic systems with KPP: Part I—theory and software tools," *Atmospheric Environment*, Vol. 37, 2003, pp. 5083–5096.
- [176] Sandu, A., Daescu, D. N., Carmichael, G. R., and Chai, T., "Adjoint sensitivity analysis of regional air quality models," *Journal of Computational Physics*, Vol. 204, No. 1, 2005, pp. 222 – 252.
- [177] Sandu, A. and Zhang, L., "Discrete second order adjoints in atmospheric chemical transport modeling," *Journal of Computational Physics*, Vol. 227, No. 12, 2008, pp. 5949 – 5983.
- [178] Ranzi, E., Frassoldati, A., Grana, R., Cuoci, A., Faravelli, T., Kelley, A., and Law, C., "Hierarchical and comparative kinetic modeling of laminar flame speeds of hydrocarbon and oxygenated fuels," *Progress in Energy and Combustion Science*, Vol. 38, No. 4, 2012, pp. 468 – 501.